Alma Mater Studiorum – Università di Bologna

DOTTORATO DI RICERCA IN

Meccanica e scienze avanzate dell'ingegneria
Progetto n° 4: Meccanica dei materiali e processi tecnologici

Ciclo XXIII

**Settore scientifico-disciplinare di afferenza:** ING-IND/18

# MODELLING, DIAGNOSTICS AND TRANSPORT PROPERTIES OF THERMAL PLASMAS FOR INDUSTRIAL APPLICATIONS

**Presentata da:** **Paolo Sanibondi**

**Coordinatore Dottorato** **Relatore**

**Prof. Giangiacomo Minak** **Prof. Emanuele Ghedini**

**Esame finale anno 2011**

# INDEX

# INTRODUCTION

Thermal plasma science is a challenging field among applied physics on which numerous industrial applications have been developed such as spray deposition, cutting, welding, extractive metallurgy, waste treatment, and nano-powder synthesis. These processes are characterized by an atmospheric pressure partially ionized plasma discharge in which complex and still not completely understood mass, momentum and energy transport phenomena occur, which depend strongly on the choice of device geometries and of different operating conditions. As a consequence, key concepts in innovative solutions for thermal plasma industrial technologies are based on a deeper understanding of plasma physics.

During my three years Ph.D. course at DIEM, University of Bologna, I've been involved in the activities of the *Research group for industrial application of thermal plasmas* and I focused my studies on the development of different techniques for the investigation of thermal plasmas devices, with particular attention to plasma physics: modelling, diagnostics and transport properties.

In particular, I worked on the calculation of thermodynamic and transport properties for different mixtures of industrial interest. I developed self-consistent codes for the calculation of equilibrium composition, of atomic and molecular partition functions, and of collision integrals through an adaptive triple integration method. I developed codes for the calculation of equilibrium and non-equilibrium transport properties using two state-of-the-art methods. Results of these activities will be presented in *Chapter 2 - "Equilibrium and non-equilibrium thermodynamic and transport properties of thermal plasma for industrial applications"* and they have been reported in the following papers published on international journals:

1. Colombo V, Ghedini E, Sanibondi P, "Thermodynamic and transport properties in non-equilibrium argon, oxygen and nitrogen thermal plasmas", Progress in Nuclear Energy 50 (2008) 921
2. Colombo V, Ghedini E, Sanibondi P, "Two-temperature thermodynamic and transport properties of argon-hydrogen and nitrogen-hydrogen plasmas", J. Phys. D: Appl. Phys. 42 (2009) 055213
3. Colombo V, Ghedini E, Sanibondi P, "Two-temperature thermodynamic and transport properties of carbon-oxygen plasmas", accepted for publication in Plasma Sources Sci. Technol. (2011)

Also, some results have been presented at international conferences:

1. Colombo V, Ghedini, Sanibondi P, "Thermodynamic and transport properties of carbon-oxygen mixtures in non-equilibrium" oral presentation at ICTT-2009
2. Colombo V, Ghedini E, Sanibondi P, "Thermodynamic and transport properties of H35 and F5 plasma cutting mixtures in non-equilibrium", oral presentation at 35th IEEE International Conference on Plasma Science, 2008

Moreover, I contributed to the improvement of a computational tool for the modelling of inductively coupled RF plasma torches, transferred arc DC plasma torches and

hybrid DC-RF plasma torches, with particular interest for the application of these models to the investigation of the treatment of micro-sized powders, of non-equilibrium phenomena, and of the synthesis of nano-powders. I developed a library written in C language to customize the commercial software ANSYS FLUENT to include an accurate description of the diffusion of binary mixtures of gases through a "combined" approach, a non-equilibrium two-temperature model and a model for the synthesis of nano-powders through the "moment" method. This research has been part of the SIMBA project founded by the 7$^{th}$ European Framework Programme, FP7-NMP-2008-SMALL-2. Results from these activities will be presented in *Chapter 3 - Modelling of Inductively Coupled Plasma Torches for industrial applications* and in *Chapter 4 – SIMBA-Scaling-up of ICP technology for continuous production of metallic nanopowders for battery applications*. These results have been reported in the following papers on international journals:

1. Colombo V, Ghedini E, Sanibondi P, "Three-dimensional investigation of particle treatment in a RF thermal plasma with reaction chamber", Plasma Sources Sci. Technol. 19 (2010) 065024
2. Colombo V, Ghedini E, Sanibondi P, "3-D static and time-depending modelling of DC and RF thermal plasmas for industrial applications", Advances in Science and Technology 66 (2010) 1-10
3. Colombo V, Ghedini E, Sanibondi P, "A three-dimensional investigation of the effects of excitation frequency and sheath gas mixing in an atmospheric-pressure inductively-coupled plasma system", J. Phys. D: Appl. Phys. 43 (2010) 105202
4. Colombo V, Ghedini E, Boselli M, Sanibondi P and Concetti A, "3D static and time-dependent modelling of a dc transferred arc twin torch systems" accepted for publication in J. Phys. D: Appl. Phys.
5. Boselli M, Colombo V, Ghedini E and Sanibondi P, "Time Dependent Modelling of Droplet Detachment in GMAW Including Metal Vapor Diffusion", submitted to IEEE-TPS Image in Plasma Science
6. Colombo V, Concetti A, Ghedini E, Gherardi M and Sanibondi P, "3-D Time-Dependent Large Eddy Simulation of Turbulent Flows in an Inductively Coupled Thermal Plasma Torch with Reaction Chamber", submitted to IEEE-TPS Image in Plasma Science

Also, some results have been presented at international conferences:

1. Colombo V, Ghedini E, Boselli M, Concetti A and Sanibondi P, "3D time-depending modelling of a DC transferred arc twin torch system" oral presentation at European Plasma Conference, HTPP-11, Brussels, 27 June - 2 July, 2010
2. Colombo V, Ghedini E, Gherardi M and Sanibondi P "Three-dimensional simulations of RF thermal plasma torches with reaction chamber: process design for powder spheroidization, waste treatment and nanopowder production" poster presentation at European Plasma Conference, HTPP-11, Brussels, 27 June - 2 July, 2010
3. Colombo V, Ghedini E, Sanibondi P, "3D static and time-depending modelling of DC and RF thermal plasmas for industrial applications" invited lecture at CIMTEC 2010, Montecatini Terme, Tuscany, Italy, June 6-18 2010

4. Colombo V, Ghedini E, Boselli M, Sanibondi P, “3D Static and Time-Dependent Modelling of a DC Transferred Arc Twin Torch System with LTE and 2T models”, oral presentation at Round table on the characterization of Thermal Plasmas, Alexandria, Egypt, 2009
5. Colombo V, Ghedini E, Sanibondi P, “3-D simulations of particle heating in ICP torches with reaction chamber: effect of flow rate, composition, power and frequency”, poster presentation at 19th International Symposium on Plasma Chemistry, Bochum, Germany, July 26th - 31st, 2009

In this research field, I’ve been supervisor for the following MA thesis:

1. F. Federici "Design Oriented Modelling of DC-RF Thermal Plasma Sources", University of Bologna, June 2010
2. F. D'Alessandris “Analisi fisica e modellazione del processo di sintesi di nanopolveri assistita da sorgenti di plasma termico RF”, University of Bologna, March 2010
3. M. Gherardi “Analisi fisica e modellazione della sintesi di nanopolveri con sorgenti di plasma termico ad induzione”, University of Bologna, October 2009,
4. M. Boselli “Modellazione 3D dipendente dal tempo e in non-L.T.E. di una sorgente DC ad arco trasferito in configurazione twin-torch”, Univerisità di Bologna, March 2009

Moreover, I designed and installed at UNIBO laboratories a set of diagnostic systems - a Schlieren optical apparatus, an Optical Emission Spectroscopy (OES) system, a multi-view system for high-speed (HS) imaging and an apparatus for calorimetric measurements on ICP torches – for the analysis of thermal plasma torches. The Schlieren apparatus has been used to investigate fluid dynamic turbulent patterns in plasma arc cutting torches during the cutting phase. The recently developed OES system will be used to investigate temperature and electron density fields in both DC and RF plasma torches. The multi-view HS imaging system has been used to investigate pilot arc phase in DC cutting torches with the aid of a 3D image reconstruction of the arc through a tomographic reconstruction code that I developed.
The calorimetric apparatus has been used to investigate the lab-scale ICP torch efficiency at DIEM laboratories. Results obtained in this field will be presented in *Chapter 5 – Diagnostic tools for the investigation of thermal plasmas* and they have been published in:

1. Cantoro G, Colombo V, Concetti A, Ghedini E, Sanibondi P and Zinzani F, Rotundo F, Dallavalle S and Vancini M, "Plasma arc cutting technology: simulation and experiments" J. Phys.: Conf. Ser. 275 (2011) 012008
2. Boselli M, Cantoro G, Colombo V, Concetti A, Ghedini E, Gherardi M, Sanibondi P, “High-Speed Imaging in PAC: Multiple View and Tomographic Reconstruction of Pilot Arcing Transients”, submitted to IEEE-TPS Image in Plasma Science
3. Cantoro G, Colombo V, Concetti A, Ghedini E, Sanibondi P and Zinzani F, “Statistical Analysis of High-Speed Schlieren Imaging in PAC”, submitted to IEEE-TPS Image in Plasma Science

Also, results have been presented at international conferences:

1. Colombo V, Concetti A, Ghedini E, Sanibondi P, Rotundo F, Dallavalle S, Vancini M, “Plasma arc cutting technology: simulation and experiments” invited lecture at GD2010, Greifswald, Germany
2. Cantoro G, Colombo V, Concetti A, Ghedini E, Sanibondi P and Zinzani F, "Plasma arc cutting technology: simulation and experiments" oral presentation at European Plasma Conference, HTPP-11, Brussels, 27 June - 2 July, 2010
3. Colombo V, Concetti A, Ghedini E, Sanibondi P, Dallavalle S, Vancini M, “Recent advancements in plasma arc cutting research at UNIBO. Part I: high speed imaging of transient phenomena and Schlieren photography”, oral presentation at Round table on the characterization of Thermal Plasmas, Alexandria, Egypt, 2009

In this research field, I’ve been supervisor for the following MA and BA thesis:

1. F. Zinzani "Elaborazione statistica di dati da diagnostica high-speed schlieren imaging per l'analisi di deflussi turbolenti in plasmi termici", Università di Bologna, March 2010, MA thesis
2. F. Mossa “Diagnostica High Speed Imaging e fotografia Schlieren su plasmi termici ad arco per il taglio di materiali metallici”, Università di Bologna, 2009, MA thesis

During my Ph.D. thesis, I obtained some preliminary results in collaboration with Prof. Valerian Nemchinsky - now at Keiser University, Florida, USA – on the investigation of the anode region of high intensity arcs at atmospheric pressure in presence of metallic vapours and on the estimation of particle charging effects in nanopowder synthesis in RF plasma torches. These results will be reported in *Chapter 6 - Investigation on the effects of metallic vapours on the characteristics of the anode layer in high-intensity current arc*.

Finally, I worked at the ENVIREN regional research project for the investigation of the treatment of incinerator wastes in RF thermal plasma torches. In this field, I’ve been supervisor of the following MA and BA thesis:

1. D. Zanini “Metodologie per il trattamento dei rifiuti mediante plasma termico: vetrificazione, trattamento in-fly e con sonda ad iniezione di liquidi”, Univesità di Bologna, December 2010, MA thesis
2. L. Gasperini “Trattamenti assistiti da plasma termico induttivo per la valorizzazione di fly-ash e bottom-ash provenienti da processi di termovalorizzazione di rifiuti”, University of Bologna, 2009, BA thesis

# EQUILIBRIUM AND NON-EQUILIBRIUM THERMODYNAMIC AND TRANSPORT PROPERTIES OF THERMAL PLASMA FOR INDUSTRIAL APPLICATIONS

In this chapter, some results of the activities carried out during my Ph.D. course on the computation of thermodynamic and transport properties will be presented. These results have been already published in international journals[1-3]. My main contribution has been in the development of different C libraries for the computation of plasma composition, atomic and molecular partition functions, transport collision integrals, thermodynamic properties, and transport properties in both equilibrium and non-equilibrium conditions. In particular, non-equilibrium transport properties have been computed using two different state-of-the-art approaches. These codes have been tested and validated through comparisons with available data reported in literature.

## Introduction

In thermal plasma science, modelling plays an important role for understanding and predicting the physical behaviour of industrial technologies. Industrial plasma devices, which span on numerous fields such as deposition, cutting, welding, extractive metallurgy, waste destruction, and nanopowder synthesis, are characterized by an atmospheric pressure partially ionized plasma discharge, which falls in the field of thermal plasmas, and by the use of a wide variety of gas mixtures, depending on the specific application.

In plasma simulations, mass, momentum and energy equations, together with electromagnetic field equations, have to be solved with a coupled approach and the accuracy of results depends strongly on the use of suitable thermodynamic and transport properties.

Calculation of transport properties can be quite easily done using simplifying assumptions for the limiting cases of weakly ionized gases (Lorentzian limit) and fully ionized gases (Spitzer and Harm formulas), which is the case for thermonuclear fusion plasmas. For partially ionized gases composition is more difficult to determine and the previously mentioned simplifications can no longer be done, while a rigorous method must be used.

Methods for the computation of partially ionized thermal plasma properties have been widely studied in local thermodynamic equilibrium (LTE) and some results are reported in literature for the most commonly used pure gases and mixtures [4-8]. Thermodynamic properties computation is based on the kinetic theory for ideal gases while the calculation of transport properties is based on the solution of Boltzmann's equation using the Chapman-Enskog's method[9]. The distribution function for different species is assumed to be a Maxwellian with a first-order perturbation function which is developed in the form of a series of Sonine polynomials: this reduces the Boltzmann equation to a set of linear equations whose solution allows one to obtain transport properties. The coefficients of the set of linear equations depend on collision integrals which take into account the binary interaction between colliding species: computation of these data requires the knowledge of either the interaction potential,

which describes the collision dynamics, or requires the transport cross sections, which can be derived from differential cross sections, quantum phase shifts or experimental data.

The first part of my activities during the Ph.D. course was devoted to the development of C libraries for the calculation of transport properties for pure gases and simple mixtures in local thermodynamic equilibrium. Results obtained have been compared with data reported in literature with the final aim of validate the developed code.

However, the development and use of more and more sophisticated plasma diagnostics has shown that the assumption of local thermodynamic equilibrium often fails in thermal plasmas [10-12]: the kinetic temperature of electrons, $T_e$, can be considered different from that of heavy species, $T_h$, close to the arc electrodes or in the fringes of the arc jet because of the high temperature gradients, of the high imposed electrical field or the high stream velocity (e.g. inside nozzles of cutting torches). For the computation of non-equilibrium thermodynamic and transport properties, two local thermal non-equilibrium (NLTE) theories have been developed: Devoto[13] and Bonnefoi[14] developed a simplified theory assuming decoupling between heavy particles and electrons; recently, Rat et al. [15] developed a theory in which the coupling between particles and electrons is not neglected, giving raise to a new set of transport coefficients and coupling terms in the fluxes definition.

Thermodynamic and transport properties depend strongly on gas composition and the development of codes for their computation in custom mixtures becomes essential in industrially oriented research; such data can be found in literature mainly under LTE hypothesis and for monoatomic gases. Further work is mandatory to improve and expand available data to non-equilibrium conditions and to check the effects of different theoretical approaches and of uncertainty collisional cross sections on resulting plasma properties. Moreover, modelling of thermal plasma sources for industrial applications often requires knowledge of scarcely available non-equilibrium diatomic gases properties, like oxygen and nitrogen, since they are often used as plasma generation gases and they reach heavy particles temperature up to 30,000 K.

Transport properties in NLTE have been already calculated for pure gases (Ar, $O_2$, $N_2$, $H_2$) and for mixtures (Ar-$H_2$, Ar-$O_2$, Ar-$N_2$) with a simplified theory [11, 16-18]; applications of the new theory of Rat et al. have been already presented for Ar, Ar-He, Ar-Cu and Ar-$H_2$-He plasmas [19-21].
Ghorui et al.[12] showed that in modelling of plasma cutting torches chemical non-equilibrium effects can significantly affect the results. In order to take into account this effects in a thermal plasma modelling code, the calculation of thermodynamic and transport properties is needed at every iteration step of the fluid dynamic and diffusion equations solver, since plasma composition is no more the equilibrium one. Tabulation of these properties could simplify and speed up the calculation, but it can become a very difficult task to perform, especially in multispecies plasmas, due to the dependence of thermodynamic and transport properties on several parameters (temperature of electrons and heavy particles, number density of the various species), leading to a very huge and complex properties database.

During my Ph.D. activity I developed different C libraries for the computation of transport properties in non-equilibrium. Both the method of Devoto and the method o

Rat have been implemented in these libraries allowing the comparison between results obtained using the two approaches. Results for the computation of thermodynamic and transport properties of Ar, $O_2$, $N_2$ pure gases in non-equilibrium and of Ar-$H_2$, $N_2$-$H_2$ and C-$O_2$ mixtures in non-equilibrium will be presented.

**Properties of Ar, $O_2$ and $N_2$**

The aim of this study is to develop a code for the computation of thermodynamic and transport properties for both LTE and NLTE plasmas with arbitrary composition and to extend the temperature range of calculation of plasma properties for argon, oxygen and nitrogen with respect to existing literature.
Nitrogen transport properties in NLTE have been reported by Aubreton[17] for heavy particles temperature up to 15,000 K, which is a not sufficiently wide temperature range to cover all thermal plasmas applications, especially for plasma arc cutting.
Transport properties calculations are carried out using the electron and heavy particles decoupling approach of Devoto[13], since results coming from this theory, with the exception of diffusion coefficients, show only slight differences from that obtainable from the theory of Rat et al.
Non-equilibrium thermodynamic and transport properties at atmospheric pressure for argon, oxygen and nitrogen with electron temperature up to 45,000 K are presented. Argon and nitrogen properties have been calculated extending the temperature range currently available in literature. Oxygen properties have been calculated and compared with Ghorui et al. [18] taking into account also $O^{3+}$. Dependence of particle number densities, specific volume, specific enthalpy, specific heat, thermal conductivity, electrical conductivity and viscosity on electron temperature and on different degrees of non-equilibrium are reported. Results are compared with available data from literature in order to check the accuracy of the developed codes.

*Calculation of plasma composition*

Thermodynamic and transport properties calculation, both in LTE and NLTE, depends on plasma composition. The chemical equilibrium composition as function of temperature is used in this work for the calculation of these properties.
The appropriate method for the determination of chemical equilibrium number density in two-temperature plasmas has long been a subject of debate. In the present work, the method of Ghorui et al.[18] and Van de Sanden et al. [22] has been used.
A Maxwellian distribution of velocity characterized by the temperature $T_h$ is assumed for heavy species, while electrons have the temperature $T_e$. The parameter of thermal non-equilibrium is defined as

$$\theta = T_e/T_h \quad (1)$$

The set of equation used for the computation of number densities as a function of temperature and θ is

$$\frac{n_e n_{a^{(z+1)}}}{n_{a^{(z)}}} = 2\left(\frac{2\pi m_e k T_e}{h^2}\right)^{3/2} \frac{Q^{int}_{a^{(z+1)}}(T_e)}{Q^{int}_{a^{(z)}}(T_e)} \exp\left(-\frac{E_{a^{(z+1)}}}{kT_e}\right) \quad (2)$$

$$\frac{n_a^2}{n_m} = \frac{\left(Q^{tr}_a(T_h)\right)^2}{Q^{tr}_m(T_h)} \frac{\left(Q^{int}_a(T_e)\right)^2}{Q^{int}_m(T_h)} \exp\left(-\frac{E_m}{kT_h}\right) \quad (3)$$

$$\sum_{i}^{species} n_i Z_i = 0 \qquad (4)$$

$$p = n_e k T_e + \sum_{i}^{heavy} n_i k T_h \qquad (5)$$

Equation 2 is the chemical equilibrium equation for the ionization process proposed by Van de Sanden; equation 3 is the chemical equilibrium equation for the dissociation process used by Ghorui et al.

$Q^{tr}_i$ and $Q^{int}_i$ are the translational and internal partition function of the species i, respectively; $E_i$ is the formation energy of the species i; the subscript $a^{(z)}$ and m indicates z-times ionized species and molecules, respectively; $n_i$ and $Z_i$ are the particle density and the charge of species i, respectively.

The formation energy for electrons and neutral atoms are null; for positive ions the formation energy is equal to the energy required for ionization; for molecules $E_m$ is the dissociation energy with negative sign.

From the results reported by Rat et al.[23] it seems that a different ionization equilibrium equation was used instead of equation 2; in order to make comparison of our results with transport properties reported by Rat et al., composition of argon is also computed using a modified ionization equilibrium equation instead of 2:

$$\frac{n_e n_{a^{(z+1)}}}{n_{a^{(z)}}} = 2\left(\frac{2\pi m_e k T_e \theta}{h^2}\right)^{3/2} \frac{Q^{int}_{a^{(z+1)}}(T_e)}{Q^{int}_{a^{(z)}}(T_e)} \exp\left(-\frac{E_{a^{(z+1)}}}{kT_e}\right) \qquad (6)$$

Both sets of equations are solved using a robust algorithm, proposed by [24], originally suited for the computation of compositions in LTE, and extended by the authors to the case of NLTE plasmas.

The species considered are molecules, neutrals, electrons and ions up to the third degree of ionization.

Composition of an argon plasma is obtained considering the species Ar, $Ar^+$, $Ar^{2+}$, $Ar^{3+}$, $Ar^{4+}$ and $e^-$. For oxygen we considered $O_2$, O, $O^-$, $O^+$, $O^{2+}$, $O^{3+}$ and $e^-$; for nitrogen $N_2$, N, N+, $N^{2+}$,$N^{3+}$ and $e^-$. Data of electron energy levels of atoms and ions for the computation of internal partition function have been taken from NIST database; rotational and vibrational constants for molecules have been taken from JANAF tables. Ionization and dissociation energies are reported in table 1.

Table 1. Ionization and dissociation enrgy of different species

| Species | Energy [eV] | Species | Energy [eV] | Species | Energy [eV] |
|---|---|---|---|---|---|
| $Ar$ | 15.76 | $O$ | 13.62 | $N$ | 14.53 |
| $Ar^+$ | 27.63 | $O^+$ | 35.12 | $N^+$ | 29.6 |
| $Ar^{2+}$ | 40.74 | $O^{2+}$ | 54.93 | $N^{2+}$ | 47.45 |
| $Ar^{3+}$ | 59.81 | $O^{3+}$ | 77.42 | $N^{3+}$ | 77.48 |
| $Ar^{4+}$ | 75.01 | $O_2$ | 5.12 | $N_2$ | 9.76 |

*Calculation of partition function*

The knowledge of partition function is a prerequisite for the computation of chemical equilibrium composition.
The translational partition function is given by

$$Q_i^{tr} = \left( \frac{2\pi m_i k T_i}{h^2} \right)^{3/2} \quad (7)$$

where h is the Planck's constant.
The internal partition function of an atom or molecule is given by the sum of the electronic, rotational and vibrational contributions.
For a monoatomic gas only the electronic contribution must be considered and the internal partition function can be written as

$$Q_i^{int} = \sum_{n}^{\epsilon_n < E_i} g_n \, e^{-\epsilon_n / k T_e} \quad (8)$$

where $\varepsilon_n$ and $g_n$ are the energy and the statistical weight corresponding to the n-th energy level, respectively. The reduction of the apparent ionization potential due to the Coulomb forces has a negligible effect on the number density of species which are present in significant concentrations at atmospheric pressure and in the computation of transport properties; therefore we decided not to include this effect in our calculations.
The internal partition function for a molecule, as reported by Drellishak[25], can be written as

$$Q_m^{int} = \frac{1}{\sigma} \sum_{n} g_n \, e^{-\epsilon_{el}/k T_e} \sum_{v}^{v_{max}} \sum_{J}^{J_{max}} (2J+1) \, e^{-(\epsilon_{vib}+\epsilon_{rot})/k T_h} \quad (9)$$

where $g_n$ is the statistical weight of the electronic energy levels and $\varepsilon_{el}$, $\varepsilon_{rot}$, $\varepsilon_{vib}$ are the energy of the electronic, vibrational and rotational state, respectively; $\sigma$ is a symmetry factor that has value 1 and 2 for heteronuclear and homonuclear molecules, respectively; n, v and J are quantum number of the electronic, vibrational and rotational energy level, respectively; $v_{max}$ e $J_{max}$ identify the maximum quantum number for the vibrational and rotational energy levels: in general, we have $v_{max}$ = f(n) and $J_{max}$ = f(n,v). Maximum quantum number $v_{max}(n)$ of vibration energy levels is computed as the minimum v for which the vibrational energy is grater than the dissociation energy $D_0(n)$ of the molecule in the n-th electronic state.
The electronic energy levels of monoatomic gases are tabulated but the vibrational and rotational energy levels of molecules have to be computed starting from their spectroscopic constants.

The vibration energy of the v-th vibrational state and n-th electronic state can be computed as

$$\frac{\epsilon_{vib}(n,v)}{h\,c} = \omega_e\left(v+\frac{1}{2}\right) - \omega_e x_e\left(v+\frac{1}{2}\right)^2 + \omega_e y_e\left(v+\frac{1}{2}\right)^3 + \omega_e z_e\left(v+\frac{1}{2}\right)^4 \quad (10)$$

where $\omega_e$, $\omega_e x_e$, $\omega_e y_e$ e $\omega_e z_e$ are the spectroscopic constants of the n-th electronic state of the molecule.
The rotational energy of the molecule is given by

$$\frac{\epsilon_{rot}(n,v,J)}{h\,c} = B_v J(J+1) - D_v J^2(J+1)^2 \quad (11)$$

where

$$B_v = B_e - \alpha_e(v+\frac{1}{2}) \quad (12)$$

$$D_v = D_e - \beta_e(v+\frac{1}{2}) \quad (13)$$

where $B_e$, $D_e$, $\alpha_e$ and $\beta_e$ are spectroscopic constant corresponding to the n-th electronic state.
Maximum quantum number $J_{max}(n,v)$ of rotational energy levels can be computed following Drellishak.
When the equilibrium radii $r_e(n)$, the depth of the potential well $D_e'(n) = D_0(n) + \varepsilon_{vib}(n,0)$ and spectroscopic constant $B_e(n)$ and $\omega e(n)$ of the n-th electronic state are known, the potential energy for a diatomic irrotational (J = 0) molecule can be written as a function of internuclear distance through the Morse potential:

$$U_0(r) = D_e'\left(1 - e^{-2\beta\xi}\right) \quad (14)$$

where

$$\xi = (r - r_e)/r_e \quad (15)$$

$$\beta = \frac{\omega_e}{4\sqrt{B_e D_e'}} \quad (16)$$

When J≠0 the potential energy is given by the Morse potential plus the centrifugal potential:

$$U_J(r) = D_e'\left(1 - e^{-2\beta\xi}\right) + \frac{h}{8\pi^2 c\mu r^2}J(J+1) \quad (17)$$

where h is the Planck constant and μis the reduced mass of the two atoms in the molecule.
For a given n and v, varying J we have different curves for the potential energy.
These curves present a local maximum for radii greater than $r_e$, if $0<J<J_{max}$.
With J=0 the Morse potential alone doesn't present a local maximum; with $J>J_{max}$ the curve of potential energy doesn't have a minimum for stable states.
$J_{max}$ is a function of n and v and can be calculated with the comparison between the rovibrational energy and the energy corresponding to the local maximum of the potential energy: for a given n and v, $J_{max}$ is the minimum J for which the rovibrational energy is grater than the local maximum of the potential energy.
The radii $r_m$ corresponding to the local maximum of the potential energy is computed equating to zero the derivative of equation 17 with respect to r; the potential energy in this point is $U_{max} = U_J(r_m)$.
The rovibrational energy is given by the sum of vibrational energy 10 and rotational energy 11.

*Thermodynamic properties*

Once composition and partition functions are known, it is possible to compute the thermodynamic properties. Density, specific volume and specific gas constant can be written as

$$\rho = \sum_i n_i m_i \quad (18)$$

$$v = \frac{1}{\rho} \quad (19)$$

$$\bar{R} = \frac{p\,n}{\rho \sum_i n_i T_i} \quad (20)$$

where

$$n = \sum_i n_i$$

Internal energy can be calculated considering the translational, reactional and internal contributions:

$$e = \frac{3}{2}\frac{k}{\rho}\sum_i n_i T_i + \frac{1}{\rho}\sum_i n_i E_i + \frac{k}{\rho}\sum_i n_i T_i^2 \frac{\partial \ln Q_i^{int}}{\partial T_i} \quad (21)$$

Total specific enthalpy and total specific heat can be written as

$$h = \frac{5}{2}\frac{k}{\rho}\sum_i n_i T_i + \frac{1}{\rho}\sum_i n_i E_i + \frac{k}{\rho}\sum_i n_i T_i^2 \frac{\partial \ln Q_i^{int}}{\partial T_i} \quad (22)$$

$$c_p = \frac{\partial h}{\partial T_e} \quad (23)$$

*Method for the calculation of transport properties*

The computation of transport properties is done using the Chapman-Enskog method, assuming that the particle distribution function is a first order perturbation to the Maxwellian distribution; the perturbation is then expressed in series of Sonine polynomials, finally leading to a system of linear equation that can be suitably solved to obtain different transport properties.
In this work, both for LTE and NLTE plasmas the computation has been carried out using the expressions reported by Devoto[26]: this approach assumes complete decoupling between electrons and heavy species resulting in transport properties which are electrons dependent, functions of the temperature $T_e$, and in transport properties heavy species dependent, functions of the temperature $T_h$.

Thermal conductivity can be divided into translational, reactive and internal components. Following Devoto's approach the translational component can be written as the sum of the electron translational thermal conductivity and the heavy species translational thermal conductivity. So thermal conductivity can be written as:

$$\lambda = \lambda_{tr,e} + \lambda_{tr,h} + \lambda_r + \lambda_{int} \quad (24)$$

The electron translational thermal conductivity can be computed in the third order approximation as

$$\lambda_{tr,e} = \frac{75 n_e^2 k}{8}\left(\frac{2\pi k T_e}{m_e}\right)^{1/2} \frac{q^{22}}{q^{11}q^{22} - (q^{12})^2} \quad (25)$$

where $q^{mp}$ are terms reported by Devoto which take into account collision integrals.
The heavy species translational thermal conductivity can be written in the second order approximation as

$$\lambda_{tr,h} = -\frac{75k}{8}\frac{\sqrt{2\pi k T_h}}{|q|}\begin{vmatrix} q_{ij}^{00} & q_{ij}^{01} & 0 \\ q_{ij}^{10} & q_{ij}^{11} & n_i \\ 0 & n_j/\sqrt{m_j} & 0 \end{vmatrix} \quad (26)$$

where the terms $q_{ij}^{mp}$ follow the convention

$$q_{hk}^{mp} = \begin{matrix} q_{11}^{mp} & \cdots & q_{1N}^{mp} \\ \cdots & \cdots & \cdots \\ q_{N1}^{mp} & \cdots & q_{NN}^{mp} \end{matrix} \quad (27)$$

and N is the number of species. The terms $q_{hk}^{mp}$, which take into account collision integrals, are reported by Devoto[27].
The reaction thermal conductivity describes the thermal transport induced when products of reactions release the reaction enthalpy, when the reverse reaction occurs after diffusion into a lower temperature region.
For LTE plasmas with M independent species, it is given by the expression reported by Brokaw[28]:

$$\lambda_r = -\frac{1}{kT^2\,|A|}\begin{vmatrix} A_{11} & \cdots & A_{1M} & \Delta H_1 \\ \vdots & & \vdots & \vdots \\ A_{M1} & \cdots & A_{MM} & \Delta H_M \\ \Delta H_1 & \cdots & \Delta H_M & 0 \end{vmatrix} \quad (28)$$

where $\Delta H_i$, reaction enthalpy of the i-th reaction, can be written as

$$\Delta H_i = \sum_{k=1}^{M} \nu_{ik} h_k \quad (29)$$

where $\nu_{ik}$ are the stoichiometric coefficients of the reaction and $h_k$ are the enthalpies of the k-th species present in the reaction computed as

$$h_k = \frac{5}{2}kT + E_k + kT^2 \frac{\partial \ln Q_k^{int}}{\partial T} \quad (30)$$

Coefficients $A_{ij}$ are computed as

$$A_{ij} = \sum_{k=1}^{M-1} \sum_{l=k+1}^{M} \left(\frac{kT}{p\,D_{kl}^b}\right) x_k x_l \left[\left(\frac{\nu_{ik}}{x_k}\right) - \left(\frac{\nu_{il}}{x_l}\right)\right]\left[\left(\frac{\nu_{jk}}{x_k}\right) - \left(\frac{\nu_{jl}}{x_l}\right)\right] \quad (31)$$

where $x_k$ is the molar fraction of the k-th species; the terms $D_{kl}^b$ are the binary diffusion coefficients for the k-th and l-th species computed as

$$D_{kl}^{b} = \frac{3}{16 \sum_k n_k} \left( \frac{2\pi kT}{\mu_{kl}} \right)^{1/2} \frac{1}{\bar{Q}_{kl}^{(1,1)}} \quad (32)$$

where $Q_{ij}^{(1,1)}$ is the first order collision integral given by the expression (38).
For LTE plasmas, the internal thermal conductivity is given, under the assumption of Eucken[9], by the expression:

$$\lambda_{int} = \frac{p}{kT} \sum_j \frac{x_j c_{\mathrm{pint},j}}{\sum_i x_i / D_{ij}^{b}} \quad (33)$$

where the internal specific heat of the j-th species can be written as

$$c_{\mathrm{pint},j} = \frac{\partial h_i}{\partial T} - \frac{5}{2} k \quad (34)$$

In this work, NLTE reactive thermal conductivity has not been presented because there still exist some difficulties in calculating this property: in fact methods presented in literature require the NLTE diffusion coefficients which can be exactly computed with the non-simplified theory of Rat only.
Also, NLTE internal conductivity has not been reported because its contribution can be neglected.

Viscosity in the first order approximation is given by

$$\eta = \frac{5(2\pi kT_h)^{\frac{1}{2}}}{2|\hat{q}|} \begin{vmatrix} \hat{q}_{hk}^{00} & n_h m_h^{\frac{1}{2}} \\ n_k & 0 \end{vmatrix} \quad (35)$$

where the elements $q_{ij}^{mp}$, which take into account collision integrals, are reported in by Devoto[27].

Electrical conductivity can be computed using the expression reported by Ghorui et al. [18], neglecting the contribution of the ions:

$$\sigma = 3 \left( \frac{\pi}{2kT_e m_e} \right)^{1/2} \frac{e^2 n_e^2}{|q|} \begin{vmatrix} q^{11} & q^{12} \\ q^{21} & q^{22} \end{vmatrix} \quad (36)$$

*Collision integrals*

Expressions for transport properties contain determinants that depend on collision integrals, which are averages over a Maxwellian distribution of the transport collision cross-sections for the binary interaction between species.
For NLTE plasmas collision integrals have to be computed at the impact temperature $T^{*}_{ij}$ as proposed by Ghorui et al.:

$$T_{ij}^{*} = \frac{m_i T_j + m_j T_i}{m_i + m_j} \quad (37)$$

Collision integrals for interaction between species i and j are defined as

$$\bar{Q}_{ij}^{(l,s)}(T_{ij}^{*}) = \frac{2(l+1)}{(s+1)!(2l+1-(-1)^{l})} \int_0^{+\infty} e^{-x} x^{s+1} Q_{ij}^{(l)} \, \mathrm{d}x \quad (38)$$

where

$$x = \mu_{ij} g^2 / 2kT_{ij}^{*}.$$

In this work they were obtained in different ways. In a few cases, tabulations of collision integrals have been published and these could be used directly.
Otherwise, the transport cross section $Q_{ij}^{(l)}$ of order l can be computed as:

$$Q_{ij}^{(l)} = 2\pi \int_0^{+\infty} (1 - \cos^{l}\chi) \, b \, \mathrm{d}b \quad (39)$$

where b and χ are the impact parameter and the angle of deflection, respectively; the latter being given by the expression:

$$\chi = \pi - \int_{r_c}^{\infty} \frac{\mathrm{d}r / r^2}{[1 - 2v(r)/\mu_{ij} g^2 - b^2/r^2]} \quad (40)$$

where r and v(r) are the distance and the interaction potential between particles respectively.
When differential cross section data are available, transport cross sections can be calculated through the following expression:

$$Q_{ij}^{(l)} = \int_0^{\pi} (1 - \cos^{l}\chi) \sigma(\chi) \sin\chi \mathrm{d}\chi \quad (41)$$

For interaction with charge exchange transport cross section are given by

$$Q_{ij}^{(l)} = (A - B \ln g)^2 \quad (42)$$

where g is the relative velocity between particles; A and B are experimental constants.
When quantum effects become important in collision dynamics, computation of transport cross sections with the method of phase shift has been carried out, using the expressions reported by Devoto[26].

Tables 2, 3 and 4 summarize the methods used for the computation of collision integrals for each binary interaction and references for data needed as inputs.
Collision integrals for argon are computed as in the work of Rat et al.[23]; for oxygen and nitrogen we use those reported by Murphy[5].

Computation of transport properties up to the third order requires the knowledge of collision integrals $Q_{ij}^{(l,s)}$ with l and s satisfying the following conditions: $1 \leq l \leq 3$, $l \leq s \leq 6\text{-}l$.
For neutral-neutral, neutral-electron and neutral-ion interactions, transport cross sections can be calculated from the interaction potentials, from the differential cross sections or from the quantum phase shifts. Collision integrals not available in literature have been calculated using first order experimental transport cross section or total cross section data. For an M - $M^+$ interaction, the resonant charge exchange prevails when l is odd in collision integrals.
For elastic interaction Ar-$Ar^+$, collision integrals with l even were computed using different interaction potentials for the six states of the molecules $Ar_2^+$; experimental data were adjusted to an HH potential for distances near that of equilibrium while for long distances we have used a spline interpolation.
Finally, the collision integrals for the charged-charged interactions were calculated using the screened Coulomb potential, with Debye length defined as

$$\lambda_D = \sqrt{\epsilon_0 \, k \, T_e / e^2 \, n_e} \qquad (43)$$

The Debye length definition used by Ghorui et al. in the computation of oxygen transport properties is given by

$$\lambda_D = \left[ \frac{e^2}{\epsilon_0 k} \left( \frac{n_e}{T_e} + \sum_{i \neq e} \frac{Z_i^2 n_i}{T_i} \right) \right]^{-1/2} \qquad (44)$$

Since from the results for argon reported by Rat et al. it seems that Coulomb collision integrals were evaluated using a Debye length definition different from equation 43, in this work calculation of transport properties for argon has been carried out also using a modified Debye length definition which we suppose Rat et al. had used:

$$\lambda_D = \sqrt{\epsilon_0 \, k \, T_h / e^2 \, n_e} \qquad (45)$$

Table 2 – Methods for the computation of collision integrals for argon species

| Interaction | Method |
|---|---|
| $Ar - Ar$ | HFDTCS2 potential |
| $e - Ar$ | phase shift (0.01≤E≤1 eV |
| | phase shift (1≤E≤10 eV) |
| | diff. cross sections (E≥10 |
| $Ar - Ar^+$ elastic | HH potential, type 1 |
| $Ar - Ar^+$ inelastic | charge exchange |
| $X^{2+} - X, Y$ | polarization potential |
| $X^{3+} - X, Y$ | polarization potential |
| charged species | analytic formulas |

Table 3 – Methods for the computation of collision integrals for oxygen species

| Interaction | Method |
|---|---|
| $O_2 - O_2$ | ESMSV potential |
| $O_2 - O$ | repulsive exponential potential |
| $O - O$ | tabulated collision integrals |
| $e - O_2$ | tabulated collision integrals |
| $e - O$ | tabulated collision integrals |
| $O_2^+ - O_2$ elastic | Morse potential |
| $O_2^+ - O_2$ inelastic | charge exchange |
| $O_2^+ - O$ | polarization potential |
| $O^- - O_2$ | polarization potential |
| $O^- - O$ elastic | polarization potential |
| $O^- - O$ inelastic | charge exchange |
| $O^+ - O_2$ | polarization potential |
| $O^+ - O$ | tabulated collision integrals |
| $X^{2+} - X, Y$ | polarization potential |
| $X^{3+} - X, Y$ | polarization potential |
| charged species | analytic formulas |

Table 4 – Methods for the computation of collision integrals for nitrogen species

| Interaction | Method |
|---|---|
| $N_2 - N_2$ | repulsive exponential potential |
| $N_2 - N$ | repulsive exponential potential |
| $N - N$ | tabulated collision integrals |
| $e - N_2$ | integration of transport cross sections |
| $e - N$ | integration of cross sections |
| $N_2^+ - N_2$ elastic | polarization potential |
| $N_2^+ - N_2$ inelastic | integration of cross sections |
| $N_2^+ - N$ | polarization potential |
| $N^+ - N_2$ elastic | polarization potential |
| $N^+ - N_2$ inelastic | integration of cross sections |
| $N^+ - N$ | tabulated collision integrals |
| $X^{2+} - X, Y$ | polarization potential |
| $X^{3+} - X, Y$ | polarization potential |
| charged species | analytic formulas |

*Results*

Thermodynamic and transport properties both in LTE and NLTE for argon, oxygen and nitrogen at atmospheric pressure in the temperature range of 300-45,000 K are presented. Results for values of the non-equilibrium parameter $\theta = T_e/T_h = 1, 2, 3$ are reported.

Composition of argon, oxygen and nitrogen plasmas as a function of electron temperature for different values of θ are presented in figures 1, 7 and 13, respectively. Computation of plasma composition has been carried out using the generalized Saha equation 2 for ionization equilibrium and equation 3 for dissociation equilibrium, using $T_e$ and $T_h$ in the exponential term, respectively. Equation 3 led to a composition with a dissociation shift towards higher electron temperature as θ increases. Argon plasma composition has been computed also using equation 6 instead of 2, leading to a more pronounced increase of ion and electron densities, as θ increases. Results for composition are in good agreement with data reported by Boulos et al.[4] in LTE and by Ghorui et al.[18] in NLTE; using equation 6, results for argon composition are in agreement with those of Rat.

Specific volume, specific gas constant, Debye length (according to equation 44), total specific enthalpy and total specific heat are reported in figures 2 - 6 for argon, in figures 8 - 12 for oxygen and in figures 14 - 18 for nitrogen, as a function of electron temperature for different values of θ.
For fixed electron temperature, the specific volume decreases as θ increases.
For total specific enthalpy and total specific heat we see different behaviors when we use different equations for ionization equilibrium: in fact for argon (figure 5), when equation 2 has been used, enthalpy always decreases for increasing values of θ; when

equation 6 has been used, enthalpy increases with θ in those range of electron temperature where ionization takes place; also, we see a great decrease in oxygen and nitrogen enthalpy (figures 11 and 17) in the range of electron temperature where dissociation takes place.
Argon specific heat peaks due to ionization shift towards higher electronic temperature as θ increases when equation 2 has been used (figure 6); peaks shift towards lower temperature when equation 6 has been used. For oxygen and nitrogen (figures 12 and 18), the ionization peaks slightly shift towards higher electron temperature as θ increases; the oxygen and nitrogen dissociation peaks are governed by the heavy particle temperature: as θ increases peaks shift toward higher electron temperature; for nitrogen we can see the dissociation peak and the ionization one at the same electron temperature for θ = 3.

For thermodynamic properties, results obtained with our code are in good agreement with data reported by Boulos et al. for LTE and by Ghorui et al. for oxygen in NLTE (see figures 5, 11 and 17); for temperature higher than 40,000 K results obtained with our code for oxygen in NLTE differ slightly from those of Ghorui et al. because they didn't consider $O^{3+}$.

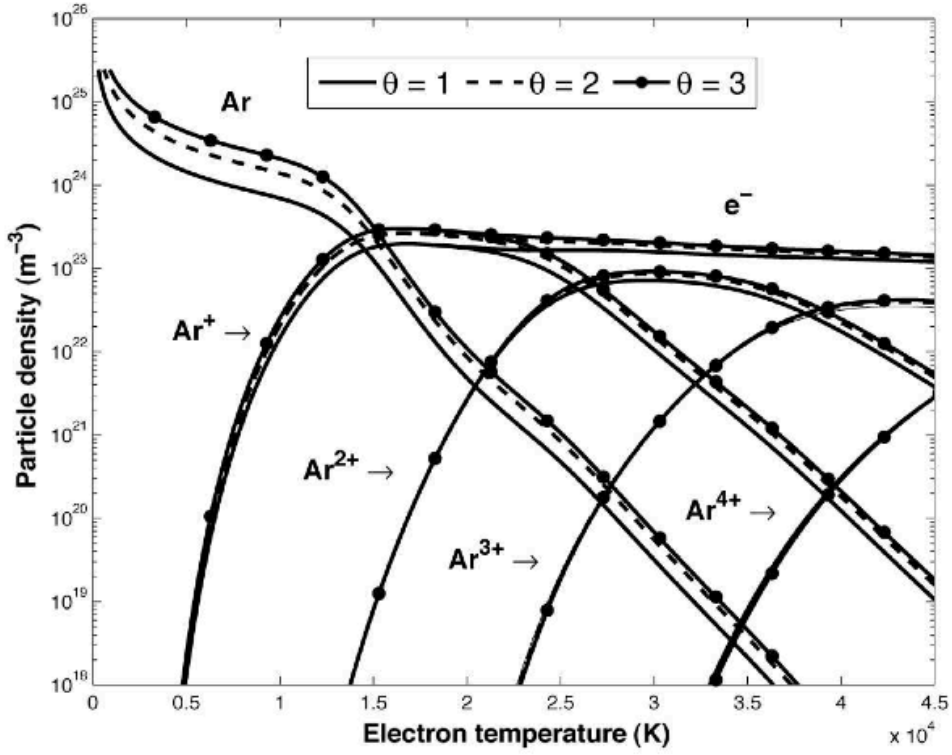


Fig. 1 - Argon composition in LTE and NLTE (taken from Ref. [1])

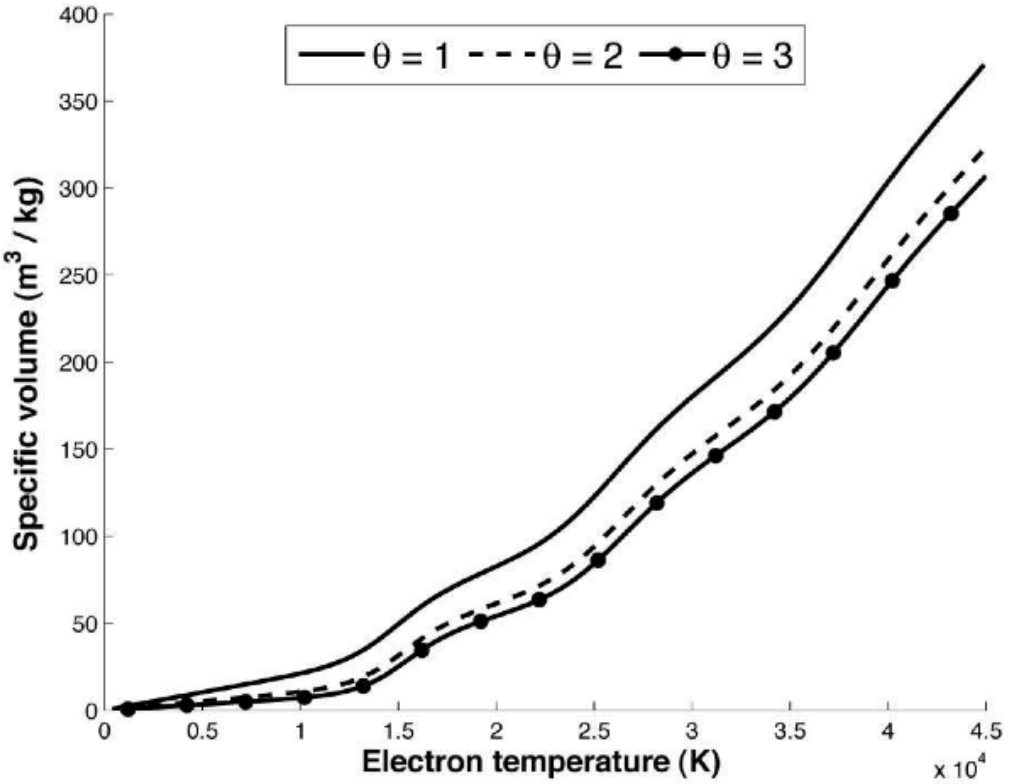


Fig. 2 - Argon specific volume in LTE and NLTE (taken from Ref. [1])

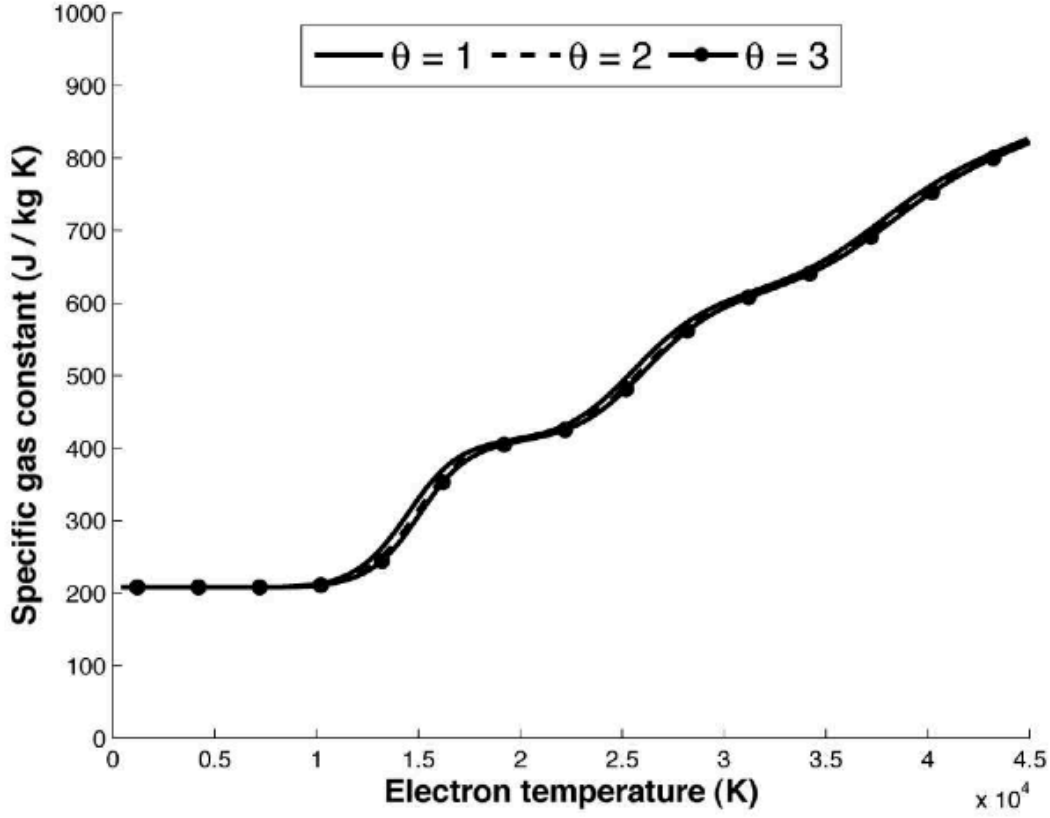


Fig. 3 - Argon specific gas constant in LTE and NLTE (taken from Ref. [1])

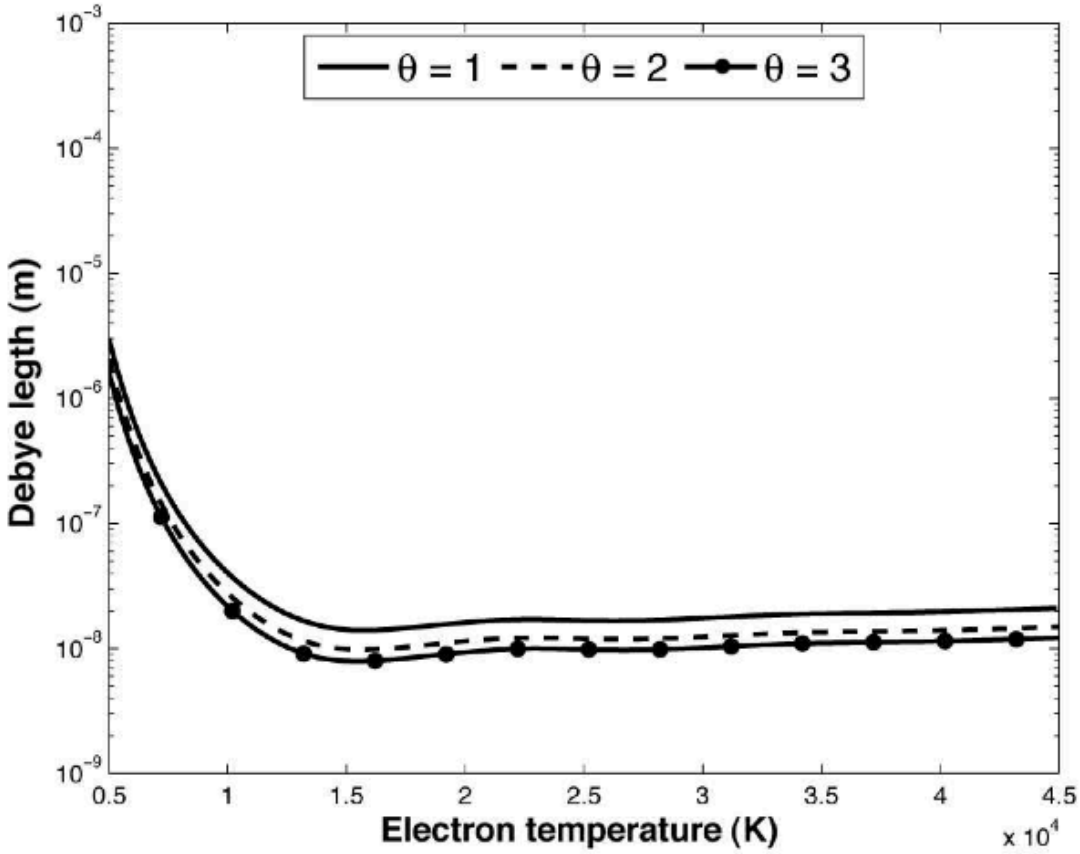


Fig. 4 - Argon Debye length in LTE and NLTE (taken from Ref. [1])

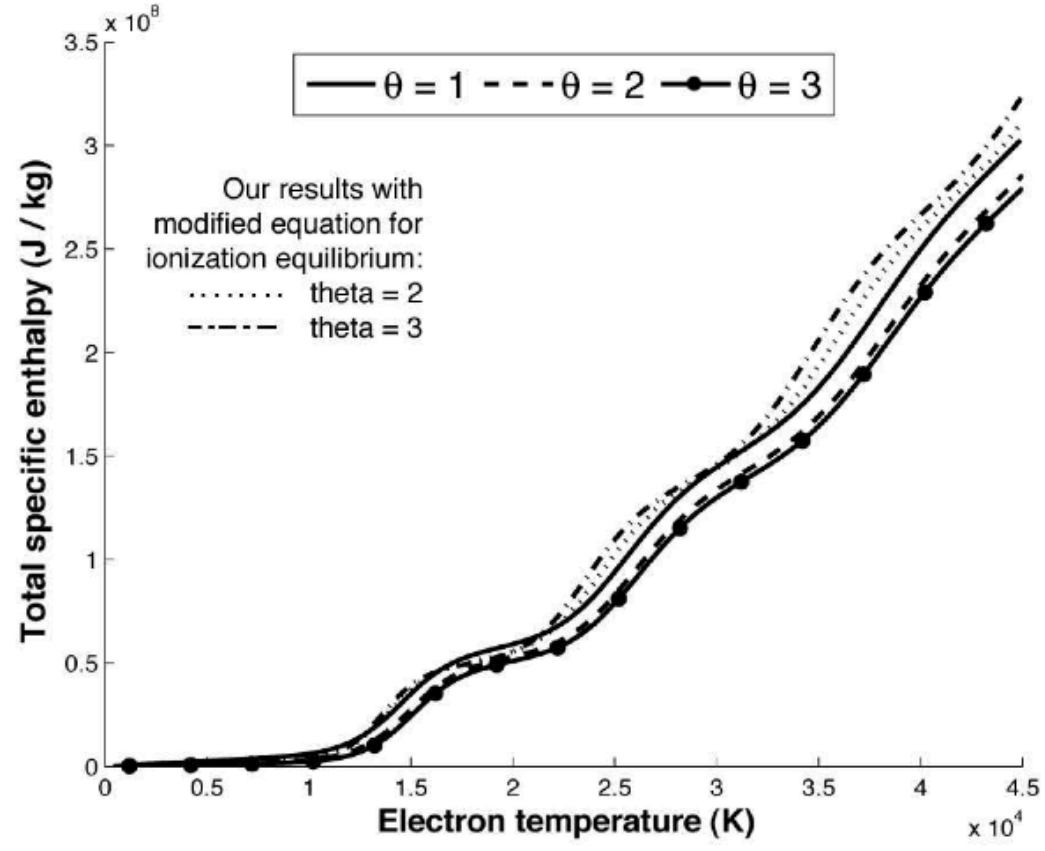


Fig. 5 - Argon total specific enthalpy in LTE and NLTE (taken from Ref. [1])

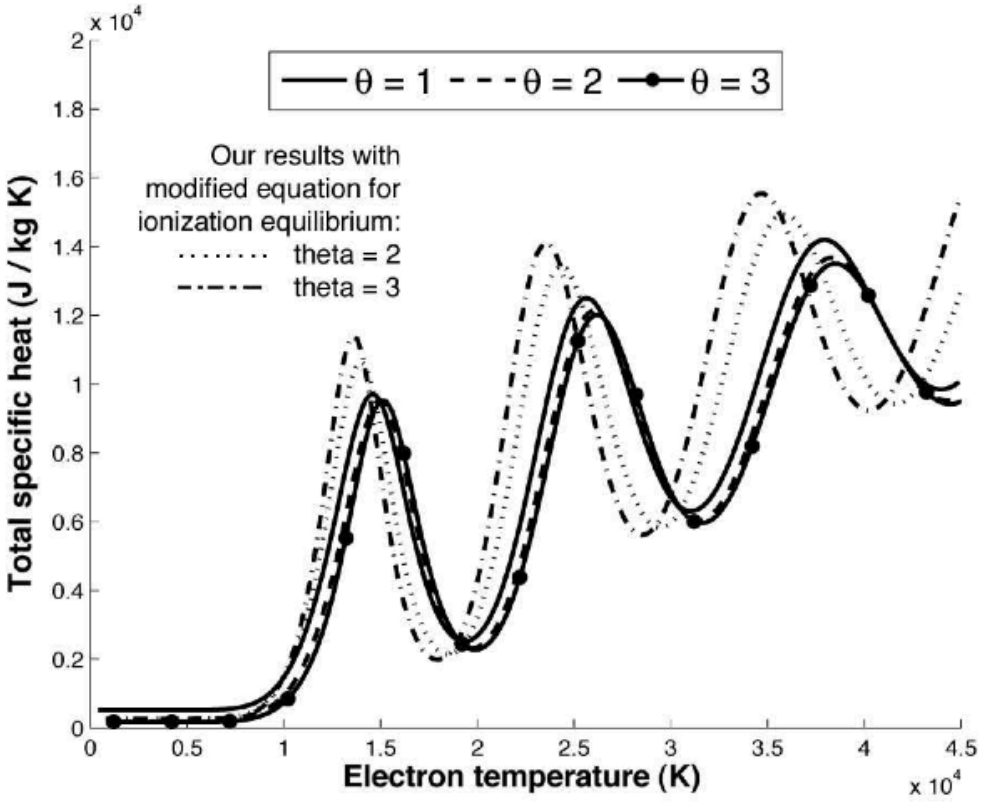


Fig. 6 - Argon total specific heat in LTE and NLTE (taken from Ref. [1])

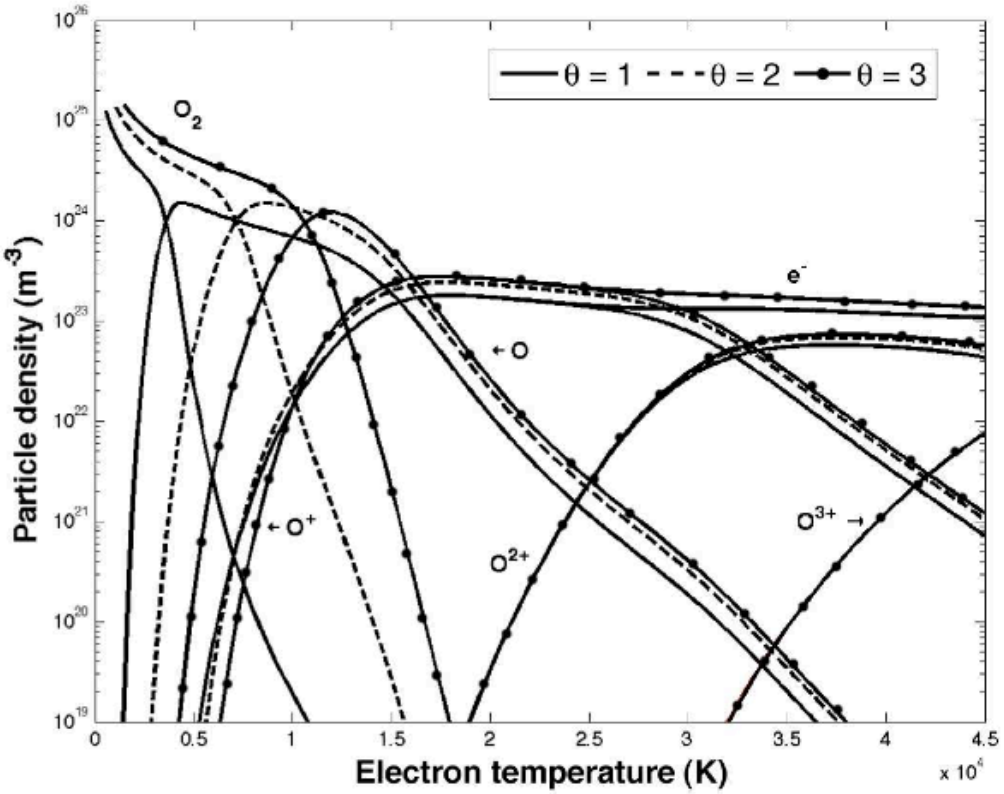


Fig. 7 - Oxygen composition in LTE and NLTE (taken from Ref. [1])

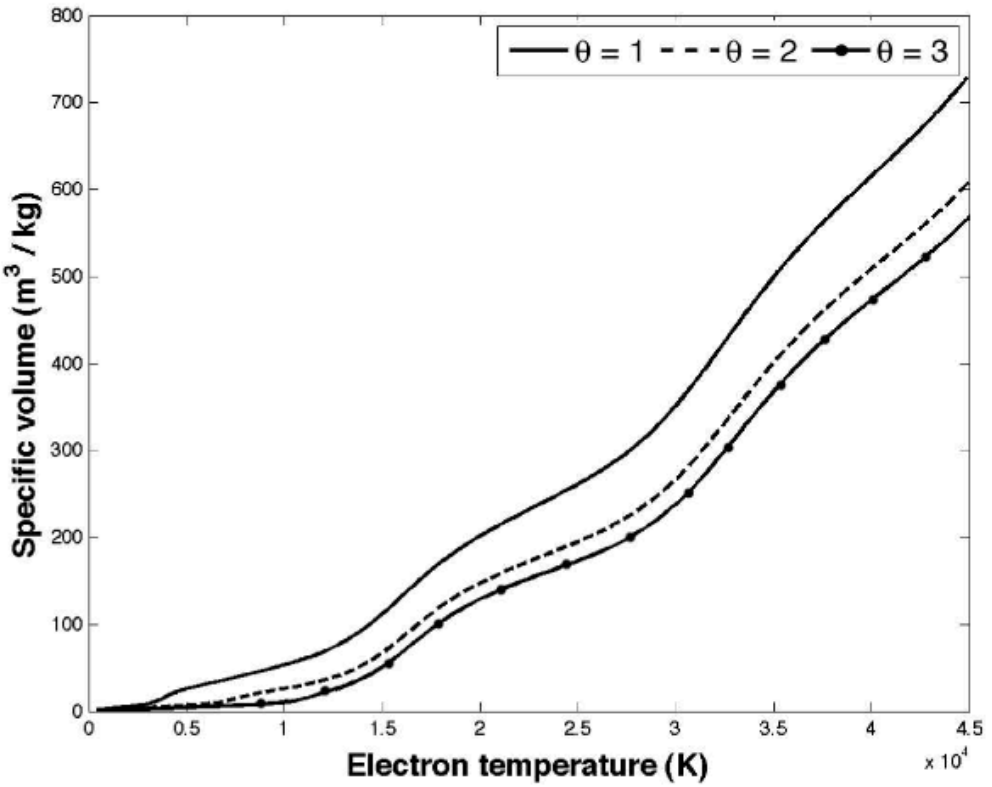


Fig. 8. Oxygen specific volume in LTE and NLTE (taken from Ref. [1])

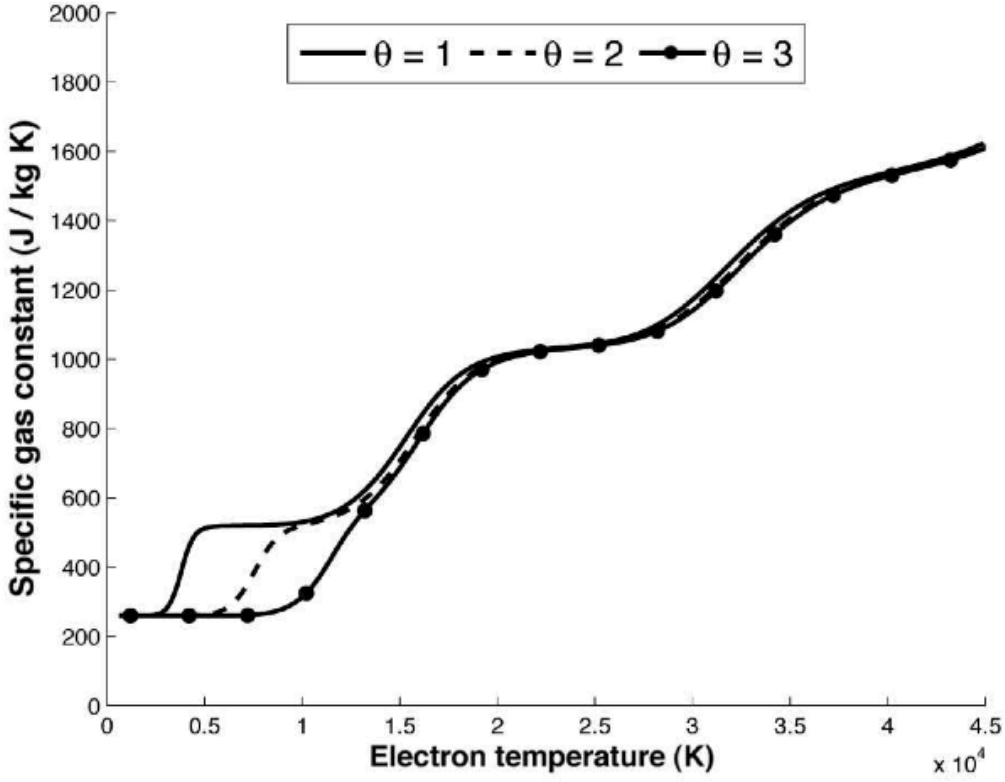


Fig. 9. Oxygen specific gas constant in LTE and NLTE (taken from Ref. [1])

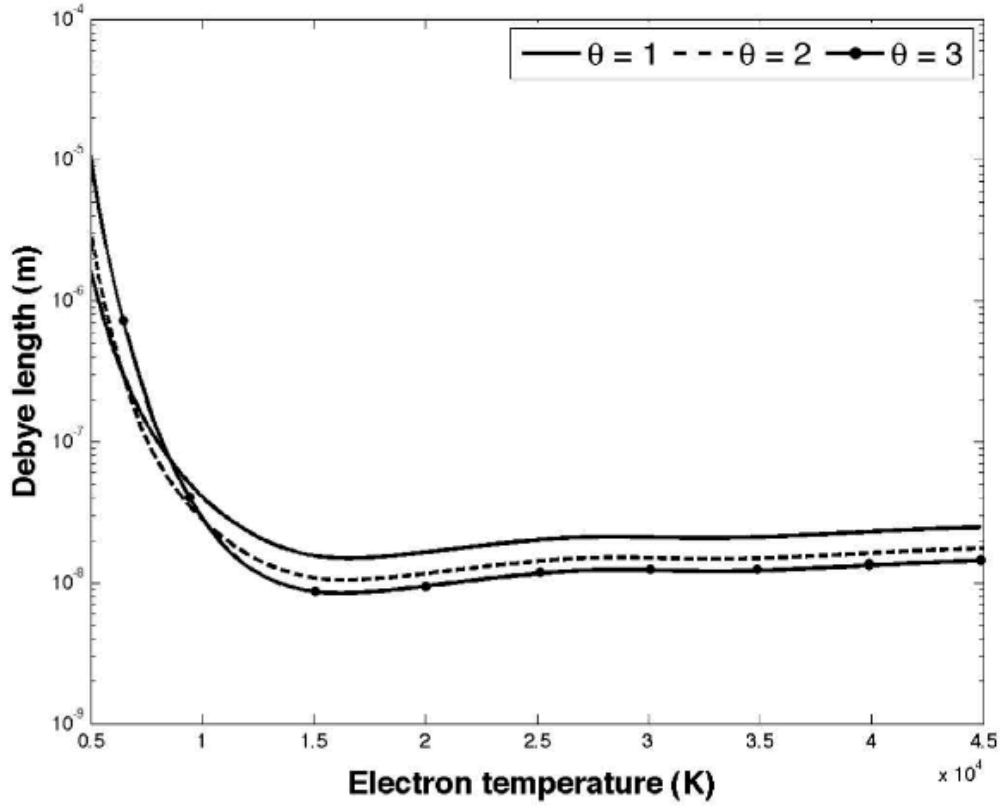


Fig. 10. Oxygen Debye length in LTE and NLTE (taken from Ref. [1])

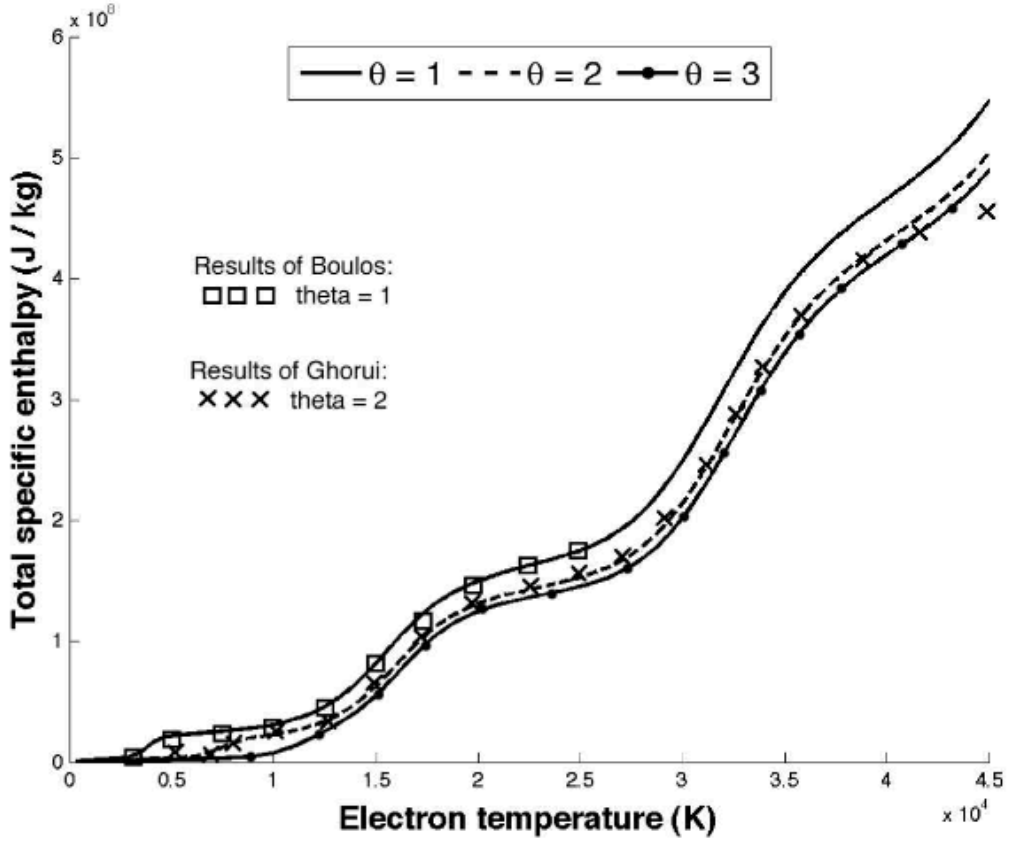


Fig. 11. Oxygen total specific enthalpy in LTE and NLTE (taken from Ref. [1])

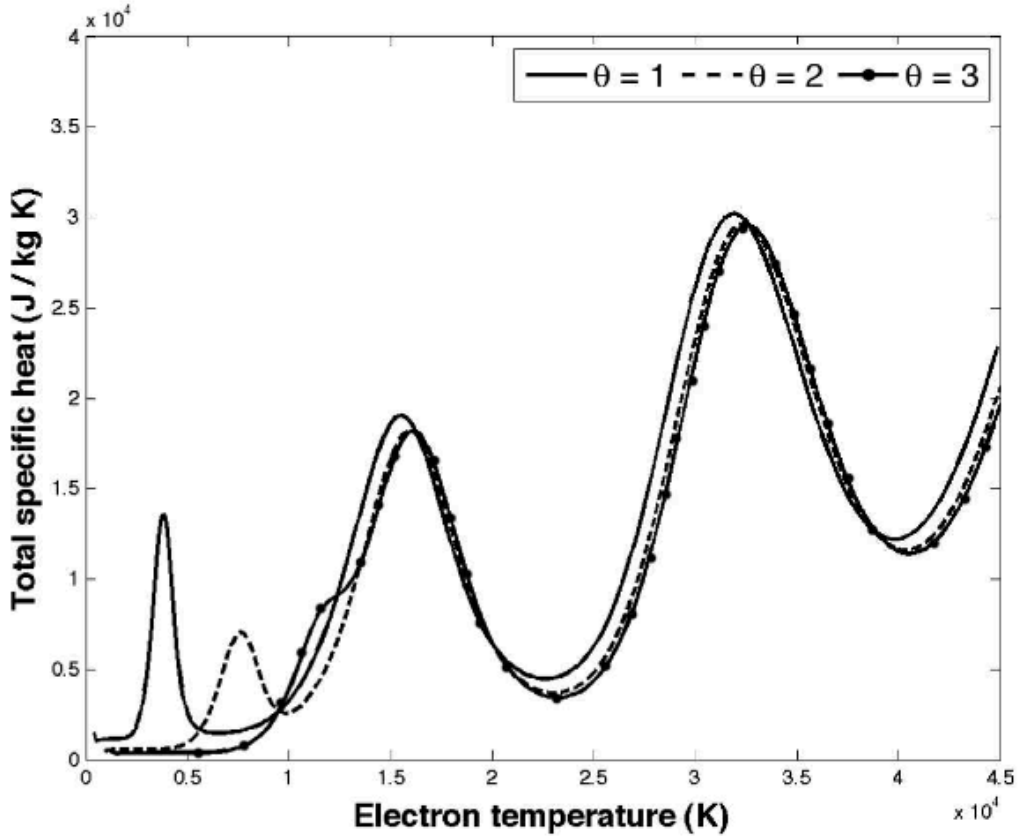


Fig. 12. Oxygen total specific heat in LTE and NLTE (taken from Ref. [1])

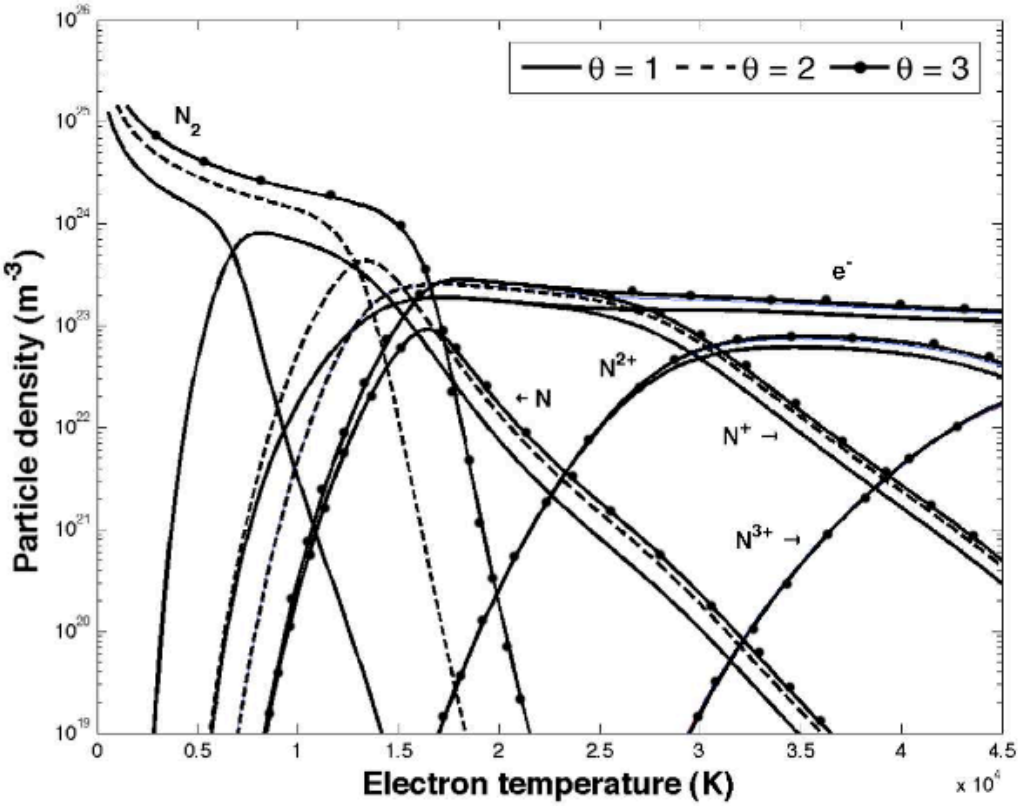


Fig. 13. Nitrogen composition in LTE and NLTE (taken from Ref. [1])

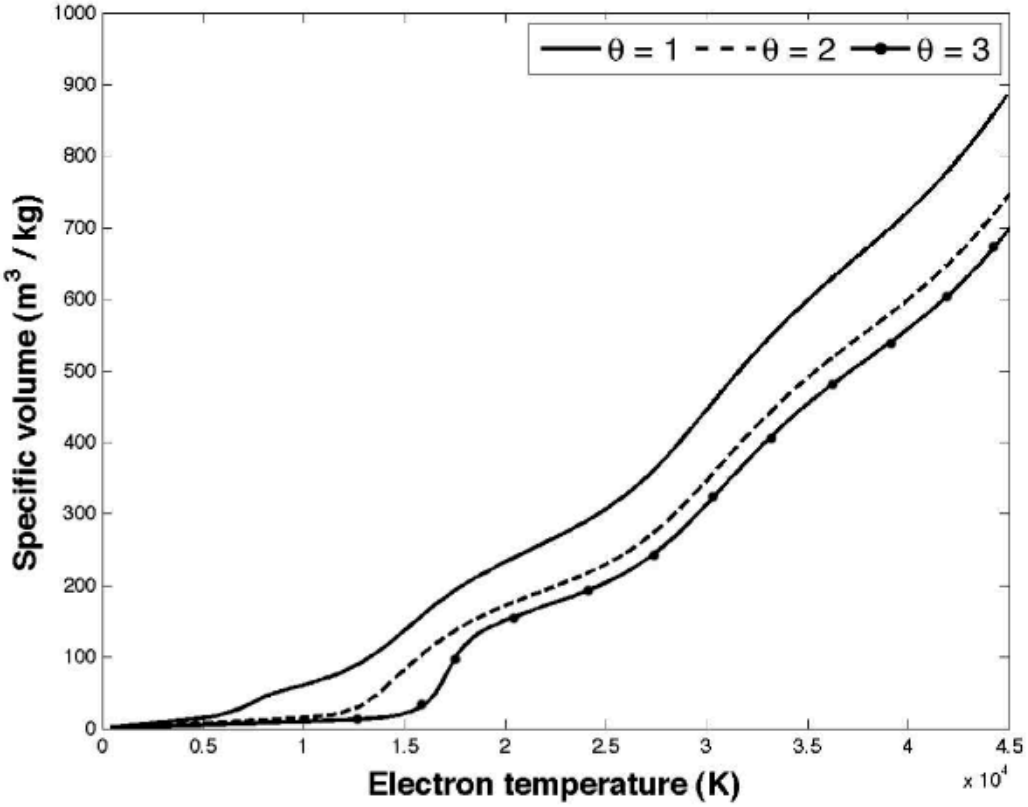


Fig. 14. Nitrogen specific volume in LTE and NLTE (taken from Ref. [1])

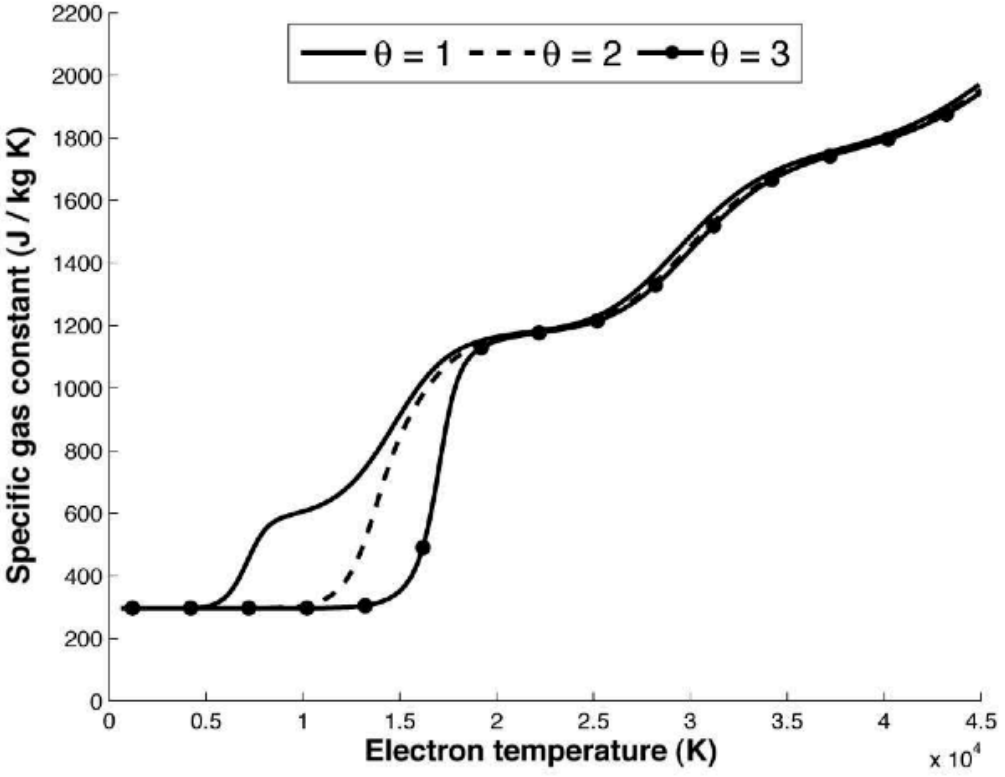


Fig. 15. Nitrogen specific gas constant in LTE and NLTE (taken from Ref. [1])

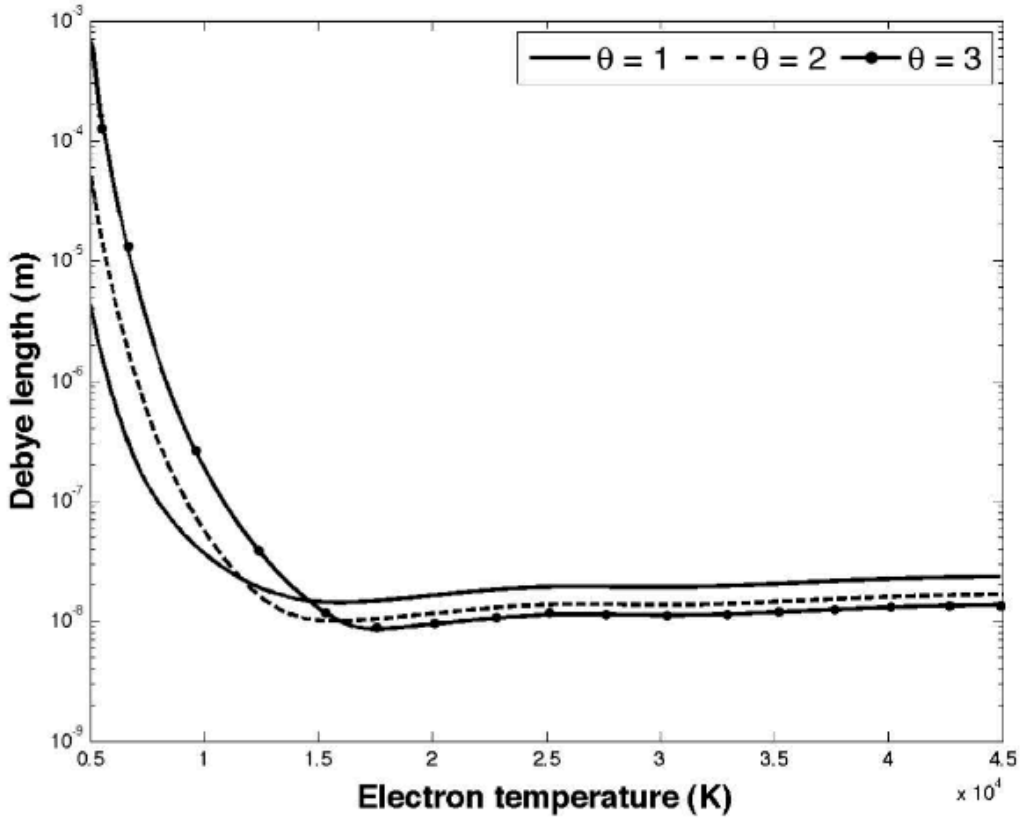


Fig. 16. Nitrogen Debye length in LTE and NLTE (taken from Ref. [1])

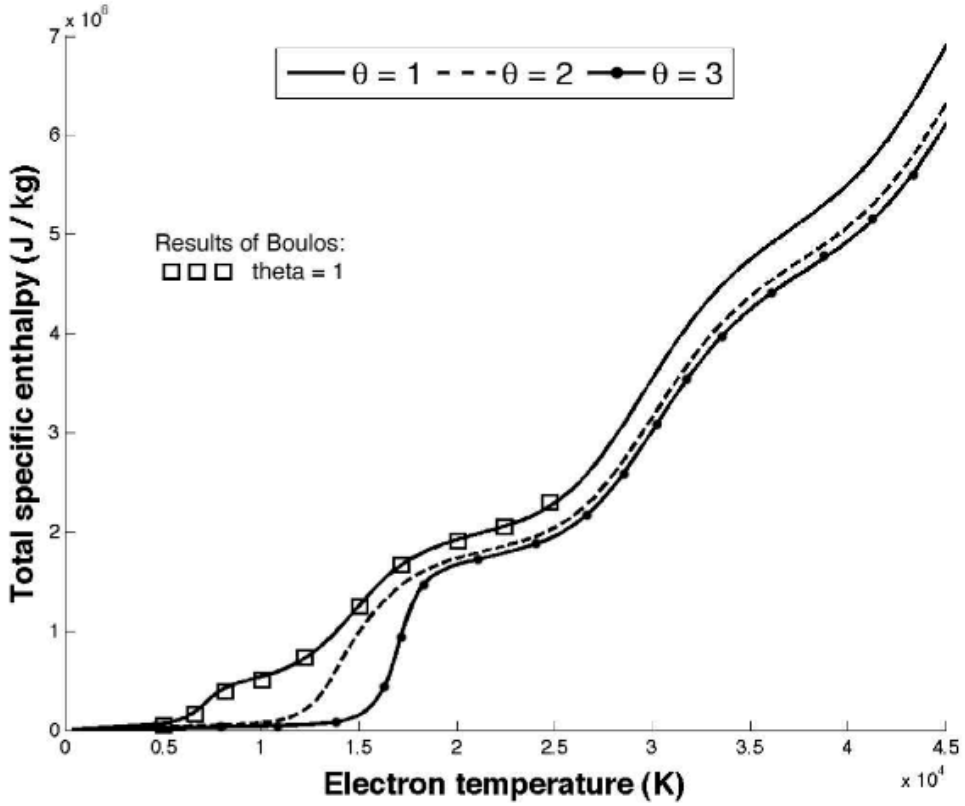


Fig. 17. Nitrogen total specific enthalpy in LTE and NLTE (taken from Ref. [1])

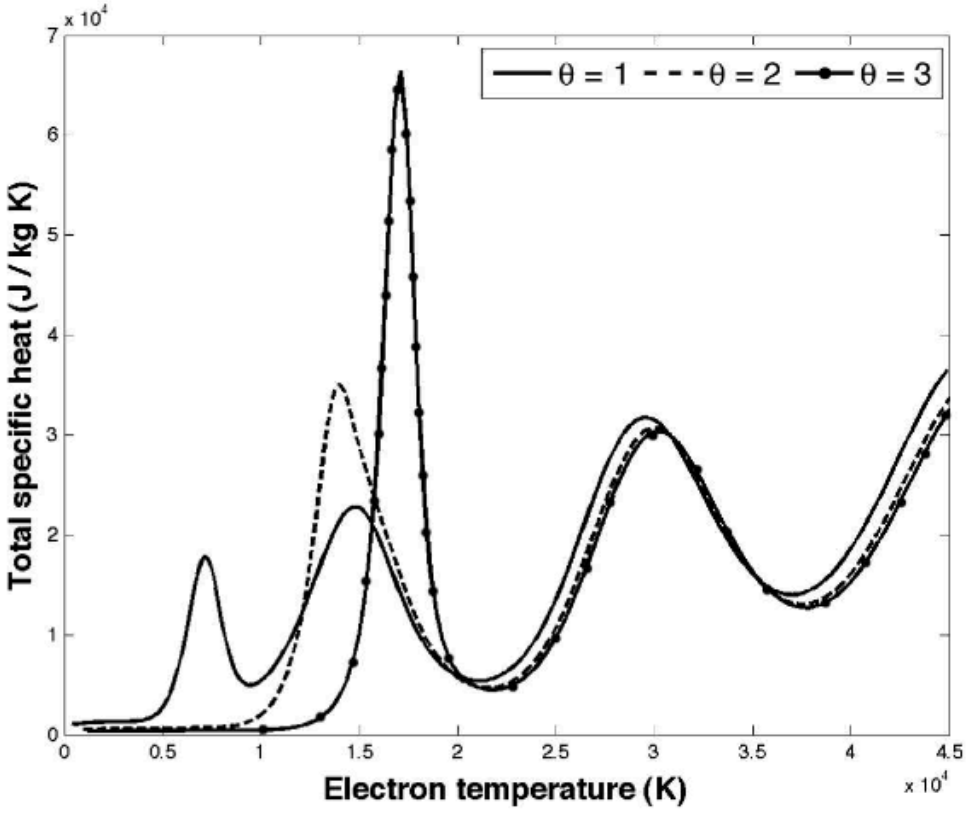


Fig. 18. Nitrogen total specific heat in LTE and NLTE (taken from Ref. [1])

*Results for transport properties*

Various components of the total thermal conductivity of argon, oxygen and nitrogen in LTE are presented in figures 19, 21 and 23, respectively.
In the range of temperature where dissociation and ionization take place, a great contribution to total thermal conductivity is given by the reactive term whereas for high temperature the translational contribution is the most important; internal thermal conductivity gives always a scarce contribution to total conductivity.
Results obtained with our code in LTE are in good agreement with data reported by Murphy[5].

Translational thermal conductivities of argon, oxygen and nitrogen for different values of θ are reported in figures 20, 22 and 24, respectively. For nitrogen and oxygen, once the dissociation temperature has been reached, the non-equilibrium thermal conductivity of electrons ($\theta > 1$) swiftly approaches the equilibrium one. Electron translational thermal conductivity shows only a minimal increment as θ increases for fixed electron temperature, since it is a property which depends mainly on electrons.
Results reported by Rat et al. for argon translational thermal conductivity differ from ours because of the difference in the formulations used for Debye length in the computation of Coulomb collision integrals: it seems that Rat et al. used the definition 45 whereas in our calculation equation 43 has been used.

Using the same definition we obtain similar results as shown in figure 20; however, slight differences still remains because of the different theory used: that of Devoto and that of Rat.
Oxygen thermal conductivity presents some differences with respect to results of Ghorui et al.: translational thermal conductivity due to heavy particles reported by Ghorui et al. are greater than ours because for e-$O_2$ and e-O interactions they use different data in the evaluation of collision integrals; translational thermal conductivity due to electrons presents slight differences at high temperature because Ghorui took in account the contribution of heavy particles in the computation of Debye length. However, our results are in good agreement with those of Murphy.

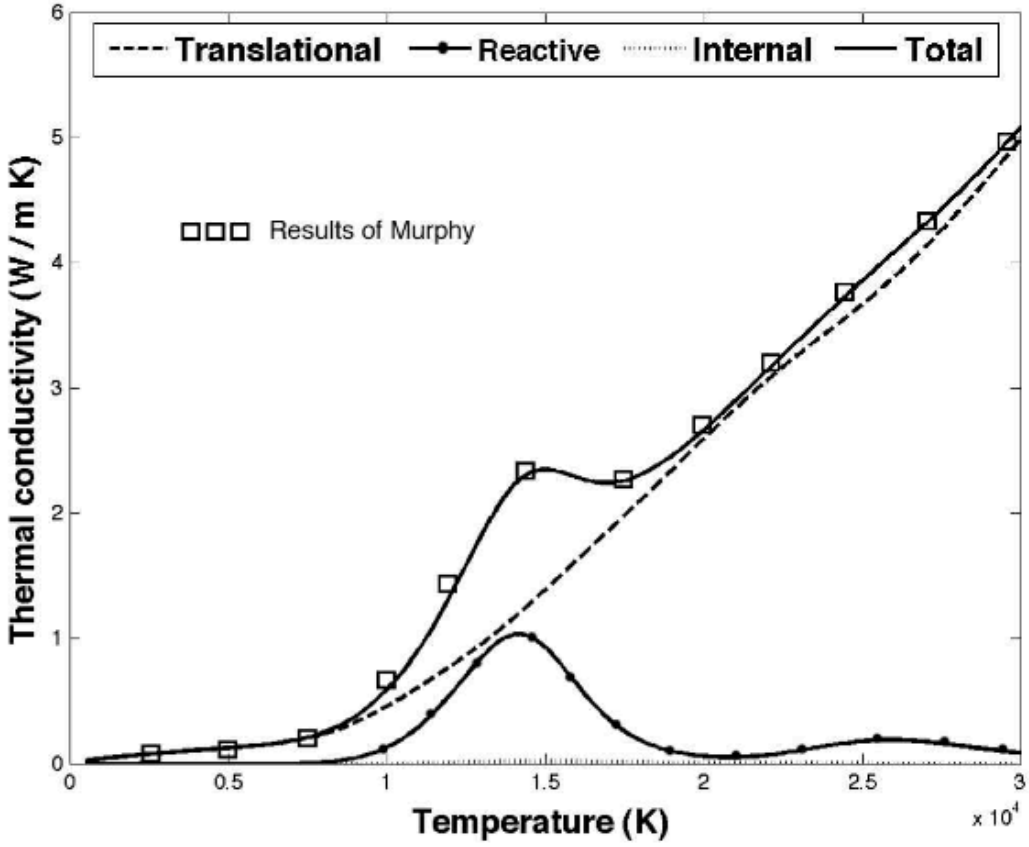


Fig. 19. Components of the thermal conductivity of argon in LTE (taken from Ref. [1])

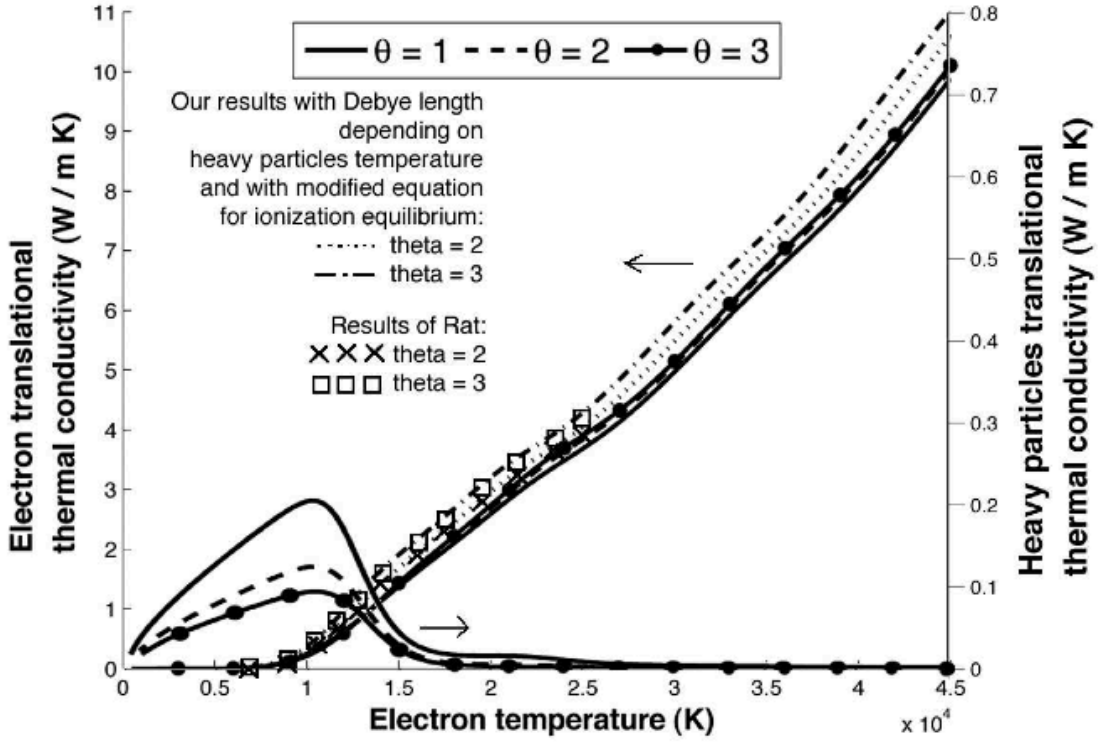


Fig. 20. Traslational thermal conductivity of argon in NLTE (taken from Ref. [1])

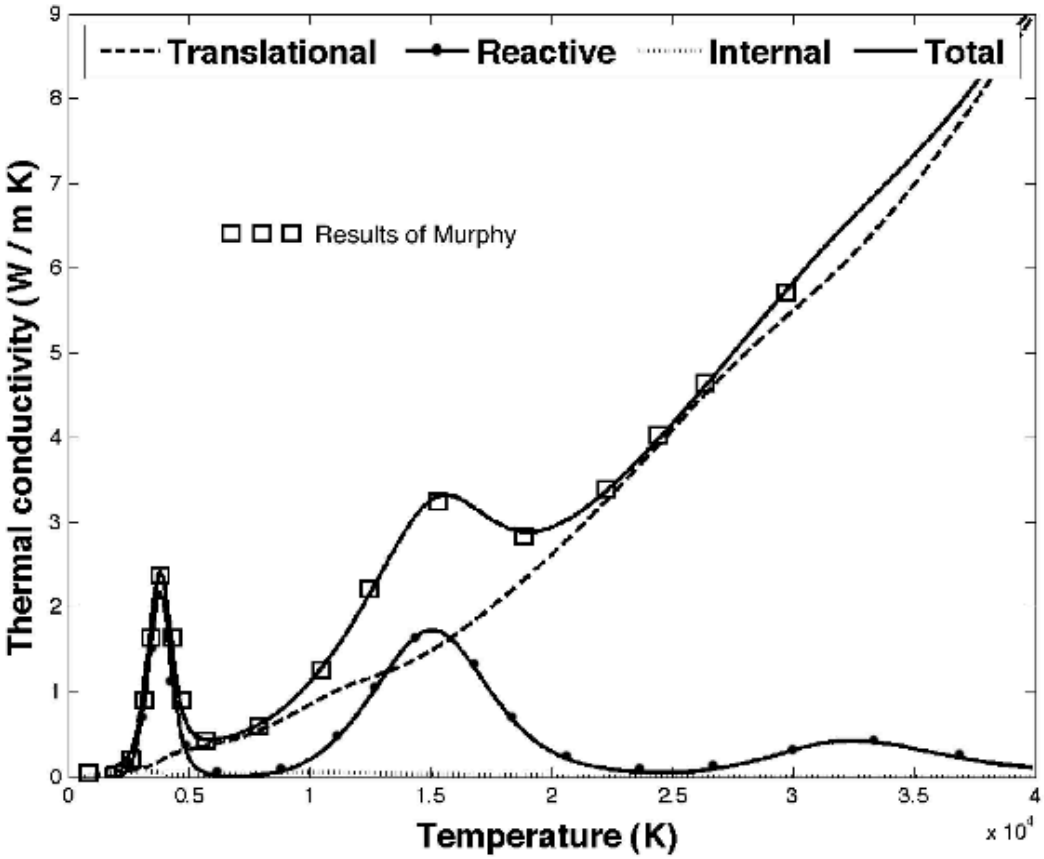


Fig. 21 - Components of the thermal conductivity of oxygen in LTE (taken from Ref.[1])

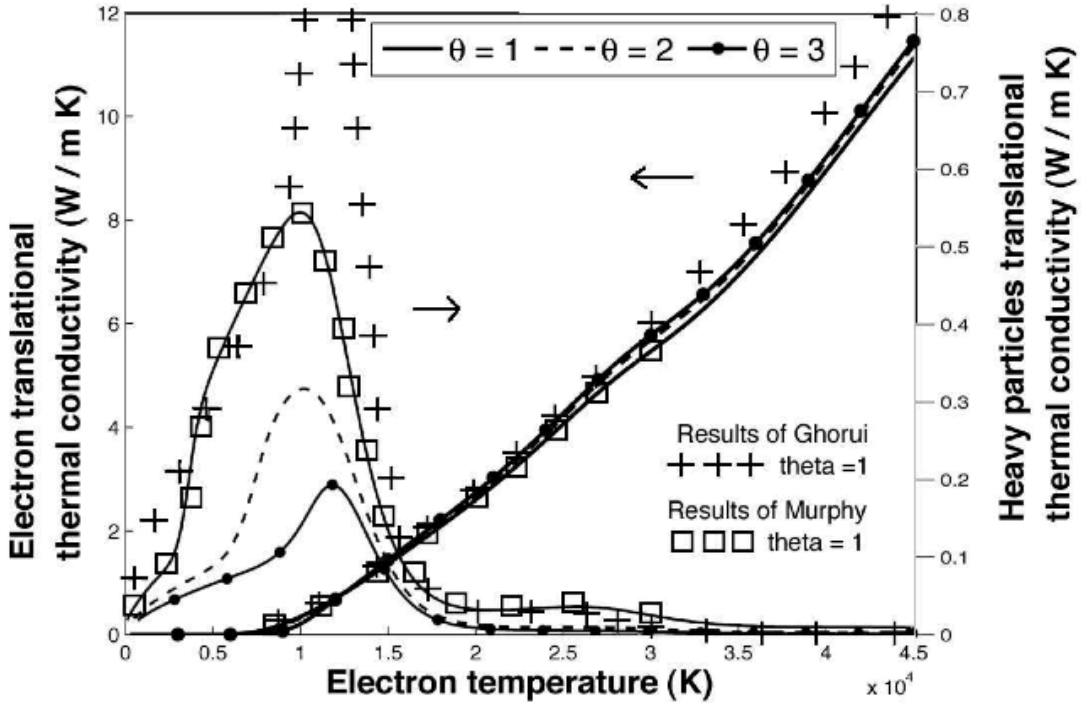


Fig. 22. Traslational thermal conductivity of oxygen in NLTE (taken from Ref. [1])

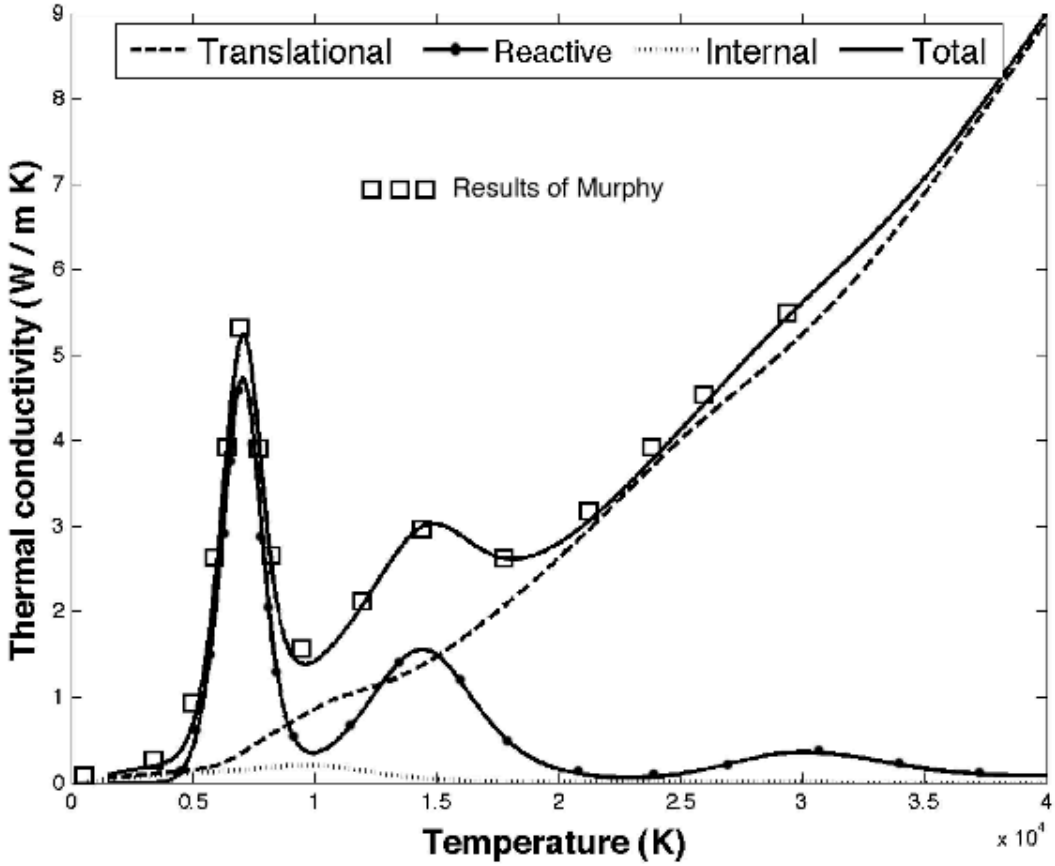


Fig. 23. Components of the thermal conductivity of nitrogen in LTE (taken from Ref. [1])

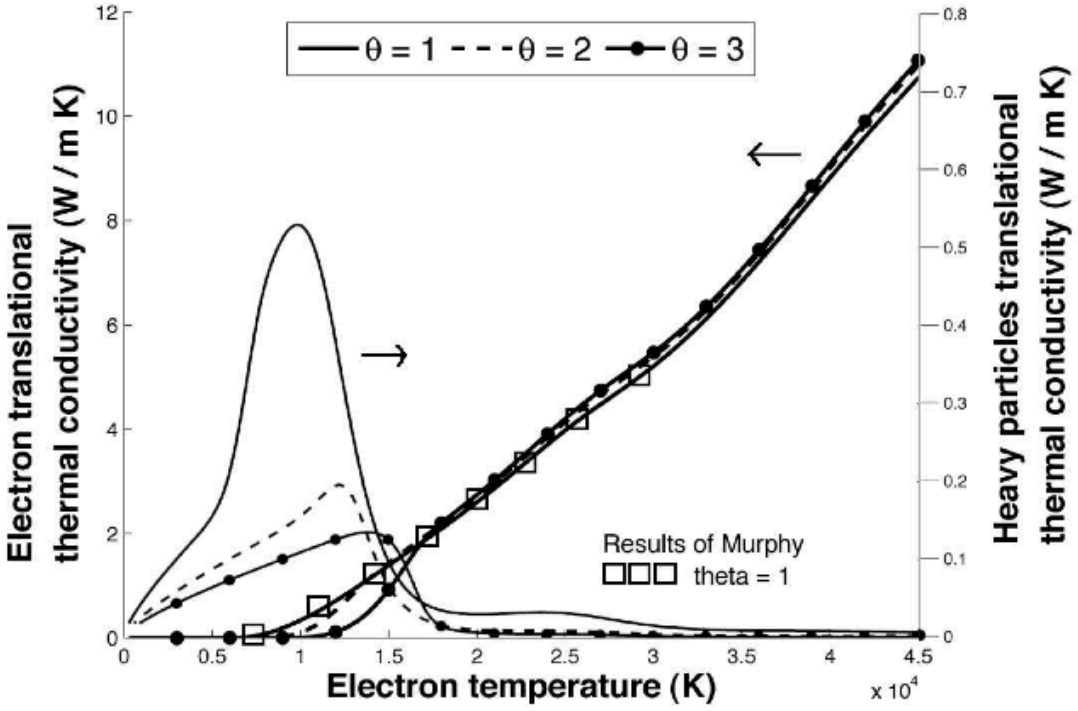


Fig. 24. Traslational thermal conductivity of nitrogen in NLTE (taken from Ref. [1])

*Viscosity*

Figures 25, 27 and 29 show NLTE results obtained with our code for the viscosity of argon, oxygen and nitrogen, respectively.
Momentum transport is responsible for viscosity of a gas. It arises due to increase in gas particle velocities with temperature, while for temperature higher than 10,000 K it decreases because the long range Coulomb forces between charged particles become important. Viscosity is primarily a property of the heavy particles; for a given $T_e$, if θ increases, $T_h$ decreases, resulting in a drop in the momentum transport and hence in a drop in the viscosity value. With increasing θ, the peak values for viscosity shift towards higher $T_e$ values.
Results have been compared with data available in literature. Viscosity of argon, oxygen and nitrogen in LTE is in good agreement with Murphy. Argon viscosity in NLTE is compared in figure 25 with results of Rat et al.: for electron temperature greater than 12,000 K results are slight different because in the computation of composition different methods have been used.
Oxygen viscosity is in good agreement with results of Ghorui et al.

*Electrical conductivity*

Figures 26, 28 and 30 present NLTE electrical conductivity of argon, oxygen and nitrogen, respectively.
Electrical conductivity depends only on collision integrals for interactions involving electrons: with higher values of θ, electrical conductivity starts rising fast once ionization temperature has been reached and then quickly stabilizes near the values observed for lower values of θ.

For $\theta > 1$, electrical conductivity of argon always increase as $\theta$ increases; in the dissociation range of temperature, oxygen and nitrogen have NLTE electrical conductivities lower than respective LTE conductivity while for electron temperature greater than 15,000 K conductivities increase as $\theta$ increases.
Figure 26 reports also the electrical conductivity of argon when the Debye length is evaluated through equation 45 and composition is computed using modified equation 6 for the ionization equilibrium: since in this case our results are in good agreement with results reported by Rat et al. it seems that Rat et al. used expression 45 to evaluate Debye length.
Slight differences still remains because of the different theory used: that of Devoto and that of Rat.
Finally, NLTE electrical conductivity of argon plasma is in good agreement with that reported by Rat when the same definition for Debye length is used.
Electrical conductivity of argon, oxygen and nitrogen in LTE are in good agreement with results reported by Murphy.
Electrical conductivity of oxygen presents different behaviour with respect to results of Ghorui et al. because they include contribution of ions in the calculation of the Debye length.

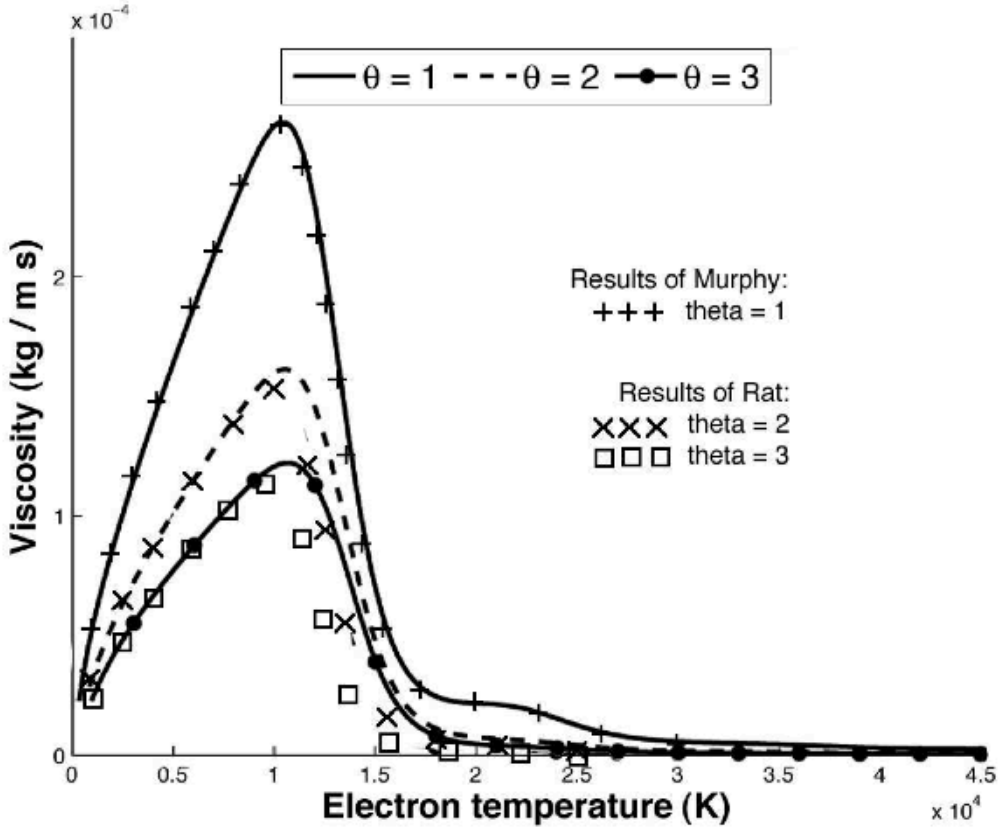


Fig. 25. Viscosity of argon in LTE and NLTE (taken from Ref. [1])

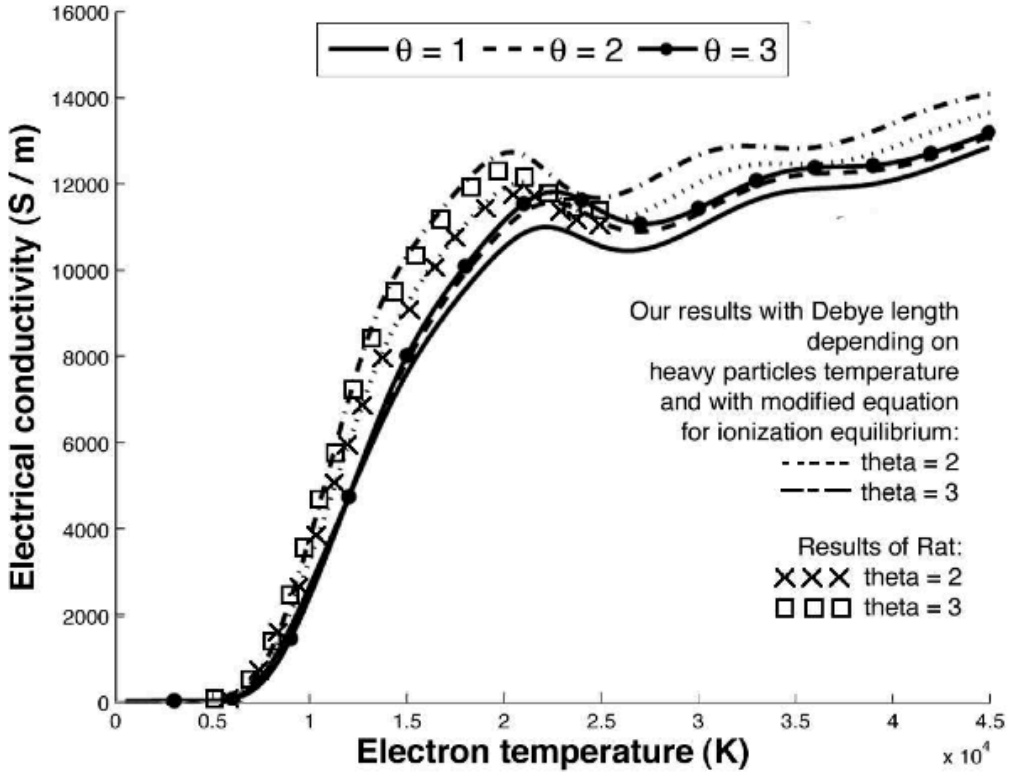


Fig. 26. Electrical conductivity of argon in LTE and NLTE (taken from Ref. [1])

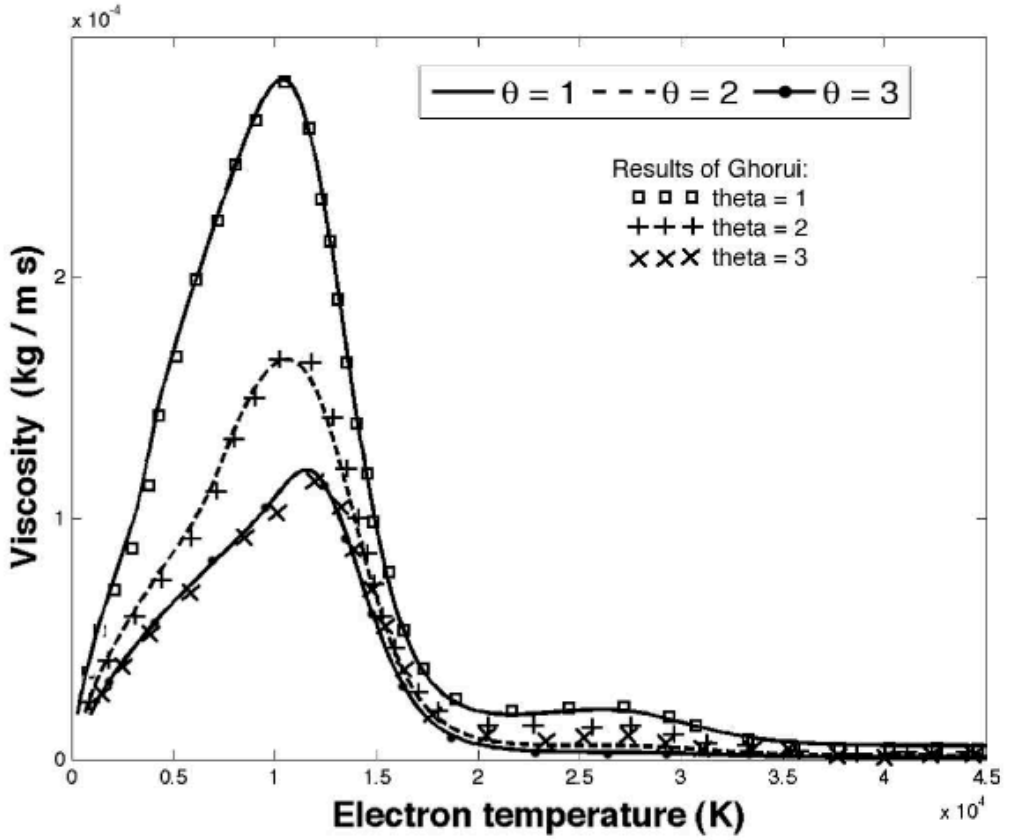


Fig. 27. Viscosity of oxygen in LTE and NLTE (taken from Ref. [1])

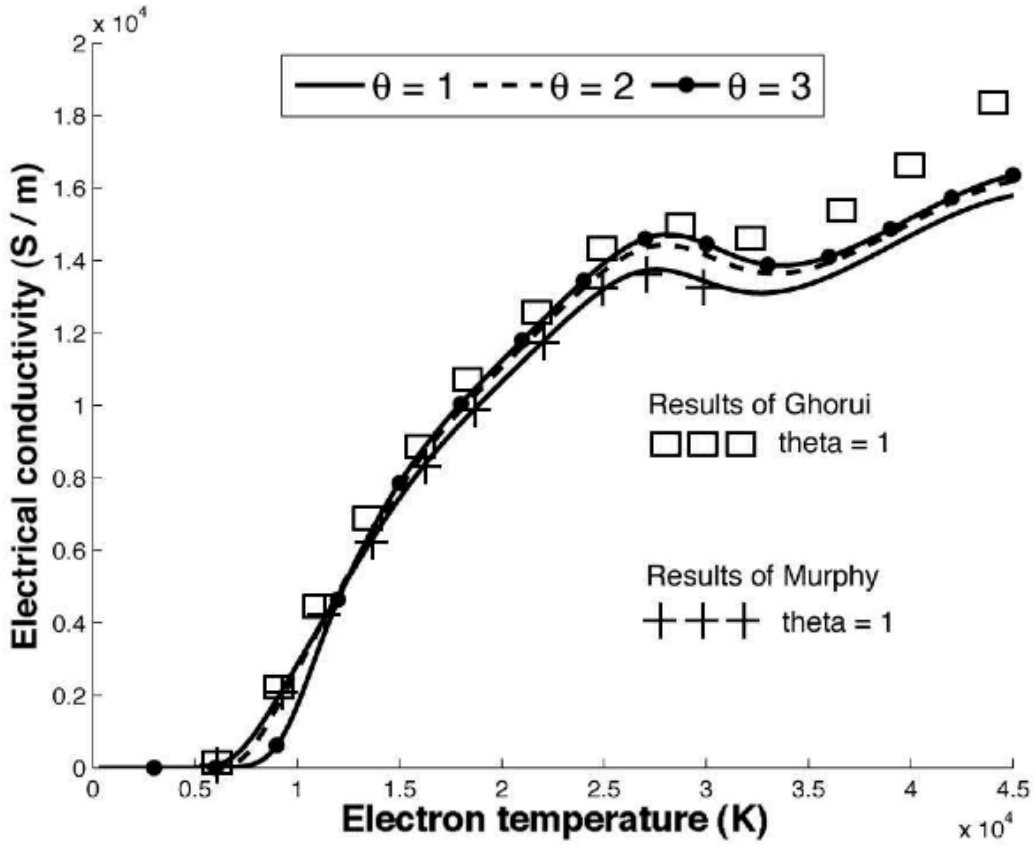


Fig. 28. Electrical conductivity of oxygen in LTE and NLTE (taken from Ref. [1])

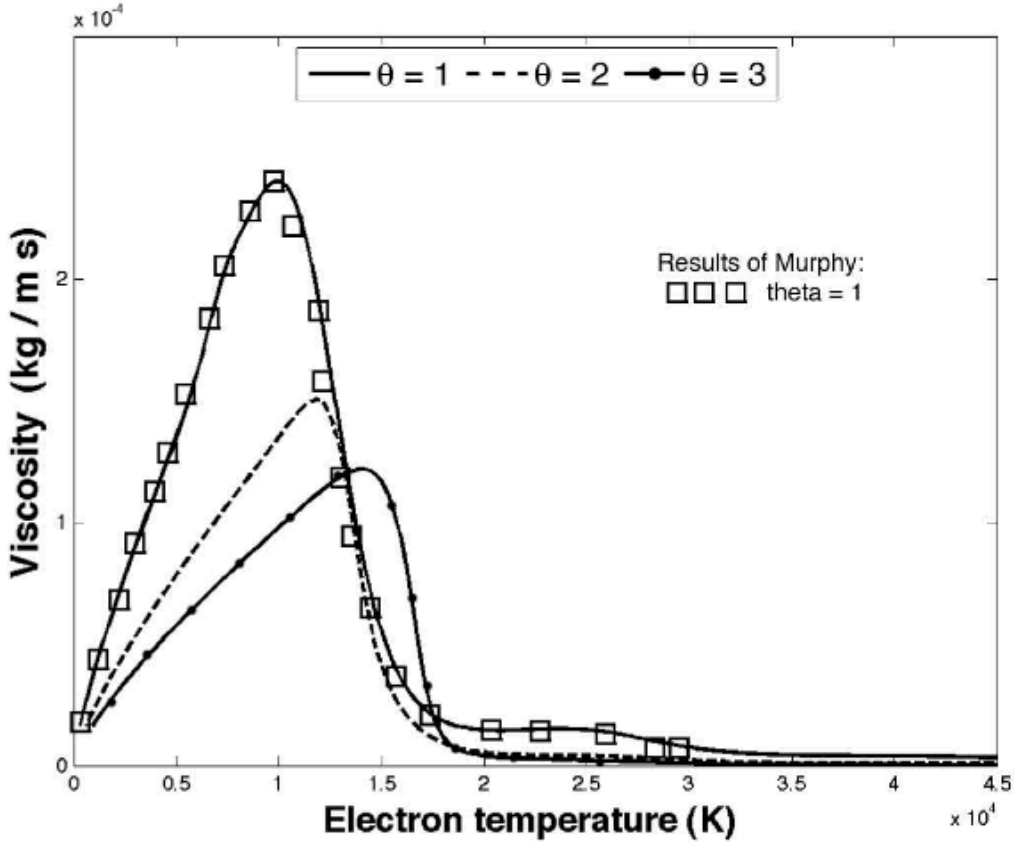


Fig. 29. Viscosity of nitrogen in LTE and NLTE (taken from Ref. [1])

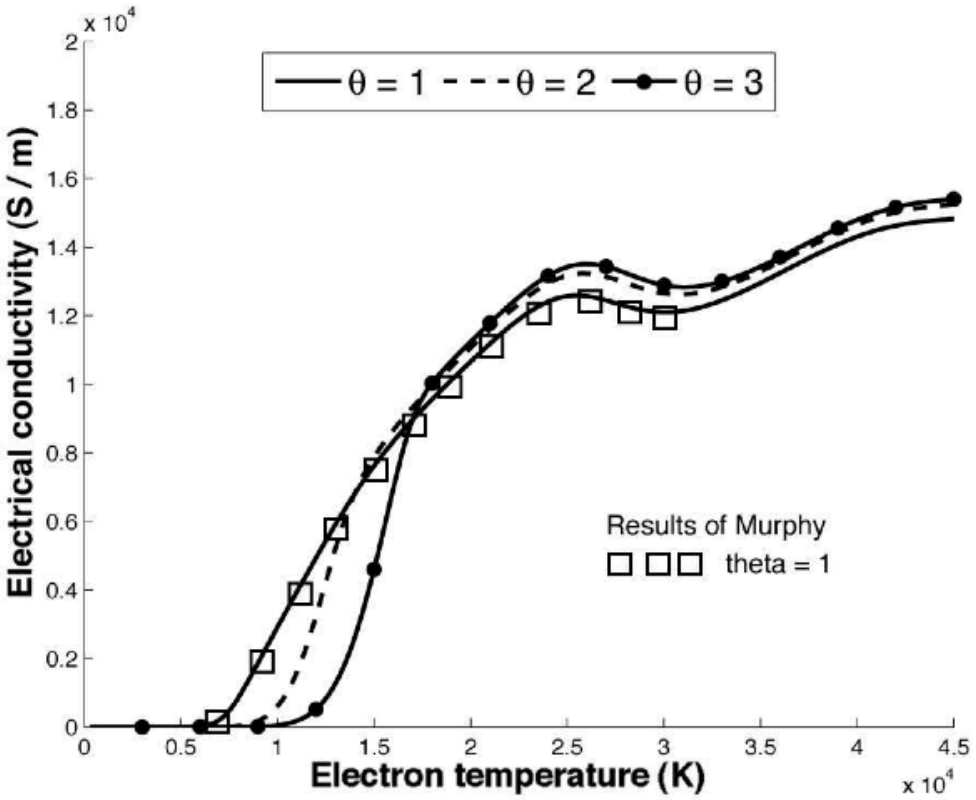


Fig. 30. Electrical conductivity of nitrogen in LTE and NLTE (taken from Ref. [1])

## Properties of Ar-$H_2$ and $N_2$-$H_2$ mixtures

In this work results for equilibrium and non-equilibrium thermodynamic and transport properties of argon-hydrogen and nitrogen-hydrogen mixtures obtained using the non-simplified approach of Rat et al. [15] are presented; our results for equilibrium transport properties of argon-hydrogen mixtures are in good agreement with previously published data of Murphy [7] whereas for nitrogen-hydrogen mixtures some discrepancies have been highlighted between data reported by Capitelli et al. [29] and our results, obtained with collision integrals recently calculated by Stallcop et al. and Sourd et al.; in non-equilibrium some discrepancies have been found between our results and those reported by Rat et al. [19, 30]: we succeeded in reproducing results reported by Rat et al. only using three modified equations instead of the ionization equilibrium equation, Debye length and electron enthalpy declared by them.

Moreover, since calculation of transport properties using this approach can be very time-consuming and therefore not suitable for its implementation in MHD equations solvers when the calculation on demand of properties is needed (e.g. in the case of chemical non-equilibrium), results obtained in this work with the simplified theory of Devoto are reported and compared with those of the non-simplified theory: in opposition to what is claimed by Rat et al., i.e. that the assumption of decoupling between electron and heavy species has a non-negligible effect on transport properties with the exception of viscosity; we found good agreement between results of the two theories also for total thermal conductivity (including electron, heavy particle and reactive contribution), electrical conductivity and diffusion coefficients of the type $D_{h-h}$ and $D_{h-e}$, where e and h stands for electrons and heavy particles, respectively.

### *Composition and thermodynamic properties*

Thermodynamic and transport properties, both in LTE and NLTE plasmas, depend strongly on composition.
LTE composition can be easily obtained through minimization of the Gibbs free energy, whereas the appropriate method for the determination of chemical equilibrium number densities in two-temperature plasmas has long been a subject of debate because different formulas for ionization equilibrium are obtained when different thermodynamic constraints are imposed. In the present work, we have used the method proposed by van de Sanden et al.

When thermal non-equilibrium occurs, due to low energy exchange between heavy particles (molecules, atoms and ions) and light particles (electrons), a maxwellian distribution of velocity characterized by the temperature $T_h$ is assumed for heavy species whereas the one for electrons is described by the temperature $T_e$. A parameter of thermal non-equilibrium can be defined as $\theta = Te/Th$.
Number densities of each species in the mixture can be computed as a function of electron temperature and θ solving the following set of equations:

$$\frac{n_e n_{a^{(z+1)}}}{n_{a^{(z)}}} = 2\left(\frac{2\pi m_e k T_e}{h^2}\right)^{3/2} \frac{Q^{int}_{a^{(z+1)}}(T_e)}{Q^{int}_{a^{(z)}}(T_e)} \exp\left(-\frac{\epsilon_{a^{(z+1)}}}{kT_e}\right) \quad (1)$$

$$\frac{n_a^2}{n_m} = \frac{\left(Q_a^{tr}(T_h)\right)^2}{Q_m^{tr}(T_h)} \frac{\left(Q_a^{int}(T_e)\right)^2}{Q_m^{int}(T_h)} \exp\left(-\frac{\epsilon_m}{kT_h}\right) \quad (2)$$

$$\sum_i^{species} n_i Z_i = 0 \quad (3)$$

$$p = n_e k T_e + \sum_i^{heavy} n_i \, k \, T_h \quad (4)$$

where $n_i$ and $m_i$ are the particles density and the mass of the i-th species, respectively; $Q^{tr}_i$ and $Q^{int}_i$ are the translational and internal partition function of the species i, respectively; $Z_i$ is the charge of species i; $\varepsilon_i$ is the formation energy of the species i; the subscript $a^{(z)}$ and m indicates z-times ionized species and molecules, respectively. The formation energy for electrons and neutral atoms are null; for positive ions the formation energy is equal to the energy required for ionization; for molecules $\varepsilon_m$ is the dissociation energy with negative sign.

We solved this set of equations using a robust algorithm originally proposed by Godin and Trepanier[24], suited for the composition computation of LTE plasmas and extended in this work to NLTE ones.

Composition of argon-hydrogen plasma has been obtained considering the species Ar, $Ar^+$, $Ar^{2+}$, $Ar^{3+}$, $Ar^{4+}$, $H_2$, H, $H^+$ and $e^-$. For nitrogen-hydrogen plasma $H_2$, H, $H^+$, $N_2$, N, $N^+$, $N^{2+}$, $N^{3+}$ and $e^-$ have been considered. Data of the electron energy levels of atoms and ions for the evaluation of their partition functions and the ionization and dissociation energies have been taken from NIST database; rotational and vibrational constants for the calculation of partition functions of molecules have been taken from JANAF tables.

Chemical equilibrium compositions for 50% argon - 50% hydrogen and for 50% nitrogen - 50% hydrogen mixtures as a function of electron temperature for different values of the non-equilibrium parameter are shown in figures 1 and 2, respectively.
For $\theta = 2$ we observe a shift of the nitrogen and hydrogen dissociation towards higher temperature resulting in a lower concentration of nitrogen and hydrogen atoms; for mixtures including nitrogen, in case of thermal non-equilibrium ionization takes place in a narrower range of temperature. Electron mole fraction decreases with growing value of $\theta$, though electron number density increases (not shown).

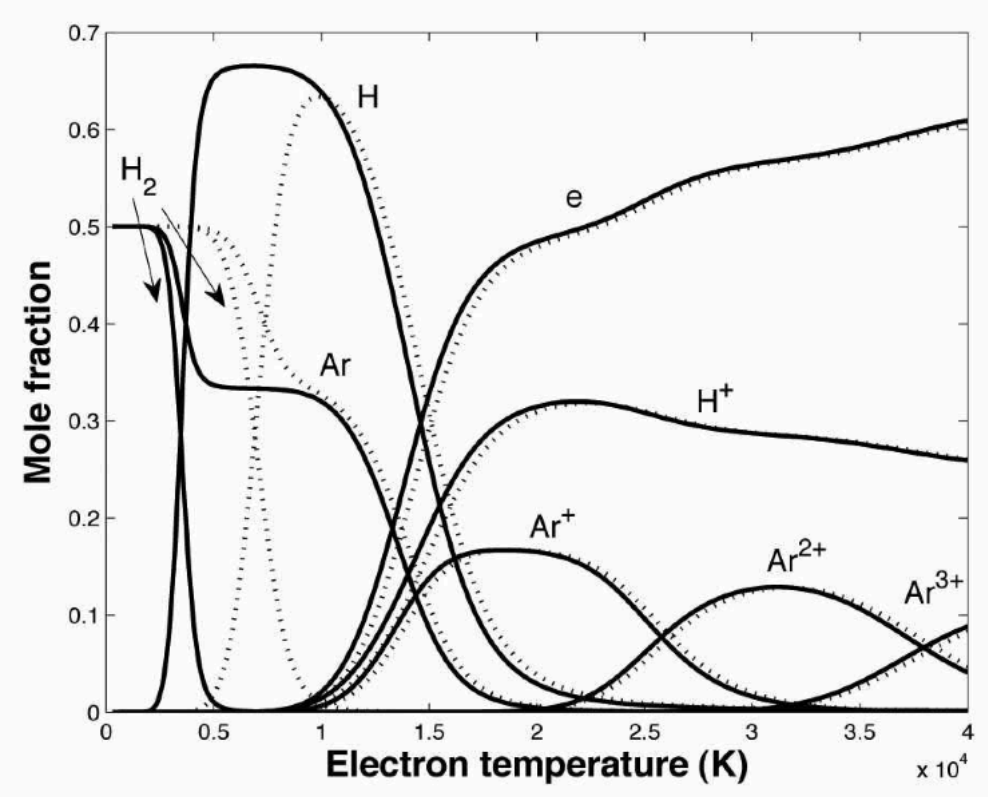


Fig. 1 - Electron temperature dependence of the mole fraction for 50% argon - 50% hydrogen mixture by mole fraction for different values of the non-equilibrium parameter: full line, $\theta = 1$, dotted line, $\theta = 2$. (taken from Ref. [2])

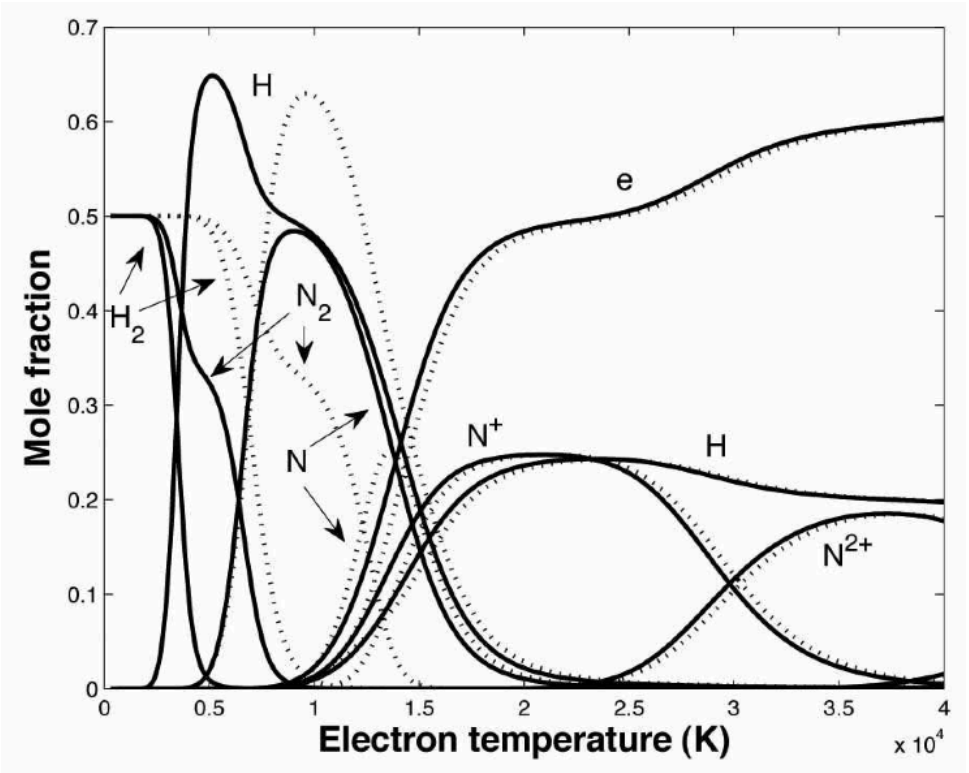


Fig. 2 - Electron temperature dependence of the mole fraction for 50% nitrogen - 50% hydrogen mixture by mole fraction for different values of the non-equilibrium parameter: full line, $\theta = 1$, dotted line, $\theta = 2$. (taken from Ref. [2])

Thermodynamic properties can be evaluated through a classical statistical mechanics approach, provided number densities and partition functions of each species are known. Density can be written as

$$\rho = \sum_i n_i m_i \qquad (5)$$

Total specific enthalpy can be calculated considering the translational, reactional and internal contributions:

$$h = \frac{5}{2}\frac{k}{\rho}\sum_i n_i T_i + \frac{1}{\rho}\sum_i n_i \epsilon_i + \frac{k}{\rho}\sum_i n_i T_i^2 \frac{\partial \ln Q_i^{int}}{\partial T_i} \qquad (6)$$

Taking pressure p, electron temperature Te and non-equilibium parameter θ as independent variables, differentiation of total enthalpy gives

$$\partial h = \left(\frac{\partial h}{\partial p}\right)_{T_e,\theta} \partial p + \left(\frac{\partial h}{\partial T_e}\right)_{p,\theta} \partial T_e + \left(\frac{\partial h}{\partial \theta}\right)_{p,T_e} \partial \theta \qquad (7)$$

The second derivative term can be interpreted as total specific heat at constant pressure and constant non-equilibrium parameter.

In this work thermodynamic properties both in LTE and NLTE for argon-hydrogen and nitrogen-hydrogen mixtures at atmospheric pressure in the temperature range 300-40,000 K have been computed.
Mass density for 50% argon - 50% hydrogen and for 50% nitrogen - 50% hydrogen mixtures as a function of electron temperature for different values of the non-equilibrium parameter are shown in figures 3 and 4, respectively. For fixed electron temperature, mass density increases as θ increases.
Total specific heat defined by the second term of equation 7 for 50% argon - 50% hydrogen and for 50% nitrogen - 50% hydrogen mixtures by mole fraction as a function of electron temperature for different values of θ are reported in figures 5 and 6, respectively.
Total specific heat of argon-hydrogen shows the characteristic peak due to the dissociation of $H_2$ (Th ≈ 3,700 K) and those due to the ionization of argon and hydrogen atoms and ions (Te ≈ 15,000 K, 25,000 K and 37,500 K); in the case of nitrogen-hydrogen mixtures, total specific heat shows peaks due to the dissociation of nitrogen and hydrogen molecules (Th ≈ 6,800 K and 3,700 K respectively) and those due to the ionization of nitrogen and hydrogen atoms and ions (Te ≈ 15,000 K and 29,500 K).
Since the dissociation peaks are governed by the heavy particle temperature, as θ increases they shift toward higher electron temperature: for θ = 3 the dissociation peak of hydrogen molecules in argon-hydrogen mixtures gives a contribution to the peak due to first ionization of argon and hydrogen atoms; in nitrogen-hydrogen mixtures, for θ = 3 the peak due to dissociation of nitrogen reaches the temperature

range where first ionization take place (Te ≈ 15,000 K) causing a pronounced shift of the atom ionization towards higher electron temperature; moreover, in this case the first ionization take place in a narrower range of electron temperature resulting in an higher peak of total specific heat.
In both argon-hydrogen and nitrogen-hydrogen mixtures the ionization peaks slightly shift towards higher electron temperature as θ increases.

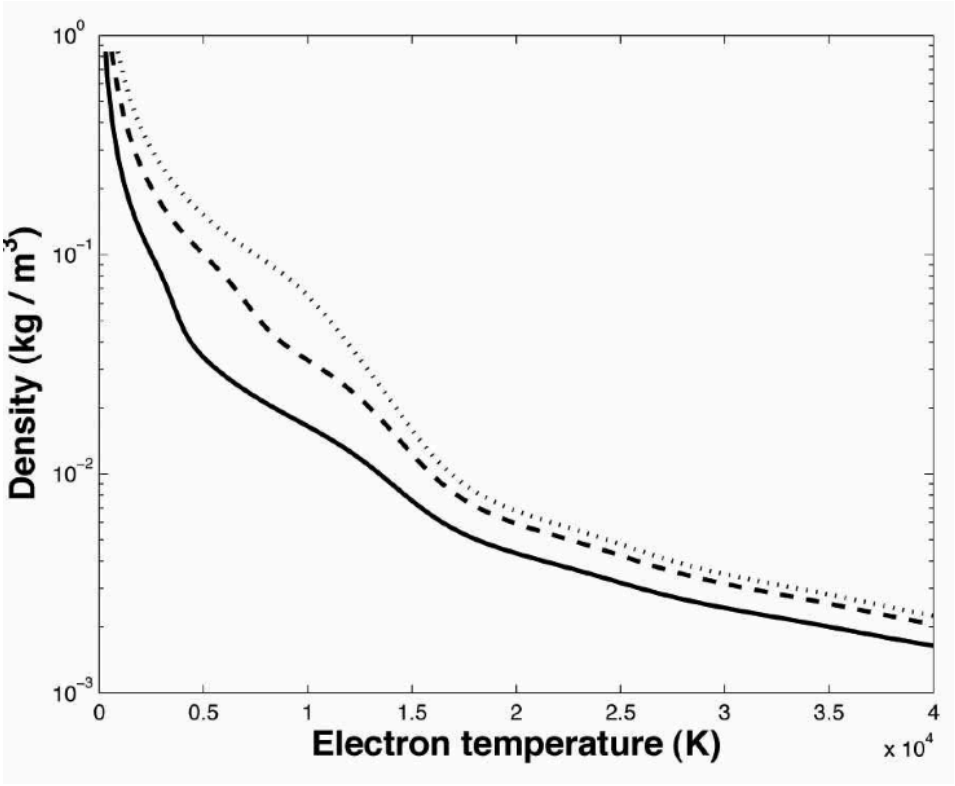


Fig. 3 - Electron temperature dependence of the mass density for 50% argon - 50% hydrogen mixture by mole fraction for different values of the non-equilibrium parameter: full line, θ = 1, dashed line, θ = 2, dotted line, θ = 3. (taken from Ref. [2])

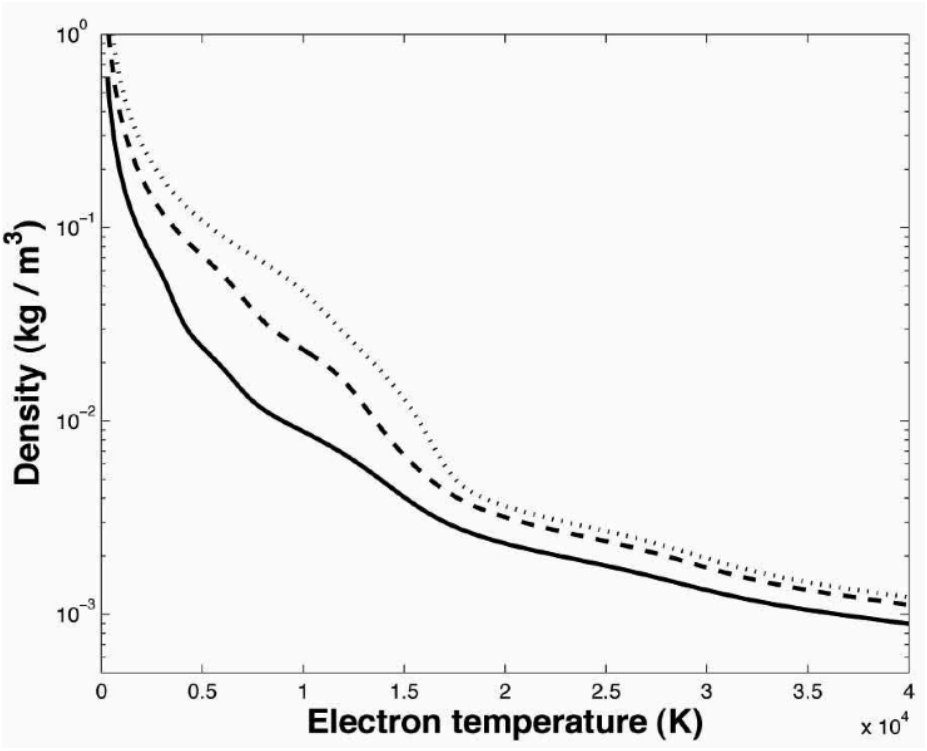


Fig. 4 - Electron temperature dependence of the mass density for 50% nitrogen - 50% hydrogen mixture by mole fraction for different values of the non-equilibrium parameter: full line, θ = 1, dashed line, θ = 2, dotted line, θ = 3. (taken from Ref. [2])

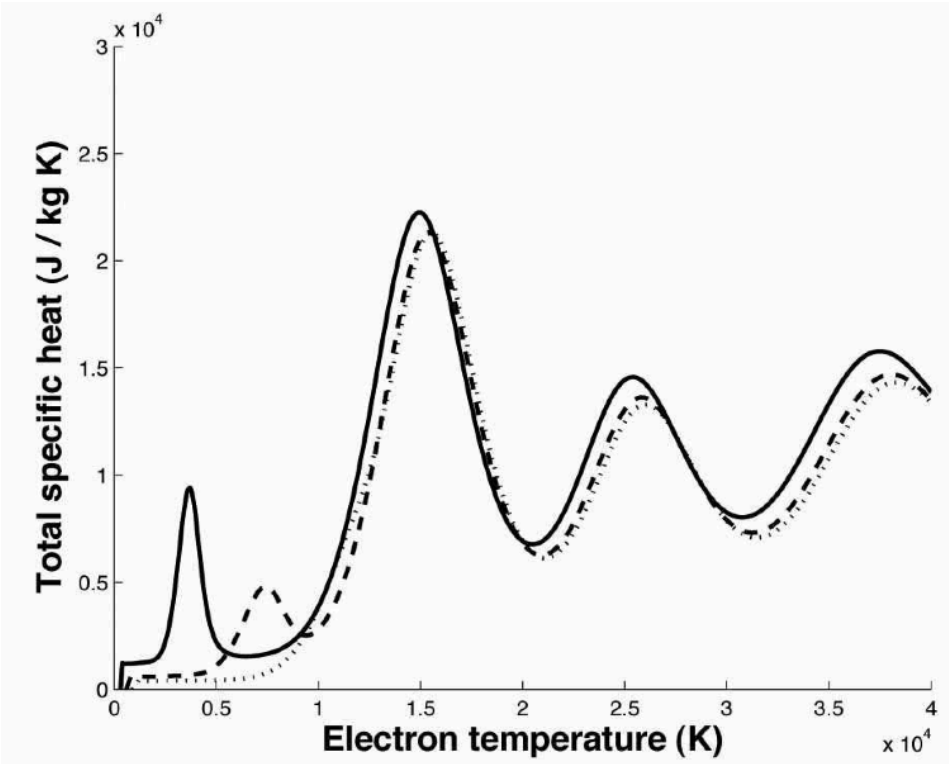


Fig. 5 - Electron temperature dependence of the total specific heat for 50% argon - 50% hydrogen mixture by mole fraction for different values of the non-equilibrium parameter: full line, θ = 1, dashed line, θ = 2, dotted line, θ = 3. (taken from Ref. [2])

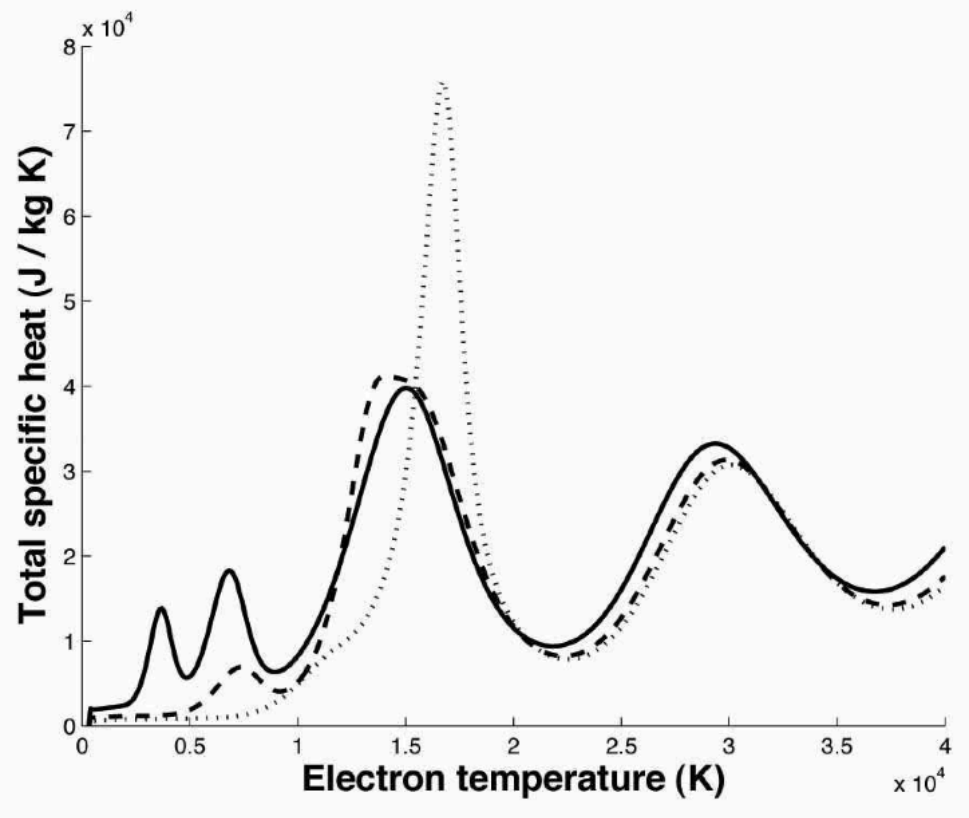


Fig. 6 - Electron temperature dependence of the total specific heat for 50% nitrogen - 50% hydrogen mixture by mole fraction for different values of the non-equilibrium parameter: full line, $\theta = 1$, dashed line, $\theta = 2$, dotted line, $\theta = 3$. (taken from Ref. [2])

*Collision integrals*

Expressions for transport properties contain determinants that depend on collision integrals, which are averages over a Maxwellian distribution of the transport cross-sections for the binary interactions between species.

Tables 1, 2, 3, 4 and 5 summarize the methods we used in the computation of collision integrals for each binary interaction and the references where we found data required in these calculations.

Collision integrals for argon interactions are computed as in the work of Rat[23]; for argon-hydrogen, hydrogen and nitrogen collision integrals we follow Murphy [7]; for nitrogen-hydrogen interactions, we collected methods for collision integrals calculation from published data (see table 5): for neutral-neutral interactions recent tabulated collision integrals by Stallcop et al. [31-34] have been chosen, taking into account molecule orientation and different excited states; for atom-$X^+$ interaction potentials reported by Sourd et al. [35] have been integrated to get transport cross sections and collision integrals whereas for $N_2$-$H^+$ interaction the Morse potential reported by Mittmann et al. [36] has been used; for minor interactions, including $N^+$-$H_2$, polarization potential has been chosen.

Table 1 – Methods for the computation of collision integrals for interactions between argon species

| Interaction | Method |
|---|---|
| $e - Ar$ | Phase shift (0.01≤E≤1 eV) |
| | Phase shift (1≤E≤10 eV) |
| | Diff. cross sections (E≥10 eV) |
| $Ar - Ar$ | HFDTCS2 potential |
| $Ar - Ar^+$ elastic | Hulburt-Hirschfelder potential |
| $Ar - Ar^+$ inelastic | Charge exchange |
| $X^{2+} - X, Y$ | Polarization potential |
| $X^{3+} - X, Y$ | Polarization potential |
| charged species | Tabulated collision integrals |

Table 2 – Methods for the computation of collision integrals for interactions between nitrogen species

| Interaction | Method |
|---|---|
| $e - N$ | Integration of cross sections |
| $e - N_2$ | Integration of transport cross sections |
| $N - N$ | Tabulated collision integrals |
| $N - N^+$ | Tabulated collision integrals |
| $N - N_2$ | Repulsive exponential potential |
| $N^+ - N_2$ elastic | Polarization potential |
| $N^+ - N_2$ inelastic | Integration of cross sections |
| $N_2 - N_2$ | Repulsive exponential potential |
| $X^{2+} - X, Y$ | Polarization potential |
| $X^{3+} - X, Y$ | Polarization potential |
| charged species | Tabulated collision integrals |

Table 3 – Methods for the computation of collision integrals for interactions between hydrogen species

| Interaction | Method |
|---|---|
| $e - H$ | Integration of transport cross sections |
| $e - H_2$ | Integration of transport cross sections |
| $H - H$ | Tabulated collision integrals |
| $H - H^+$ elastic | Exponential repulsive potential |
| $H - H^+$ inelastic | Integration of transport cross sections |
| $H - H_2$ | Tabulated collision integrals |
| $H^+ - H_2$ elastic | Polarization potential |
| $H^+ - H_2$ inelastic | Integration of transport cross sections |
| $H_2 - H_2$ | Tabulated collision integrals |
| charged species | Tabulated collision integrals |

Table 4 – Methods for the computation of collision integrals for interactions between argon and hydrogen species

| Interaction | | Method |
|---|---|---|
| $Ar - H$ | | Exponential repulsive potential |
| $Ar - H^+$ | | Modified Morse potential |
| $Ar - H_2$ | | Morse potential |
| $Ar^+ - H$ | $^3\Sigma$ | Exponential repulsive potential |
| | $^1\Pi$ | Exponential repulsive potential |
| | $^3\Pi$ | Exponential repulsive potential |
| | $^1\Sigma$ | Exponential repulsive potential |
| $Ar^+ - H_2$ | elastic | Polarization potential |
| | inelastic | Integration of transport cross sections |
| $X^{2+} - X, Y$ | | Polarization potential |
| $X^{3+} - X, Y$ | | Polarization potential |
| charged species | | Tabulated collision integrals |

Table 5 – Methods for the computation of collision integrals for interactions between nitrogen and hydrogen species

| Interaction | | Method |
|---|---|---|
| $N - H$ | | Tabulated collision integrals |
| $N - H^+$ | | Hulburt-Hirschfelder potential |
| $N - H_2$ | | Tabulated collision integrals |
| $N^+ - H$ | $a\,^2\Sigma^-$ | Hulburt-Hirschfelder potential |
| | $^4\Sigma^-$ | Exponential repulsive potential |
| | $X\,^2\Pi$ | Hulburt-Hirschfelder potential |
| | $^4\Pi$ | Exponential repulsive potential |
| $N^+ - H_2$ | | Polarization potential |
| $N_2 - H$ | | Tabulated collision integrals |
| $N_2 - H^+$ | | Morse potential |
| $N_2 - H_2$ | | Tabulated collision integrals |
| $X^{2+} - X, Y$ | | Polarization potential |
| $X^{3+} - X, Y$ | | Polarization potential |
| charged species | | Tabulated collision integrals |

*Transport properties*

The computation of transport properties is usually done using the Chapman-Enskog method, assuming that distribution functions of particles are first order perturbations to the Maxwellian distribution; perturbations are then expressed in series of Sonine polynomials, finally leading to a system of linear equations that can be suitably solved to obtain different transport properties.
Expressions for the calculations of these properties have been obtained by Devoto, Bonnefoi and Rat et al. following two different approaches: Devoto and Bonnefoi assume complete decoupling between electrons and heavy species, resulting in a simplified approach whereas Rat et al. recently developed a non-simplified method which retain the coupling.

For LTE plasmas, results obtained with the simplified theory are in good agreement with those of the non-simplified theory; for NLTE plasmas, Rat et al. stated that the simplified method of Devoto and Bonnefoi can't be used to evaluate correctly diffusion coeffients, electrical conductivity and electron translational thermal conductivity.

In this work, electrical conductivity and translational thermal conductivities have been computed with the method reported by Rat et al.; for the evaluation of the reactive thermal conductivity the approach reported by Rat et al. has been followed; internal thermal conductivity has been neglected because of its small contribution. Viscosity has been calculated using the simplified approach of Devoto because results are very close to those obtained with the non-simplified theory, as reported by Rat et al.

Moreover, results for electrical conductivity, thermal conductivities, including reactive contribution, and few diffusion coefficients obtained using also the approach of Devoto are shown in comparison with results obtained with the theory of Rat et al.; in the calculation of the reactive thermal conductivity the knowledge of ordinary diffusion coefficients is a prerequisite; in the simplified framework following Hirschfelder et al. the latter have been approximated as

$$D_{ij} = \frac{F^{ji} - F^{ii}}{m_j |F|} \quad (16)$$

where $F^{ij}$ are the cofactors of the matrix F whose elements are defined as

$$F_{ij} = \frac{1}{\rho}\left[\frac{n_i}{D^b_{ij}} + \sum_{l \neq i} \frac{n_i m_j}{m_i D^b_{il}}\right](1 - \delta_{ij}) \quad (17)$$

The binary diffusion coefficients have been evaluted through the formula reported by Rat et al. :

$$D^b_{ij} = \left(\frac{2\pi k}{\mu_{ij} T^*_{ij}}\right)^{1/2} \frac{3 T_i g_{ij}}{16 n \bar{Q}^{(1,1)}_{ij}} \quad (18)$$

where n is the total number density, $\theta_{ij}$ = Ti/Tj and

$$g_{ij} = \frac{(m_j + m_i\theta_{ji})^2 (m_i + m_j\theta_{ji})^3}{\theta^{5/2}_{ji}(m_j + m_i)^5} \quad (19)$$

Transport properties both in LTE and NLTE for argon-hydrogen and nitrogen-hydrogen mixtures at atmospheric pressure in the temperature range 300-40,000 K are presented. Results for values of the non-equilibrium parameter θ = 1, 2, 3 and for different mixture concentrations are reported. Comparisons with results reported by Murphy in LTE and Rat et al. in NLTE are shown.

In the framework of non-simplified theory of Rat et al., we succeeded in reproducing results reported by Rat et al. for electrical and thermal conductivities of pure argon and of argon-hydrogen mixtures only using three modified equations instead of the declared ionization equilibrium equation, Debye length and electron enthalpy; the modified set of equations is given by

$$\frac{n_e n_{a^{(z+1)}}}{n_{a^{(z)}}} = 2\left(\frac{2\pi m_e k T_e \theta}{h^2}\right)^{3/2} \frac{Q^{int}_{a^{(z+1)}}(T_e)}{Q^{int}_{a^{(z)}}(T_e)} \exp\left(-\frac{\epsilon_{a^{(z+1)}}}{kT_e}\right) \quad (20)$$

$$\lambda_D = \sqrt{\epsilon_0 \, k \, T_h / e^2 \, n_e} \quad (21)$$

$$h_e = \frac{5}{2} k T_e \theta \quad (22)$$

whereas the declared (correct) one is given by

$$\frac{n_e n_{a^{(z+1)}}}{n_{a^{(z)}}} = 2\left(\frac{2\pi m_e k T_e}{h^2}\right)^{3/2} \frac{Q^{int}_{a^{(z+1)}}(T_e)}{Q^{int}_{a^{(z)}}(T_e)} \exp\left(-\frac{\epsilon_{a^{(z+1)}}}{kT_e}\right) \quad (23)$$

$$\lambda_D = \sqrt{\epsilon_0 \, k \, T_e / e^2 \, n_e} \quad (24)$$

$$h_e = \frac{5}{2} k T_e \quad (25)$$

where equation 21 is cited in Ref. [23] and [30] as "equation of van de Sanden", both referring to Ref. [22]; equation 22 is reported in Ref. [23], section 3, and in Ref. [30], section 3; equation 25 is cited in Ref. [19] referring to the work of Bonnefoi et al. [37].
It should be noted that modified equations reduce to usual equations in the case of $\theta = 1$.
Moreover, results for NLTE argon composition reported by Trelles et al. [11], which was computed using the usual form of the Saha equation (eq. 1), are in agreement with our results (not shown here, see Ref. [1]), supporting our supposition that at least results reported by Rat et al. for pure argon were obtained using a set of equations different from the ones declared by them.

Total thermal conductivity of various argon-hydrogen mixtures and nitrogen-hydrogen mixtures in non-equilibrium have been calculated; NLTE thermal conductivity, for different values of θ, for 50% argon - 50% hydrogen and for 50% nitrogen - 50% hydrogen mixtures are presented.
Thermal conductivity has been evaluated with respect to heavy particles temperature gradient, that is

$$\vec{q} = -\lambda \vec{\nabla} T_h .$$

Figure 7 presents thermal conductivity for 50% argon - 50% hydrogen mixture for various values of θ; the dissociation peak of hydrogen shifts towards higher electron temperatures as θ increases because the dissociation reaction constant depends on heavy particles temperature.

Figure 8 presents thermal conductivity for 50% nitrogen - 50% hydrogen mixture for various values of θ; three peaks are clearly distinguished for θ = 1 whereas for higher θ the dissociation peaks reach the ionization peak.

In the temperature range where dissociation and ionization take place, a great contribution to total thermal conductivity is given by the reactive term, whereas for temperatures higher than 15,000 K the translational contribution is the most important.

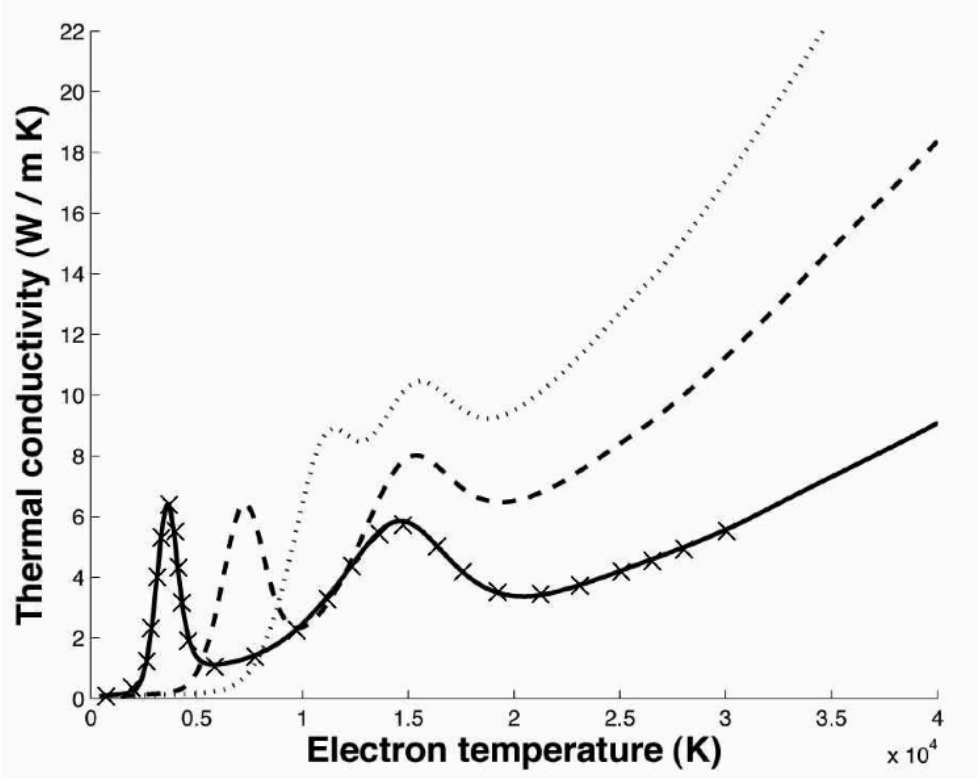


Fig. 7 - Electron temperature dependence of the thermal conductivity for 50% argon - 50% hydrogen mixture by mole fraction for different values of the non-equilibrium parameter: full line, θ = 1, dashed line, θ = 2, dotted line, θ = 3; the symbol x shows results in LTE of Murphy. (taken from Ref. [2])

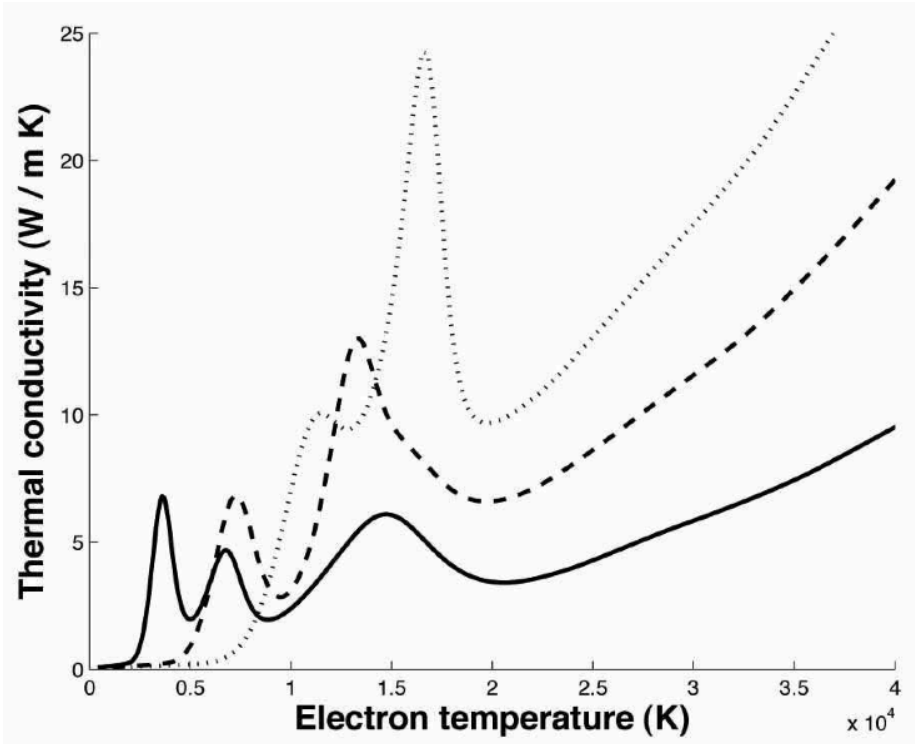


Fig. 8 - Electron temperature dependence of the thermal conductivity of 50% nitrogen - 50% hydrogen mixture by mole fraction for different values of the non-equilibrium parameter: full line, $\theta = 1$, dashed line, $\theta = 2$, dotted line, $\theta = 3$. (taken from Ref. [2])

Electrical conductivity, for different values of θ, for 50% argon - 50% hydrogen and for 50% nitrogen - 50% hydrogen mixtures are reported in figures 9 and 10 respectively.

At low temperature, for increasing values of θ, conductivities for 50% argon - 50% hydrogen and for 50% nitrogen - 50% hydrogen mixtures decrease because dissociation shifts towards higher electron temperatures.

For electron temperatures higher than 15,000 K conductivity increases with growing values of θ: even though in figure 1 and 2 we observe that electron mole fraction decreases as θ increases, electron number density increases with growing values of non-equilibrium parameter (not shown) and this justifies the increase in electrical conductivity.

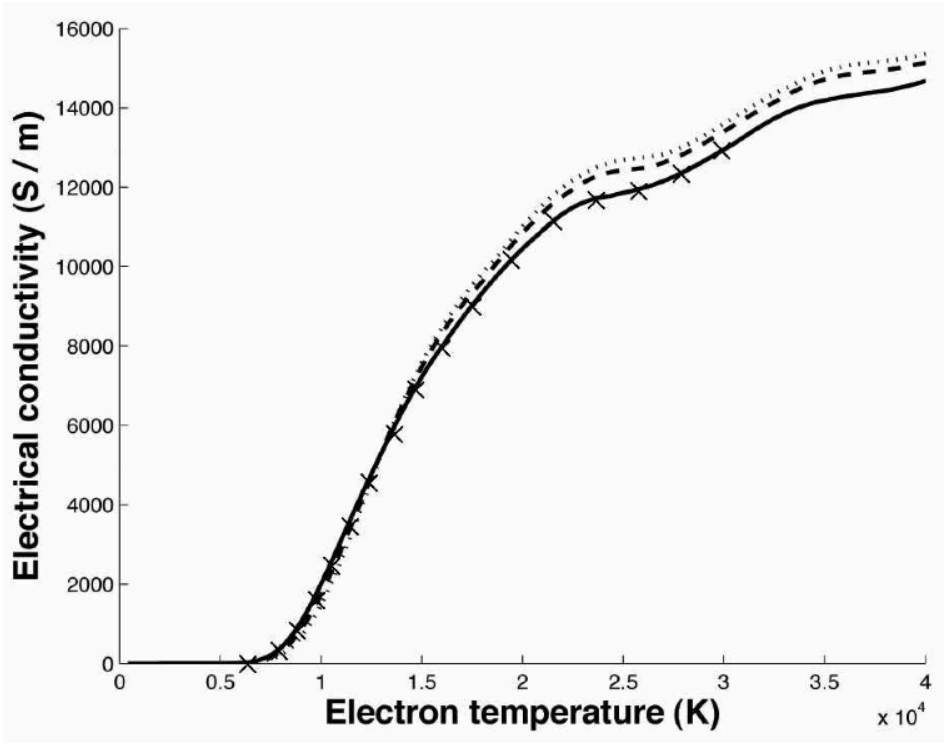


Fig. 9 - Electron temperature dependence of the electrical conductivity for 50% argon - 50% hydrogen mixture by mole fraction for different values of the non-equilibrium parameter: full line, $\theta = 1$, dashed line, $\theta = 2$, dotted line, $\theta = 3$; the symbol x shows results in LTE of Murphy. (taken from Ref. [2])

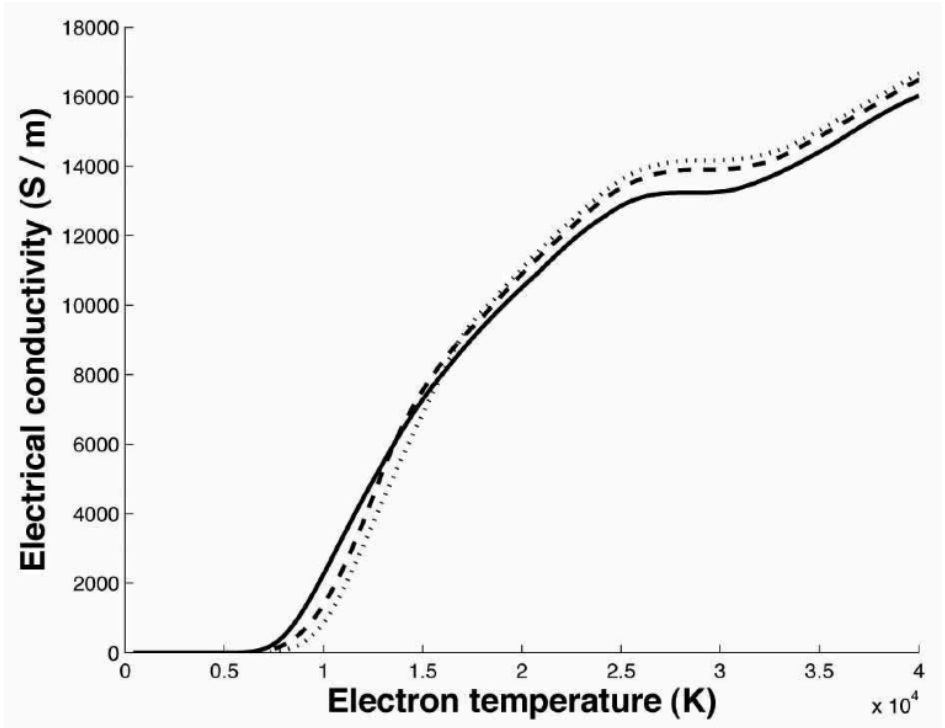


Fig. 10 - Electron temperature dependence of the electrical conductivity for 50% nitrogen - 50% hydrogen mixture by mole fraction for different values of the non-equilibrium parameter: $\theta = 1$, dashed line, $\theta = 2$, dotted line, $\theta = 3$. (taken from Ref. [2])

Viscosity, for different values of θ, for 50% argon - 50% hydrogen and for 50% nitrogen - 50% hydrogen mixtures are reported in figures 11 and 12, respectively. With growing values of the non-equilibrium parameter, we observe a lower viscosity peak around Te ≈ 10,000 K and a shift of ionization onset toward higher electron temperature; the latter effect is more pronounced in the case of nitrogen-hydrogen mixtures since nitrogen dissociation occurs at higher heavy particle temperature (Th ≈ 6,800 K) than hydrogen dissociation (Th ≈ 3,700 K), resulting in a proportionally greater shift towards higher electron temperature as θ increases.

Results for thermal conductivity, electrical conductivity and viscosity for 50% argon - 50% hydrogen in LTE are in good agreement with data reported by Murphy (see figures 7, 9 and 11).

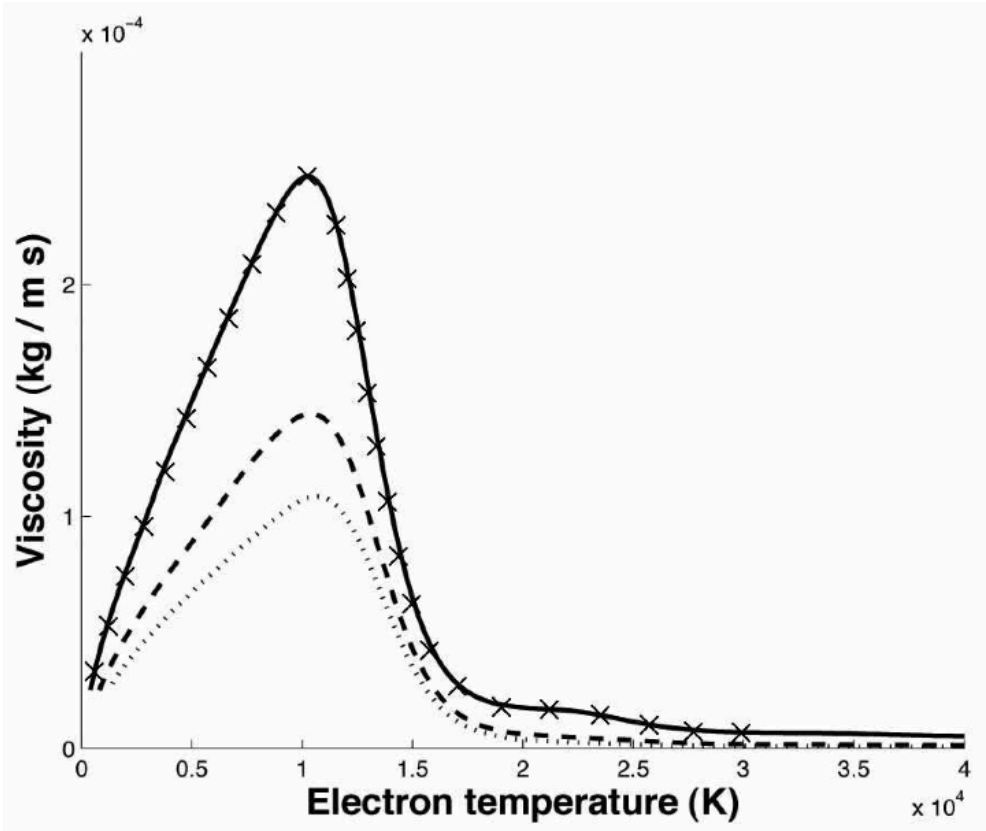


Fig. 11 - Electron temperature dependence of the viscosity for 50% argon - 50% hydrogen mixture by mole fraction for different values of the non-equilibrium parameter: full line, θ = 1, dashed line, θ = 2, dotted line, θ = 3; the symbol x shows results in LTE of Murphy. (taken from Ref. [2])

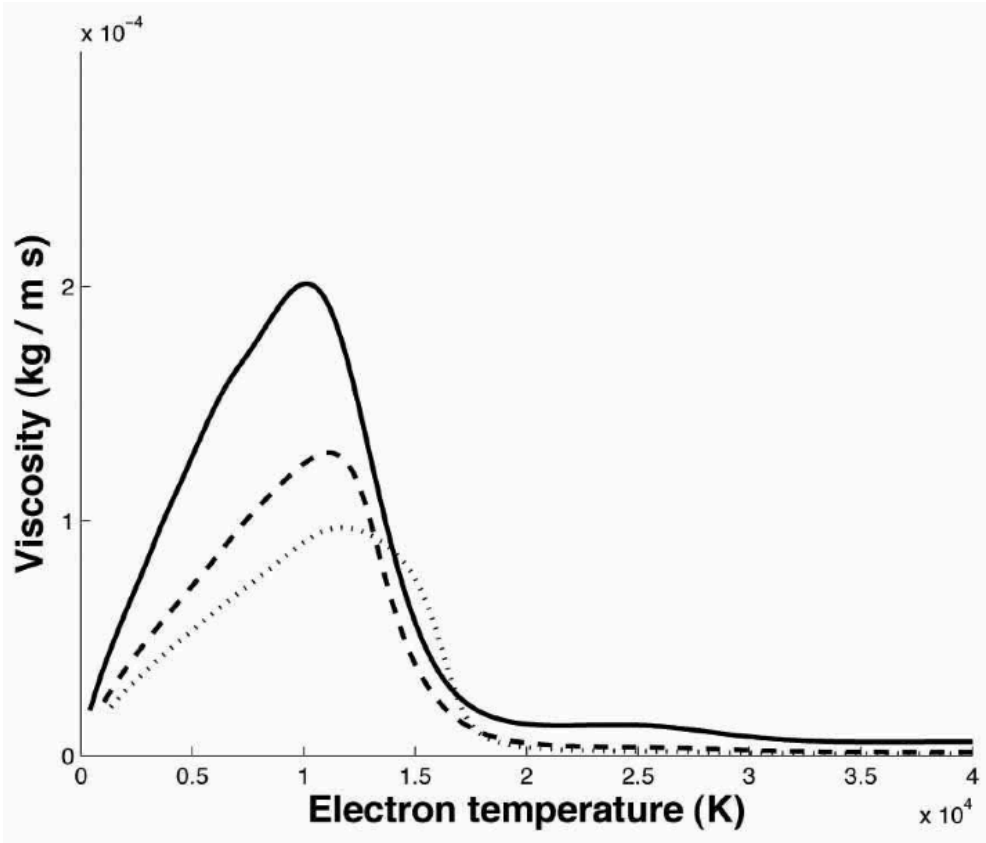


Fig. 12 - Electron temperature dependence of the viscosity for 50% nitrogen - 50% hydrogen mixture by mole fraction for different values of the non-equilibrium parameter: full line, $\theta = 1$, dashed line, $\theta = 2$, dotted line, $\theta = 3$. (taken from Ref. [2])

*Comparisons between Rat's theory and Devoto's theory*

Results for total thermal conductivity and electrical conductivity for 50% argon - 50% hydrogen mixture for $\theta = 2$ are shown in figures 13 and 14, respectively. Comparisons between results obtained with the simplified theory and the non-simplified theory are shown. Moreover, data reported by Rat et al. and results obtained using the modified set of equations in the framework of non-simplified theory (see equations 20-22) are presented.

Both for total thermal conductivity and electrical conductivity results obtained with the simplified theory of Devoto are very similar to those obtained with the non-simplified theory.
Results reported by Rat are in good agreement with those presented in this work with the modified set of equations: only slight discrepancies are evident in the dissociation peak of total thermal conductivity because different temperatures were used in the dissociation equilibrium equation in the calculation of composition; Rat introduced an intermediate temperature $T_{ex}$ because in the recombination reaction the involved third particle can be either an heavy particle or an electron; in this work, following Ghorui[18], the temperature of heavy particles has been used. Our results for the dissociation peak of the total thermal conductivity are in good agreement with those obtained by Rat using the kinetic approach for the calculation of composition instead of the equilibrium constant one.

Moreover, it should be noted that the NLTE reactive thermal conductivity and the NLTE electrical conductivity calculated with the simplified theory are very close to those obtained with the non-simplified one, even if they depend on diffusion coefficients (see figures 13 and 14).

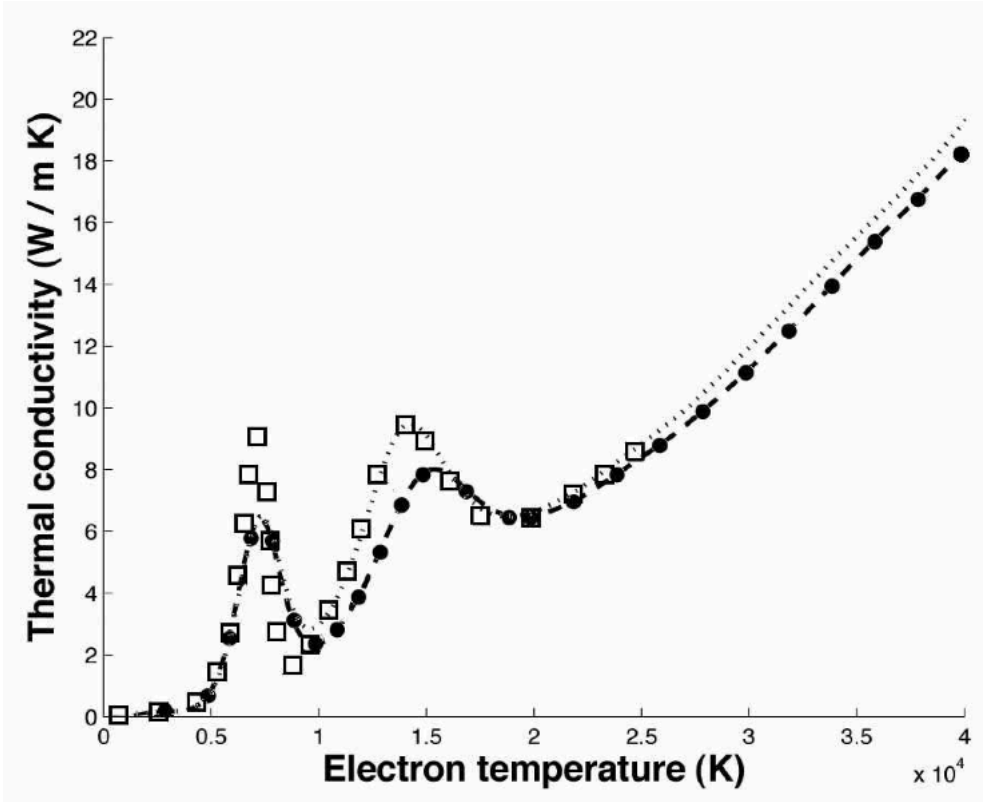


Fig. 13 - Electron temperature dependence of the total thermal conductivity for 50% argon - 50% hydrogen mixture by mole fraction for $\theta = 2$: dashed line - results of this work obtained with the Rat non-simplified theory with the usual set of equations; dotted line - results of this work obtained with the Rat theory with the modified set of equations; full circles - results of this work obtained with the simplified theory of Devoto using usual equations; open squares - results reported by Rat. (taken from Ref. [2])

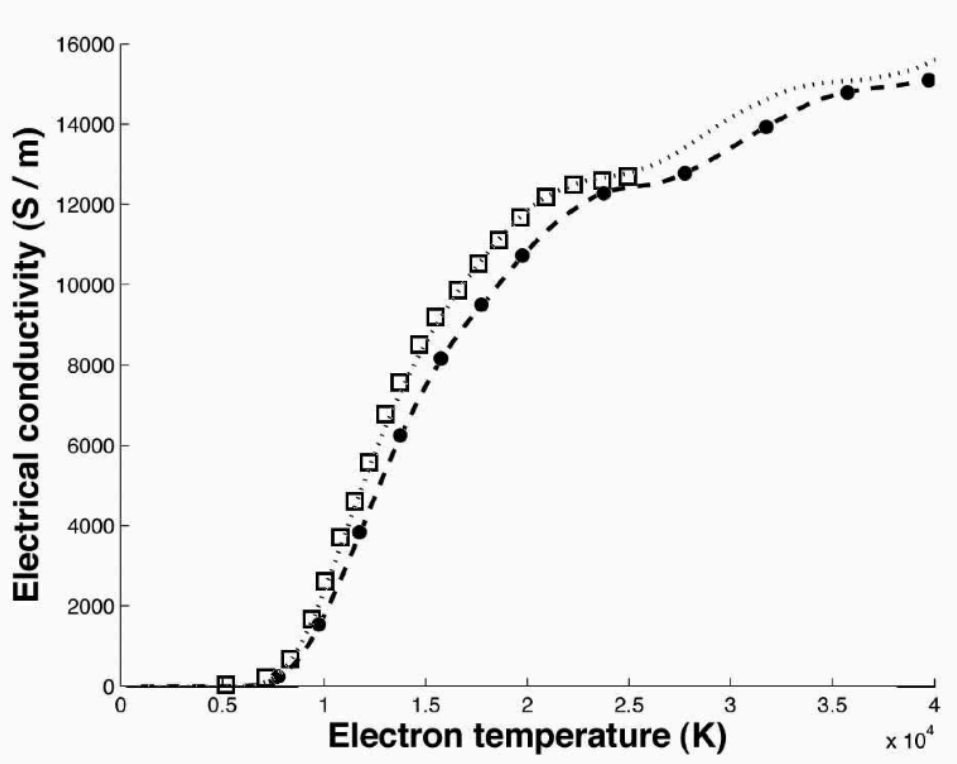


Fig. 14 - Electron temperature dependence of the electrical conductivity for 50% argon - 50% hydrogen mixture by mole fraction for $\theta = 2$: dashed line - results of this work obtained with the Rat non-simplified theory with the usual set of equations; dotted line - results of this work obtained with the Rat theory with the modified set of equations; full circles - results of this work obtained with the simplified theory of Devoto using usual equations; open squares - results reported by Rat. (taken from Ref. [2])

Some of the results we obtained for the ordinary diffusion coefficients are reported in figures 15 and 16 in order to compare results of the simplified theory with those of the non-simplified theory.

Results we obtained with the simplified theory of Devoto are in good agreement with those we obtained with the non-simplified theory of Rat for $\theta = 1$.

For NLTE plasmas the ordinary diffusion coefficients of the type $D_{e\text{-}h}$, where e and h stands for electrons and for heavy particles respectively, obtained in this work in the framework of simplified theory differ from those we obtained with the non-simplified theory (as an example see figure 15). However, results for the diffusion coefficients of the type $D_{h\text{-}e}$ we obtained using the two theories are very similar: figure 16 shows the ordinary diffusion coefficient for hydrogen atoms and electrons, that is $D_{H\text{-}e}$; in this case results of the simplified theory are in agreement with those of the non-simplified one also in NLTE (see in the figure the lines corresponding to $\theta = 2$). The same behavior has been observed for other diffusion coefficients of the type $D_{h\text{-}e}$.

Also for diffusion coefficients of the type $D_{h\text{-}h}$ we obtained very similar results using the two approaches.

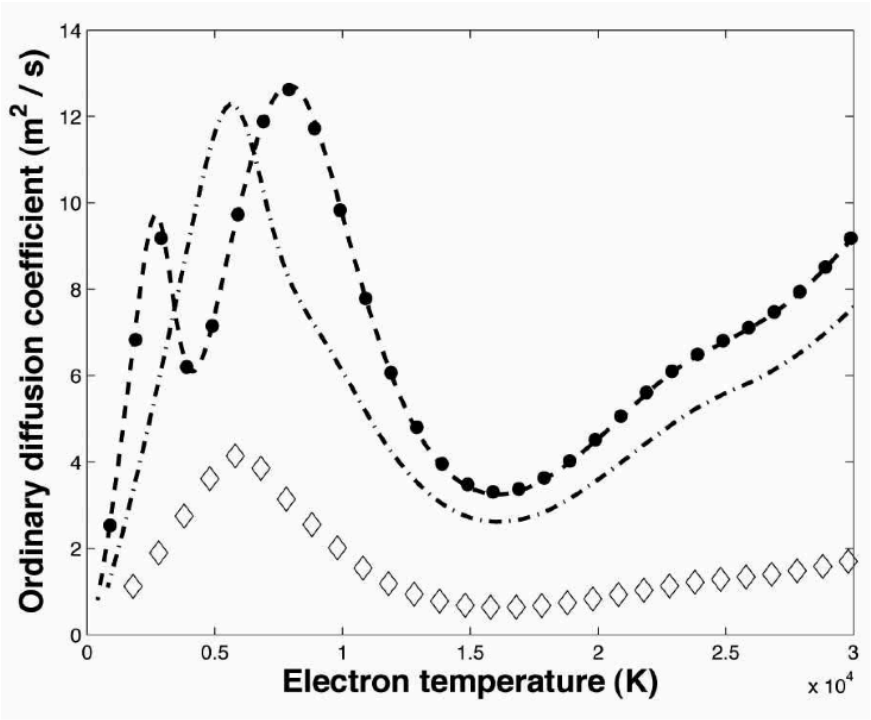


Fig. 15 - Electron temperature dependence of the ordinary diffusion coefficient $D_{e\text{-}H}$ for 50% argon - 50% hydrogen mixture by mole fraction: dashed line - results for θ= 1 with theory of Rat; full circles - results for θ = 1 with theory of Devoto; chain line - results for θ = 2 with theory of Rat; open diamonds - results for θ = 2 with theory of Devoto (taken from Ref. [2])

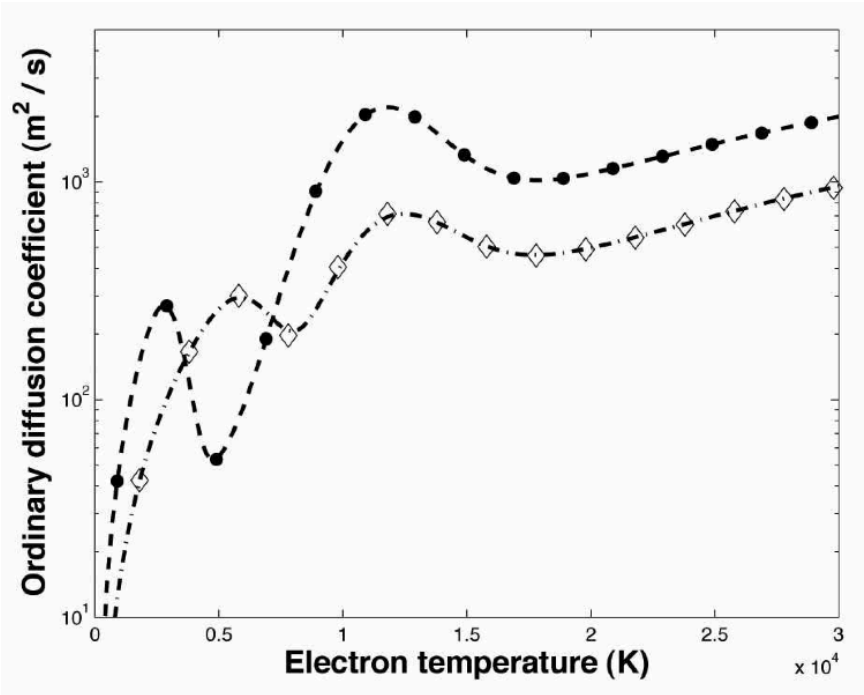


Fig. 16 - Electron temperature dependence of the ordinary diffusion coefficient $D_{H\text{-}e}$ for 50% argon - 50% hydrogen mixture by mole fraction: dashed line - results for θ = 1 with theory of Rat; full circles - results for θ = 1 with theory of Devoto; chain line - results for θ = 2 with theory of Rat; open diamonds - results for θ = 2 with theory of Devoto. (taken from Ref. [2])

*Nitrogen-Hydrogen mixtures*

In figure 17 thermal conductivity of nitrogen - hydrogen mixtures for $\theta = 1$ are reported: nitrogen dissociation peak appears between the dissociation peak of hydrogen and the ionization peak of hydrogen and nitrogen.
Intermediate nitrogen-hydrogen mixtures present three peaks; the ionization peak attains its maximum for 25% nitrogen - 75% hydrogen mixture whereas the peaks due to dissociation of nitrogen and hydrogen reach their maximum for pure nitrogen and pure hydrogen, respectively.
For electron temperatures higher than 25,000 K thermal conductivity increases for increasing concentration of hydrogen.

Electrical conductivity of various nitrogen-hydrogen mixtures in LTE ($\theta = 1$) are presented in figures 18 and 19. At low electron temperatures ($Te < 15{,}000$ K) conductivity decreases with growing concentration of hydrogen (see figure 19); at high temperatures, where second ionization of nitrogen starts, electrical conductivity increases for increasing concentration of hydrogen (figure 18).

Viscosity of various nitrogen-hydrogen mixtures in LTE ($\theta = 1$) are presented in figure 20: for temperature lower than 15,000 K the viscosity of nitrogen is much greater than that of hydrogen; for temperature higher than 25,000 K the viscosity of nitrogen starts to decrease because of the second ionization onset; around 30,000 K nitrogen viscosity becomes lower than hydrogen viscosity.

In figure 21 comparisons between our results for total thermal conductivity for 75% nitrogen - 25% hydrogen mixture in LTE and those reported by Capitelli et al. are shown; differences in collision integral data (up to 20% for the interaction $N\text{-}N^+$ around 14,000 K) result in discrepancies between results for the peak due to first ionization; moreover, the slight shift of the hydrogen dissociation peak is probably due to differences in both the hydrogen dissociation energy used in the computation of composition and the collision integrals for the interactions $H_2\text{-}H_2$ and $H_2\text{-}H$.

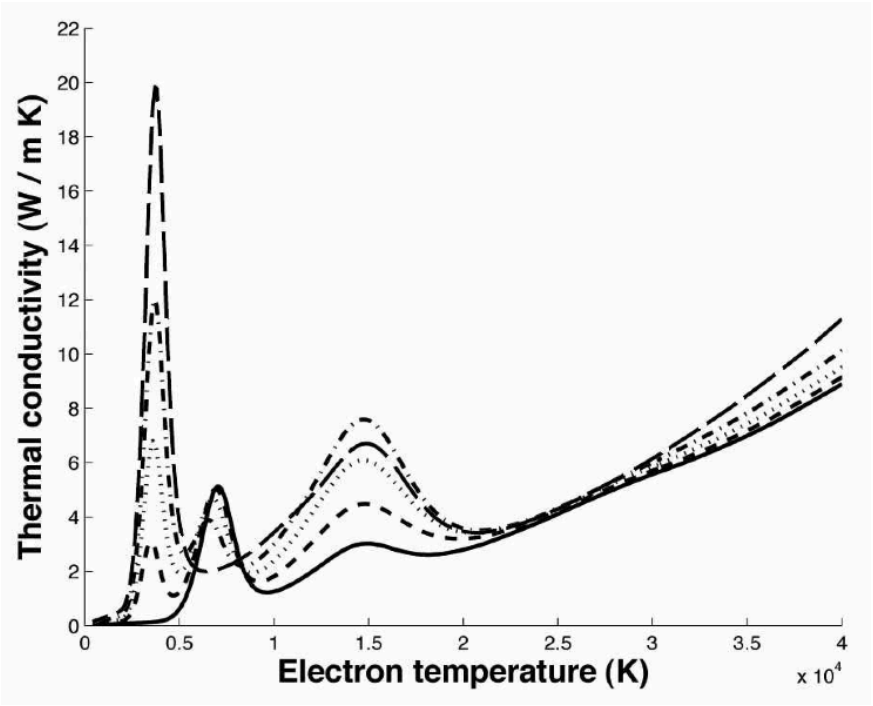


Fig. 17 - Electron temperature dependence of the thermal conductivity for nitrogen-hydrogen mixtures in LTE: full line - 100% nitrogen; dashed line - 75% nitrogen, 25% hydrogen; dotted line - 50% nitrogen, 50% hydrogen; chain line - 25% nitrogen, 75% hydrogen; long broken line - 100% hydrogen. Percentages refer to mole fractions. (taken from Ref. [2])

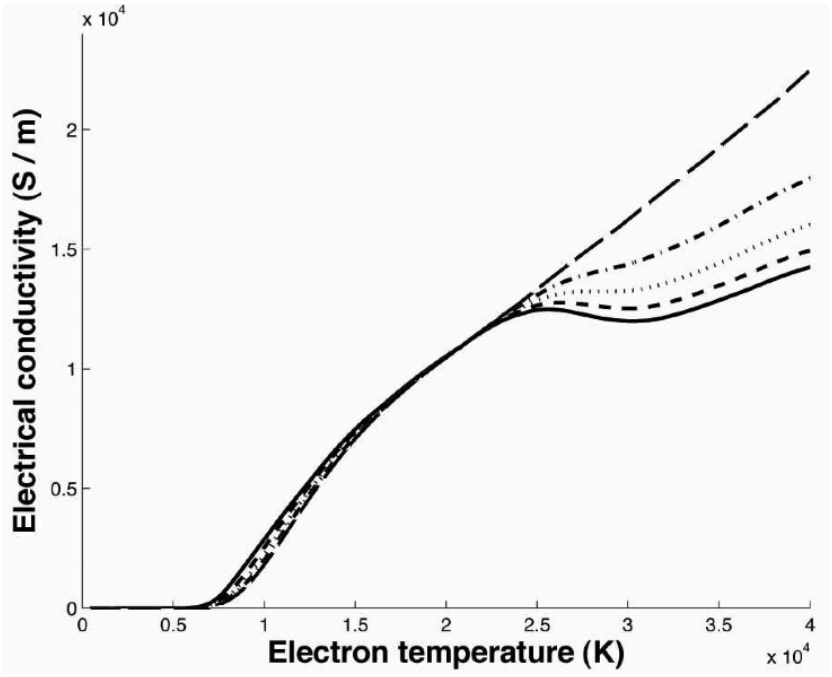


Fig. 18 - Electron temperature dependence of the electrical conductivity for nitrogen-hydrogen mixtures in LTE: full line - 100% nitrogen; dashed line - 75% nitrogen, 25% hydrogen; dotted line - 50% nitrogen, 50% hydrogen; chain line - 25% nitrogen, 75% hydrogen; long broken line - 100% hydrogen. Percentages refer to mole fractions. (taken from Ref. [2])

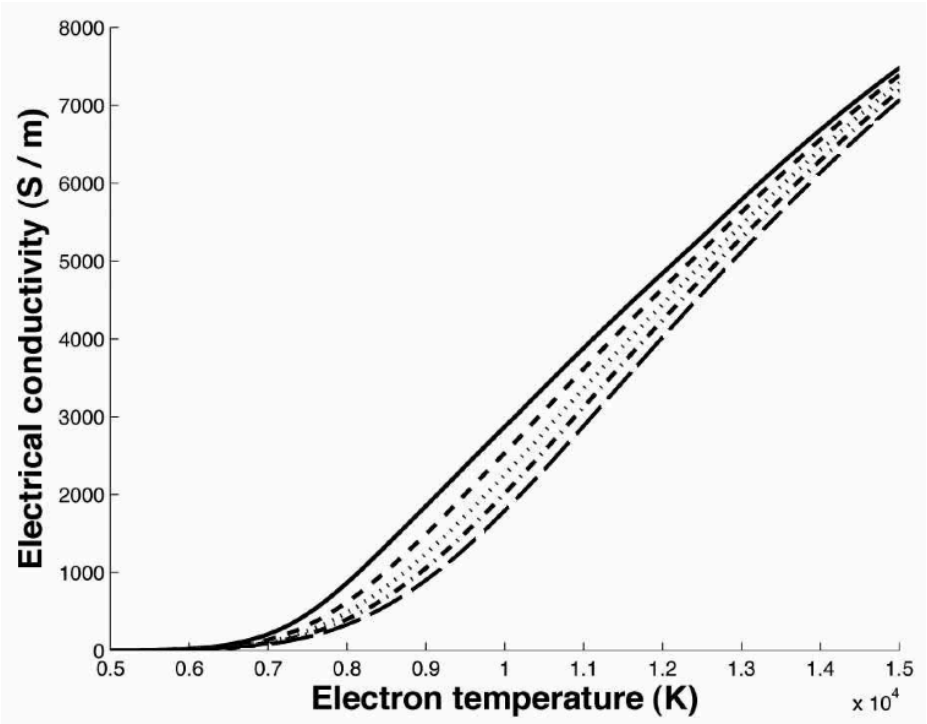


Fig. 19 - Detail of the electrical conductivity for nitrogen-hydrogen mixtures in LTE in the electron temperature range 5,000-15,000 K: full line - 100% nitrogen; dashed line - 75% nitrogen, 25% hydrogen; dotted line - 50% nitrogen, 50% hydrogen; chain line - 25% nitrogen, 75% hydrogen; long broken line - 100% hydrogen. Percentages refer to mole fractions. (taken from Ref. [2])

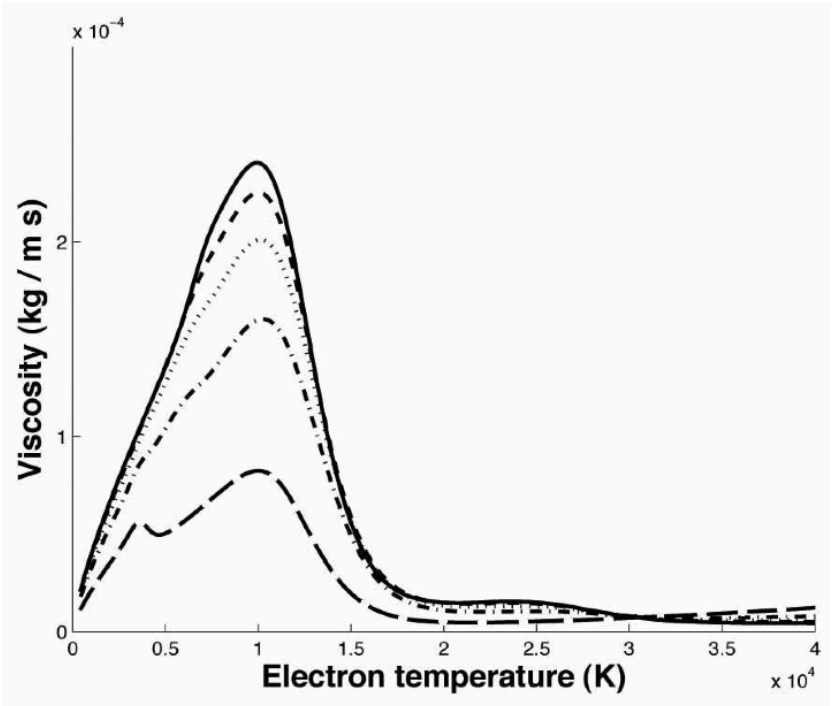


Fig. 20 - Electron temperature dependence of the viscosity for nitrogen-hydrogen mixtures in LTE: full line - 100% nitrogen; dashed line - 75% nitrogen, 25% hydrogen; dotted line - 50% nitrogen, 50% hydrogen; chain line - 25% nitrogen, 75% hydrogen; long broken line - 100% hydrogen. Percentages refer to mole fractions. (taken from Ref. [2])

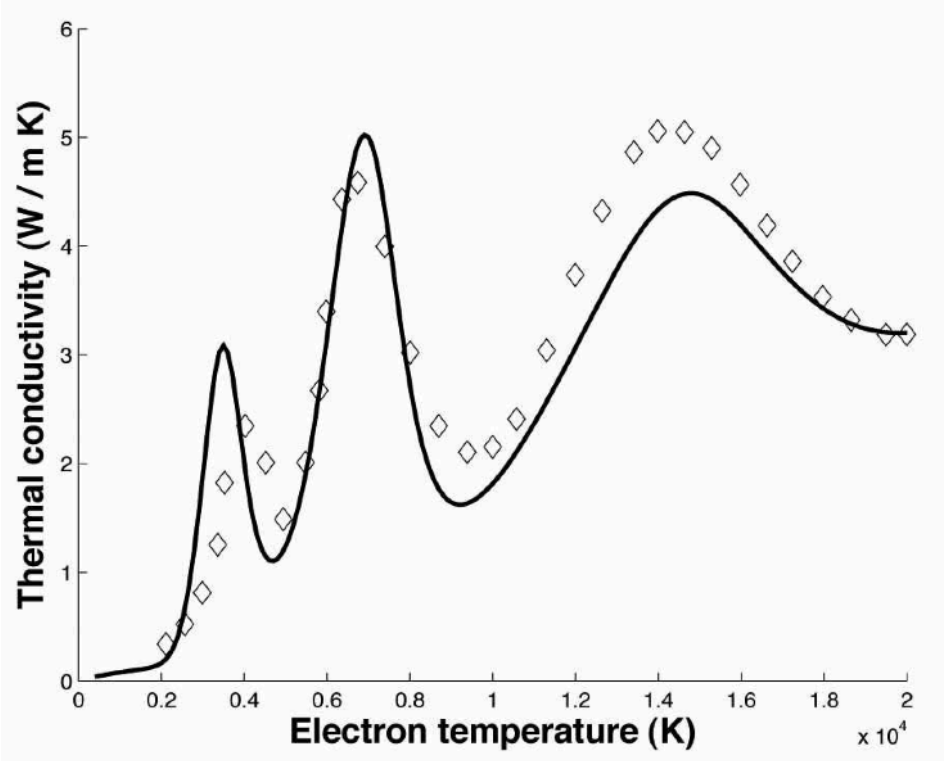


Fig. 21 - Detail of the temperature dependence of the total thermal conductivity for 75% nitrogen - 25% hydrogen mixture by mole fraction in LTE: full line - results of this work; open diamonds - results reported by Capitelli et al. (taken from Ref. [2])

## Properties of carbon-oxygen plasmas

Carbon-oxygen plasmas are widely encountered in metallurgical applications, for example in high-power AC three-phase furnaces with carbon electrodes where methane and oxygen are supplied within the crucible to enhance the scrap melting process. Moreover, an increasing interest has been noted in using carbon-oxygen mixtures in DC non-transferred arc torches for spraying applications: in this case, the non-equilibrium modeling seems to be mandatory in order to accurately predict the unstable behavior of the reattachment process.

The most reliable way to obtain plasma properties, for a wide variety of mixtures in the range 300-30,000 K, is the kinetic theory of ideal gases for thermodynamic properties and the approximate solution of the Boltzmann equation based on the Chapman-Enskog method for transport properties. These methods have been widely studied in local thermodynamic equilibrium (LTE) and some results are reported in literature for the most commonly used pure gases and mixtures including carbon-oxygen mixtures[35, 38-41].

However, departures from thermal equilibrium, where electron temperature differs from that of heavy species, can arise in thermal plasmas when electron concentration is not high enough to allow sufficient transfer of energy between the electrons and heavy species. Moreover, also high electric fields (since $(T_e-T_h)/T_e$ is proportional to $(E/p)^2$), high fluid velocity and high temperature gradients may induce thermal non-equilibrium conditions.
For the computation of non-equilbrium (NLTE) thermodynamic and transport properties, two theories have been developed: in the past, Devoto developed a simplified theory (later improved by Bonnefoi) which considers complete decoupling between heavy particles and electrons, since they assumed that the change of the perturbation function of electrons is greater than that of heavy species during interactions involving both types of particles. Recently, Rat et al. developed a theory in which the coupling between particles and electrons is not neglected, giving rise to a new set of transport coefficients and coupling terms in the fluxes definition.

Transport properties in NLTE have been already calculated for pure gases (Ar, $O_2$, $N_2$, $H_2$) and for mixtures (Ar-$H_2$, Ar-$O_2$, Ar-$N_2$, $N_2$-$O_2$) with the simplified theory; applications of the new theory of Rat et al. have been already presented for Ar, Ar-He, Ar-Cu, Ar-$H_2$, Ar-$H_2$-He and $N_2$-$H_2$ plasmas[2]; however, to our knowledge, no data have been published for thermodynamic and transport properties of carbon-oxygen mixtures in non-equilibrium.

In this work results for non-equilibrium thermodynamic and transport properties of carbon-oxygen mixtures obtained using both the approach of Rat et al. and the simplified method of Devoto are presented; moreover, LTE results for transport properties of carbon-oxygen mixtures computed using Lennard-Jones potentials are reported and compared with results obtained using more recent potential data. Results for the $CO_2$ mixture in LTE are reported showing good agreement with previously published data.

*Composition*

Even though results will be presented only in the temperature range 300 - 30,000 K, calculations have been carried out up to 60,000 K; for this reason, composition of carbon-oxygen plasma has been obtained considering the species C, $C^+$, $C^{2+}$, $C^{3+}$, $C^{4+}$, $O^2$, O, $O^+$, $O^{2+}$, $O^{3+}$, $O^{4+}$, CO, $CO_2$ and $e^-$.
Molecular ions have been not included in the calculations because their concentration at atmospheric pressure is below $10^{-3}$ and they have negligible effects on thermodynamic and transport properties.
Data of the electron energy levels of atoms and ions for the evaluation of their partition functions and the ionization and dissociation energies have been taken from NIST database; rotational and vibrational constants for the calculation of partition functions of molecules have been taken from JANAF tables.

Chemical equilibrium composition for $CO_2$ as a function of electron temperature for LTE conditions is shown in figure 1. At room temperature the gas is composed by $CO_2$ molecules, that dissociate in CO and $O_2$ at temperatures around 4,000 K; for increasing temperatures, the latter dissociates around 4,500 K in atomic oxygen whereas single carbon atoms appears at 6,000 K from the dissociation of CO. Carbon ionization starts at 7,000 K whereas oxygen ions become relevant around 10,000 K. Double ionized particles appear over 20,000 K.

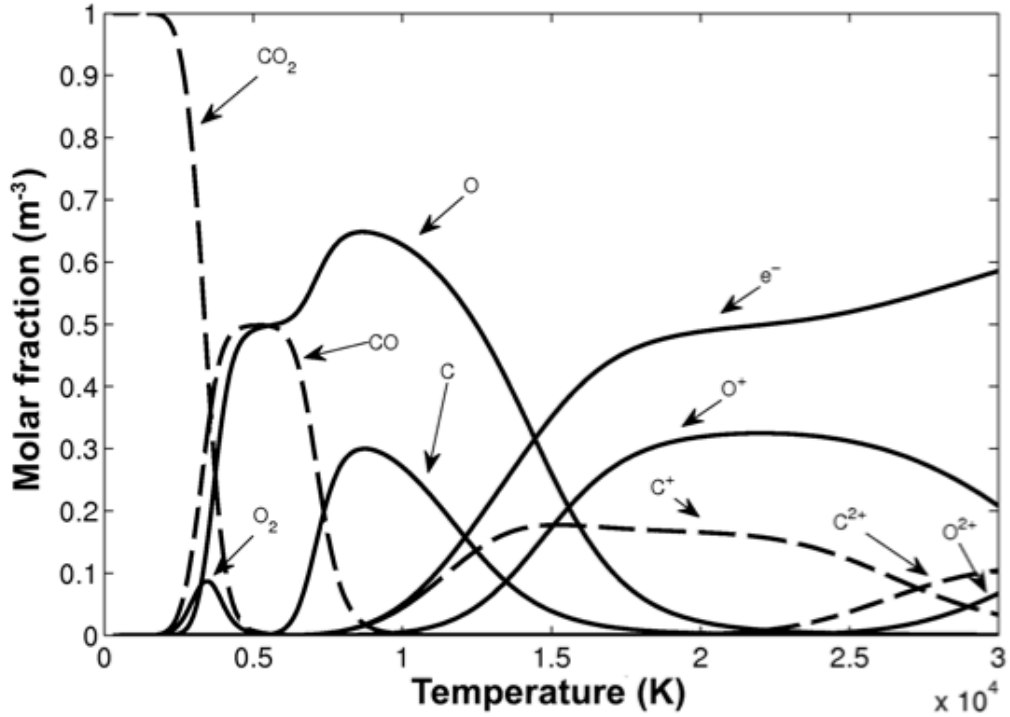


Fig. 1 - Temperature dependence of the composition for $CO_2$ mixture. (taken from Ref. [3])

Thermodynamic properties can be evaluated through a classical statistical mechanics approach, provided number densities and partition functions of each species are known. Density can be written as

$$\rho = \sum_i n_i m_i \quad (5)$$

Total specific enthalpy can be calculated considering the translational, reactional and internal contributions:

$$h = \frac{5}{2}\frac{k}{\rho}\sum_i n_i T_i + \frac{1}{\rho}\sum_i n_i \epsilon_i + \frac{k}{\rho}\sum_i n_i T_i^2 \frac{\partial \ln Q_i^{int}}{\partial T_i} \quad (6)$$

Taking pressure p, electron temperature Te and non-equilibium parameter θ as independent variables, differentiation of total enthalpy gives

$$\partial h = \left(\frac{\partial h}{\partial p}\right)_{T_e,\theta} \partial p + \left(\frac{\partial h}{\partial T_e}\right)_{p,\theta} \partial T_e + \left(\frac{\partial h}{\partial \theta}\right)_{p,T_e} \partial \theta \quad (7)$$

The second derivative term can be interpreted as total specific heat at constant pressure and constant non-equilibrium parameter.

Thermodynamic properties both in LTE and NLTE for carbon-oxygen mixtures at atmospheric pressure in the temperature range 300-30,000 K have been reported in figures 2 and 3.
At the onset of ionization, for fixed heavy particle temperature, the mass density decreases as θ increases. In thermal equilibrium, the total specific heat shows the typical peaks due to dissociation of $CO_2$ and $O_2$ molecules around 4,000 K, to dissociation of CO around 7,000 K and to ionization of carbon and oxygen atoms at 15,000 K. Since heavy particle temperature has a dominant effect on the localization of dissociation peaks on the electron temperature axis, they shift towards higher electron temperature as θ increases, causing also a pronounced shift of the atom ionization in the same direction.
For $\theta > 1$ the first ionization takes place in a narrower range of electron temperature, resulting in a higher peak of total specific heat. For comparison purposes, the results obtained by Sourd et al. for LTE total specific heat have been reported in figure 3 and a good agreement has been found.

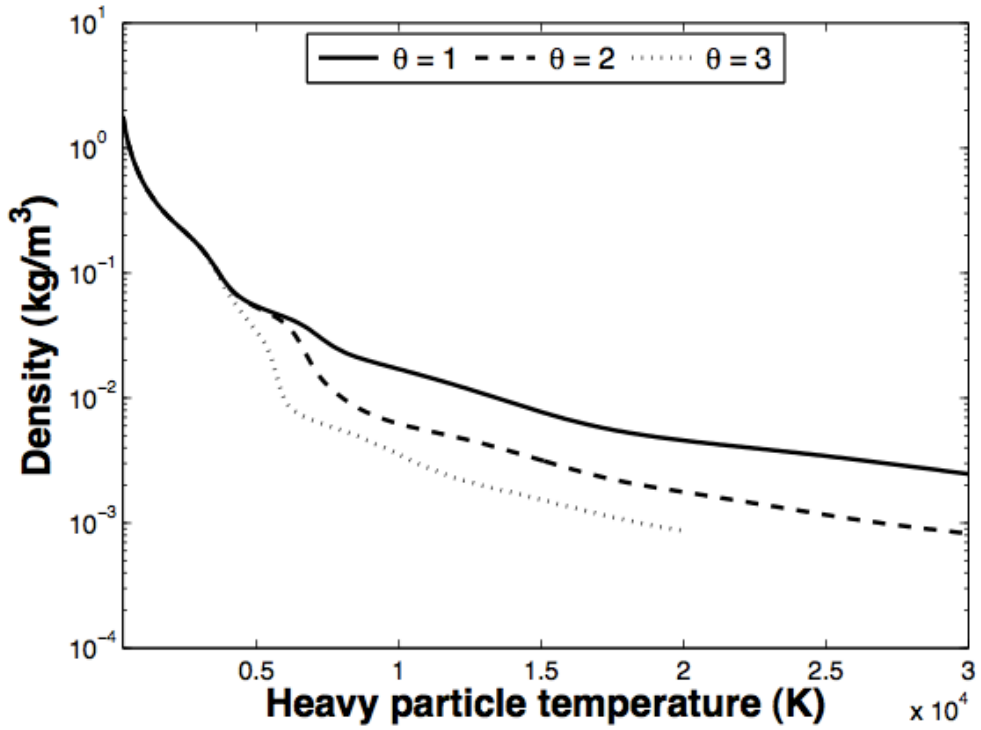


Fig. 2 - Electron temperature dependence of the mass density for $CO_2$ mixture for different values of the non-equilibrium parameter. (taken from Ref. [3])

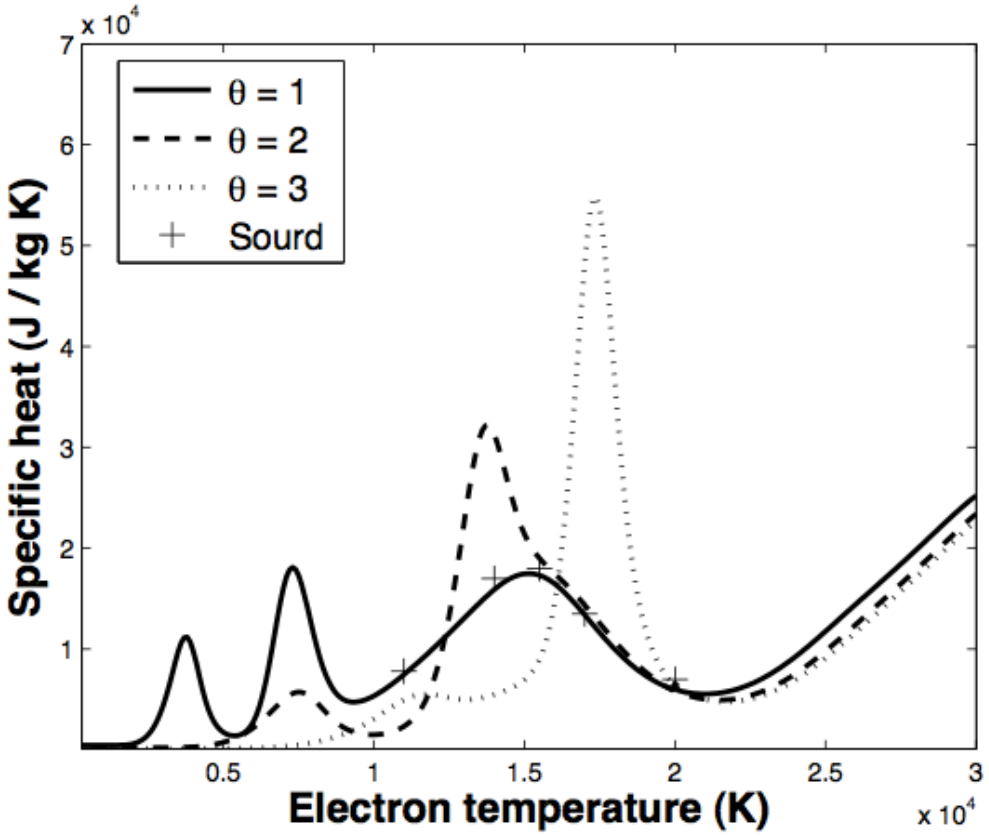


Fig. 3 - Electron temperature dependence of the total specific heat for $CO_2$ mixture for different values of the non-equilibrium parameter. (taken from Ref. [3])

*Collision integrals*

The calculation of transport properties requires the knowledge of collision integrals, which are averages over a Maxwellian distribution of the transport cross-sections for the binary interactions between species.
Collision integrals for the interaction between species i and j are defined as

$$\bar{Q}_{ij}^{(l,s)}(T_{ij}^*) = \frac{2(l+1)}{(s+1)!(2l+1-(-1)^l)} \int_0^{+\infty} e^{-x} x^{s+1} Q_{ij}^{(l)} \, \mathrm{d}x \tag{8}$$

where

$$x = \mu_{ij} g^2 / 2kT_{ij}^*$$

and the effective temperature of collision is defined as

$$T_{ij}^* = \left( \frac{1}{m_i + m_j} \left( \frac{m_i}{T_j} + \frac{m_j}{T_i} \right) \right)^{-1} \tag{9}$$

Computation of transport properties up to the third order requires the knowledge of collision integrals $Q_{ij}^{(l,s)}$ with l and s satisfying the following conditions: $1 \leq l \leq 3$, $l \leq s \leq 5$.
In this work they were obtained in different ways: in a few cases, tabulations of collision integrals have been published and these could be used directly; collision integrals needed in non-equilibrium computations, i.e. $Q_{ij}^{(2,5)}$, $Q_{ij}^{(3,4)}$ and $Q_{ij}^{(3,5)}$, can be obtained from published data using recursion formulae.
Collision integrals which are not tabulated were obtained integrating transport cross sections which are defined by

$$Q_{ij}^{(l)} = 2\pi \int_0^{+\infty} (1 - \cos^l \chi) \, b \, \mathrm{d}b \tag{10}$$

where b and $\chi$ are the impact parameter and the angle of deflection respectively; the latter being given by the expression

$$\chi = \pi - \int_{r_c}^{\infty} \frac{\mathrm{d}r / r^2}{[1 - 2v(r)/\mu_{ij} g^2 - b^2/r^2]} \tag{11}$$

where r and v(r) are the distance and the interaction potential between particles, respectively.

When differential cross section data are available, transport cross sections can be calculated through the following expression:

$$Q_{ij}^{(l)} = \int_0^{\pi} (1 - \cos^l \chi)\sigma(\chi) \sin \chi \mathrm{d}\chi \quad (12)$$

where σ(χ) is the differential cross section.

For interactions in which charge exchange occurs, collision integrals with odd order l include both elastic and inelastic interactions:

$$\bar{Q}^{(l,s)} = [(\bar{Q}_{in}^{(l,s)})^2 + (\bar{Q}_{el}^{(l,s)})^2]^{1/2} \quad (13)$$

where subscripts in and el represent inelastic and elastic collision integrals, respectively. Transport cross sections for inelastic interactions can be expressed as:

$$Q_{ij}^{(l)} = (A - B ln\, g)^2 \quad (14)$$

where g is the relative velocity between particles and A and B are experimental constants; collision integrals for these interactions can be computed using analytical expressions.
In the cases where quantum effects become important in collision dynamics, we have computed transport cross sections with the method of phase shift, using the expressions reported by Devoto and Meeks.

Finally, the collision integrals for the charged-charged interactions were calculated using the screened Coulomb potential; in the evaluation of Debye legth only the contribution of electrons has been considered:

$$\lambda_D = \sqrt{\epsilon_0 \, k \, T_e / e^2 \, n_e} \quad (15)$$

Accurate potential data (in the Hulburt-Hirschfelder form) for the computation of collision integrals for binary interactions between species in the carbon-oxygen mixtures have been taken from the works by Sourd et al. and Aubreton et al.
Data for binary interactions between oxygen species have been taken from Murphy[5].
For comparison purposes, transport properties have been calculated also starting from collision integrals for the neutral-neutral interactions obtained using Lennard-Jones potentials. These data have been taken from Pateyron et al. [40] and André et al[39].

*Transport properties*

The computation of transport properties is usually done using the Chapman-Enskog method, assuming that distribution functions of particles are first order perturbations to the Maxwellian distribution; perturbations are then expressed in series of Sonine polynomials, finally leading to a system of linear equations that can be suitably solved to obtain different transport properties.

*$CO_2$ transport properties in non-equilibrium: comparison between Devoto's theory and Rat's theory.*

Expressions for the calculations of these properties have been obtained by Devoto, Bonnefoi and Rat following two different approaches: Devoto and Bonnefoi assume complete decoupling between electrons and heavy species, resulting in a simplified approach whereas Rat recently developed a non-simplified method which retain the coupling.
For LTE plasmas, results obtained with the simplified theory are in good agreement with those of the non-simplified theory; for NLTE plasmas, Rat stated that the simplified method of Devoto and Bonnefoi can't be used to evaluate correctly diffusion coeffients, electrical conductivity and electron translational thermal conductivity.

In this work, electrical conductivity and thermal conductivity have been computed with both methods. For the evaluation of the reactive thermal conductivity the approach reported by Rat has been followed; internal thermal conductivity has been neglected because of its small contribution. Viscosity has been calculated using the simplified approach of Devoto because results are very close to those obtained with the non-simplified theory, as reported by Rat.

Moreover, results for electrical conductivity, thermal conductivities, including reactive contribution, and few diffusion coefficients obtained using also the approach of Devoto are shown in comparison with results obtained with the theory of Rat et al; in the calculation of the reactive thermal conductivity the knowledge of ordinary diffusion coefficients is a prerequisite; in the simplified framework following Hirschfelder the latter have been approximated as

$$D_{ij} = \frac{F^{ji} - F^{ii}}{m_j |F|} \quad (16)$$

where $F^{ij}$ are the cofactors of the matrix F whose elements are defined as

$$F_{ij} = \frac{1}{\rho}\left[\frac{n_i}{D^b_{ij}} + \sum_{l \neq i} \frac{n_i m_j}{m_i D^b_{il}}\right](1 - \delta_{ij}) \quad (17)$$

The binary diffusion coefficients have been evaluted through the formula reported by Rat et al:

$$D^b_{ij} = \left(\frac{2\pi k}{\mu_{ij} T^*_{ij}}\right)^{1/2} \frac{3 T_i g_{ij}}{16 n \bar{Q}^{(1,1)}_{ij}} \quad (18)$$

where n is the total number density, $\theta_{ij}$ = Ti/Tj and

$$g_{ij} = \frac{(m_j + m_i\theta_{ji})^2(m_i + m_j\theta_{ji})^3}{\theta_{ji}^{5/2}(m_j + m_i)^5} \quad (19)$$

In the calculation of transport properties using the Rat's theory, the coefficients of the linear system of equations have been evaluated taking into account their dependence on Te/Th and on the species mass ratio.

Transport properties both in LTE and NLTE for carbon-oxygen mixtures at atmospheric pressure in the temperature range 300-30,000 K are presented. Results for values of the non-equilibrium parameter θ = 1, 2, 3 and for different mixture concentrations are reported. Transport properties have been calculated using interaction potentials of the type Hulrburt-Hirschfelder (HH).

Total thermal conductivity for various carbon-oxygen mixtures in non-equilibrium have been calculated. Thermal conductivity has been evaluated with respect to heavy particles temperature gradient, that is

$$\vec{q} = -\lambda\vec{\nabla}T_h$$

Figure 4 presents thermal conductivity for $CO_2$ mixture for various values of θ; the dissociation peak of $CO_2$ shifts towards higher electron temperatures as θ increases because the dissociation reaction constant depends on heavy particles temperature: three peaks are clearly distinguishable for θ = 1 whereas for higher θ the dissociation peaks reach the ionization peak.
In the temperature range where dissociation and ionization take place, a great contribution to total thermal conductivity is given by the reactive term, whereas for temperatures higher than 15,000 K the translational contribution is the most important.

Electrical conductivities, for different values of θ, for $CO_2$ mixture are reported in figure 5.
At low temperature, for increasing values of θ, conductivities for $CO_2$ mixtures decrease because ionization shifts towards higher electron temperatures.
For electron temperatures higher than 17,000 K conductivity increases with growing values of θ.

Both for thermal and electrical conductivity, comparisons between results obtained using the Rat's theory and the Devoto's theory are shown in figures 4 and 5, respectively: results obtained with the simplified theory of Devoto are very similar to those obtained with the non-simplified theory.

Viscosity, for different values of θ, for $CO_2$ mixture is reported in figure 6. With growing values of the non-equilibrium parameter, we observe a decreasing viscosity peak around Te ≈ 10,000 K and a shift of ionization onset toward higher electron temperature.

Some of the results we obtained for the ordinary diffusion coefficients are reported in figure 7, in order to compare the results of the simplified theory with those of the non-

simplified theory. The results obtained with the simplified theory of Devoto are in good agreement with those we obtained with the non-simplified theory of Rat et al. for $\theta = 1$. For non-equilibrium plasmas the ordinary diffusion coefficients of the type $D_{e\text{-}h}$, where e and h stand for electrons and for heavy particles respectively, obtained in this work in the framework of the simplified theory differ from those we obtained with the non-simplified theory. However, the results for the diffusion coefficients of the type $D_{h\text{-}e}$ that we obtained using the two theories are very similar.
Also for diffusion coefficients of the type $D_{h\text{-}h}$ we obtained very similar results using the two approaches.
Moreover, it should be noted that the NLTE reactive thermal conductivity and the NLTE electrical conductivity calculated with the simplified theory are very close to those obtained with the non-simplified one, even if they depend on diffusion coefficients.

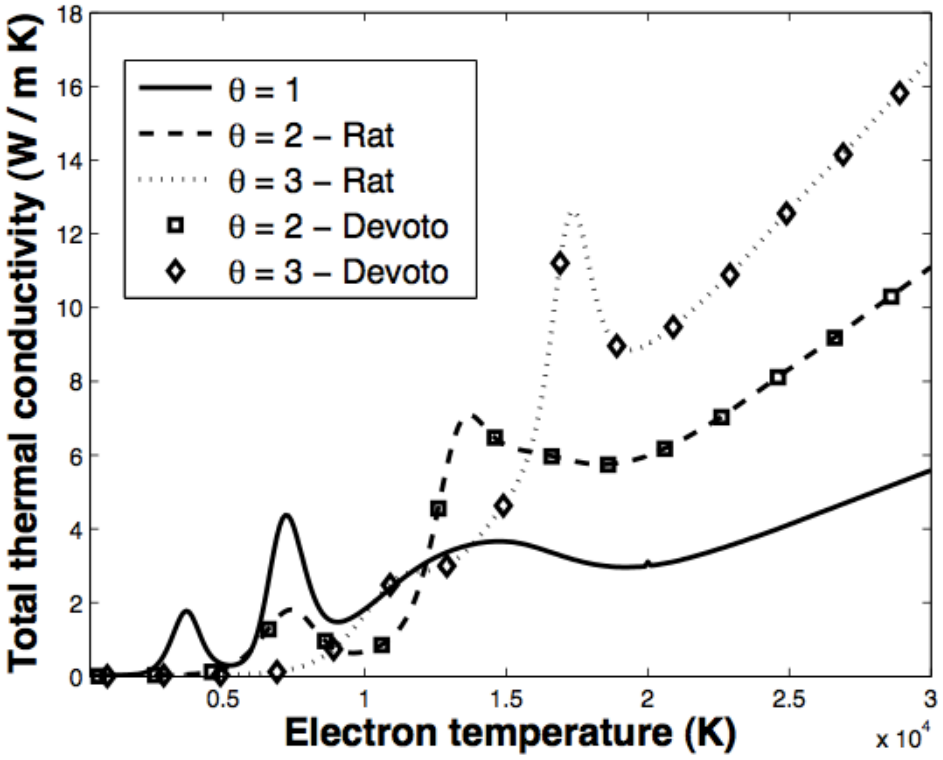


Fig. 4 - Electron temperature dependence of the thermal conductivity for $CO_2$ mixture for different values of the non-equilibrium parameter. (taken from Ref. [3])

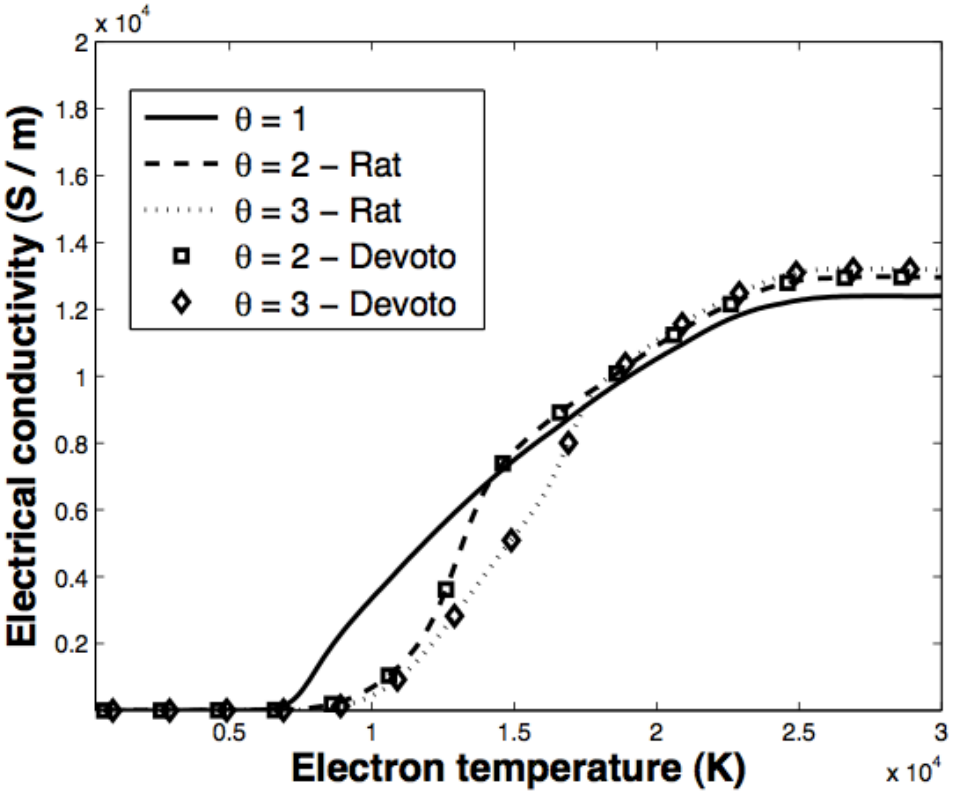


Fig. 6 - Electron temperature dependence of the electrical conductivity for $CO_2$ mixture for different values of the non-equilibrium parameter. (taken from Ref. [3])

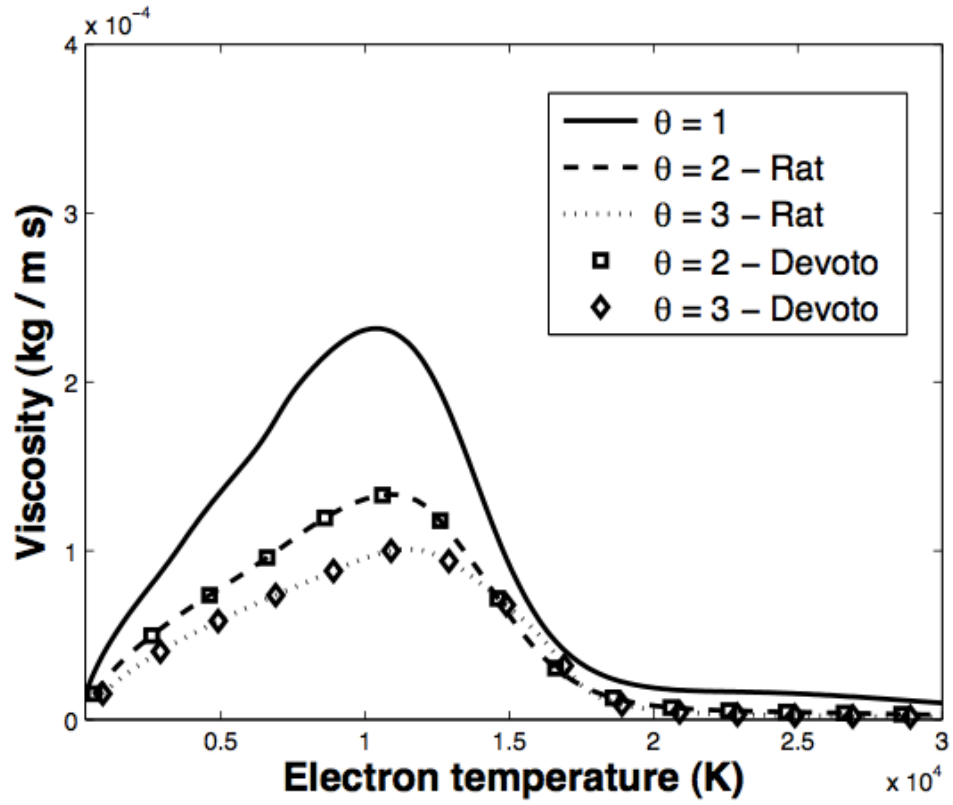


Fig. 6 - Electron temperature dependence of the viscosity for $CO_2$ mixture for different values of the non-equilibrium parameter. (taken from Ref. [3])

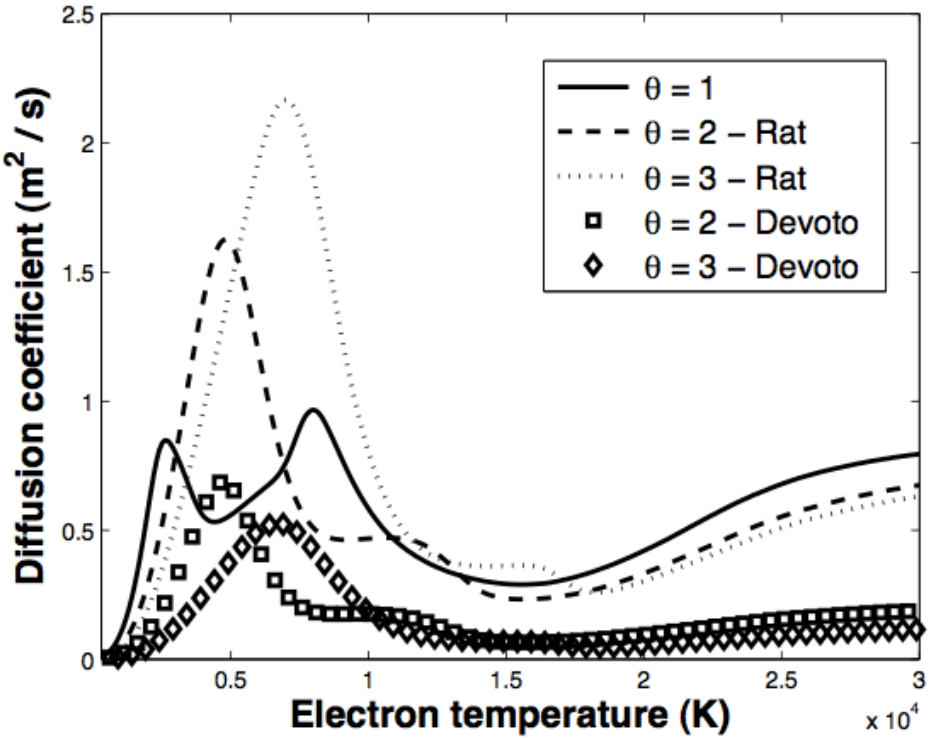


Fig. 7 - Electron temperature dependence of the ordinary diffusion coefficient $D_{e\text{-}c}$ for $CO_2$ mixture for different values of the non-equilibrium parameter. (taken from Ref. [3])

*Comparison between transport properties computed using different collision integrals*

In this work, transport properties have been calculated both using recently published interaction potentials of the type Hulrburt-Hirschfelder (HH) and using simplified potentials of the type Lennard-Jones (LJ).

Results for thermal conductivity, electrical conductivity and viscosity for $CO_2$ mixture in equilibrium have been reported in figures 8, 9 and 10, respectively.
For thermal conductivity, the main differences between the two approaches are related to the temperature range where CO dissociation occurs (around 7,000 K) and in the ionization peak around 15,000 K. The latter consideration holds also for viscosity. The maximum relative difference between the two approaches is 16% and 13% for thermal conductivity and viscosity, respectively. For electrical conductivity almost no differences have been obtained.

Our results have been compared with results reported in literature, showing good agreement when the same set of collision integrals has been used.

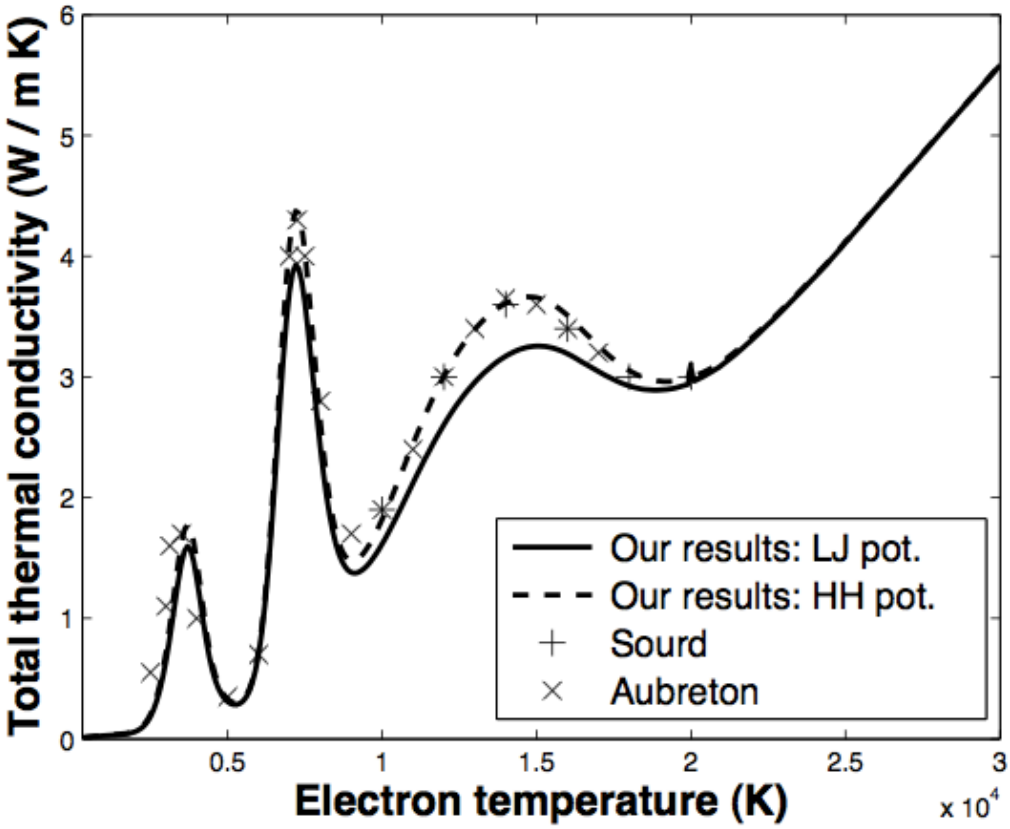


Fig. 8 - Temperature dependence of the thermal conductivity for $CO_2$ mixture for different sets of collision integrals. (taken from Ref. [3])

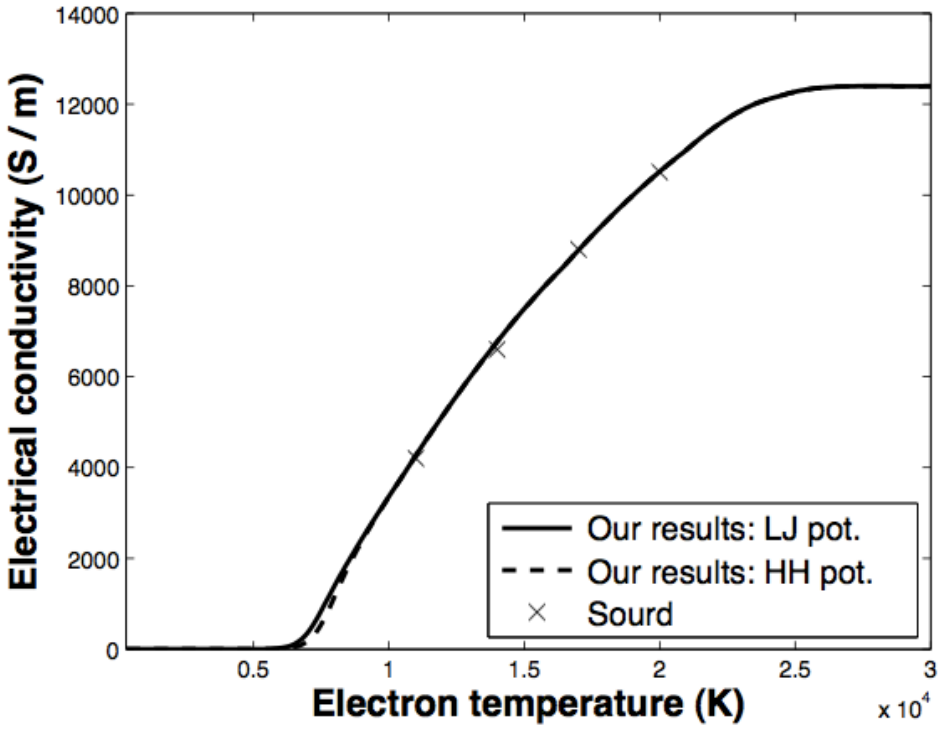


Fig. 9 - Temperature dependence of the electrical conductivity for $CO_2$ mixture for different sets of collision integrals. (taken from Ref. [3])

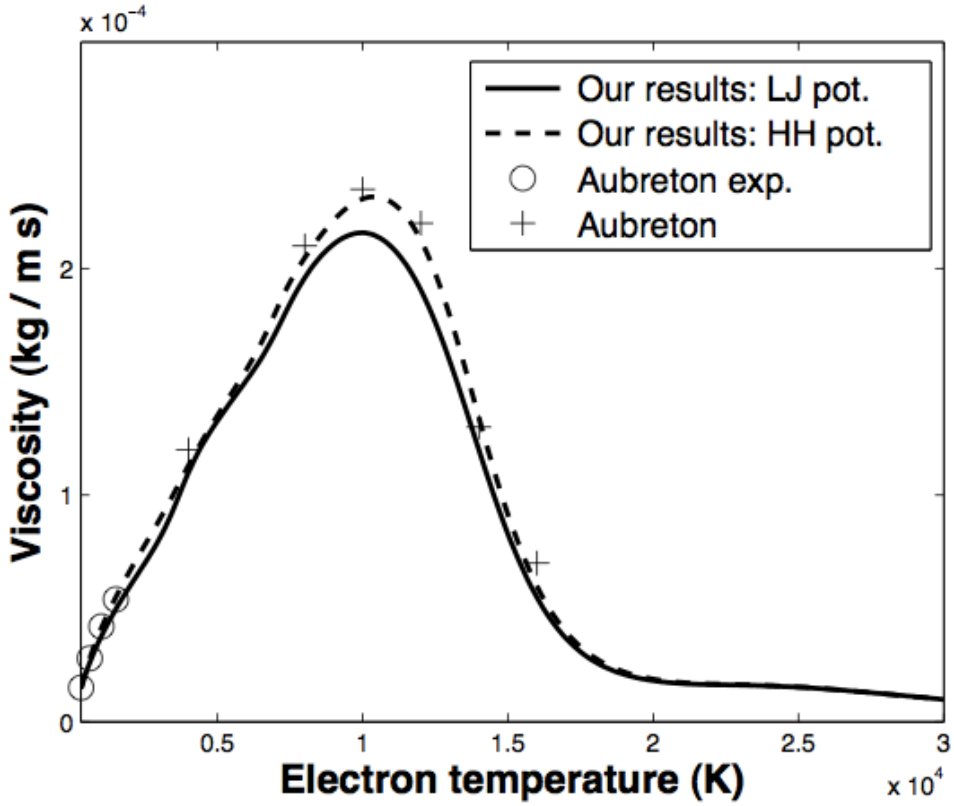


Fig. 10 - Temperature dependence of the viscosity for $CO_2$ mixture for different sets of collision integrals. (taken from Ref. [3])

*Transport properties for different carbon-oxygen mixtures*

Transport properties depend strongly on composition. In this section, we reported equilibrium transport properties for different percentages of carbon concentration, with the final aim of highlighting the main effects of the presence of this element in a oxygen gas.

In figure 11, thermal conductivity for different carbon-oxygen mixtures is reported: for pure oxygen, the only peak due to dissociation is that of $O_2$ molecules, which has been obtained around 4,000 K; for increasing concentration of carbon ($CO_2$ mixture), the peak related to CO dissociation becomes evident at 7,000 K; for higher carbon concentration (CO mixture), the peak due to $O_2$ dissociation disappears; when the gas is composed by carbon only, there are no peaks due to dissociation.
The ionization peak increases at low carbon concentration, but for higher concentration than that of the CO mixture this peak is lowered and shifted towards low temperatures.

Electrical conductivity for different carbon-oxygen mixtures has been reported in figure 12: at low temperatures (below 15,000 K) the conductivity increases with the carbon concentration as a result of the lower ionization energy of carbon with respect to oxygen; at higher temperatures the inverse behavior has been found.

Viscosity for pure oxygen is the highest among the mixtures considered; the presence of carbon induces a decrease in viscosity for the whole temperature range investigated (see figure 13).

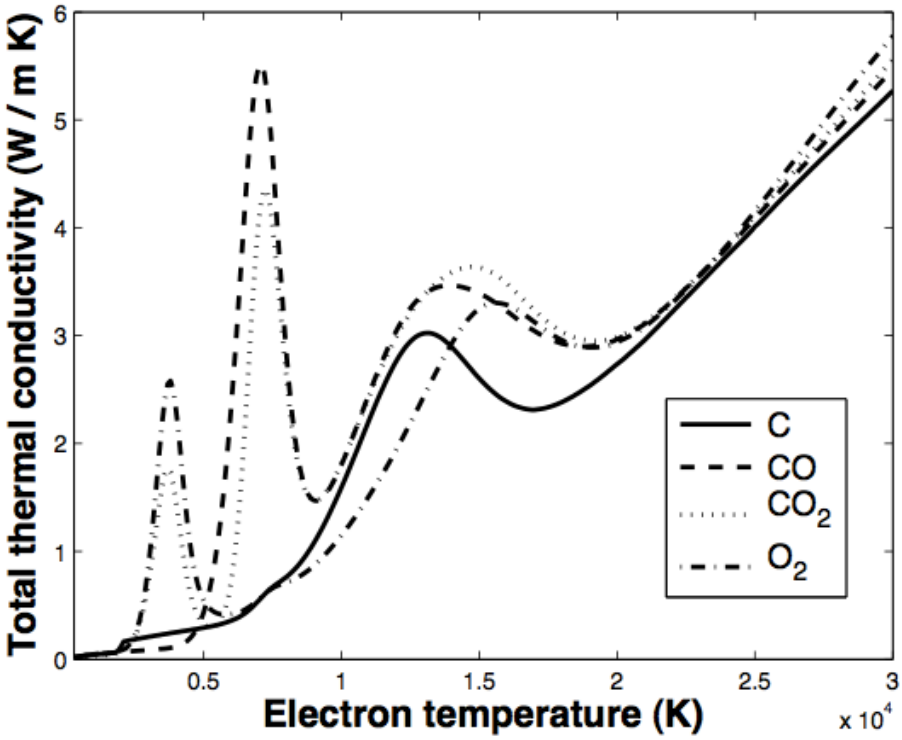


Fig. 11 - Temperature dependence of the thermal conductivity for different carbon-oxygen mixtures in equilibrium. (taken from Ref. [3])

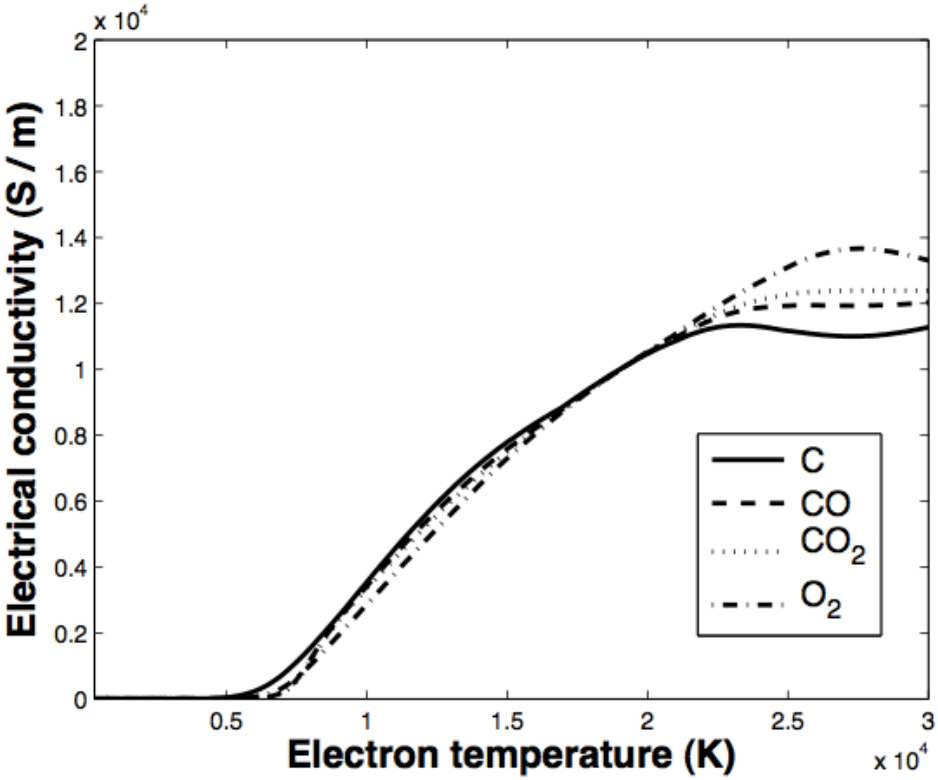


Fig. 12 - Temperature dependence of the electrical conductivity for different carbon-oxygen mixtures in equilibrium. (taken from Ref. [3])

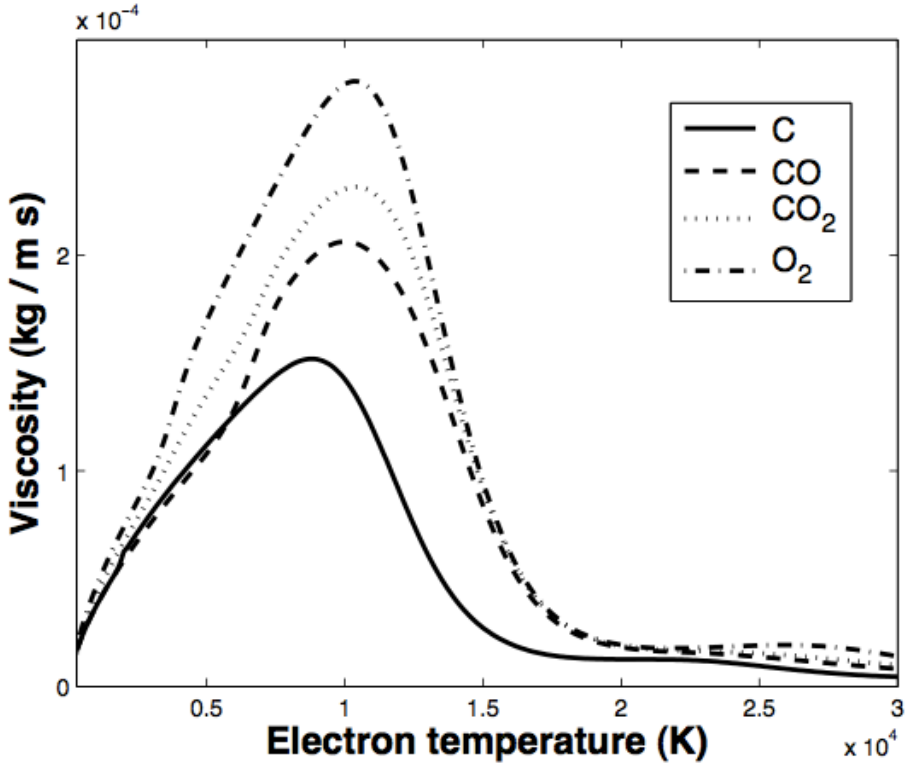


Fig. 13 - Temperature dependence of the viscosity for different carbon-oxygen mixtures in equilibrium. (taken from Ref. [3])

## Conclusions

Thermodynamic and transport properties of argon, oxygen and nitrogen plasmas in local thermodynamic equilibrium (LTE) and local thermal non-equilibrium (NLTE) up to 45,000K have been presented, extending the temperature range currently available in literature, especially for nitrogen plasma.
The accuracy of the results has been checked through comparisons with published available data: agreement is excellent for LTE, while slight differences are seen for NLTE. The main discrepancies arise when different methods for the composition computation are used or different Debye length definition is chosen in evaluating collision integrals. Slight differences between results are seen when using the decoupling method of Devoto instead of the non-simplified theory of Rat.
Thermodynamic and transport properties reported in this work have been calculated with the assumption of local chemical equilibrium, even though the developed code can work with arbitrary compositions. Composition for NLTE has been obtained using two different equilibrium equations for the ionization process, in order to compare our results with literature using the same composition calculation approaches of different authors. However, heavy species dependent transport properties show almost no influence with respect to composition calculation approach.
Thermodynamic and transport properties of argon-hydrogen and nitrogen-hydrogen plasmas in local thermodynamic equilibrium (LTE) and in local thermal non-equilibrium (NLTE) in the electron temperature range 300-40,000 K have been presented.
Results reported in this work for argon-hydrogen mixtures extend the temperature range currently available in literature, whereas results for nitrogen-hydrogen mixtures update with collision integrals recently calculated by Stallcop et al. and by Sourd et al. data reported by Capitelli et al. in LTE; in addition, to our knowledge, this work fills the lack of data for non-equilibrium properties of nitrogen-hydrogen mixtures.
We made comparisons between our results for 50% argon and 50% hydrogen and, both, data in LTE published by Murphy and data in NLTE presented by Rat et al.: excellent agreement has been found in LTE, whereas some discrepancies have been highlighted in NLTE; we succeeded in reproducing data reported by Rat et al. using modified equations for Saha chemical equilibrium equation, Debye length and electron enthalpy.
Moreover, for the computation of NLTE transport properties both the simplified method of Devoto and the non-simplified method of Rat et al. have been followed in this work: comparisons between results obtained using these two theories have shown that there are some discrepancies in ordinary diffusion coefficients of the type $D_{e\text{-}h}$ whereas there is good agreement for ordinary diffusion coefficients of the type $D_{h\text{-}e}$ and $D_{h\text{-}h}$; also, as already stated by Rat et al. for viscosity, there are no relevant discrepancies in total thermal conductivity (including reactive contribution) and electrical conductivity, even if they depend on ordinary diffusion coefficients.
In opposition to what was stated by Rat et al., we found that coupling between electrons and heavy species has no relevant effects on the prediction of non-equilibrium plasma transport properties.
Since design oriented modelling of industrial plasma cutting torches can be a very onerous task in the case of computation with large number of grid cells, the simplified approach of Devoto becomes the tool of choice, as an alternative to the more time-consuming non-simplified approach of Rat et al., in order to compute plasma properties both in LTE and NLTE. Computation of transport properties for specific

argon-hydrogen and nitrogen-hydrogen mixtures, such as H35 and F5, can be done as a particular case in the frame of this work, for modelling of plasma sources fit for cutting of stainless steel plates and for comparisons of results with diagnostics and experiments.
Thermodynamic and transport properties of carbon-oxygen plasmas in local thermodynamic equilibrium (LTE) and in local thermal non-equilibrium (NLTE) in the electron temperature range 300-30,000 K have been presented.
To our knowledge, this work fills the lack of data in literature for non-equilibrium properties of carbon-oxygen mixtures.
Results obtained highlights the fact that simplified expressions can be used for the transport property calculation: it has been shown that for carbon-oxygen mixtures no differences between results obtained using the two theories developed by Devoto and Rat et al can be appreciated for thermal conductivity, electrical conductivity and viscosity.
Moreover, LTE results for transport properties obtained using Lennard-Jones potentials have been have been compared with results obtained using more sophisticated potential data, showing that the maximum relative error is below 16% and 13% for thermal conductivity and viscosity, respectively. For electrical conductivity very similar results have been obtained using the two sets of interaction potentials.

The code that I developed and validated in this study by comparison with literature results will be used in chemical non-equilibrium plasma modelling, where composition is obtained locally taking into account species transport and reactions, in order to developed a more consistent physical model for thermal plasma discharges simulation.
Plasma modelling often requires fast and reliable ways of calculating transport properties on-demand, especially for the case of thermal and chemical non-equilibrium plasmas, or when complex plasma mixtures have to be investigated. Results from this work are available upon request and they can be used in tabulated form, with very low computational efforts.

References


1. V. Colombo, E. Ghedini and P. Sanibondi, Progress in Nuclear Energy **50** (8), 921-933 (2008).
2. V. Colombo, E. Ghedini and P. Sanibondi, Journal of Physics D: Applied Physics **42** (5), 055213 (2009).
3. V. Colombo, E. Ghedini and P. Sanibondi, Plasma Source Sci. Technol., accepted for publication (2011).
4. M. I. Boulos, P. Fauchais and E. Pfender, Thermal Plasmas: Fundamentals and Applications **1** (1994).
5. A. B. Murphy and C. J. Arundell, Plasma Chemistry and Plasma Processing **14** (4), 451-490 (1994).
6. A. B. Murphy, IEEE Trans. Plasma Sci. **25** (5), 809 (1997).
7. A. B. Murphy, Plasma Chemistry and Plasma Processing **20** (3), 279-297 (2000).
8. A. D'Angola, G. Colonna, C. Gorse and M. Capitelli, European Physical Journal D **46** (1), 129-150 (2008).
9. J. O. Hirschfelder, C. F. Curtiss and R. B. Bird, *Molecular Theory of Gases and Liquids*. (1954).
10. M. Tanaka and M. Ushio, Journal of Physics D: Applied Physics **32** (10), 1153-1162 (1999).
11. J. P. Trelles, J. V. R. Heberlein and E. Pfender, Journal of Physics D: Applied Physics **40** (19), 5937-5952 (2007).
12. S. Ghorui, J. V. R. Heberlein and E. Pfender, Journal of Physics D: Applied Physics **40** (7), 1966-1976 (2007).
13. R. S. Devoto, Physics of Fluids **10** (10), 2105-2112 (1967).
14. C. Bonnefoi, State Thesis, University of Limoges, 1983.
15. V. Rat, P. André, J. Aubreton, M. F. Elchinger, P. Fauchais and A. Lefort, Physical Review E - Statistical, Nonlinear, and Soft Matter Physics **64** (2 II), 264091-2640920 (2001).
16. J. Aubreton, C. Bonnefoi and J. M. Mexmain, Rev. Phys. Appl. **21** (6), 365-376 (1986).
17. J. Aubreton, M. F. Elchinger and P. Fauchais, Plasma Chemistry and Plasma Processing **18** (1), 1-27 (1998).
18. S. Ghorui, J. V. R. Heberlein and E. Pfender, Plasma Chemistry and Plasma Processing **27** (3), 267-291 (2007).
19. V. Rat, P. André, J. Aubreton, M. F. Elchinger, P. Fauchais and A. Lefort, Plasma Chemistry and Plasma Processing **22** (4), 475-493 (2002).
20. J. Aubreton, M. F. Elchinger, P. Fauchais, V. Rat and P. André, Journal of Physics D: Applied Physics **37** (16), 2232-2246 (2004).
21. J. Aubreton, M. F. Elchinger, V. Rat and P. Fauchais, Journal of Physics D: Applied Physics **37** (1), 34-41 (2004).
22. M. C. M. Van De Sanden, P. P. J. M. Schram, A. G. Peeters, J. A. M. Van Der Mullen and G. M. W. Kroesen, Physical Review A **40** (9), 5273-5276 (1989).
23. V. Rat, P. André, J. Aubreton, M. F. Elchinger, P. Fauchais and D. Vacher, Journal of Physics D: Applied Physics **35** (10), 981-991 (2002).
24. D. Godin and J. Y. Trépanier, Plasma Chemistry and Plasma Processing **24** (3), 447-473 (2004).

25. K. S. Drellishak, D. P. Aeschliman and A. Bulent Cambel, Physics of Fluids **8** (9), 1590-1600 (1965).
26. R. S. Devoto, Physics of Fluids **10** (2), 354-364 (1967).
27. R. S. Devoto, Physics of Fluids **9** (6), 1230-1240 (1966).
28. R. S. Brokaw, The Journal of Chemical Physics **32** (4), 1005-1006 (1960).
29. M. Capitelli, C. Gorse and P. Fauchais, J. Physique **38** (6), 653 (1977).
30. V. Rat, A. P., J. Aubreton, M. F. Elchinger, P. Fauchais and A. Lefort, Plasma Chemistry and Plasma Processing **22** (4), 453-474 (2002).
31. J. R. Stallcop, C. W. Bauschlicher, H. Partridge, S. R. Langhoff and E. Levin, J. Chem. Phys. **97** (8), 5578 (1992).
32. J. R. Stallcop, H. Partridge, S. P. Walch and E. Levin, J. Chem. Phys. **97** (5), 3431 (1992).
33. J. R. Stallcop, H. Partridge and E. Levin, Phys. Rev. **62** (6), 062709 (2000).
34. J. R. Stallcop, H. Partridge and E. Levin, Phys. Rev. **64** (4), 042722 (2001).
35. B. Sourd, J. Aubreton, M. F. Elchinger, M. Labrot and U. Michon, J. Phys. D: Appl. Phys. **39** (6), 1105 (2006).
36. H. U. Mittmann, H. P. Weise, A. Ding and A. Henglein, Z. Naturf. **26**, 1282 (1971).
37. C. Bonnefoi, J. Aubreton and J. M. Mexmain, Z. Naturf. **40**, 885 (1985).
38. J. Aubreton, M. F. Elchinger, A. Hacala and U. Michon, Journal of Physics D: Applied Physics **42**, 095206 (2009).
39. P. André, L. Brunet, W. Bussiere, J. Caillard, J. M. Lombard and J. P. Picard, European Physical Journal D **25**, 169 (2004).
40. B. Pateyron, G. Delluc and P. Fauchais, Plasma Chemistry and Plasma Processing **25**, 485 (2005).
41. M. Tanaka, S. Tashiro, M. Ushio, T. Mita, A. B. Murphy and J. J. Lowke, Vacuum **80**, 1195 (2006).

# MODELLING OF INDUCTIVELY COUPLED PLASMA TORCHES FOR INDUSTRIAL APPLICATIONS

In this chapter, results of the activities carried out during my Ph.D. studies on the modelling of Inductively Coupled Plasma Torches (ICPT) will be presented. My contribution has been mainly in the implementation of C libraries in the framework of the commercial CFD software ANSYS FLUENT [1]. I developed an accurate model for the diffusion of binary non-reactive mixtures, using the so-called "combined" method of Murphy, and I implemented a model for the synthesis of nano-powders in plasma reactors, the so-called "moment" model. For the diffusion model, I developed the codes for the calculation of combined diffusion coefficients and I implemented the diffusion model in the FLUENT environment including demixing effects. For the "moment" model, I implemented the physical model in the FLUENT framework developing appropriate C libraries using User Defined Functions.
The developed models have been used to investigate thermo-fluid-dynamic fields and particle heating in a ICPT system with non-axi-symmetric reaction chamber using a fully 3D approach. Some consideration on nano particle charging during synthesis in ICPT reactors will be presented at the end of the chapter. Some results reported in this chapter have been already published on international journals[2, 3].

## Introduction

Inductively coupled plasma torches have been widely used both for laboratory scale studies and for successful industrial applications, thanks to their unique characteristics: high energy density, high volume, high purity and high scalability [4]. The range of possible applications includes powder spheroidization [5-7], waste treatment [8, 9], thermal spray [10, 11], while, in the last decade, increasing attention has been given to synthesis of nano-powders [12-18].

Since the beginning of the development of this technology during the '60s of the last century [19], numerical modelling has been a powerful tool in order to predict typical values for the plasma properties (for example temperature, velocity, coupled power, electro-magnetic fields) and plasma behaviour under different operating conditions. Numerical modelling has allowed a deep insight in the understanding of thermal plasma processes. This is especially true when diagnostics is limited because of the torch setup configuration and operating conditions: e. g. in the investigation of phenomena taking place in commercial torches for industrial applications, which usually have opaque walls and can be operated with step-like changes of coupled power. Optical emission spectroscopy of the high temperature plasma bubble can't be used with these type of torches, whereas enthalpy probe can be used in the tail of the plasma jet only, because of too high heat fluxes inside the torch.

The first generation of these codes was one-dimensional, aiming at the calculation of the radial profile of temperature and of electro-magnetic fields in the coil region [20, 21]; the evolution of simulation tools towards two-dimensional models allowed the description of more realistic thermo-fluid-dynamic fields, with coupled electro-

magnetic ones and particle heating, including plasma-particle interaction and diffusion of vapours from particles [22, 23].

The development of high capability computers and clusters in the '90s of the last century and at the beginning of the new millennium has allowed the implementation of more and more sophisticated modelling approaches [9] including supersonic flows [24], turbulence models [25], thermal non-equilibrium through two-temperature models [26-28], chemical non-equilibrium [29, 30], accurate description of diffusion processes for complex mixtures [31-33] and three-dimensional geometries [34, 35].

Although an attempt to include some minor effects of the spiral shape of the coil using two-dimensional codes has been made by Xue et al. [36], the use of 3-D codes has proved to be a key factor in order to accurately describe ICP torches: the inherently three-dimensional shape of the helicoidal coil induces the generation of non-axisymmetric thermal and fluid-dynamic fields which couldn't be predicted using 2-D codes, as it has been reported for a commercial laboratory scale torch [2, 37] and for spectrometry torches [38], just to cite a few.

Increasing attention is given to three-dimensional effects in temperature and velocity fields which arise taking into account realistic three-dimensional geometries: e.g. the effects of the real coil shape, the detailed inlet gas region of the torch and the transverse injection of cold jets have already been studied.

In this chapter, the model developed during my Ph.D. course will be presented in detail. They include a three-dimensional code for the evaluation of the effects of changing coil current frequency in inductively coupled plasma torches, a detailed description of diffusion through a combined approach by Murphy[31], a particle heating model for the evaluation of thermal histories of powders injected in ICP torches, a moment model for the evaluation of nanopowder production in ICP systems. Consideration of nano-particle charging in thermal plasma will be discussed.

**Three-dimensional investigation of the effects of excitation frequency and sheath gas mixing in an atmospheric-pressure inductively-coupled plasma system**

The scope of this study is to investigate by means of a fully three-dimensional code the influence of different coil current frequencies on thermo-fluid-dynamic fields, the hydrogen mixing in an argon primary gas and the flow patterns and temperature distributions which take place in a reaction chamber with a lateral gas outlet system and two observation windows suitable for diagnostics.
The induction torch chosen for this study is one of the most common commercial models: a Tekna Plasma Systems Inc. model PL-35.
A previous work [2] has shown that torch configurations with high-frequency and high turn coil density can result in almost axisymmetric plasma discharges inside the torch. Thus, the first goal of this paper is to give deeper insights about the influence of frequency alone on the three-dimensional shape of temperature, velocity and composition fields inside the torch.
This study is in line with the fact that the same torch can be operated with different coil current frequencies, depending on the configuration of the RF generator connected thereto, and that typical values for this parameter in a Tekna PL-35 torch are 3 MHz and 13.56 MHz. We concentrated on these values for coil current frequency since they are commonly used in many systems for both research and production purposes and they are dedicated by law to industrial applications in many countries.
The second goal and third goals of this work arise from the fact that different gas mixtures (inert, oxidant, reducing) can be injected in the torch[5, 16] and that in powder processing applications the induction torch is usually used in connection with a reaction chamber in order to obtain conditions for pressure and gas composition suitable for the purpose of treating and processing injected raw materials.
In powder spheroidization, waste treatment and nano-powder production an argon-hydrogen mixture is usually used [6, 39] since the higher specific heat and the higher thermal conductivity of hydrogen results in a higher plasma enthalpy and in a higher heat flux to the particles. Argon-hydrogen is usually injected as sheath gas and hydrogen has small mole fractions (less than 10%) to preserve the quartz tube from overheating. The second goal is thus to accurately investigate the diffusion of hydrogen from the sheath gas, since powder treatment processes are very sensitive to hydrogen content in the core of the discharge.
The diffusion of gases in induction torches has been studied in many papers with different approaches, including combined diffusion[31] and chemical non-equilibrium[40]. Some works by Tanaka [28, 29], Watanabe et al. [41, 42] and other authors [30, 43] implemented the second approach, obtaining accurate prediction of species distribution in the torch: as a drawback, in those papers, demixing due to mole fraction and temperature gradients has not been investigated.
On the contrary, a combined diffusion approach has been used by Chen[44], but the effects of demixing have not been discussed in detail, although results for the mass fraction of hydrogen shows that it occurs in the near-wall region.
In this study we considered diffusion of hydrogen from the secondary gas with a combined diffusion approach in a three-dimensional framework, including investigation of different relevant demixing mechanisms (mole fraction and temperature gradients).

The third goal of this paper is to predict flow patterns inside a non-axisymmetric reaction chamber with a lateral outlet gas system and investigate the influence of advection on temperature distribution in the tail of the plasma discharge. This type of investigation is of interest for nano-powder synthesis applications, where main processes (particle nucleation and growth) take place in the low temperature (over-saturated) zone located in the downstream region of the torch [16].
Inductively coulpled plasma torches have been investigated also using thermal non-equilibrium approaches [36]: these studies have shown that for pressure higher that 0.5 bar NLTE conditions exists only in the discharge fringes (near cold gas injection regions and torch walls) where high temperature gradients exist. Moreover, for argon-hydrogen mixtures Ye et al. [45] showed that NLTE effects are much less pronounced that in the case of pure argon, as a result of higher electron-heavy particle cross section for hydrogen species than for argon species. Consequently, in this paper, since an atmospheric pressure argon-hydrogen plasma has been considered, a LTE approach has been chosen.

*Modeling approach*

The following hypothesis are assumed in the present calculations:

- Plasma is in local thermodynamic equilibrium (LTE);
- Combined diffusion approach of Murphy is used to model the diffusion in a mixture of two non-reactive gases;
- Turbulent effects are taken in account through RNG k-ε model;
- Plasma is optically thin and radiative losses are taken in account considering only the presence of argon in the mixture;
- Composition is computed taking in account six species: Ar, $Ar^+$, $H_2$, H, $H^+$ and electrons;
- Viscous dissipation term in the energy equation is neglected;
- Displacement currents are neglected.

The physical behavior of the plasma has been modeled removing any axisymmetric assumption and a fully 3D model has been implemented in the FLUENT environment. The governing equations can be written as

$$\nabla \cdot (\rho \vec{v}) = 0 \quad (1)$$

$$\nabla \cdot (\rho \vec{v}\vec{v}) = -\nabla p + \nabla \cdot \tau + \rho \vec{g} + F_L \quad (2)$$

$$\nabla \cdot (\rho \vec{v} h) = -\nabla \cdot \left( \frac{k_{eff}}{c_p} \nabla h \right) + \nabla \cdot \left( \sum_i h_i \left( \vec{J}_i + \frac{k_{eff}}{c_p} \nabla \overline{Y}_i \right) \right) + P_J - Q_r - Q_L \quad (3)$$

where ρ is the plasma density, v is the velocity, p is the pressure, τ is the viscous stress tensor, $h$ is the total enthalpy, $k_{eff}$ is the effective thermal conductivity that includes both laminar and turbulent contributions; $c_p$ is the specific heat at constant pressure, g is the gravitational force and $Q_r$ is the volumetric radiative loss; $Q_L$ is the

plasma-particle exchange term; $Y_i$ and $J_i$ are the mass fraction and the diffusion current of the i-th gas.
The Lorentz forces $F_L$ and Joule dissipation $P_J$ can be written as

$$F_L = \frac{1}{2}\Re(\boldsymbol{J} \times \boldsymbol{B}^*) \quad (4)$$

$$P_J = \frac{1}{2}\Re(\boldsymbol{J} \cdot \boldsymbol{E}^*) \quad (5)$$

where **J** is the complex phasor for the current density induced in the plasma, **B** is the magnetic induction complex phasor, **E** is the electric field complex phasor. The superscript "*" indicates the complex conjugate. Using the commercial software FLUENT to solve fluid equations, the Lorentz forces, ohmic heating, radiative loss terms and energy sources due to diffusion must be taken into account by using suitable User-Defined Functions written in C language.

Diffusion of gases can be described using the combined approach of Murphy, assuming local chemical equilibrium. This method allows to treat diffusion of gases containing a large number of species (six species in our case) solving only (N-1) equations, where N is the number of gases in the mixture (N=2 in our simulations), leading to a great reduction in computational time.
Moreover, this method can be considered as accurate as a fully multi-component diffusion approach provided that local chemical equilibrium has been reached; as shown by Rini for air plasmas, this conditions is verified in ICP torches for pressure greater that 0.3 bar.
The FLUENT software provides modules for the solution of diffusion equations with the following form:

$$\nabla \cdot \left(\rho \vec{v} \overline{Y}_i\right) + \nabla \cdot \vec{J}_i = 0$$

where diffusion currents $\mathbf{J}_i$ can be written as

$$\boldsymbol{J}_i = -\left(\frac{\mu_t}{Sc} + \rho D_i^Y\right)\nabla \overline{Y}_i - D_i^T \nabla \ln T$$

where $Y_i$, $D_i^Y$ and $D_i^T$ are mass fraction, the mass fraction diffusion coefficient and the temperature diffusion coefficient for the i-th gas, respectively; $\mu_t$ is the turbulent viscosity and Sc is the Schmidt number taken equal to 0.7.

Using the same symbols introduced by Murphy and taking

$$\nabla \overline{x}_i = \left(\partial \overline{x}_i / \partial \overline{Y}_i\right)\nabla \overline{Y}_i + \left(\partial \overline{x}_i / \partial T\right)\nabla T,$$

the combined diffusion equations given by Murphy for a binary mixture composed by the gases i and j can be solved in the FLUENT environment setting

$$D_i^Y = \frac{n^2}{\rho^2}\overline{m}_i\overline{m}_j\overline{D_{ij}^x}\frac{\partial\overline{x}_i}{\partial\overline{Y}_i}$$

$$D_i^T = \overline{D_{ij}^T} + \frac{n^2}{\rho}\overline{m}_i\overline{m}_j\overline{D_{ij}^x}T\frac{\partial\overline{x}_i}{\partial\overline{T}}$$

where $D^x_{ij}$ and $D^T_{ij}$ are the combined diffusion coefficients due to mole fraction gradients and due to temperature gradients, respectively.
It should be noted that temperature diffusion coefficient $D^T_i$ includes some of the effects of diffusion due to mole fraction gradients (the second term in equation 9) and those of diffusion due to temperature gradients ($D^T_{ij}$).
Diffusion due to pressure gradients and electric fields have been reasonably neglected.

Turbulent effects in the downstream region of the discharge have been included in the flow calculations using the RNG k-ε model:

$$\nabla\cdot(\rho k\boldsymbol{v}) = \nabla\cdot(\alpha_k\mu_{eff}\nabla k) + G_k + G_b - \rho\epsilon$$

$$\nabla\cdot(\rho\epsilon\boldsymbol{v}) = \nabla\cdot(\alpha_\epsilon\mu_{eff}\nabla\epsilon) + C_{1\epsilon}\frac{\epsilon}{k}(G_k + C_{3\epsilon}G_b) - C_{2\epsilon}\rho\frac{\epsilon^2}{k} - R_\epsilon$$

where $G_k$ and $G_b$ represents the generation of turbulence kinetic energy due to the mean velocity gradients and buoyancy, respectively; the quantities $\alpha_k$ and $\alpha_\varepsilon$ are the inverse effective Prandtl numbers for k and ε, respectively; $C_{1\varepsilon}$, $C_{2\varepsilon}$ and $C_{3\varepsilon}$ are constants with values 1.42, 1.68 and 0.09, respectively.
The turbulent viscosity, the inverse effective Prandtl numbers, the turbulent thermal conductivity, the turbulent diffusion coefficients and the source term $R_\varepsilon$ are computed from the RNG theory as described in Fluent user's guide.

Turbulent wall function has been chosen according to mesh size near the chamber and torch walls: since in this region the grid is sufficiently fine (cell characteristic length less than 0.2 mm), the viscosity-affected near-wall sub-layer could be fully resolved and the transition to turbulent regions could be modeled using an enhanced wall treatment, which include the traditional two-layer zonal model.

The electromagnetic field generated by the current flowing in the coil ($\mathbf{J}_{coil}$) and by the induced currents in the plasma ($\mathbf{J}$) can be described by means of Maxwell's equations written in their vector potential formulation:

$$\nabla^2\boldsymbol{A} - i\omega\mu_0\sigma\boldsymbol{A} + \mu_0\boldsymbol{J}_{coil} = 0$$

where $\mu_0$ is the magnetic permeability of the free space, σ is the plasma electrical conductivity, and $\omega=2\pi f$, f being the frequency of the electromagnetic field. The electric field complex phasor **E** and the magnetic field complex phasor **B** are obtained from the vector potential complex phasor **A** with the following expressions: $\mathbf{E} = -i\omega\mathbf{A}$, $\boldsymbol{B} = \nabla\cdot\boldsymbol{A}$. In this work, we have used the simplified Ohm's law $\mathbf{J} = \sigma\mathbf{E}$.

*Computational domain and boundary conditions*

The domain considered in the calculations includes a PL-35 torch and a non-axysimmetric reaction chamber with two observation windows (OW1 and OW2) and a lateral gas outlet tube. A schematic of the computational domain is reported in figure 1. The origin of z-axis is located at the top of the torch.

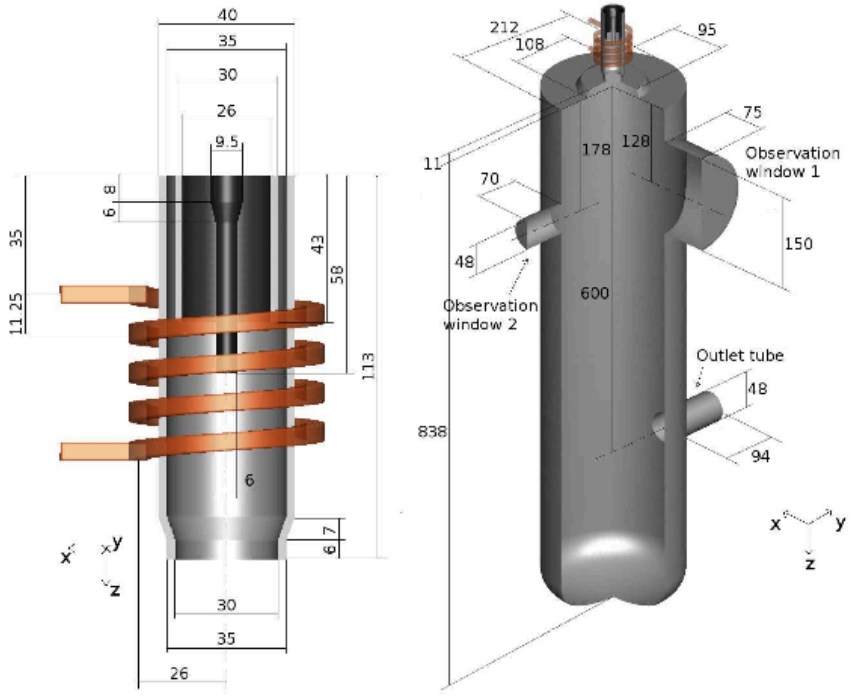


Fig. 1 - Detail of the PL-35 torch geometry and reaction chamber geometry - dimensions in mm. (taken from Ref. [2])

Gas is supplied to the torch through three inlets: carrier gas from the axially movable probe tip, primary gas from the inlet between the probe and the quartz tube and sheath gas from the inlet between the quartz and ceramic tubes; mass flow rates are 2.5 slpm of Ar, 15 slpm of Ar and 60 slpm of Ar + 4.5 slpm of $H_2$ for carrier gas, central gas and sheath gas, respectively. A no-slip boundary condition is assumed on internal walls.

In order to reduce the total number of cells in the computation grid, the inlet regions of the primary and secondary gas (8 separate injection points for the tangential injection of the primary gas and 18 points for the axial injection of the secondary gas) have been idealized with two annular inlets with uniform gas injection, since it has been shown that results are only slightly sensible to this simplification.
The equation of energy has been solved including in the domain the solid regions inside the quartz and ceramic tubes, whereas the EM field has been computed using the extended field approach, thus solving the EM equations in a cylindrical domain around the torch (150 mm diameter, 113 mm height) with vanishing vector potential on its surface. A fixed temperature (300 K) has been imposed at the internal walls of the chamber and at the external walls of the torch. The torch and the reaction chamber operate at atmospheric pressure.

*Plasma properties*

Plasma thermodynamic and transport properties have been computed using 4th order Chapman-Enskog method, including Ar, $Ar^+$, $H_2$, H, $H^+$ and electrons in the computation of composition[46].
Combined diffusion coefficients have been computed following Murphy. In order to carry out the computation of equilibrium composition, data for partition function calculations have been obtained from JANAF tables and NIST database. Each iteration, plasma properties have been updated on the basis of the local temperature and local mass fraction of hydrogen in the mixture.
Radiation losses have been taken in account using data reported by Beulens [47] for atmospheric pressure plasmas. Radiation losses due to the presence of hydrogen have been neglected because, to the knowledge of the authors, no reliable radiation power data are available for argon-hydrogen mixtures and radiative emission due to hydrogen is substantially lower than that of argon; moreover, in these simulations, hydrogen contribution to radiation can be reasonably neglected owing to small mass fraction of this gas (maximum $Y_H = 0.0045$).

*Results and discussion*

Computations have been carried out for a plasma source operating at 3 MHz (case C1) and for the same system with coil current frequency set to 13.56 MHz (case C2). In both cases, the current intensity has been adjusted to make the total Joule power dissipated in the plasma discharge equal to 15 kW: in case C1 the current is 210 A whereas in case C2, as a result of the higher frequency, its value must be set at 117 A.

*Three-dimensional effects on temperature and velocity fields inside the torch*

In figure 2 the temperature field on two orthogonal planes passing through the axis of the torch for case C1 and C2 is reported.
The maximum temperature for case C1 (11713 K) is located approximately at the same axial position of the probe tip (z = 60 mm), whereas for case C2 the maximum temperature (11606 K) is reached at z = 49 mm; in both cases, owing to the shielding effect of the induced currents, the maximum temperature is located at an off-axis position (r = 9 mm and r = 10 mm for case C1 and C2, respectively). As shown in the x-y cross sections reported in figures 2-c and 2-f, at the torch outlet the distribution of temperature is strongly deviated in the positive y-direction for the case at 3 MHz, whereas it is almost axisymmetric for the case with 13.56 MHz. As can be seen from temperature distributions reported on the cross sections at 58 mm and 85 mm, the non-axisymmentry for the case C1 is lower in the mid-coil region of the torch than at the outlet, whereas for case C2 it is more pronounced at z = 58 mm.
Logarithmic contours of Joule dissipation and Lorentz forces for case C1 and C2 are reported in figures 3 and 4, respectively; according to previous works on simulation of ICP torches with various frequencies imposed to the coil current, the Joule

dissipation inside the torch for case C1 is concentrated in a larger region than for case C2, as a result of a bigger skin depth.
A similar distribution is obtained for Lorentz forces (figures 3-c, 3-d, 4-c and 4-d), because both Joule dissipation and Lorentz forces arise in the regions characterized by higher plasma conductivity.
Temperature and Joule power distributions along the x and y axis for case C1 and C2 at z = 85 mm are reported in figure 5.
A non-axisymmetry is present for the temperature distribution along the y-axis for the case at 3 MHz (C1), whereas for the case C2 the temperature profiles along x-axis and y-axis are similar and almost axisymmetric.
For the case at 3 MHz the Joule power has a peak at r = 0.01 m and high values (order of magnitude = $10^8$ W/m$^3$) are present also inside the hot region of the discharge, whereas for the case at 13.56 MHz the peaks are located at r = 0.013 m but with a strong decrease of Joule power in the central portion of the torch and negligible values for r < 0.005 m.
A strong non-axisymmetry in Joule power distribution is present for both cases along the y-axis; for case C2 it is located at radial coordinate greater than 0.01 m, whereas for the case at 3 MHz the non-axisymmetry is pronounced also inside the discharge.
Since non-axisymmetries in temperature and Joule distributions are mainly located along the y-axis direction, in figure 6 a detail of the Lorentz force field along y-axis at different z-axis position for case C1 and C2 are reported: the higher value of the skin depth in case C1 leads to a larger region with high values (order of magnitude = $10^4$ N/m$^3$) of Lorentz forces (0.005 < r < 0.015 m for case C1, 0.009 < r < 0.015 for case C2).
Since Joule power distribution, Lorentz forces and temperature field are coupled by means of the electrical conductivity field, it is difficult to state whether the non-axisymmetric distribution of the temperature field is the effect or the cause for other non-axisymmetries.
However, the only source of non-axisymmetry in the torch is the helicoidal shape of the induction coil; a previous work [48] has shown that non-axisymmetric temperature distribution inside the inductively coupled plasma torch results a consequence of the unbalanced Lorentz forces due to the first and the last coil turns, which pull the discharge in opposite y-directions leading to a 'torque' on the discharge. In this work, lower maximum absolute values of Lorentz forces have been obtained for the case with higher coil current frequency. As a consequence, it can be argued that a lower torque is applied to the discharge and that fluid-dynamic inertia prevails over Lorentz forces resulting in an almost axisymmetric discharge.
In figure 7 a detailed view of velocity magnitude field inside the torch is reported for both case C1 and C2. The velocity magnitude field for case C1 is strongly deviated towards the positive y-direction as a result of the non-axisymmetric viscosity and density fields, which in turn depend on mass fraction and temperature fields.
On the contrary, the velocity magnitude field is almost axisymmetric for the case C2.
In figure 8 different components of the plasma velocity inside the torch are shown: in case C1 the non-axisymmetric Joule power dissipation, Lorentz forces and temperature fields induce an increase in the y-component of the plasma velocity below the probe tip, whereas the y-component of the velocity for case C2 and the x-component for both cases are almost axisymmetric.

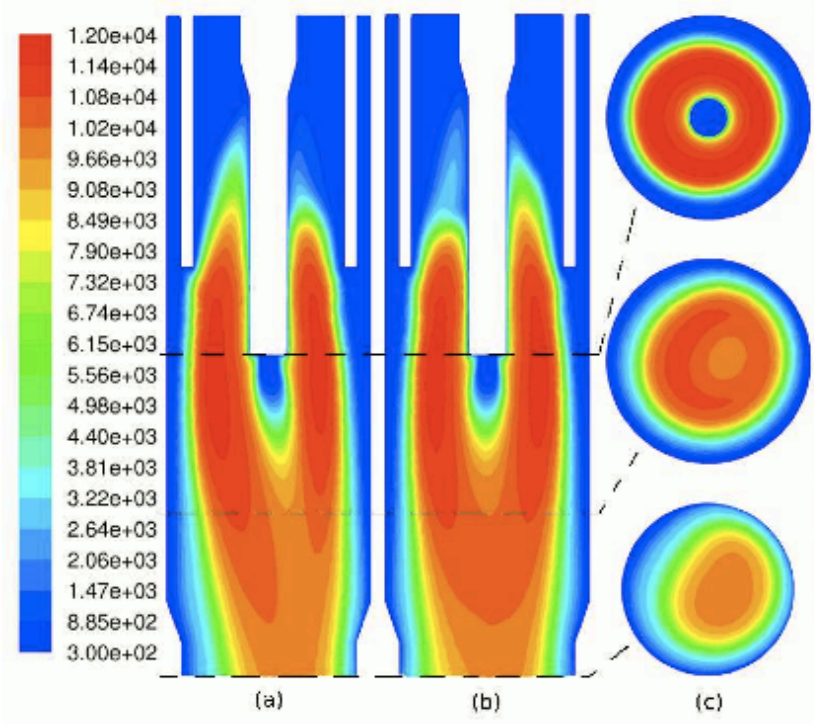


Fig 1 (a-c) - Detail of the temperature field (K) inside the torch: case C1 - plane y-z (a), plane x-z (b) and x-y sections with positive x-axis oriented to the top at z = 58 mm, z = 85 mm and z = 112 mm (c). (taken from Ref. [2])

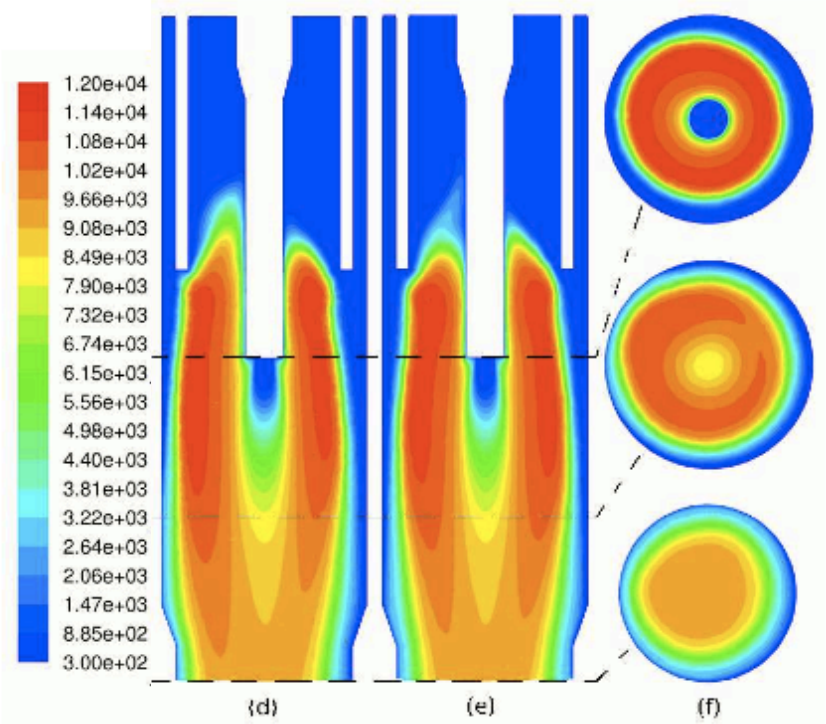


Fig 1 (d-f) - Detail of the temperature field (K) inside the torch: case C2 - plane y-z (d), plane x-z (e) and x-y sections with positive x-axis oriented to the top at z = 58 mm, z = 85 mm and z = 112 mm (f). (taken from Ref. [2])

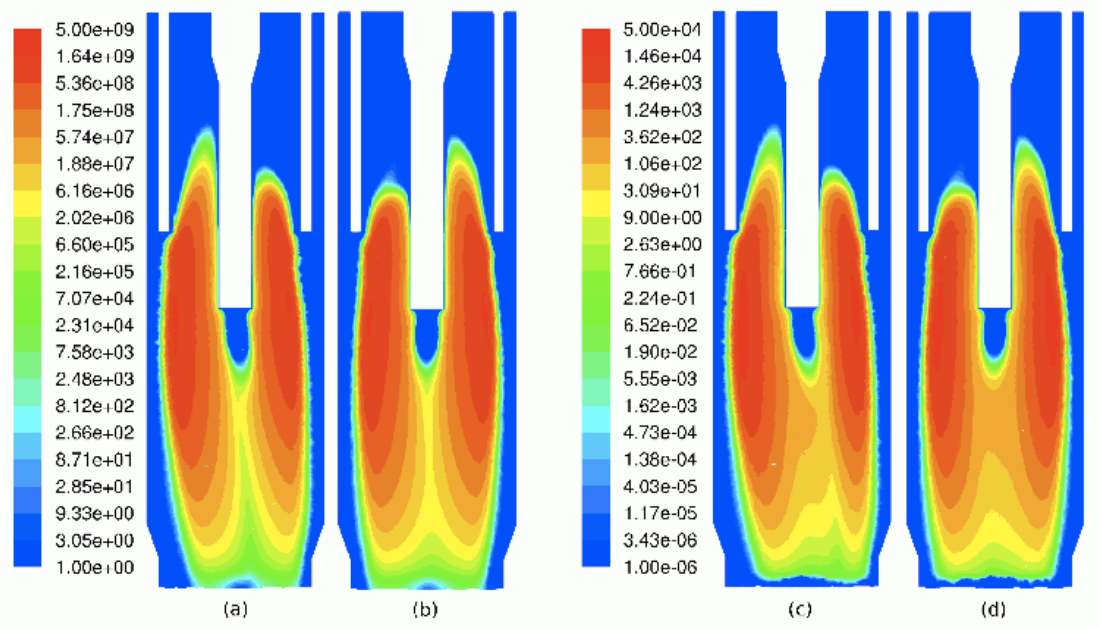


Fig. 2 - Case C1 - Detail of the Joule power (W/m^3) inside the torch: plane y-z (a) and plane x-z (b); detail of the Lorentz force magnitude (N/m^3) inside the torch: plane y-z (c) and plane x-z (d). (taken from Ref. [2])

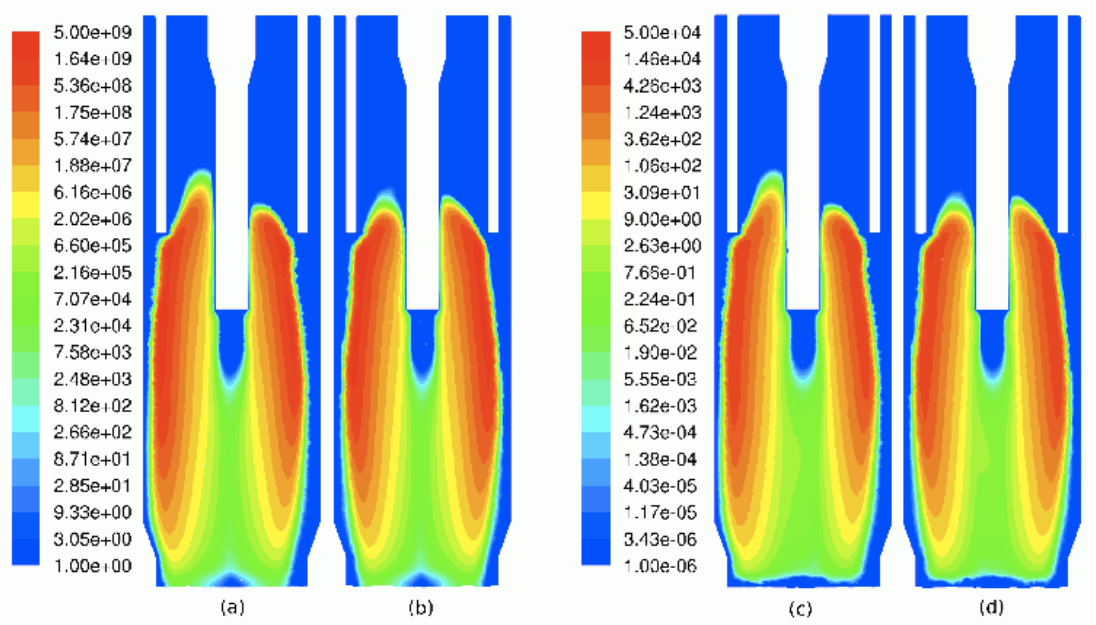


Fig. 3 - Case C2 - Detail of the Joule power (W/m^3) inside the torch: plane y-z (a) and plane x-z (b); detail of the Lorentz force magnitude (N/m^3) inside the torch: plane y-z (c) and plane x-z (d). (taken from Ref. [2])

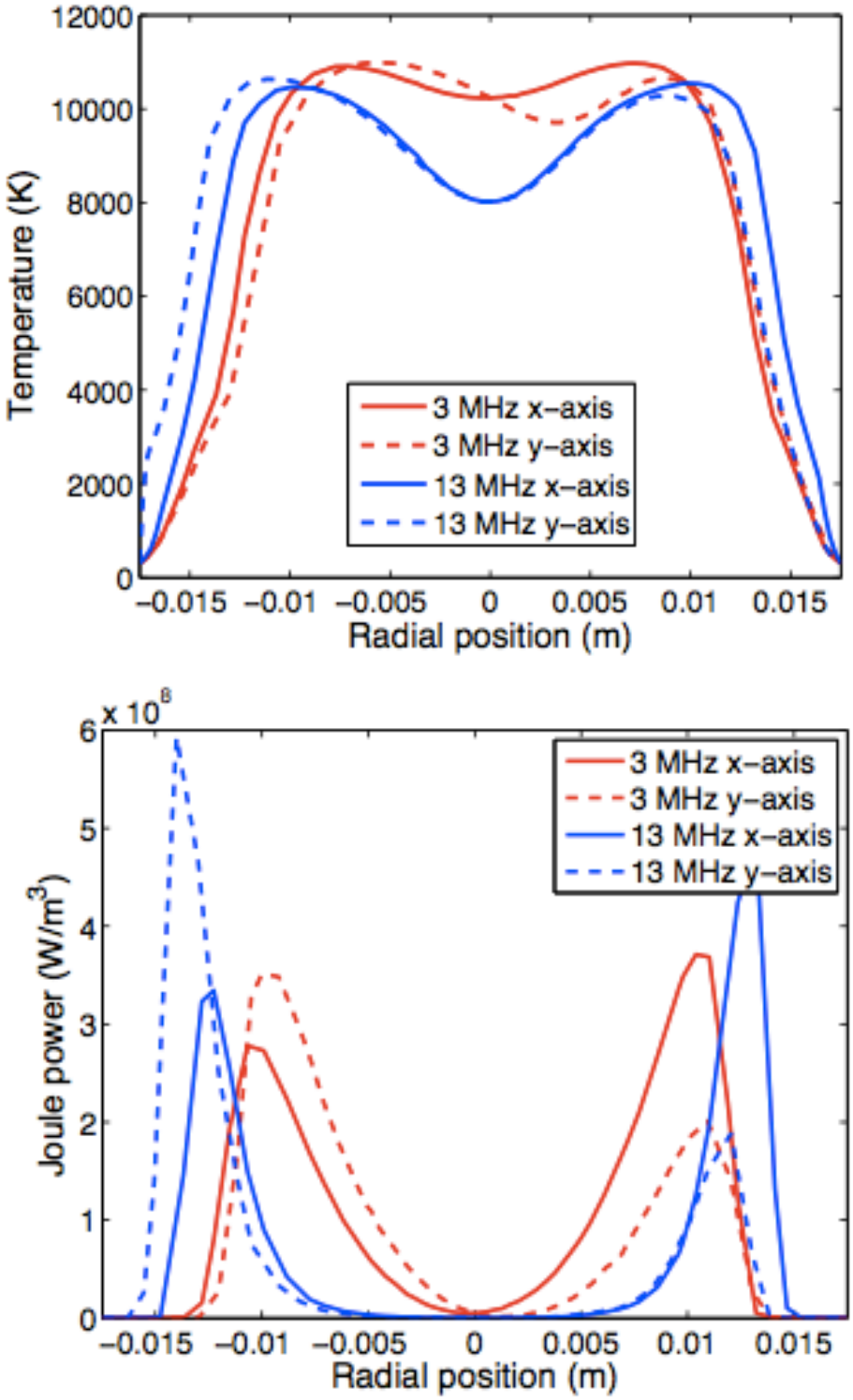


Fig. 5 - Temperature (left) and Joule power (right) for cases C1 and C2 along the x-axis and the y-axis at z = 85 mm. (taken from Ref. [2])

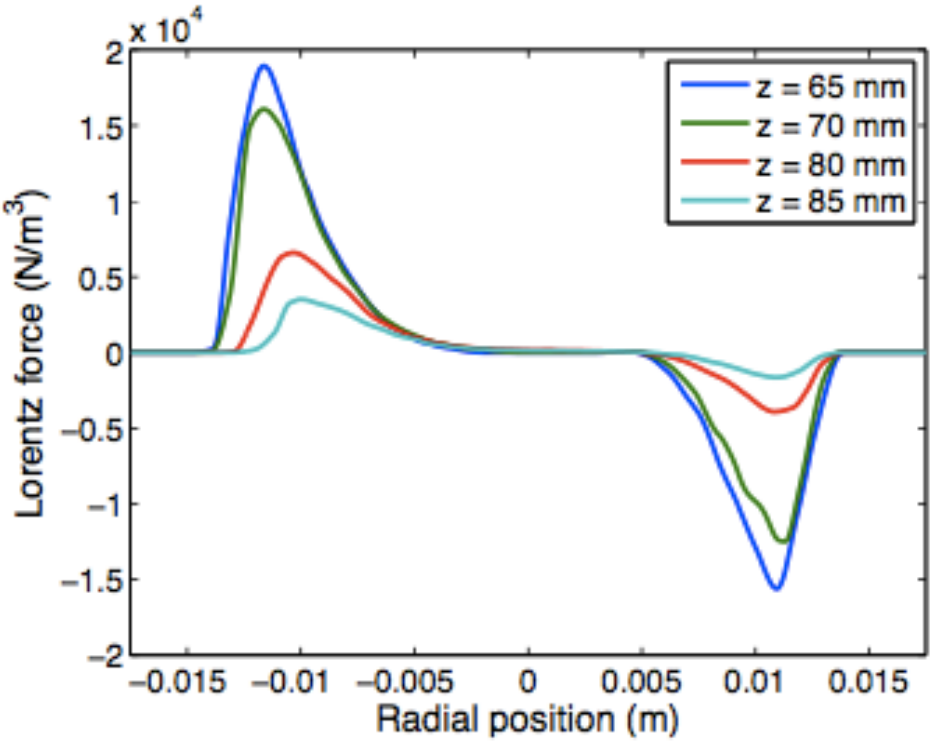


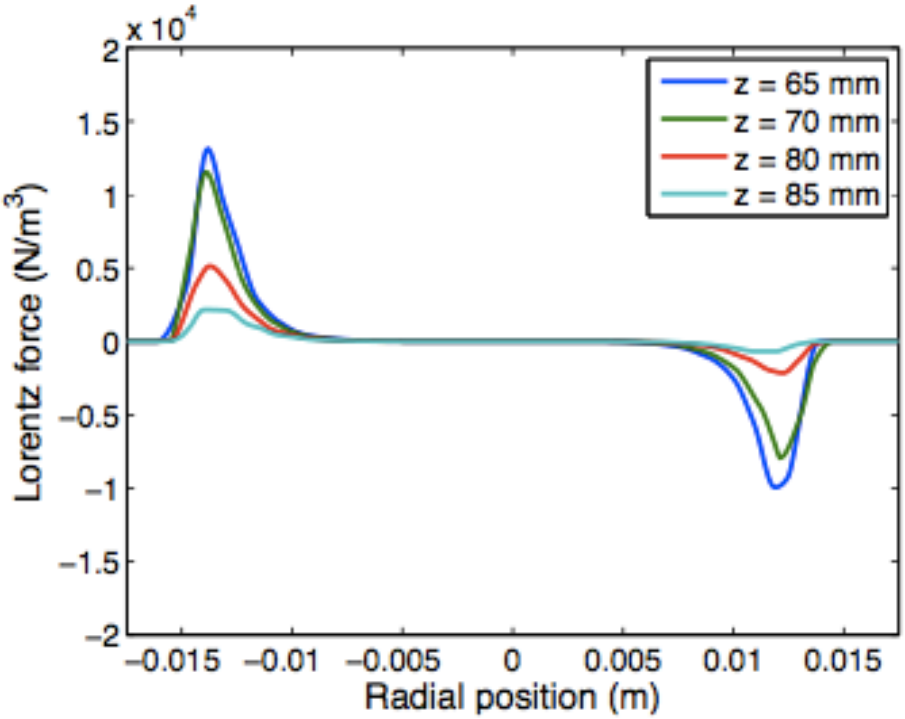


Fig. 6 - Lorentz forces for case C1 (left) and case C2 (right) along the y-axis at different z-positions. (taken from Ref. [2])

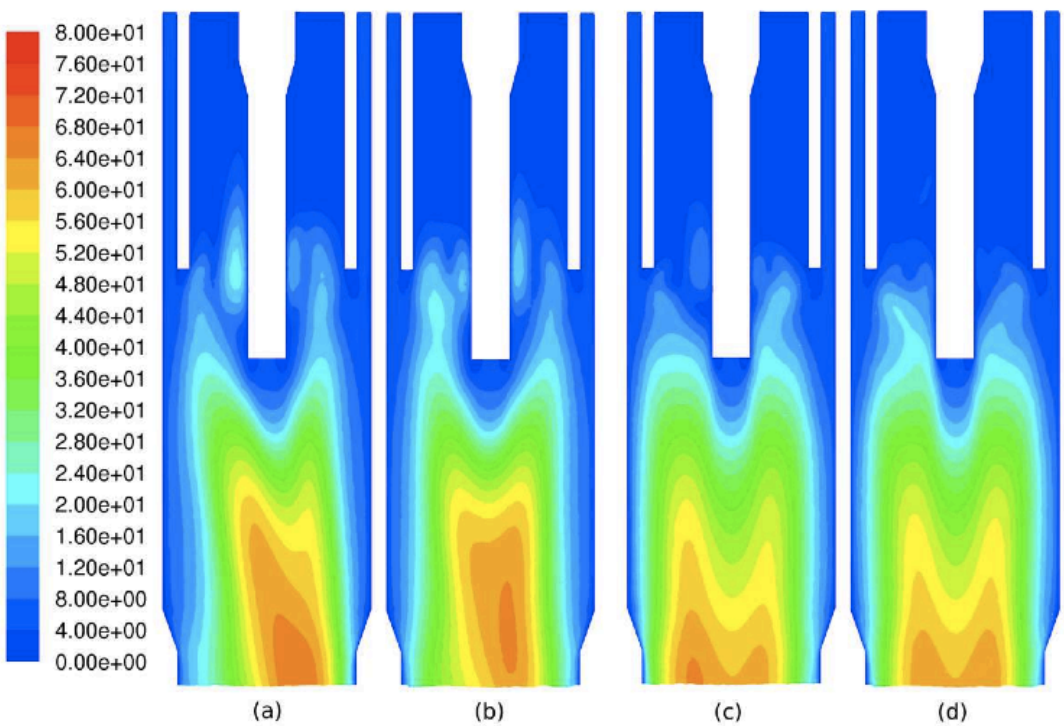


Fig. 7 - Detail of the field of the magnitude of the velocity (m/s) inside the torch: case C1 - plane y-z (a) and plane x-z (b); case C2 - plane y-z (c) and plane x-z (d). (taken from Ref. [2])

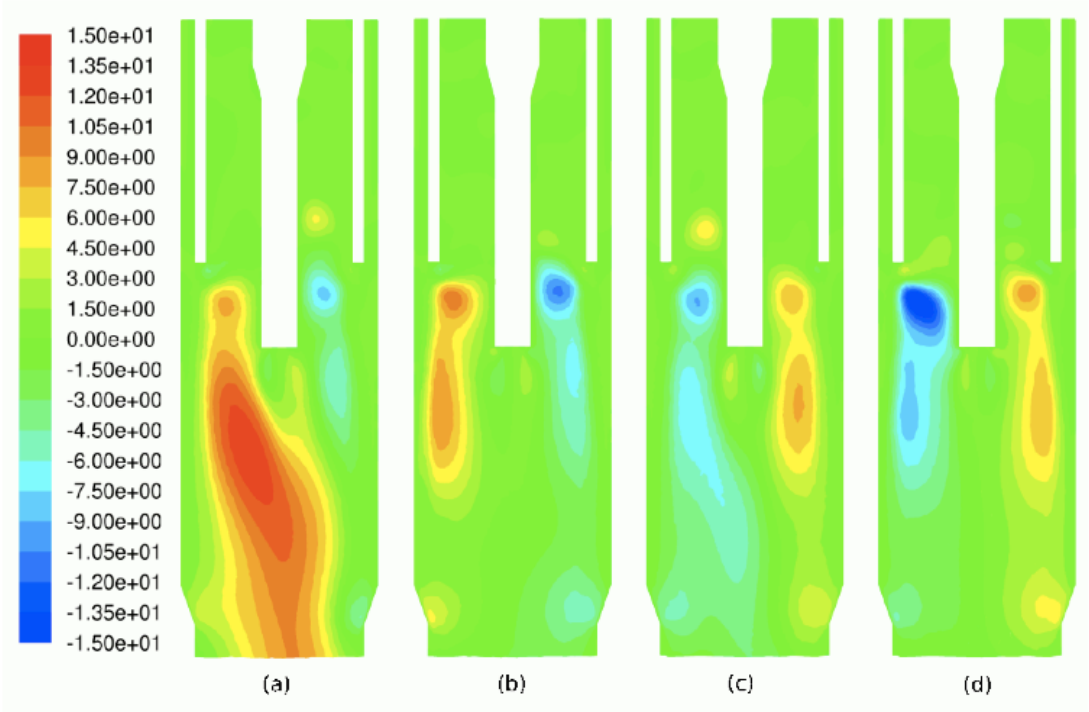


Fig. 8 - Velocity field components (m/s): y-component on the y-z plane for cases C1 (a) and C2 (b); x-component on the x-z plane for cases C1 (c) and C2 (d). (taken from Ref. [2])

*Temperature and velocity fields in the reaction chamber*

Figure 9 reports the temperature fields in the reaction chamber on two orthogonal planes passing through the axis of the torch, for case C1 and C2.
Temperature in the downstream region of the torch for case C1 is generally lower than for case C2; in fact, the iso-surfaces at 2640 K extend up to 110 mm and 188 mm below the torch exit for the first and second case, respectively. This can be attributed to the lower power dissipated through radiation inside the torch: the larger region at high temperature in case C1 leads to a higher radiative dissipation (7.2 kW) with respect to case C2 (5.4 kW) and to a lower enthalpy flux entering the reaction chamber (6.9 kW for case C1 and 8.2 kW for case C2).
In the region below the torch outlet, for both case C1 and C2, the temperature field is markedly non-axisymmetric. Since in the chamber there is no heating power, a non-axisymmetric temperature distribution can be determined by advection and conduction only: as far as in both cases conduction losses are determined by the same chamber geometry, different directions of the plasma tail temperature distribution can be attributed mainly to different recirculation flow patterns in the chamber.
In figure 10 different flow patterns in the reaction chamber are reported for C1 and C2. In case C1 the flow exiting the torch is deviated towards both the observation window OW1 and the outlet tube of the chamber, as can be seen from the pathlines released from the plasma gas inlet shown in figures 10-a and 10-b; the temperature iso-surfaces in the reaction chamber for case C1 (figure 9-a and 9-b) are similarly deviated.
In case C2 both the flow pattern and the temperature iso-surfaces are deviated in the direction of observation windows OW1 and OW2 (figures 9-c, 9-d, 10-a and 10-b).
In the reaction chamber the energy transport by conduction is enhanced by turbulent diffusion. A direct correlation exist between turbulent thermal conductivity and turbulent viscosity.
In figure 11 the turbulent viscosity ratio fields in the reaction chamber for case C1 and C2 are reported.
This parameter is defined as the ratio between turbulent and molecular viscosities and can be considered as an index of turbulence intensity. Below the torch outlet the turbulent viscosity ratio reaches high values (greater than 50) as a consequence of recirculation flows, for both case C1 and C2.

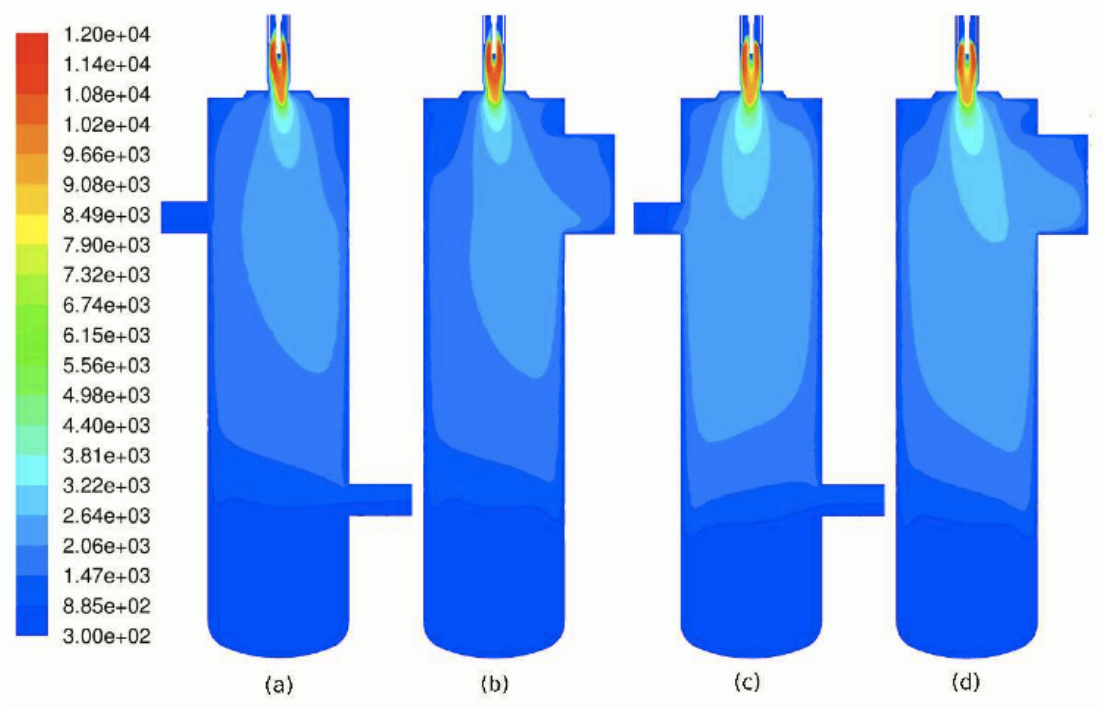


Fig. 9 - Temperature field (K) in the reaction chamber: case C1 - plane y-z (a) and plane x-z (b); case C2 - plane y-z (c), plane x-z (d). (taken from Ref. [2])

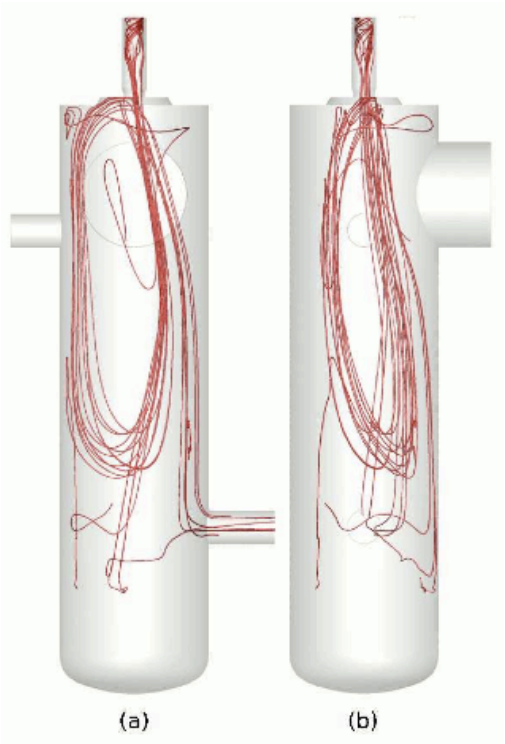


Fig. 10(a-b) - Pathlines released from plasma gas inlet: case C1 - y-z view (a), x-z view (b). (taken from Ref. [2])

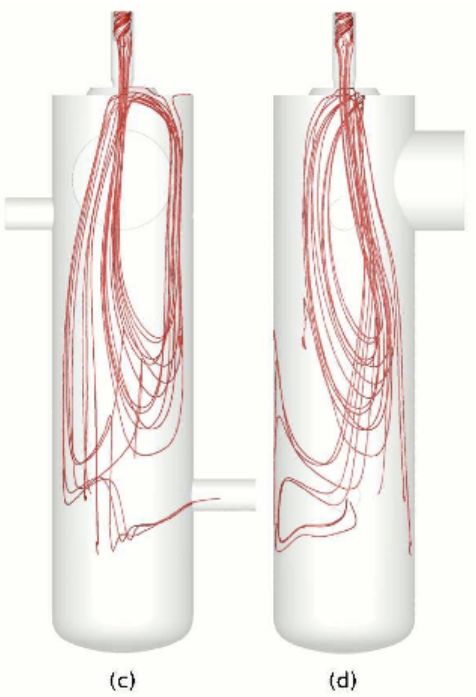


Fig. 10(c-d) - Pathlines released from plasma gas inlet: case C2 - y-z view (c), x-z view (d). (taken from Ref. [2])

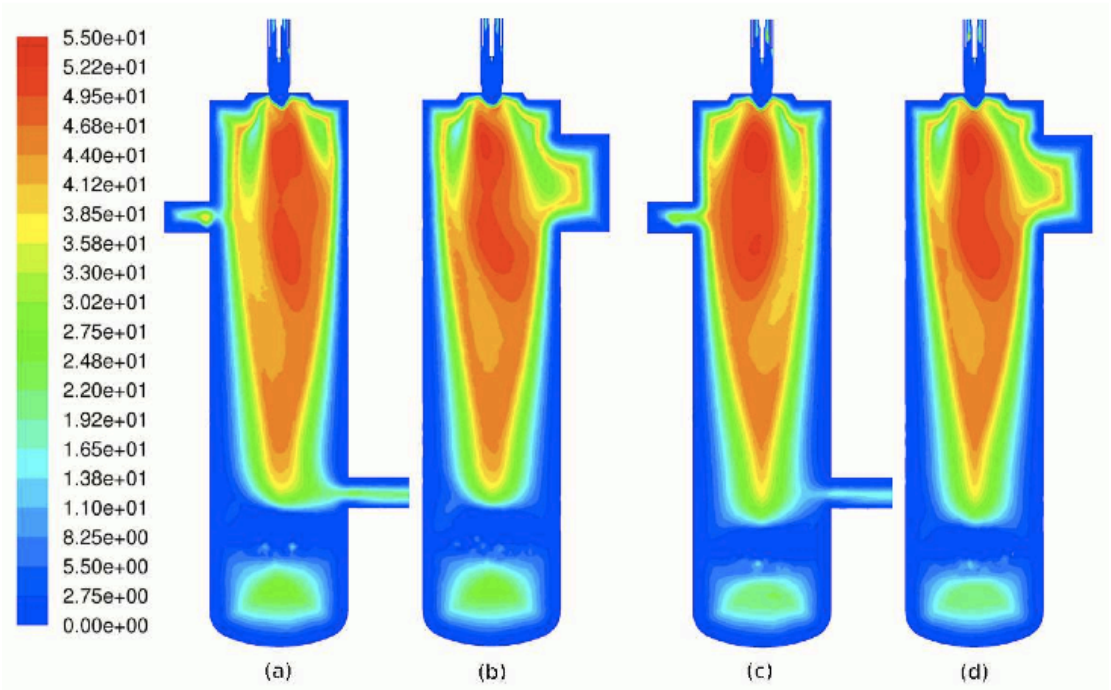


Fig. 11 - Turbulent viscosity ratio: case C1 - plane y-z (a) and plane x-z (b); case C2 - plane y-z (c) and plane x-z (d). (taken from Ref. [2])

*Mass fraction fields and demixing effects*

Three-dimensional effects in the temperature field lead to non-axisymmetric mass fraction fields as shown in figure 12 and 13 for case C1 and C2, respectively. Hydrogen mass fraction profile along y-axis at z = 95 mm is reported in figure 14.

As can be seen from these pictures, for both case C1 and C2 a strong accumulation of hydrogen can be evidenced near the torch wall (12-e); however, for case C1 the region with higher mass fraction of hydrogen (Y_H > 0.003) is larger for negative y-axis positions than for positive ones (figures 12-c and 14); in case C2 the accumulation is even stronger than in case C1 (see figure 14) but the region with higher values of mass fraction is more axisymmetric (figure 13-e); on the contrary, in case C2 a non-axysimmetric distribution has been obtained for the region with lower values of the hydrogen mass fraction (Y_H < 0.003), as can be seen in figures 13-c, 13-e and 14.
In the reaction chamber three-dimensional composition fields arise near the top wall and in the observation window OW2 (figures 12-a, 12-b, 13-a and 13-b).

Hydrogen injected from the secondary gas inlet moves towards the central region of the torch according to three mechanisms: diffusion due to mass fraction gradients, turbulent diffusion and thermal diffusion. The latter, as shown in figure 15, generally entails the diffusion of argon towards lower temperature regions; however, on the contrary, for a temperature range between 2000 K and 5000 K, the temperature diffusion coefficient for argon $D_i^T$ is negative, as a result of hydrogen dissociation, and the argon is pushed towards higher temperature regions. In this range of temperature, it is known that negative values of the temperature derivative of the argon mole fraction exist for argon-hydrogen mixtures, leading to negative values of the temperature diffusion coefficient for argon (see equation 9). In figure 16 different contribution to temperature diffusion coefficient have been reported for the temperature range 300 K - 12000 K: thermal diffusion contribution due to temperature gradients ($D_{ij}^T$) is always positive whereas the one due to mole fraction gradients (the second term in equation 9) is generally null with exception of dissociation and ionization temperature ranges where it assumes negative and positive values, respectively. Temperature diffusion coefficient is responsible for the effect of demixing.

As can be seen in figures 12-a, 12-b, 13-a and 13-b, at the outlet of the quartz tube, hydrogen diffuses towards the central region of the plasma discharge mainly as a result of mass fraction and temperature gradients, since turbulence in this region is negligible (see figure 11); since there are strong temperature gradients near the internal wall of the torch, thermal diffusion acts mainly as an obstacle to the diffusion of hydrogen towards the central region.

Negative values of argon temperature diffusion coefficient around 3300 K and positive values for lower temperature result in an accumulation of hydrogen in the temperature region where the coefficient is null (T = 2000 K).
In fact, hydrogen mass fraction has its maximum value ($Y_H = 0.0045$) in the fringes of the discharge and this is greater than the mass fraction of hydrogen in the inlet sheath gas ($Y_H$ at inlet = 0.00374).
In figure 14 hydrogen mass fraction and argon temperature diffusion coefficient along the y-axis at z = 85 mm have been reported: peaks in hydrogen mass fraction are strongly correlated with negative peaks in argon temperature diffusion coefficients and they are located where temperature is about 2000 K, i.e. the just below the dissociation temperature range.

As can be seen in figure 15, for temperature higher than 4500 K the argon temperature diffusion coefficient is positive. The point of transition between negative and positive values is a dispersion point for hydrogen: in presence of a temperature gradient, hydrogen at temperature lower than the transition temperature is pushed towards lower temperature zones whereas hydrogen at temperature higher than the transition temperature is pushed towards higher temperature ones; this results in a hydrogen dispersion towards lower or higher temperatures. This is clear from figure 14 where mass fraction of hydrogen has been plotted: for case C1 a local minima which correspond to dispersion points are found at y = -0.011 m and y = 0.013 m whereas for case C2 they are located at y = -0.015 m and y = 0.012 m.

Similar results have been obtained also by Chen for a different ICP torch configuration and the accumulation of hydrogen in the cold boundary layer of a thermal spray torch was simulated using a two-temperature combined diffusion approach. These results are in agreement also with previous investigations by Murphy in which a peak of hydrogen mass fraction has been predicted in the low-temperature fringes of a free burning arc.

In the reaction chamber, hydrogen diffusion is dominated by turbulence: the viscosity ratio reaches values of the order of 50 where the gas expands in the reaction chamber, as shown in figure 11, and the hydrogen is almost completely mixed (figures 12-a, 12-b, 13-a and 13-b).
In the fringes of the plasma plume in the reaction chamber, where temperature is below the dissociation range, thermal diffusion pushes hydrogen (almost completely in its molecular form) towards higher temperature regions.

In figure 17 the mass fraction of hydrogen is reported for a fictitious case where thermal diffusion due to temperature gradients has been neglected. The temperature coefficient used has been plotted in figure 16 for Y_H = 0.002. For both cases C1 and C2, the mass fraction in the chamber is almost constant, as a result of null temperature diffusion coefficient below the dissociation temperature range.
In the torch, the accumulation of hydrogen in the fringes of the discharge is enhanced, since the positive contribution to the temperature coefficient due to temperature gradients has been neglected. Thus, according to previous investigations by Murphy on free-burning arcs, the accumulation of hydrogen in the fringes of the discharge can be attributed mainly to diffusion due to mole fraction gradients.

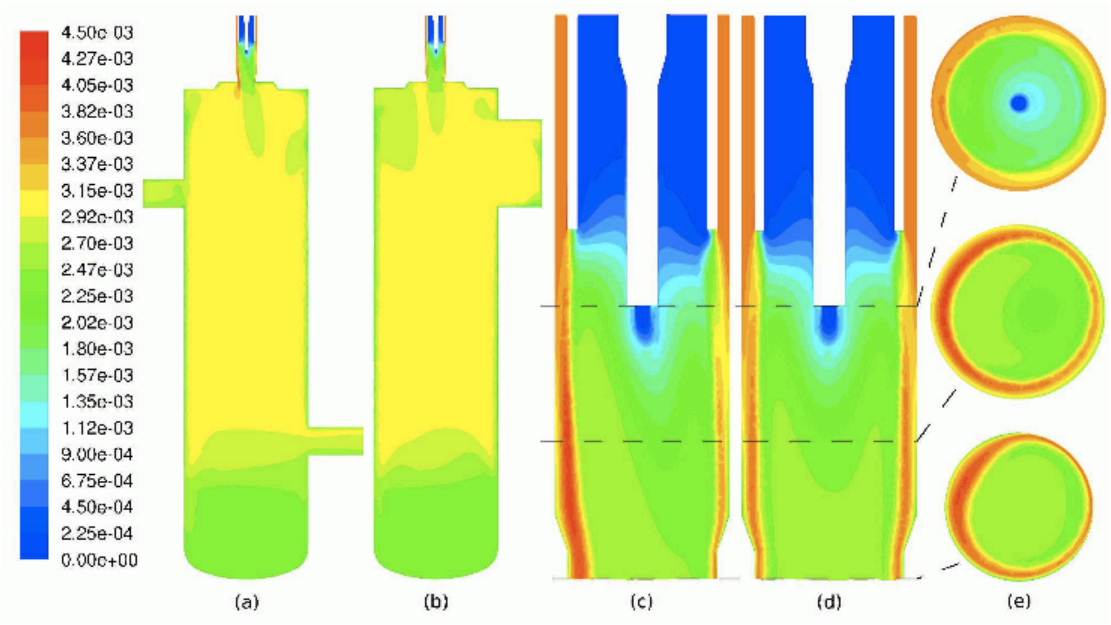


Fig. 12 - Case C1 - Mass fraction of hydrogen: plane y-z (a) and plane x-z (b); detail of the mass fraction of hydrogen inside the torch: plane y-z (c), plane x-z (d) and x-y sections with positive x-axis oriented to the top at z = 58 mm, z = 85 mm and z = 112 mm (e). (taken from Ref. [2])

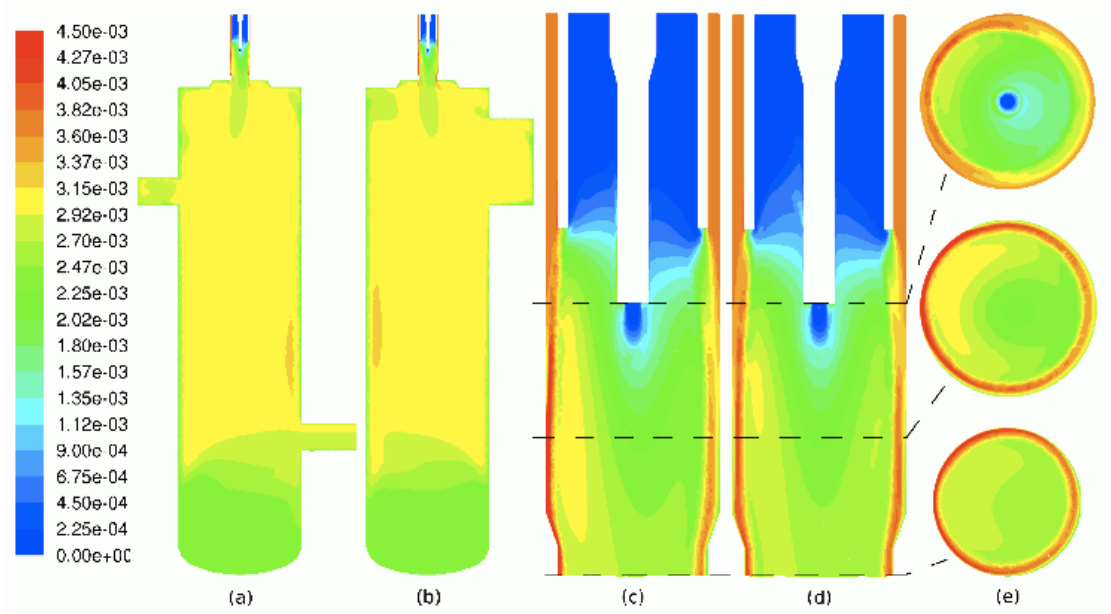


Fig. 13 - Case C2 - Mass fraction of hydrogen: plane y-z (a) and plane x-z (b); detail of the mass fraction of hydrogen inside the torch: plane y-z (c), plane x-z (d) and x-y sections with positive x-axis oriented to the top at z = 58 mm, z = 85 mm and z = 112 mm (e). (taken from Ref. [2])

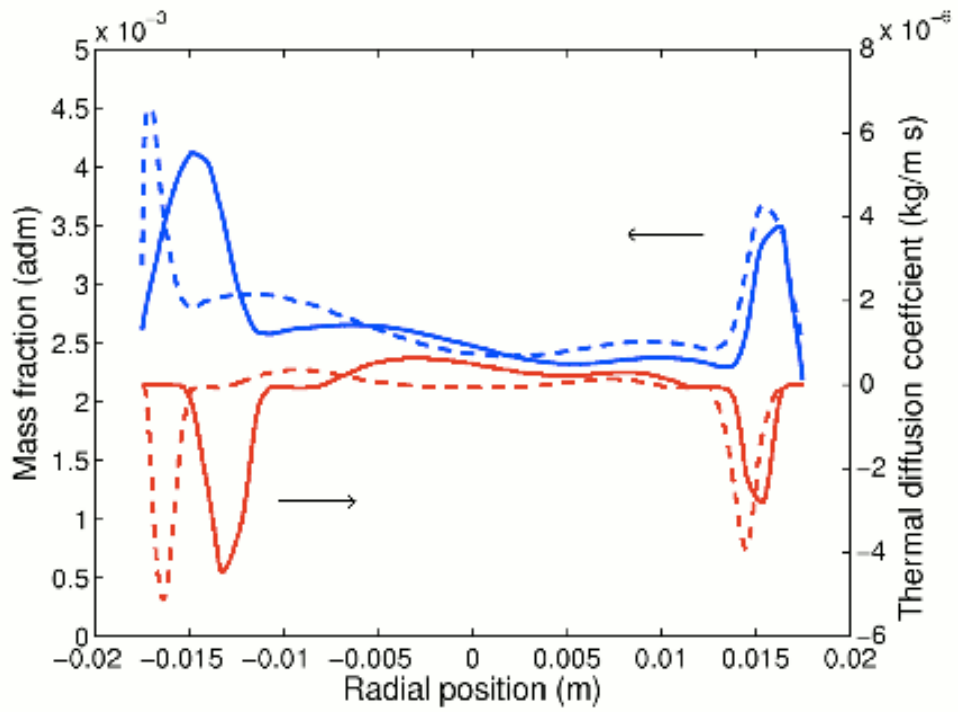


Fig. 14 - Hydrogen mass fraction and argon temperature diffusion coefficient along y-axis at z = 95 mm: case C1 full line, case C2 dashed line. (taken from Ref. [2])

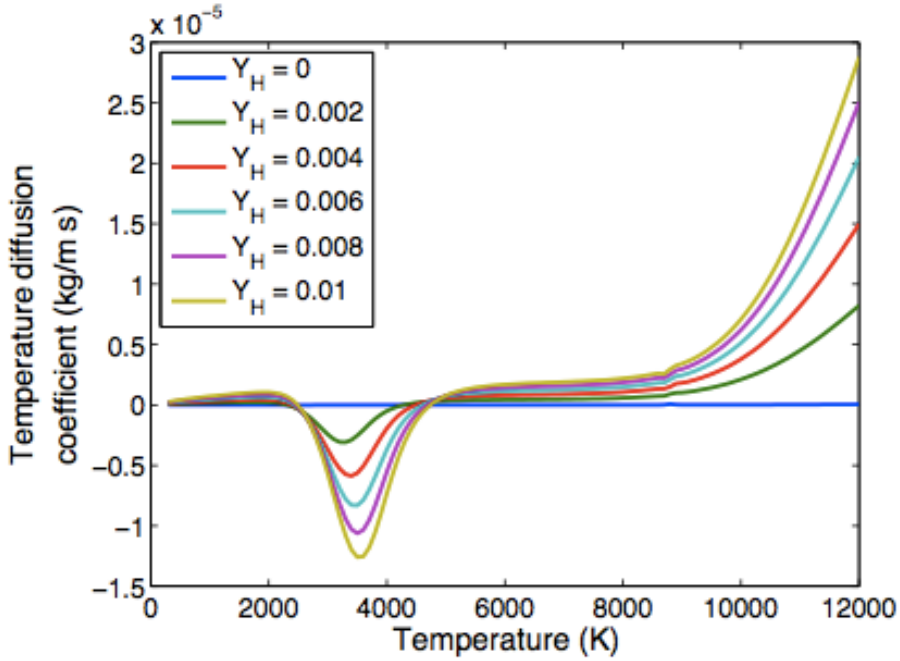


Fig. 15 - Argon temperature diffusion coefficients ($D^{T}_{Ar}$) as a function of temperature for argon-hydrogen mixtures, for constant mass fractions of hydrogen. (taken from Ref. [2])

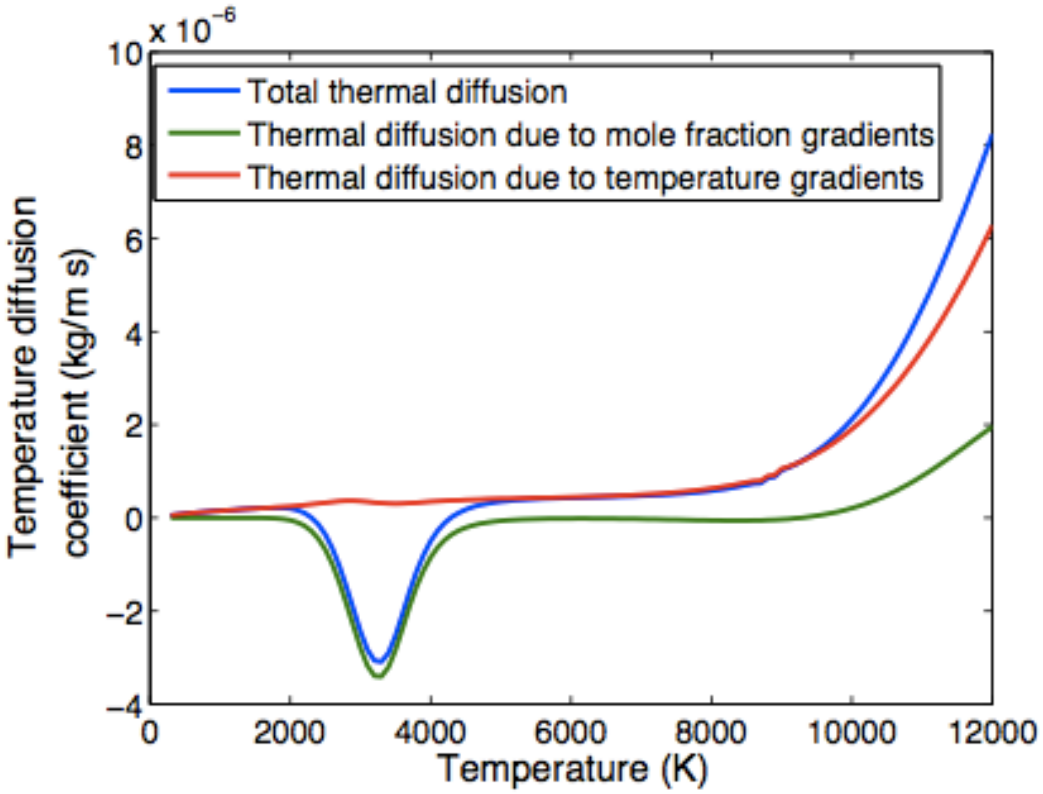


Fig. 16 - Different contributions to argon temperature diffusion coefficient ($D^{T}_{Ar}$) as a function of temperature for argon-hydrogen mixtures, for constant mass fraction of hydrogen ($Y_H = 0.002$). (taken from Ref. [2])

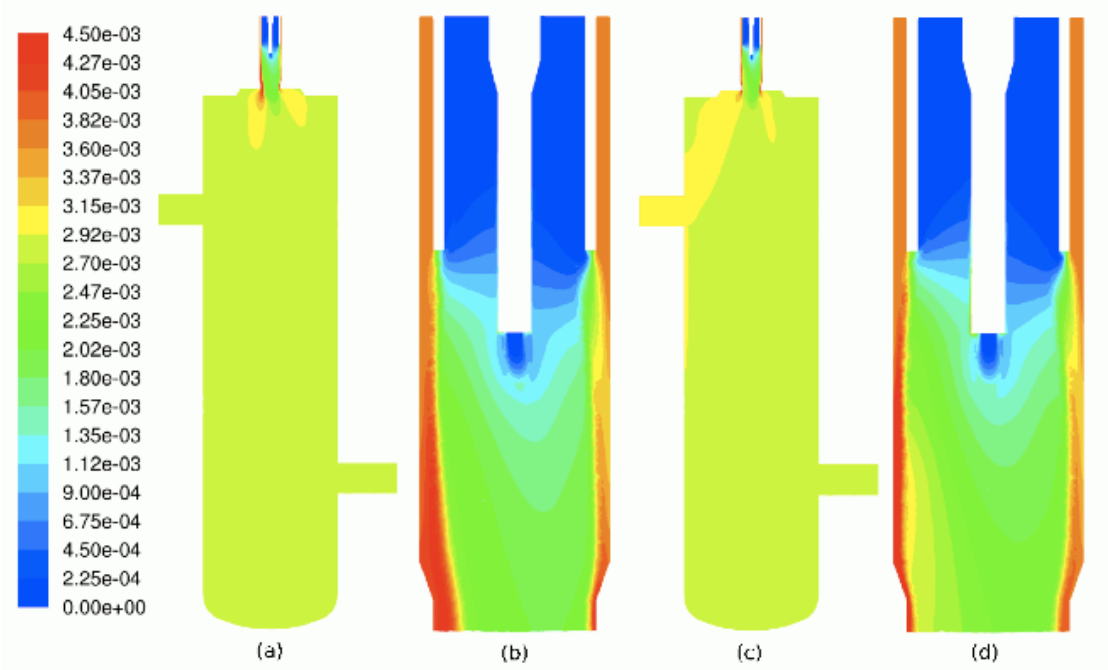


Fig. 17 - Mass fraction of hydrogen on plane y-z neglecting thermal diffusion due to temperature gradients: case C1 - chamber view (a) and torch view (b); case C2 - chamber view (c) and torch view (d). (taken from Ref. [2])

**Three-dimensional investigation of particle treatment in a RF thermal plasma with reaction chamber**

Three-dimensional trajectories and thermal histories for particles heated in ICP torches have been already reported by some of the authors including particle turbulent dispersion (Colombo 2004, Colombo 2007).

Experimental and numerical studies on particle heating in ICP torches have shown that the thermal behaviour of powders is strongly dependent on many parameters, including both operating conditions and powder characteristics (Boulos 2004, Boulos 1998, Boulos 1995). Among these parameters, the frequency of coil excitation current has not been investigated experimentally because, usually, for a given RF generator the frequency is fixed and the user, requiring the substitution of different internal components of the generator, cannot easily modify it. Thus, the effects of the variation of this parameter on the characteristics of the plasma discharge (Boulos 1993, Colombo 2010) and on the effectiveness of powder treatment (Shigeta 2004, Shigeta 2005) have been investigated using numerical models only.
For a laboratory scale torch designed to investigate nano-powder synthesis, Shigeta (Shigeta 2004), using a two-dimensional model, predicted that the change in frequency from 0.5 MHz to 13.56 MHz results in the absence of recirculating flows at the top of the coil, in particle trajectories closer to the torch axis and in lower heat flux to the particles. Moreover, Shigeta (Shigeta 2005) showed that coil frequency is an effective factor to control the size distribution of the synthesized nano-particles.

The aim of the present study is to investigate by means of a fully three-dimensional numerical code (Colombo 2004) the effect of frequency on powder treatment, since it has been studied up to now using two-dimensional models only. For a commercial torch (Tekna Plasma System, model PL-35), Colombo et al. (Colombo 2010) predicted plasma velocity and temperature fields for frequency set at 3 MHz and 13.56 MHz; for the lowest frequency the first and the last coil turns induce unbalanced Lorentz forces in the discharge that prevail over fluid-dynamic inertia, resulting in non-axisymmetric thermo-fluid-dynamic fields; at higher frequency, the lower absolute value of Lorentz forces and the smaller volume of the discharge where they are applied, induces a lower unbalance between the force exerted on the discharge; thus, it has been argued that fluid-dynamic inertia prevails over the torque applied to the discharge by the coil and the resulting temperature field is more axisymmetric. Moreover, the temperature field in the reaction chamber has been simulated and its three-dimensional shape has been correlated with different types of recirculation flow arising when a non-axisymmetric reaction chamber that includes a lateral outlet tube is used. On the basis of these results, also a non-axisymmetric behaviour of injected particles is expected.

In this study, a three-dimensional numerical model of a Tekna PL-35 torch with non-axisymmetric laboratory scale reaction chamber has been developed in order to investigate particle treatment for realistic geometry and in typical operating conditions.
In fact, powder treatment processes, such as powder spheroidization and synthesis of nano-particles, include a reaction chamber to attain optimal operating conditions (for example for what regards gas composition and pressure).

In order to account for the variable axial position of the injection probe, which is usually modified by the user to optimize the process, computations have been carried out for two different computational domains, which differ for the axial position of the probe.
In accordance with Colombo et al. [2], 3 MHz and 13.56 MHz have been selected as representative coil frequencies among those allowed and used in industrial applications.

The test case settings correspond to the usual operating conditions used for particle spheroidization, although main conclusions of this study could be accounted also for other applications, such as thermal spray, thin film deposition on substrate and synthesis of nano-powders; in this last case the accurate prediction of particle behaviour is a key point in the development of a successful industrial process.

*Modeling approach*

The following hypothesis are assumed in the present calculations:

- Plasma is in local thermodynamic equilibrium (LTE);
- Combined diffusion approach of Murphy is used to model the diffusion in a mixture of two non-reactive gases;
- Turbulent effects are taken into account through RNG k-ε model;
- Plasma is optically thin and radiative losses are taken into account considering only the presence of argon in the mixture;
- Composition is computed taking into account six species: Ar, $Ar^+$, $H_2$, H, $H^+$ and electrons;
- Viscous dissipation term in the energy equation is neglected;
- Displacement currents are neglected.

*Fluid and electromagnetic model*

The physical behavior of the plasma has been modeled removing any axisymmetric assumption and a fully 3D model has been implemented in the FLUENT environment.
The governing equations can be written as

$$\nabla \cdot (\rho \vec{v}) = 0$$

$$\nabla \cdot (\rho \vec{v}\vec{v}) = -\nabla p + \nabla \cdot \tau + \rho \vec{g} + F_L$$

$$\nabla \cdot (\rho \vec{v} h) = -\nabla \cdot \left( \frac{k_{eff}}{c_p} \nabla h \right) + \nabla \cdot \left( \sum_i h_i \left( \vec{J}_i + \frac{k_{eff}}{c_p} \nabla \overline{Y}_i \right) \right) + P_J - Q_r - Q_L$$

$$\nabla \cdot \left( \rho \vec{v} \overline{Y}_i \right) + \nabla \cdot \vec{J}_i = 0$$

where ρ is the plasma density, v is the velocity, p is the pressure, τ is the viscous stress tensor, *h* is the total enthalpy, $k_{eff}$ is the effective thermal conductivity that includes both laminar and turbulent contributions; $c_p$ is the specific heat at constant

pressure, g is the gravitational force and $Q_r$ is the volumetric radiative loss; $Q_L$ is the plasma-particle exchange term; $Y_i$ and $J_i$ are the mass fraction and the diffusion current of the i-th gas.

Diffusion of hydrogen from the secondary gas as been modeled using the accurate method named combined diffusion of Murphy (Murphy 1993, Murphy_combined], since the plasma is assumed to be in local chemical equilibrium. Diffusion due to pressure gradients and electric fields have been reasonably neglected.

Turbulent effects in the downstream region of the discharge have been included in the flow calculations using the RNG k-ε model. Turbulent contributions to viscosity and thermal conductivity have been calculated starting from k and ε fields: $\mu_t = \rho C_\mu k^2/\varepsilon$ and $k_t = c_p \mu_t / Pr_t$, where $C_\mu$ is a constant equal to 0.09 and $Pr_t$ is the turbulent Prandtl number calculated according to the RNG theory.

The electromagnetic field generated by both the alternating coil current and the induced currents in the plasma have been described by means of Maxwell's equations written in their vector potential formulation. Solving these equations, it is possible to calculate the Lorentz forces $F_L$ and Joule dissipation $P_J$. Detail of the thermo-fluid-dynamic model can be found in a previous work by the authors (Colombo 2010).

*Particle heating model*

The particles are assumed to be spherical and with a negligible internal resistance to heat transfer. The particles trajectory is obtained by solving the following equation of motion:

$$\frac{d\vec{v}_p}{dt} = \left(\frac{3\rho C_D}{4 d_p \rho_p}\right) |\vec{v} - \vec{v}_p| (\vec{v} - \vec{v}_p) + \vec{g} - \left(\frac{36\mu^2}{\rho \rho_p d_p^2}\right) B \nabla \ln T$$

where $v_p$, $d_p$, $\rho_p$ are the velocity, diameter and density of the particle, respectively; g is the gravitational acceleration. The first term on the right side represents the fluid drag force, whereas the last one is the thermophoretic force. The drag coefficient $C_D$ has been computed as in (Colombo 2004):

$$C_D = \begin{cases} \left(\frac{24}{Re_\infty}\right) & \text{for } Re_\infty < 0.2 \\ \left(\frac{24}{Re_\infty}\right)(1 + 0.1875 Re_\infty) & \text{for } 0.2 < Re_\infty < 2 \\ \left(\frac{24}{Re_\infty}\right)(1 + 0.11 Re_\infty^{0.81}) & \text{for } 2 < Re_\infty < 21 \\ \left(\frac{24}{Re_\infty}\right)(1 + 0.189 Re_\infty^{0.632}) & \text{for } 21 < Re_\infty < 200 \end{cases}$$

where the Reynolds number has been obtained as $Re_\infty = \rho |v| d_p / \mu$, where μ is the plasma viscosity.
The thermophoretic coefficient has been obtained following Talbot et al. (Talbot) as

$$B = C_s \frac{(k/k_p) + C_t \mathrm{Kn}}{(1 + 3C_m \mathrm{Kn})(1 + 2(k/k_p) + 2C_t \mathrm{Kn})}$$

where $k_p$ is the thermal conductivity of particle material; $C_s$, $C_t$ and $C_m$ are three constants equaling 1.17, 2.18, and 1.14, respectively. The Knudsen number is defined as $Kn = 2\lambda/d_p$ where the mean-free-path length is computed as $\lambda=\mu(0.499p(8m/\pi kT)^{0.5})^{-1}$, where m is the molecular mass of the plasma gas.

The heating history of the particle in the solid-phase is obtained by solving the energy balance equation:

$$q = \begin{cases} m_p c_p \frac{dT_p}{dt} & \text{for } T_p < T_m \text{ or } T_m < T_p < T_v \\ \frac{\rho_p d_p \lambda_m}{6} \frac{dx}{dt} & \text{for } T_p = T_m \\ -\frac{\rho_p \lambda_v}{2} \frac{dd_p}{dt} & \text{for } T_p = T_v \end{cases}$$

where $m_p$, $c_p$, $\lambda_m$ and $\lambda_v$ are the mass, the specific heat, the melting and vaporization latent heats for the particles, respectively; $T_m$ and $T_v$ are the melting and boiling temperatures for the particle material, respectively; x is the liquid phase fraction; q is the net heat to the particle given by

$$q = A_p h_c (T - T_p) - A_p \epsilon \sigma \left(T_p^4 - T_a^4\right)$$

where $A_p$ is the surface area of the particle; ε is the emissivity of the particle material; σ is the Stefan-Boltzmann constant; $T_a$ is the room temperature (300 K). The convective coefficient $h_c$ has been calculated taking into account local value of the plasma properties (Colombo 2004).

*Computational domain, material properties and boundary conditions*

The geometry considered in the calculations include a Tekna PL-35 torch and a non-axisymmetric reaction chamber with two observation windows and a lateral gas outlet tube. A schematic is reported in figure fig. 1: the coordinate system is oriented as shown in the schematic and its origin is located on the torch axis at the top of the torch domain. Two torch configurations have been considered, which differ for the probe axial position only: probe tip at 55 mm and 45 mm upstream of the torch outlet.

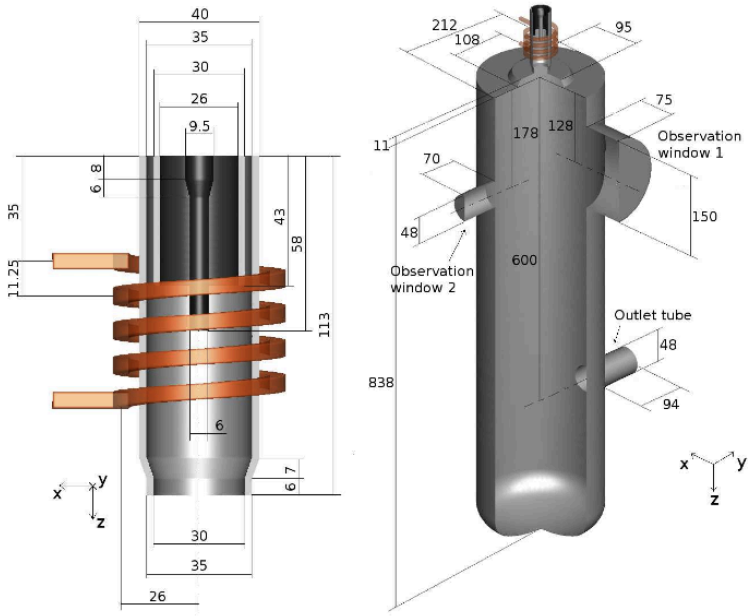


Fig. 1 - Detail of the PL-35 torch geometry and reaction chamber geometry - dimensions in mm. (taken from Ref. [3])

Plasma thermodynamic and transport properties have been computed using 4-th order Chapman-Enskog method, including Ar, $Ar^+$, $H^2$, H, $H^+$ and electrons in the computation of composition (Colombo 2009). Combined diffusion coefficients have been computed following Murphy (Murphy 1993). In order to carry out the computation of equilibrium composition, data for partition function calculations have been obtained from JANAF tables (JANAF) and NIST database (NIST). Each iteration, plasma properties have been updated on the basis of the local temperature and local mass fraction of hydrogen in the mixture. Radiation losses have been taken in account using data reported by Beulens et al. (Beulens) for atmospheric pressure plasmas.

Gas is supplied to the torch through three regions: carrier gas from the (axially movable) injection probe tip (orifice diameter equal to 2 mm), primary gas from the annular region between the probe and the quartz tube (with a tangential component of 15 degrees) and sheath gas from the region between the quartz and ceramic tubes (axial injection); mass flow rates are set to 2.5 slpm of Ar, 15 slpm of Ar and 60 slpm of Ar + 4.5 slpm of $H_2$ for carrier gas, central gas and sheath gas, respectively. No slip condition is assumed on internal walls. The equation of energy has been solved including in the domain the solid regions inside the quartz and ceramic tubes, whereas the EM field has been computed using the extended field approach (Colombo 2003d), thus solving the EM equations in a cylindrical domain around the torch (150 mm diameter, 113 mm height) with vanishing vector potential on its surface. A preliminary calculation (not reported here for the sake of conciseness) has shown that EM fields in the reaction chamber don't influence the behavior of the plasma discharge; thus, they have been neglected in the present work.

In each case, the coil current intensity has been adjusted to make the total Joule power dissipated in the plasma discharge equal to 15 kW. The torch and the reaction

chamber operate at atmospheric pressure. At the internal walls of the chamber and at the external walls of the torch, a fixed temperature (300 K) has been imposed.

In all cases we considered alumina particles ($Al_2O_3$, see table 1 for properties) axially released from the carrier gas inlet with a Rosin-Rammler size distribution function: the mass fraction of particles with diameter greater than d has been set to $Y_d = \exp(-(d/d_m)^n)$ with mean diameter $d_m$ = 80 um and spread parameter n = 3.6, while the distribution is limited between 25 um and 125 um.
Powders velocity at the inlet of the injection probe has been taken equal to that of the carrier gas.

**Table 1.** Physical properties for alumina powders

| Property | Units | Value |
|---|---|---|
| $\rho_p$ | [kg / m$^3$] | 3900 |
| $c_p$ sol. | [J / kg K] | 913.099 + 0.2119 T + 0.0001 T$^2$ |
| $c_p$ liq. | [J / kg K] | 1020 |
| $\lambda_m$ | [J /kg] | $1.065 \cdot 10^6$ |
| $\lambda_v$ | [J /kg] | $2.466 \cdot 10^7$ |
| $T_m$ | [K] | 2326 |
| $T_v$ | [K] | 3800 |
| $\epsilon$ sol. | [adm] | 0.3 |
| $\epsilon$ liq. | [adm] | 0.9 |
| $k_p$ | [W / m K] | 9.2264 - 5.5338 T + 2.8358 T$^2$ - 0.6124 T$^3$ |

*Results and discussion*

Since the main goal of this paper is to investigate the effect of coil current frequency on the trajectories of powders heated in the plasma, two sets of simulations have been carried out at 3 MHz and 13.56 MHz, respectively, with different powder feed rates and two injection probe tip positions.

It is well known that powder feed rate influences strongly the effectiveness of the powder treatment: for increasing values of the feed rate a stronger plasma cooling by the particle stream is expected (Proulx 1987); this phenomena is known as loading effect and it is the most important issue to be solved when up-scaling the ICP assisted process. In order to investigate the influence of the powder feed rate under different coil current frequencies, computations have been done for two frequencies (3 MHz and 13.56 MHz) with different values of powder feed rate (2, 5, 10 and 20 g/min), being the injection probe fixed at 55 mm upstream of the torch outlet.

Moreover, injection probe position is an important operating parameter which can be used to optimize the process, since it can influence strongly the trajectories and the thermal histories of the treated particles. As shown experimentally by Fan et al. (Boulos 1998), optimal conditions for powder treatment include an injection probe position well inside the discharge, below the recirculation flows occurring near the top of the coil; thus, injected particles follow an almost straight line and only a limited turbulent dispersion of powders inside the torch occurs. As a drawback, such a

position of the probe results in a lower energy exchange between the hot core of the plasma and the particles. In this work, two different probe positions have been examined: probe tip at 55 mm and 45 mm upstream of the torch exhaust.

*Particle trajectories under different coil current frequencies*

First, we considered two cases with powder feed rate set to 10 g/min and injection probe tip positioned 55 mm upstream of the torch outlet; coil current frequency has been set set at 3 MHz and 13.56 MHz, respectively.

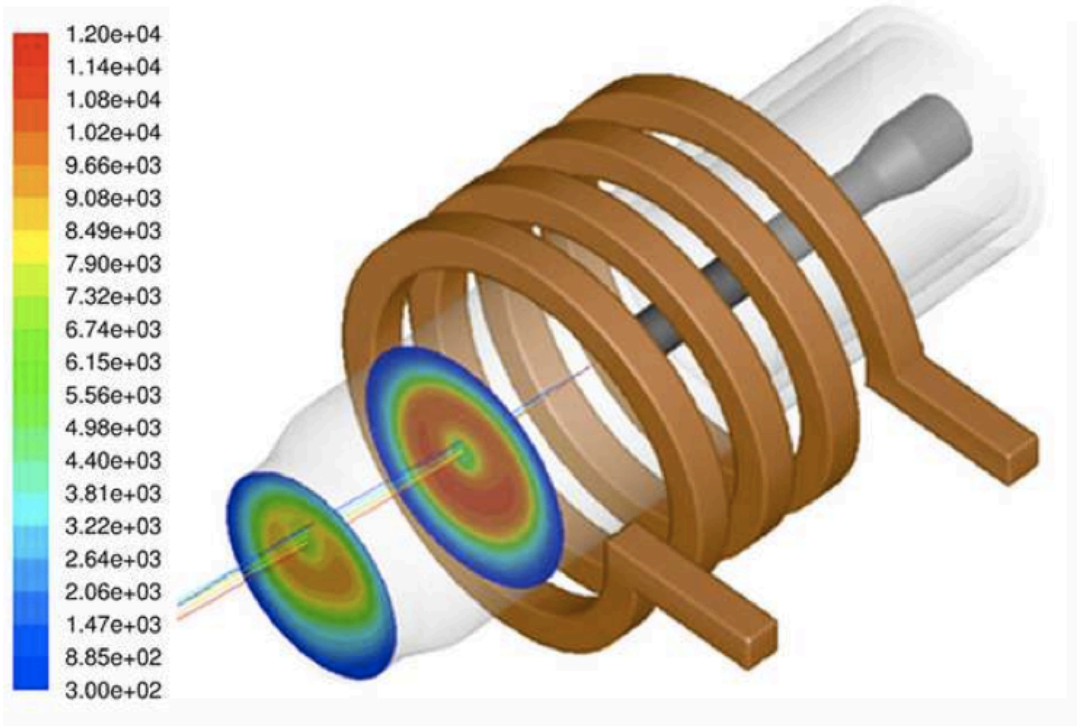


Fig. 2 - Case at 3 MHz - Tracks of particles with different initial diameter (different line colors from blue, 25 um, to red, 125 um, step by 25 um) released from a central injection point on the probe tip; temperature iso-contours (K) on two x-y planes at z = 85 mm and z = 113 mm. Powder feed rate set to 10 g/min; probe tip at 55 mm upstream of the torch outlet. (taken from Ref. [3])

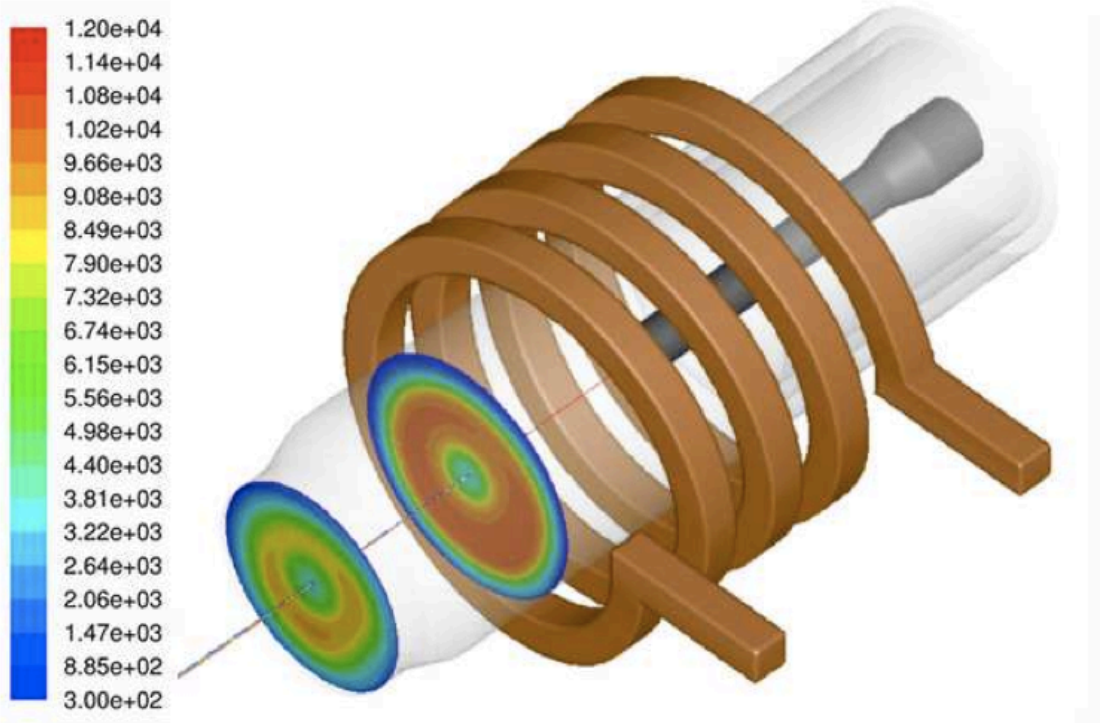


Fig. 3 - Case at 13.56 MHz - Tracks of particles with different initial diameter (different line colors from blue, 25 um, to red, 125 um, step by 25 um) released from a central injection point on the probe tip; temperature iso-contours (K) on two x-y planes at z = 85 mm and z = 113 mm. Powder feed rate set to 10 g/min; probe tip at 55 mm upstream of the torch outlet. (taken from Ref. [3])

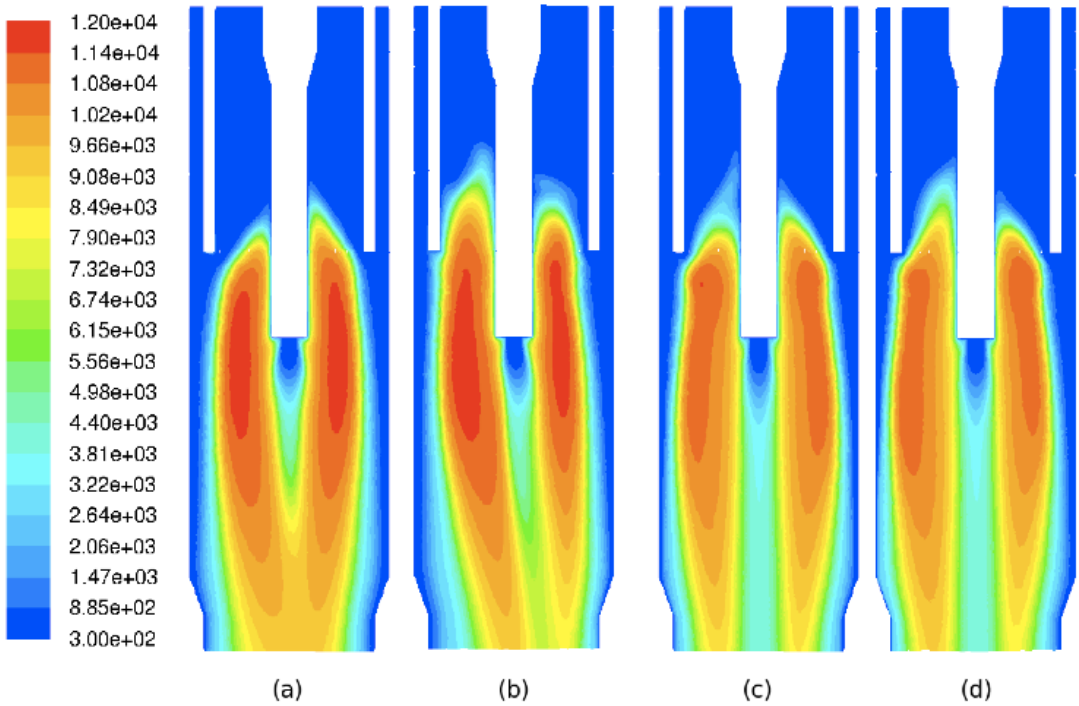


Figure 4 - Temperature distribution (K) for the case at 3 MHz, plane x-z (a) and plane y-z (b), and for the case at 13.56 MHz, plane x-z (c) and plane y-z (d). Powder feed rate set to 10 g/min; probe tip at 55 mm upstream of the torch outlet. (taken from Ref. [3])

In figures 2 and 3 trajectories of particles released from a central injection point of the probe tip are reported for the two cases. For every particle diameter a single trajectory is shown; in order to capture the mean behavior of particles, in this picture trajectories are calculated without taking into account turbulent dispersion.
For the case at 3 MHz (figure 2), particles with diameter lower than 75 um are deviated from torch axis, whereas particles with higher diameter follow a straighter line.
For the case at 13.56 MHz (figure 3), in the whole range of particle diameter considered, all the trajectories are almost on the axis.
In the same figures, plasma temperature iso-contours on plane x-y at z = 85 mm and z = 113 mm for the two cases are reported: a non-axisymmetric temperature distribution can be evidenced for the case with lower frequency, with a non radially centered region cooled by heat exchange with powders. When the frequency is set at 13.56 MHz an axisymmetric cooled region has been obtained.

In figure 4 the temperature fields inside the torch for the two cases are reported. Maximum temperature (11700 K and 11430 K for the case at 3 MHz and 13.56 MHz, respectively) is reached at an off-axis position, as a consequence of magnetic field screening due to induced currents in plasma (skin effect); moreover, along the axis, a low temperature region results as a consequence of particle-plasma heat exchange. For the case at 3 MHz (figures 4-a and 4-b) the discharge is deviated in the positive y-direction, whereas for the case at 13.56 MHz (figures 4-c and 4-d) the temperature fields is almost axisymmetric.
For the first case, also the low temperature channel due to heat exchange with powders is deviated with respect to the torch axis.

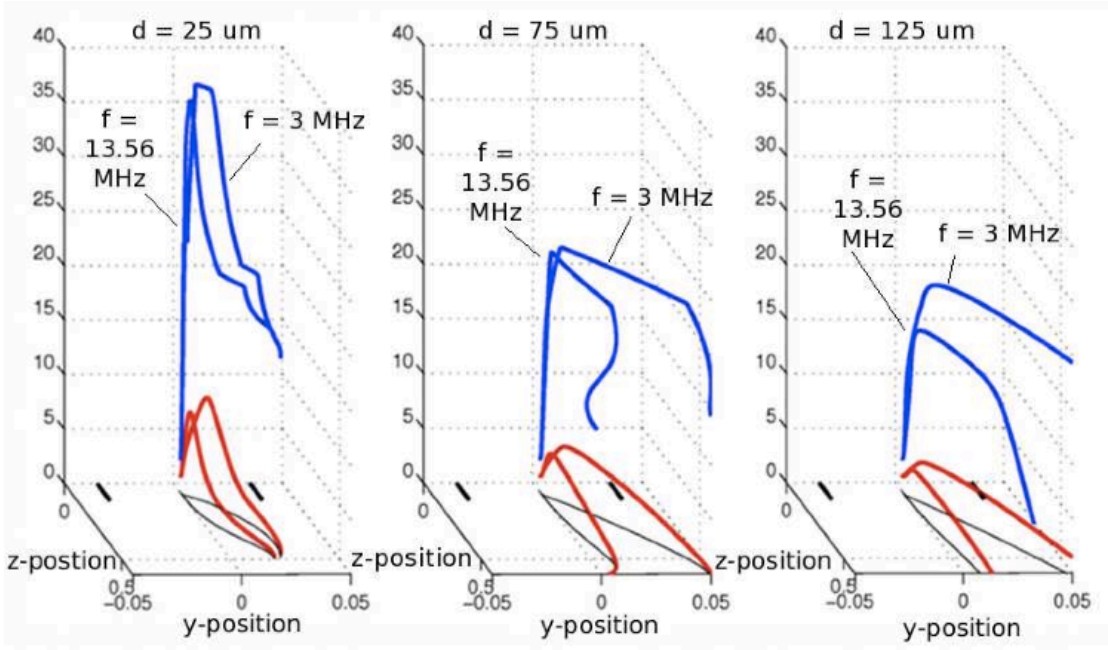


Fig. 5 - Temperature (K/100) in blue and velocity (m $s^{-1}$/7.5) in red of particles with different initial diameter released from a central injection point on the probe tip for cases at 3 MHz and 13.56 MHz, respectively; particle position shown with projections on the y-z plane; torch walls shown as bold black lines; powder feed rate set to 10 g/min; probe tip at 55 mm upstream of the torch outlet. (taken from Ref. [3])

In figure 5 trajectories, temperature and velocity for particles released from a central injection point on the probe tip are reported. It should be stressed that in this way it is possible to visualize all the relevant properties of the tracked particles: particle velocity, temperature and position on the y-z plane. The position of the particles has been highlighted in these pictures by means of orthogonal projections on the y-z plane (black lines). It is shown that particles treated at 3 MHz are strongly deviated in the y-direction, regardless of particle diameter. However, particles with higher diameter are characterized by higher thermal and momentum inertia.

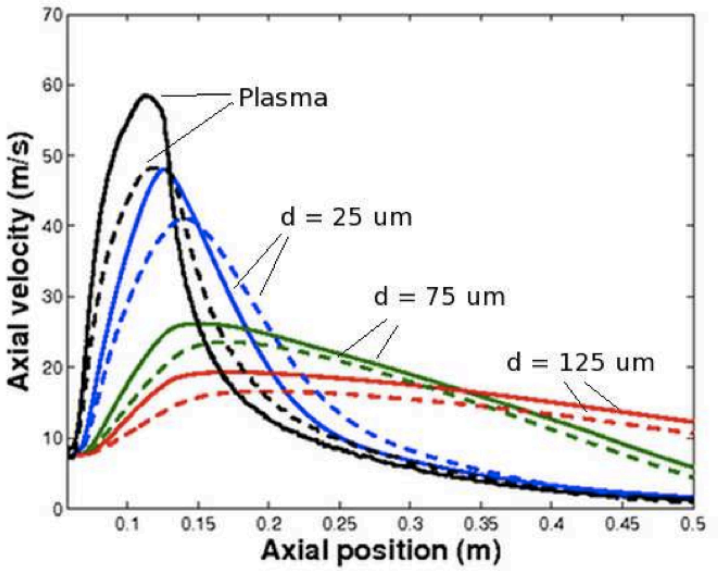


Fig. 6 - Axial velocity of particles released from a central injection point on the probe tip for cases with frequency set at 3 MHz (continuous line) and at 13.56 MHz (dashed line); powder feed rate set to 10 g/min; probe tip at 55 mm upstream of the torch outlet. (taken from Ref. [3])

In figure 6 particle axial velocities alone as a function of axial position for the two cases are shown. Particles with higher diameter have a lower velocity within the torch region ($z<0.113$ m) where they are less accelerated by the plasma drag forces with respect to those with lower diameter; higher velocities for particles with higher diameter have been obtained in the chamber region ($z>0.113$ m), where plasma tends to decelerate particles.

Particle velocity in the torch region is higher for the case at lower frequency, as a result of a lower loading effect; in the chamber, plasma velocity is lower for the case with lower frequency, but particle velocities are still higher than for 13.56 MHz, with the exception of particles with d = 25 um.

Higher values for particle velocities are directly correlated with higher plasma temperature along the particle trajectories and, thus, with higher plasma velocity.

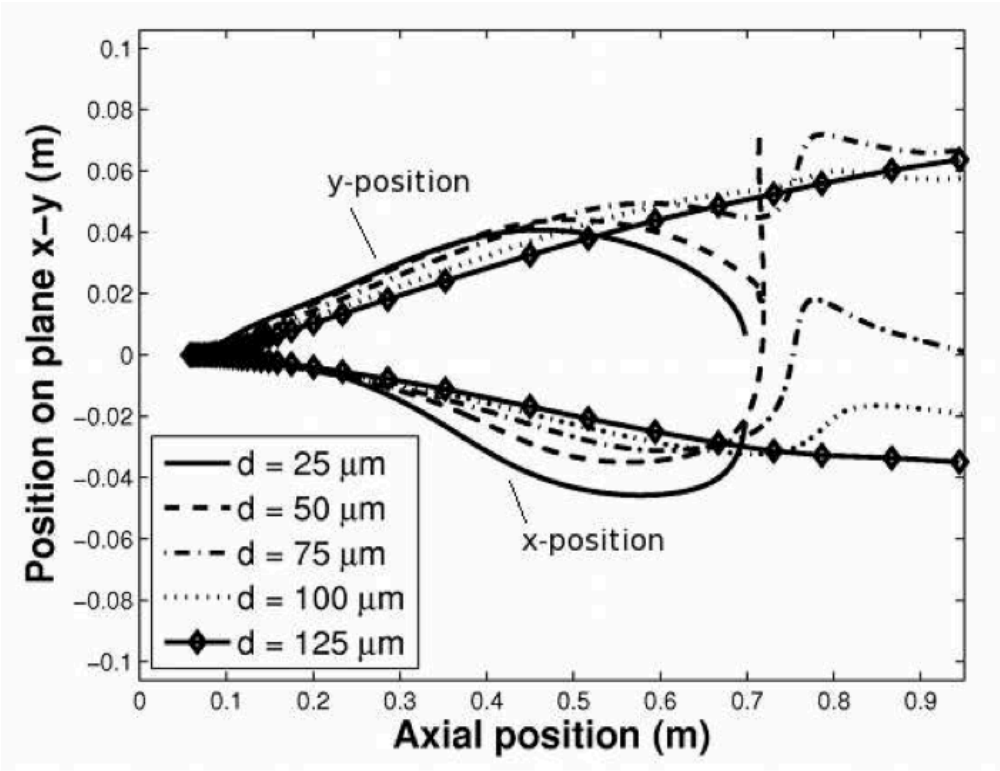


Fig. 7 - Particle position for the case at 3 MHz. Powder feed rate set to 10 g/min; probe tip at 55 mm upstream of the torch outlet. (taken from Ref. [3])

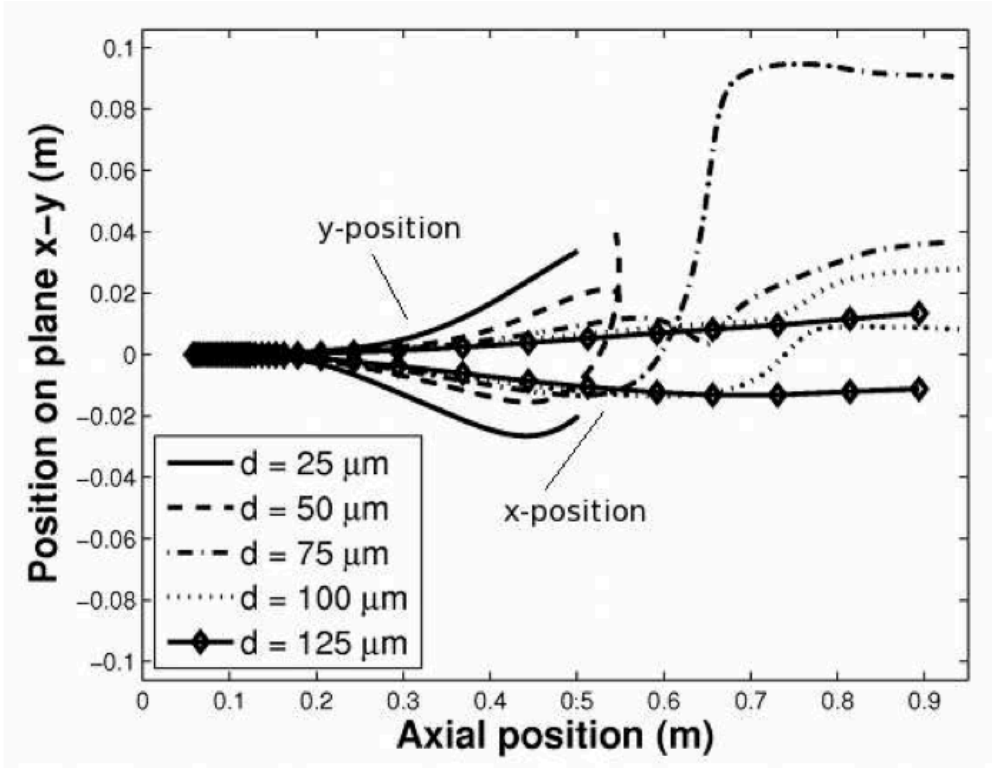


Fig. 8 - Particle position for the case at 13.56 MHz. Powder feed rate set to 10 g/min; probe tip at 55 mm upstream of the torch outlet. (taken from Ref. [3])

A detail of particle trajectories for two cases are reported in detail in figures 7 and 8, respectively.
In the first case, trajectories are strongly deviated from torch and chamber axis.
In the case with higher frequency, particles are deviated from the axis only when they reach the chamber (z>0.113 m) as a consequence of non-axisymmetric recirculation flows due to the lateral gas outlet tube.

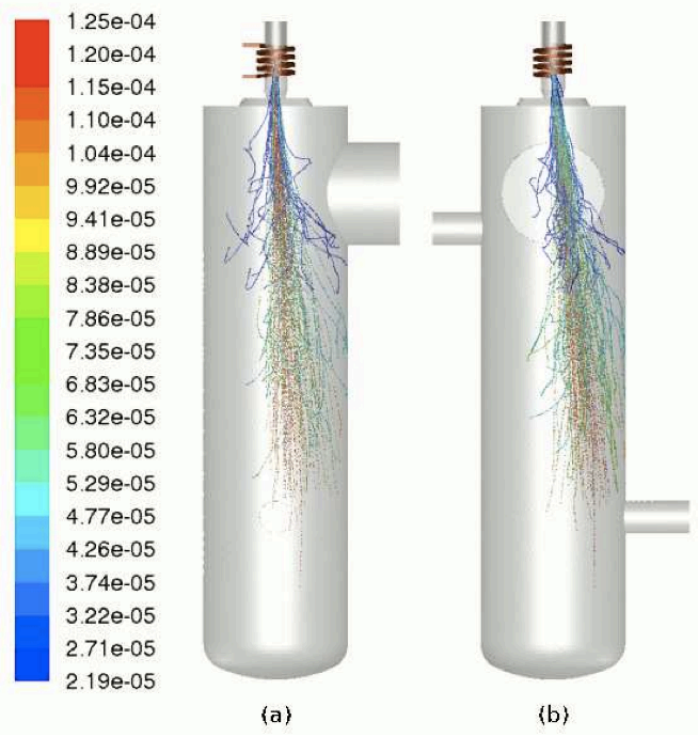


Fig. 9 - Particle trajectories colored by particle diameter (m) for the case at 3 MHz: plane x-z (a) and plane y-z (b). Powder feed rate equal to 10 g/min; probe tip at 55 mm upstream of the torch outlet. (taken from Ref. [3])

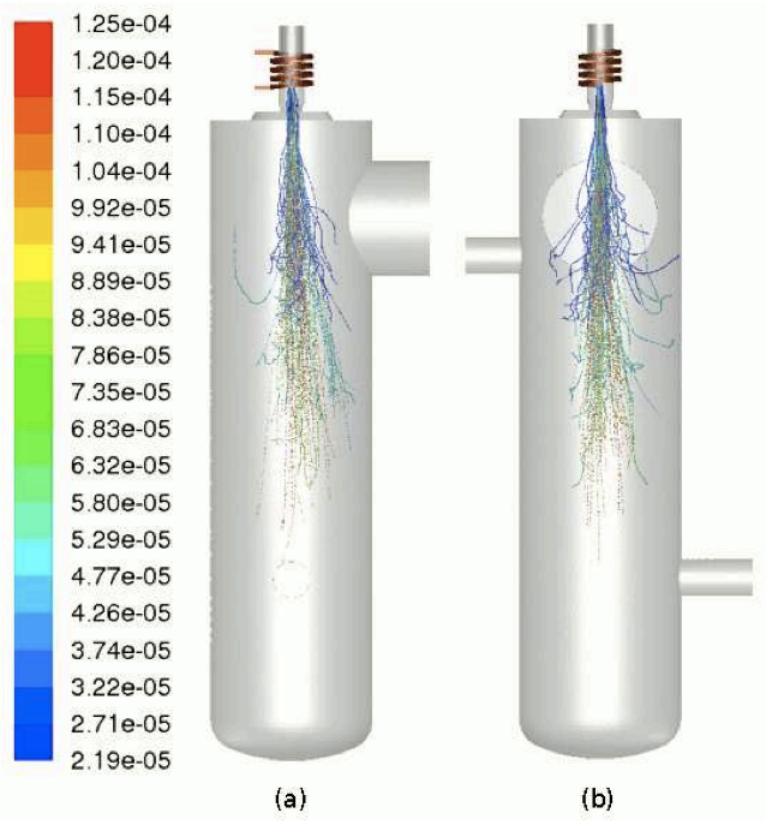


Fig. 10 - Particle trajectories colored by particle diameter (m) for the case at 13.56 MHz: plane x-z (a) and plane y-z (b). Powder feed rate equal to 10 g/min; probe tip at 55 mm upstream of the torch outlet. (taken from Ref. [3])

Once the trajectories of single particles have been analyzed, the collective behavior of injected powders for the two cases must be taken into account, with trajectories calculated including turbulent dispersion (figures 9 and 10).
For the case at 3 MHz a strongly deviated particle stream has been obtained, whereas for the case at higher frequency a quite axisymmetric stream resulted: this is in line with the behavior obtained for single particle trajectory without turbulent dispersion, leading to the conclusion that single particles released from a central injection point on the probe tip could be considered as representative of the collective behavior of powders released from the whole probe tip.
Deviation from axial symmetry in particle trajectories for the cases with lower frequency is directly connected with non-axisymmetric plasma temperature and velocity fields, since the main forces acting on particles are those due to fluid drag (see equation 1).

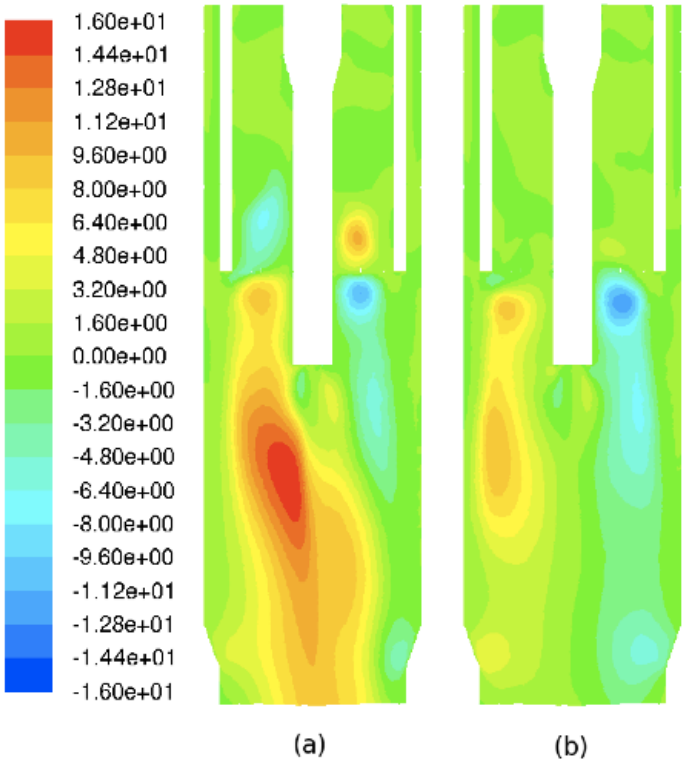


Fig. 11 - Detail of the y-velocity field (m/s) inside the torch on plane y-z: frequency set at 3 MHz (a) and at 13.56 MHz (b); powder feed rate set to 10 g/min; probe tip at 55 mm upstream of the torch outlet. (taken from Ref. [3])

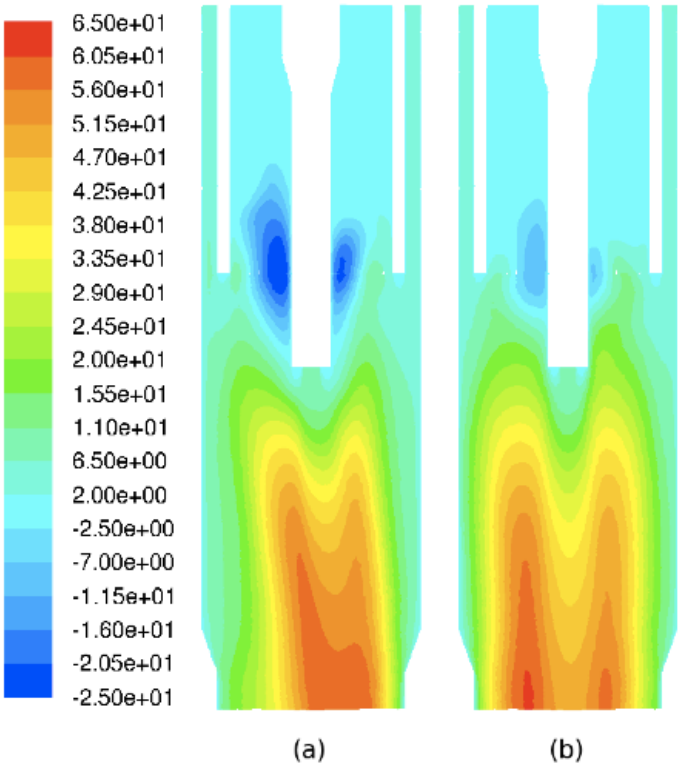


Fig. 12 - Detail of the z-velocity field (m/s) inside the torch on plane y-z: frequency set at 3 MHz (a) and at 13.56 MHz (b); powder feed rate set to 10 g/min; probe tip at 55 mm upstream of the torch outlet. (taken from Ref. [3])

In figure 11-a and 11-b the iso-contours of the y-component of the plasma velocity field are reported for cases at 3 MHz and 13.56 MHz, respectively: in the first case, strongly deviated fields have been obtained, which lead to non-axisymmetric particle trajectories by means of the drag forces. A great difference between high and low frequency can be seen in the y-component of the velocity field; in the case at 3 MHz y-velocity is strongly non-axisymmetric.
The z-component velocity field on the plane y-z is reported in figures 12-a and 12-b for two cases. For the case at 3 MHz (figure 12-a) the z-component of the velocity field is strongly non-axisymmetric and recirculation flows are present near the probe tip (negative axial velocity), whereas for the case at 13.56 MHz the axial velocity is almost axisymmetric and the intensity of recirculation flows is lower.
Non-axisymmetric velocity fields resulted as a consequence of temperature (shown in figure 4) and Joule power distributions with a high degree of deviation from axial symmetry, which in turn arise when unbalanced Lorentz forces prevail over fluid-dynamic inertia as recently shown by the authors (Colombo 2010). It should be noted that for the case at 13.56 MHz the values for the z-component of the plasma velocity are generally higher than for the case at 3 MHz.

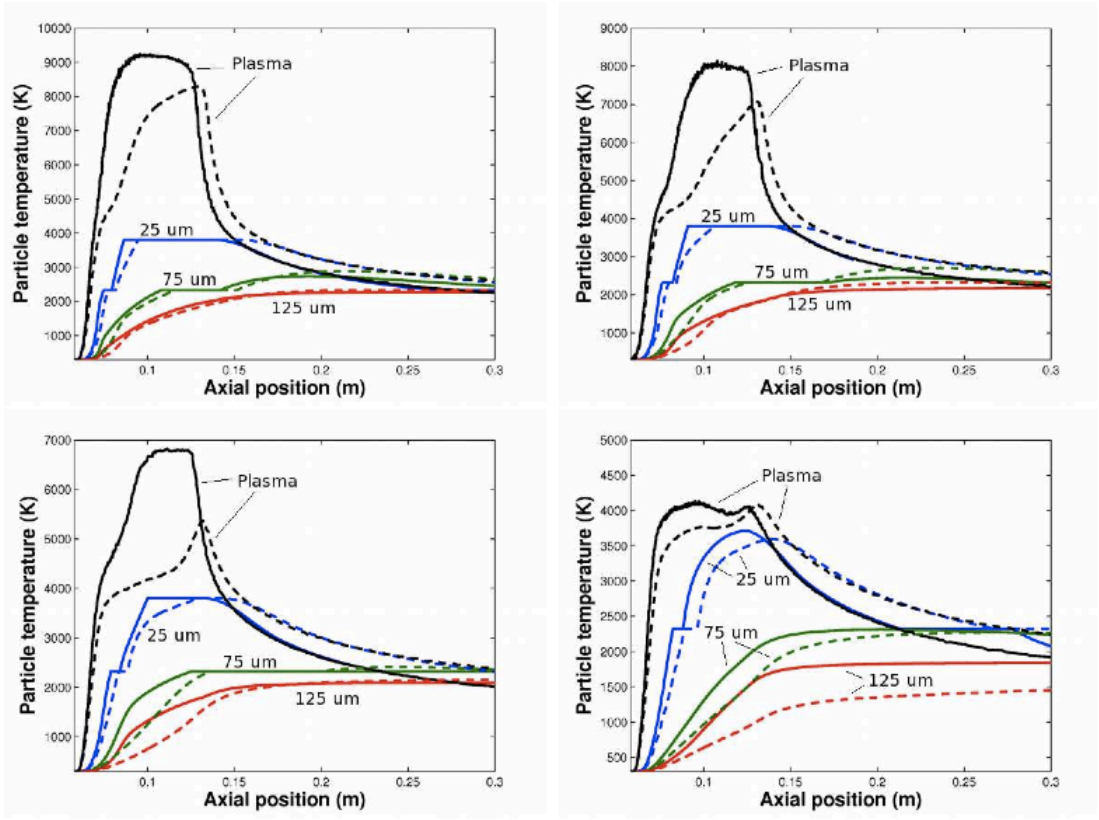


Fig. 13 - Temperature of particles released from a central injection point on the probe tip for cases with frequency set at 3 MHz (continuous line) and at 13.56 MHz (dashed line); powder feed rate set to 2 g/min (top-left), 5 g/min (top-right), 10 g/min (bottom-left) and 20 g/min (bottom-right); probe tip 55 mm upstream of the torch outlet. Mean plasma temperature computed along particle trajectories. (taken from Ref. [3])

*Effects of powder feed rate, injection probe position and frequency on plasma and particle temperature*

We now consider the cases with probe tip set 55 mm upstream of the torch outlet, for different powder feeding rates.
particle temperatures as a function of different values of the powder feed rate and different particle initial diameters are shown in figure 13.

For powder feed rate set to 2 g/min (top-left in figure 13), almost no plasma cooling in the torch region has been predicted for the case at 3 MHz, whereas for higher frequency it is substantial. In both cases, a strong evaporation occurs for 25 um particles, whereas melting point is reached for diameters below 75 um.
For higher powder feed rates, a great difference in loading effect has been evidenced for different frequencies: for the case at 13.56 MHz, plasma cooling is generally more pronounced. For the case with powder feed rate set to 10 g/min (bottom-left in figure 13) and frequency equal to 3 MHz, evaporation is reached for particles with the lowest diameter among the ones here considered (25 um); whereas for the case with the same powder feed rate but higher frequency, lower plasma temperatures along the particle trajectory induce no particle evaporation. Particles with diameter equal to 25 um are almost isothermal with the fluid for in the chamber region ($z>0.113$ m).
For powder feed rate set to 20 g/min (bottom-right in figure 13), the loading effect for the case at 3 MHz becomes comparable with the one characterizing the 13.56 MHz case, but thermal histories of the particles are still frequency dependent.

The higher coil current frequency leads to lower plasma temperature inside the torch and to higher temperature in the chamber with respect to 3 MHz (see figure 13): as a result, the same trend has been obtained also for the particle temperatures when powder feed rate is lower than 20 g/min. On the contrary, for the latter, particles with initial diameter higher than 75 um have lower temperature in the chamber in the case with higher frequency.
Lower particle heating inside the torch in the case of higher frequency was previously predicted also by Shigeta (Shigeta 2004), who also studied particle heating in a ICP torch under different frequencies.
However, since the domain of his simulations included only the torch region, he could not conclude that a higher heating is obtained in the chamber for the case with higher frequency.
Moreover, loading effects were not considered by Shigeta, whereas it is shown in this paper that they play an important role in investigating the effectiveness of powder treatment at different coil current frequencies.

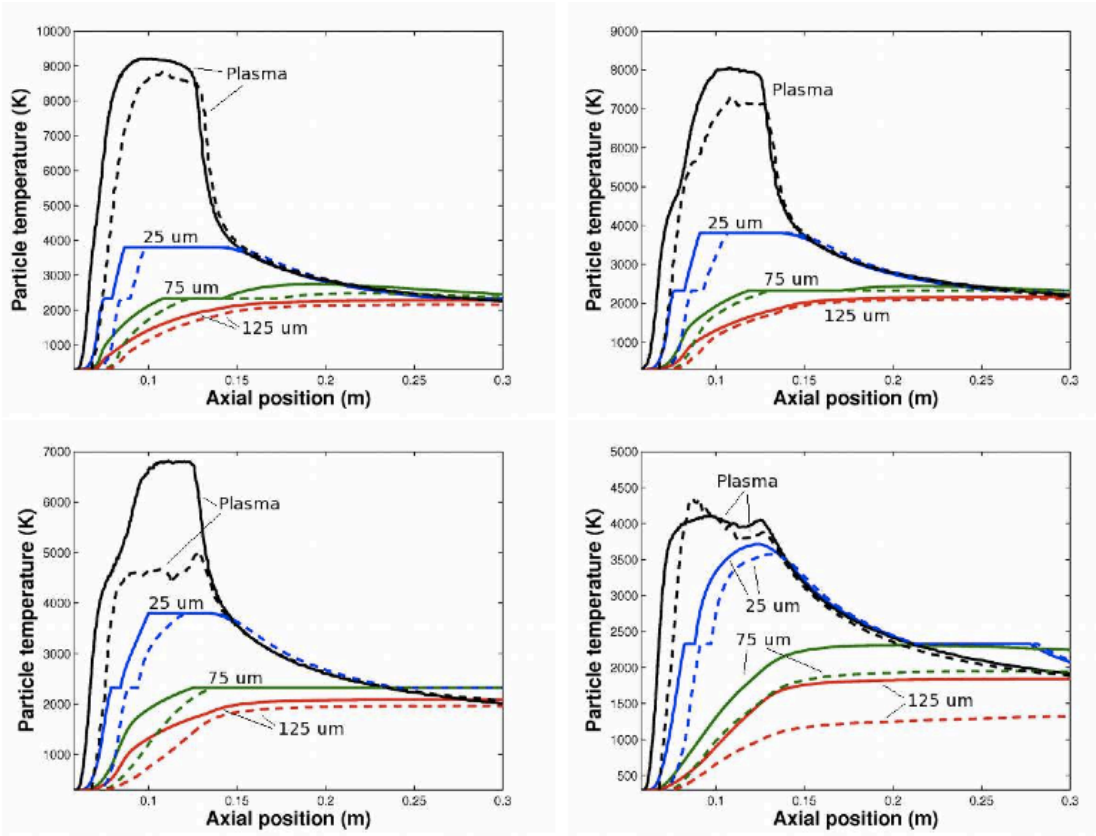


Fig. 14 - Temperature of particles released from a central injection point on the probe tip for cases with probe tip at 55 mm (continuous line) and at 45 mm (dashed line) upstream of the torch outlet; powder feed rate set to 2 g/min (top-left), 5 g/min (top-right), 10 g/min (bottom-left) and 20 g/min (bottom-right); frequency set at 3 MHz. (taken from Ref. [3])

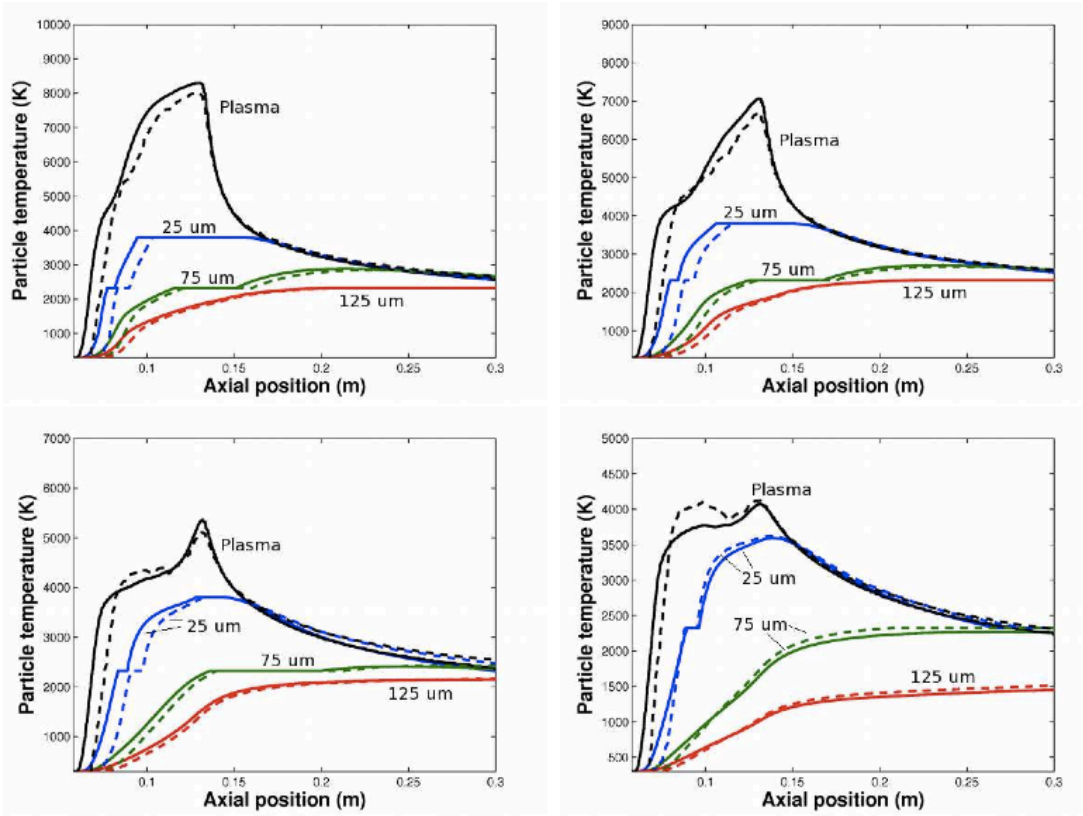


Fig. 15 - Temperature of particles released from a central injection point on the probe tip for cases with probe tip at 55 mm (continuous line) and at 45 mm (dashed line) upstream of the torch outlet; powder feed rate set to 2 g/min (top-left), 5 g/min (top-right), 10 g/min (bottom-left) and 20 g/min (bottom-right); frequency set at 13.56 MHz. (taken from Ref. [3])

Particle thermal histories with probe at different positions (55 mm and 45 mm upstream the torch outlet, respectively) are reported in figures 14 and 15, for 3 MHz and 13.56 MHz, respectively, and for different powder feed rates.
For the lower frequency (figure 14), when the probe tip is shifted towards the torch outlet, plasma temperature along the particle trajectories decreases strongly with increasing powder feed rate.
The same trend can be observed for particle temperatures. Positioning the probe tip nearer to the torch outlet produces in the torch region almost the same effects obtainable for higher frequency positioning the probe 55 mm upstream of the torch exit (lower particle heating and higher loading effect); however, in the reaction chamber the particle temperatures are generally higher for higher frequency.

At 13.56 MHz (figure 15), an axial shifting of the probe from 55 mm to 45 mm upstream of the torch exit induces only small changes in plasma and particle temperatures. However, particle temperatures are generally lower with the most downstream position. On the contrary, with feed rate set to 20 g/min the particle temperatures are slightly lower for the case with probe tip at 55 mm upstream of the torch outlet.

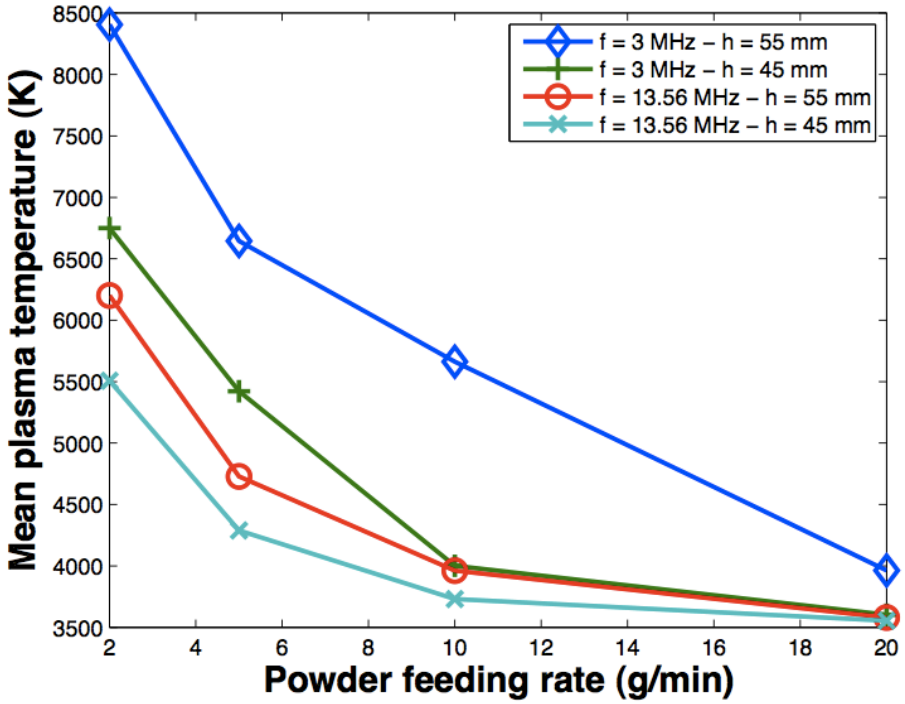


Fig. 16 - Mean plasma temperature along particle trajectories calculated for axial position varying between z = 0.07 m and z = 0.113 m (torch outlet); probe tip position (h) computed as distance upstream of the torch outlet. (taken from Ref. [3])

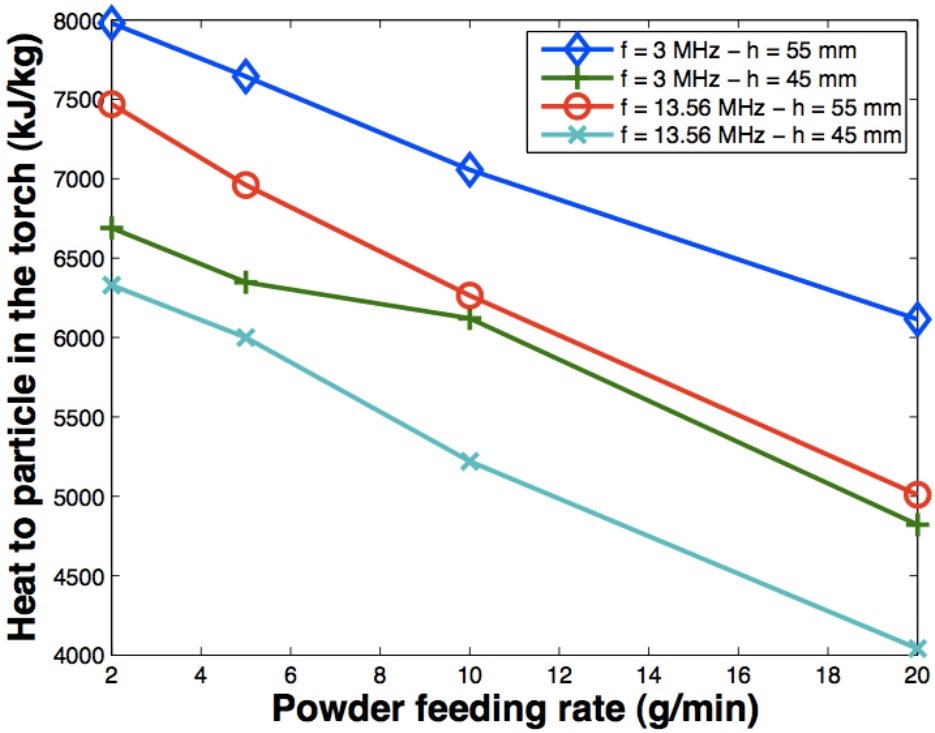


Fig. 17 -Plasma-particle heat exchange in the torch, normalized using powder feeding rate; probe tip position (h) computed as distance upstream of the torch outlet. (taken from Ref. [3])

Loading effects can be evidenced from mean plasma temperature along particle trajectories as a function of powder feed rate (figure 16).
A stronger loading effect, accordingly with previous results (Proulx 1987), has been obtained for increasing powder feed rate: plasma temperature along the particle trajectories decreases for increasing powder feed rate.
At 3 MHz, plasma cooling is less pronounced than in the cases at 13.56 MHz; moreover, as powder feed rate increases, the increase in loading effect is lower for the lower frequency case.
In the case at 3 MHz with probe tip at 55 mm upstream of the torch outlet, particles are injected in the hot core of the plasma, where Joule dissipation balances plasma heat losses by plasma-particle heat exchange.
The higher loading effect for 13.56 MHz is a consequence of the typical means of Joule dissipation inside the discharge: in this case, as a consequence of a smaller skin depth, Joule dissipation is concentrated near the torch walls and the effect of cooling in the central region of the plasma is balanced by heat conduction only, resulting in a more pronounced loading effect.
Similar conclusions can be drawn for the cases with probe tip shifted at 45 mm upstream of the torch outlet: in this case, the particles are not injected in the plasma hot core and the fluid cooling due to plasma-particle interaction produces a more pronounced loading effect (lower mean plasma temperature along particle trajectories).

Figure 17 shows that for both 3 MHz and 13.56 MHz, particles injected with the probe at a higher position (55 mm upstream of the torch outlet) receive an higher amount of energy with respect to those injected with a probe 45 mm upstream the torch outlet, as a consequence of a longer particle path inside the plasma core and of a lower loading effect.
As the powder feed rate increases, the amount of energy per unit mass of injected particles decreases, as a consequence of the loading effect.
The highest amount of energy transmitted to the powders in the torch has been obtained for the case at 3 MHz and probe tip at 55 mm upstream of the torch outlet.

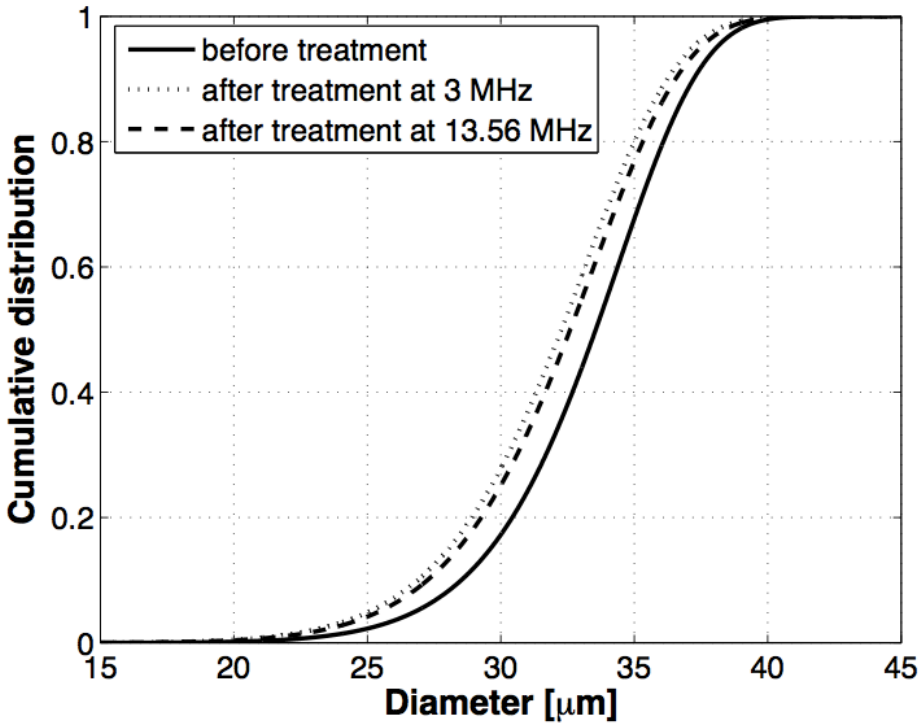


Fig. 18 - Cumulative distribution function of powders before and after plasma treatment for cases with frequency set at 3 MHz and at 13.56 MHz, powder feed rate set to 2 g/min; probe tip at 55 mm upstream of the torch outlet. (taken from Ref. [3])

In figure 18 the cumulative distribution for particles before and after treatment has been reported for two cases which differ for the coil current frequency. In order to estimate the change in the distribution function induced by the plasma process, two simulations have been carried out for a smaller size-distribution function (22 um < $d_p$ < 44 um) and low powder feed rate (2 g/min), allowing particles to reach the evaporation and, thus, the reduction in diameter. The probe tip has been set at 55 mm upstream of the torch outlet.
The mean diameter of the distribution function after treatment for 3 MHz is slightly lower than for 13.56 MHz, as a consequence of the higher amount of energy received by the plasma flow inside the torch and as consequence of a lower loading effect.

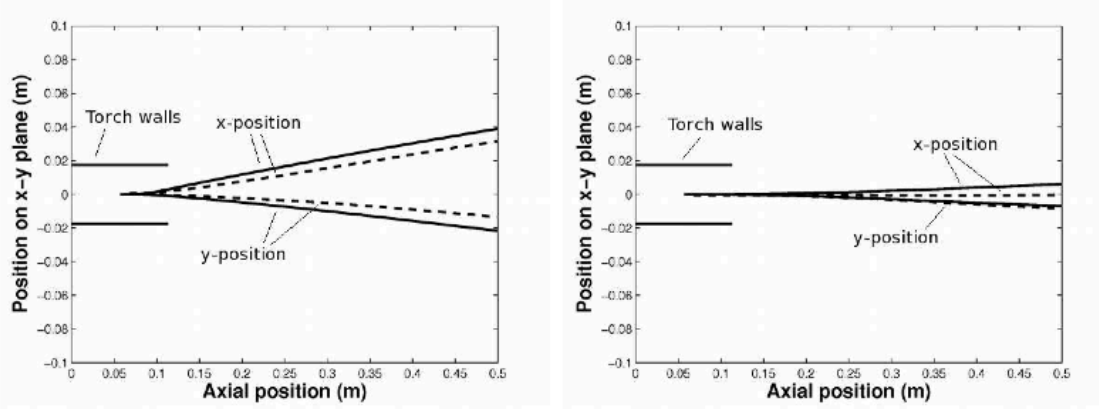


Fig. 19 - Position on plane x-y of particles released from a central injection point on the probe tip for cases with probe tip at 55 mm (continuous line) and at 45 mm (dashed line) upstream of the torch outlet; frequency set at 3 MHz (left) and at 13.56 MHz (right); powder feed rate set to 10 g/min. (taken from Ref. [3])

Finally, it should be noted that particle trajectories for the case at 3 MHz with probe at 45 mm from the torch outlet are less deviated in both x and y direction, with respect to the case at 3 MHz with probe at 55 mm (figure 19); in the case at higher frequency, the trajectories follow a straight path for both probe positions.

**Modelling of nanopowder synthesis in inductively coupled radio-frequency thermal plasma systems**

In the last decade many studies have been directed towards nano-powder synthesis in thermal plasmas, already widely used for many industrial applications including thermal spray, powder spheroidization and waste treatment. Inductively coupled plasma torches (ICPT) have been found to be very promising devices for nano-particle production, thanks to their advantages such as high purity, high energy density, high chemical reactivity, large volume and long residence time. This process also promises high scalability thanks to the use of solid primary material, high versatility thanks to the possibility of tailoring thermo-fluid-dynamics fields and plasma gases. This technology allows obtaining nano-particles with narrow particle size distribution (PSD), given the high cooling rate ($10^4$-$10^5$ $Ks^{-1}$) that can be found in the tail of the ICPT.

Several experimental studies on ICPT synthesized nano-powder have been conducted, but due to measurements limitations only final products can be analysed and no information about the processes of particles nucleation and growth can be obtained.

Numerical modelling is a powerful tool for predicting plasma properties and to obtain deeper understanding of the physical processes involved in nano-particle synthesis.

Nano-particle formation in plasma systems have been modelled extensively in the past, mainly using two different numerical models to solve the aerosol general dynamic equation (GDE). In moment method a uni-modal log-normal profile of the PSD is often assumed for mathematical closure; while this model can save computational time, the PSD is known to strongly deviate from the log-normal distribution. Contrarily, in discrete-sectional method no assumptions are made on the PSD, but the computational expense is higher. A third model has been proposed, named nodal method, based on the concept of nodal discretization and the coupling between the vapour phase and the particle discrete regime by a nucleation source term.

In the present work a 2-D moment method for the study of the synthesis of Si nano-powders inside a RF plasma apparatus with reaction chamber is presented; precursor powder trajectories, thermal history and vaporization are also taken into account.

Besides, no computational model actually accounts for the effects of turbulence on particle synthesis, despite the strong turbulent behaviour displayed by the thermo fluid dynamic fields inside the apparatus. Thus, as the second aim of this work, a way to model turbulence effects is proposed and the induced changes are introduced in the moment method; the modified synthesis process has therefore been investigated and notable results are presented.

*Mathematical model for the nanopowder synthesis process*

Nano-particle synthesis is a complex process that can be described by the aerosol GDE, proposed by Friedlander[49]:

$$\frac{\partial}{\partial t}n(v_p)+\overline{\nabla}\cdot[\bar{u}n(v_p)]=\overline{\nabla}\cdot[D(v_p)\overline{\nabla}n(v_p)]+I\delta_D(v_p-v_p^*)-\frac{\partial}{\partial v_p}[Gn(v_p)]$$
$$+\frac{1}{2}\int_0^{v_p}\beta(v_p',v_p-v_p')n(v_p')n(v_p-v_p')dv_p'-\int_0^{\infty}\beta(v_p,v_p')n(v_p)n(v_p')dv_p'$$

where $n$ is the PSDF, $v_p$ is the particle volume, $\bar{u}$ is the particle velocity, $D$ is the particle diffusion coefficient, $I$ is the nucleation rate, $\delta_D$ is the Dirac delta function, $G$ is the heterogeneous condensation growth rate, $\beta$ is the interpolative collision frequency function and the suffix * denotes critical state.
According to Friedlander, stable nuclei formed from the precursor vapour at a defined nucleation rate are transported by convection and diffusion through the surrounding fluid, growing because of vapour condensing on their surface and collisions with other particles.
The nucleation rate I can be written as:

$$I=\frac{\beta(v_{monomer},v_{monomer})N_S^2S}{12}\sqrt{\frac{\Theta}{2\pi}}\exp\left(\Theta-\frac{4\Theta^3}{27(\ln S)^2}\right) \qquad (3.13)$$

in which the subscripts monomer and S, respectively, denote the monomers of the material and the saturated state. The supersaturation ratio S is defined using the vapour pressure and the saturation pressures

$$S=\frac{P_{vap}}{P_{sat}} \qquad (3.14)$$

Subscript vapour stands for the material vapour. The normalized surface tension Θ is defined with

$$\Theta=\frac{\sigma_{st}s_{monomer}}{\sigma T} \qquad (3.15)$$

where $\sigma_{st}$ is the material surface tension, whereas s is the monomer surface area.
Homogeneous nucleation produces nuclei with a critical size because the nuclei smaller than the critical size are unstable and easily evaporate. The critical volume $v_p$* can be estimated as:

$$v_p^*=\frac{\pi}{6}\left(\frac{4\sigma_{st}v_{monomer}}{\sigma T\ln(S)}\right) \qquad (3.16)$$

The particle growth rate by heterogeneous condensation G is simply estimated using the bombardment of monomers on the nucleus' surface:

$$G = \frac{dv_p}{dt} = \frac{\pi d_p^2 v_{monomer}\left(p_{vap} - p_{sat}\right)}{\left(2\pi m_{monomer}\sigma T\right)^{1/2}} \qquad (3.17)$$

In a free molecular regime, the collision frequency function β between nanoparticles with volume $v_p$ and $v_p$' is written as

$$\beta\left(v_p, v_p^{'}\right) = \left(\frac{3}{4\pi}\right)^{1/6}\left(\frac{6\sigma}{T}\right)^{1/2}\left(\frac{1}{v_p} + \frac{1}{v_p^{'}}\right)^{1/2}\left(v_p^{1/3} + v_p^{'1/3}\right)^2 \qquad (3.18)$$

The diffusion coefficient D of the nanoparticles with the volume $v_p$ is given similarly as

$$D\left(v_p\right) = \frac{\sigma T}{3\pi\eta}\left[\left(\frac{\pi}{6v_p}\right)^{1/3} + 3.314l\left(\frac{\pi}{6v_p}\right)^{2/3}\right] \qquad (3.19)$$

where η is the dynamic viscosity of the plasma and l is the mean free path of gas particles, which can be written as

$$l = \frac{\eta}{\rho}\left(\frac{\pi m_{gas}}{2\sigma T}\right)^{1/2} \qquad (3.20)$$

It is generally difficult to solve Eq. 30 because of its nonlinearity. For that reason, several numerical methods to solve it have been proposed and applied to the plasma-aided nanoparticle formation processes.

*Method of moments for the solution of GDE*

For the present study, the method using the moments of the PSDF, the so-called moment method, is adopted because the spatial distribution of the growing nanoparticles with each size is obtainable even if the flow field has a negative velocity such as a counter-flow or a circulating zone.
In this method, the PSD function is assumed to be of the log-normal type.
The mathematical expression of this distribution is

$$f(x;\mu,\sigma) = \frac{1}{x\sigma\sqrt{2\pi}}e^{-\frac{\left[\ln(x)-\mu\right]^2}{2\sigma^2}} \qquad x > 0 \qquad (4.2)$$

which is completely defined by the two parameters μ e σ.
The log-normal distribution as a function of x for μ = 1 and for different values of σ is reported in figure 1.

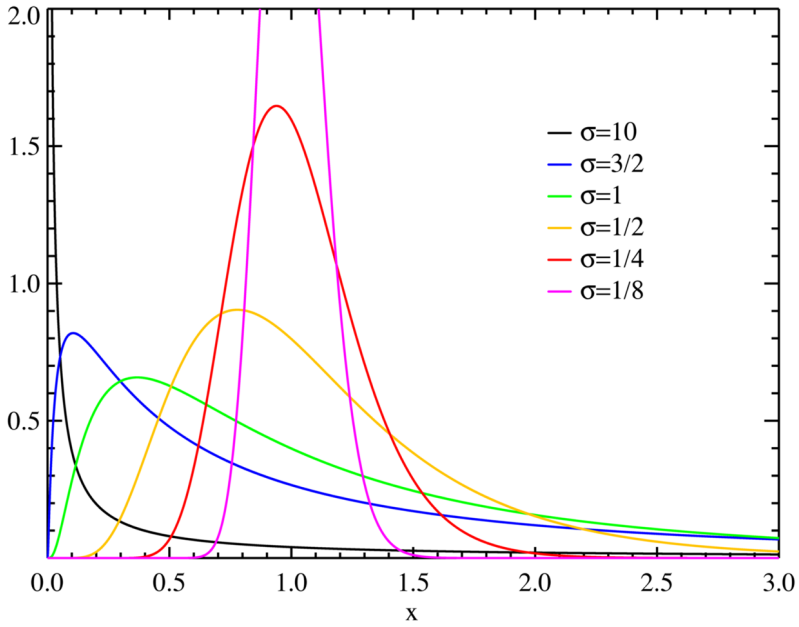


Fig. 1 - Log-normal distribution as a function of x for μ = 1 and for different values of σ

The moment method handles the first three moments of the PSD function:

$$M_0 = \int_0^\infty n\left(v_p\right) dv_p \qquad (4.3)$$

$$M_1 = \int_0^\infty v_p n\left(v_p\right) dv_p \qquad (4.4)$$

$$M_2 = \int_0^\infty v_p^2 n\left(v_p\right) dv_p \qquad (4.5)$$

where $M_0$, $M_1$ e $M_2$ represent the moments of order 0, 1 and 2, respectively.
The zero-th moment and the first moment are, respectively, the total concentration and the total volume of the generated nanoparticles. The second moment is also known to be proportional to the total light scattering by the nanoparticles when they have much smaller size than the wavelength of the incident light.
Consequently, GDE equations can be transformed into the simultaneous moment transport equations in a steady state as

$$\bar{u} \cdot \bar{\nabla} M_k = [\dot{M}_k]_{nucl} + [\dot{M}_k]_{cond} + [\dot{M}_k]_{coag} + [\dot{M}_k]_{diffusion} \quad (k = 0,1,2)$$

where the source terms represent the net rate of production of the k-th moment due to nucleation, condensation, coagulation and diffusion.
The mean volume $v_g$ e volume standard deviation $\sigma_g$. could be calculated starting from the three moments as:

$$v_g = \frac{M_1^2}{M_0^{3/2} M_2^{1/2}} \qquad (4.11)$$

$$\ln^2 \sigma_g = \frac{1}{9} \ln\left(\frac{M_0 M_2}{M_1^2}\right) \qquad (4.10)$$

The k-th moment could be evaluated using the following approximation:

$$M_k = M_0 v_g^k \exp\left(\frac{9}{2} k^2 \ln^2 \sigma_g\right) \qquad (4.16)$$

Source terms for moment transport equation will be now explained. The Nucleation source term can be written as

$$[\dot{M}_k]_{\text{nucleation}} = I \cdot v_p^{*k} \quad (k = 0,1,2)$$

where I is the homogeneous nucleation rate e $v_p^*$ is the critical volume.

The source term related to condensation of vapour phase on the nanoparticle surface is given by

$$[\dot{M}_k]_{\text{condensation}} = \begin{cases} 0 & (k=0) \\ \xi_1 (S-1) M_{2/3} & (k=1) \\ 2\xi_1 (S-1) M_{5/3} & (k=2), \end{cases}$$

where

$$\xi_1 = v_{monomer} N_s (36\pi)^{1/3} \left(\frac{\sigma T}{2\pi m_{monomer}}\right)^{1/2} \qquad (4.14)$$

in which $m_{monomer}$ and $v_{monomer}$ are the mass and the volume of the gas monomer, respectively. $N_s$ is the concentration of the vapour particles in the saturation state at a given temperature T that is related to the vapour saturation pressure by $p_{sat} = N_s kT$. The source term due to coagulation is given by

$$[\dot{M}_k]_{\text{coagulation}} = \begin{cases} -\xi_2 \zeta_0 (M_{2/3} M_{-1/2} + 2M_{1/3} M_{-1/6} + M_{1/6} M_0) & (k=0) \\ 0 & (k=1) \\ 2\xi_2 \zeta_2 (M_{5/3} M_{1/2} + 2M_{4/3} M_{5/6} + M_{7/6} M_1) & (k=2), \end{cases}$$

where

$$\xi_2 = \left(\frac{3}{4\pi}\right)^{1/6} \left(\frac{6\sigma T}{\rho_p}\right)^{1/2} \qquad (4.18)$$

$$\zeta_0 = 0.633 + 0.092\sigma_g^2 - 0.022\sigma_g^3 \qquad (4.19)$$

$$\zeta_2 = 0.39 + 0.5\sigma_g - 0.214\sigma_g^2 + 0.029\sigma_g^3 \qquad (4.20)$$

The source term due to diffusion is given by

$$[\dot{M}_k]_{\text{diffusion}} = \nabla \cdot D_k \nabla M_k \quad (k = 0,1,2)$$

where laminar diffusion coefficients have been computed as

$$D_k = \begin{cases} \xi_3 v_g^{-1/3} \exp\left(\frac{1}{2}\ln^2\sigma_g\right) + \xi_4 v_g^{-2/3} \exp\left(2\ln^2\sigma_g\right) & \text{k = 0} \\ \xi_3 v_g^{-1/3} \exp\left(-\frac{5}{2}\ln^2\sigma_g\right) + \xi_4 v_g^{-2/3} \exp\left(-4\ln^2\sigma_g\right) & \text{k = 1} \\ \xi_3 v_g^{-1/3} \exp\left(-\frac{11}{2}\ln^2\sigma_g\right) + \xi_4 v_g^{-2/3} \exp\left(-10\ln^2\sigma_g\right) & \text{k = 2} \end{cases} \qquad (4.7)$$

where

$$\xi_3 = \frac{\sigma T}{3\pi\eta}\left(\frac{\pi}{6}\right)^{1/3} \qquad (4.8)$$

$$\xi_4 = \frac{\sigma T}{3\pi\eta} 3{,}314l\left(\frac{\pi}{6}\right)^{2/3} \qquad (4.9)$$

In addition, the vapour concentration must be solved simultaneously. The conservation equation of the vapour is written as follows

$$\boldsymbol{u} \cdot \nabla N_{\text{vapor}} = \nabla \cdot (D_{\text{vapor}} \nabla N_{\text{vapor}}) + \dot{N}_{\text{vapor}}.$$

The net production rate of the vapour is estimated using contributions from evaporation, nucleation, and condensation, as

$$\dot{N}_{\text{vapor}} = [\dot{N}_{\text{vapor}}]_{\text{evaporation}} - I \cdot \frac{v_p^*}{v_{\text{monomer}}} - \frac{[\dot{M}_1]_{\text{condensation}}}{v_{\text{monomer}}}$$

*Turbulence model*

Turbulence in plasma thermo fluid dynamics is usually modelled incrementing viscosity, conductivity and mass transport coefficients by adding turbulent terms; in nano-powder synthesis modelling, this is taken into account only for determining vapour behaviour, adding a turbulent term to the classical laminar diffusion coefficient:

$$D_{vap}^{tot} = D_{vap}^{L} + D_{vap}^{T}$$

The laminar term $D_{vap}^{L}$ of the total vapour diffusion coefficient $D_{vap}^{tot}$ is calculated by Hirschfelder's formula based on the Chapman-Enskog method, while the turbulent term is expressed by:

$$D_{vap}^{T} = \frac{\mu_T}{\rho Sc}$$

where $Sc$ is the Schmidt number, $\rho$ is the plasma density and $\mu_T$ is the turbulent viscosity, included in the flow calculations using the turbulence model.
This typical mass transport treatment is here extended to the particle diffusion model, where nano-powder total diffusion coefficient takes the form:

$$D_k^{tot} = D_k^L + D_k^T$$

where $D_k^L$ is the laminar diffusion coefficient of the k-th moment of the PSD.
The turbulent diffusion coefficient $D_k^T$ is expressed by:

$$D_k^T = \frac{\mu_T}{\rho Sc}$$

While particle diffusion can be modelled in analogy to vapour diffusion, it is not as easy for processes that involve interaction between various particles or between particles and vapour. A comparison between particle size and Kolmogorov's length scale $\boldsymbol{\mu}$ inside the reaction chamber has been carried out, the latter being a scale related to eddies size defined as:

$$\mu = \left( \frac{\nu^3}{\varepsilon} \right)^{1/4}$$

where $\nu$ is the effective viscosity and $\varepsilon$ turbulent dissipation rate.

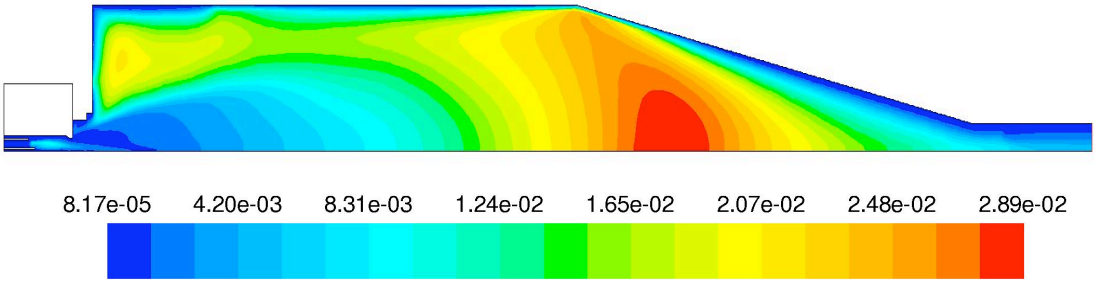


Fig. 2 - Kolmogorov's length scale (m) inside the computational domain.

According to the results shown in Figure 2, the characteristic eddies length is much larger than the expected nano-powders in the whole reaction chamber. This means that particles interacting with other or with vapour monomers are all subject to the same turbulent eddy, herein their relative movement is not modified and turbulence should be neglected in this regard.

According to the Kolmogorov's scale analysis previously discussed, turbulent effects are limited to the diffusion process, described in the moment method as:

$$[\dot{M}_k]_{diffusion} = \overline{\nabla} D_k^{tot} \overline{\nabla} M_k \quad (k = 0,1,2)$$

Nucleation, condensation and coagulation processes are not influenced by turbulence, hence the related source terms do not differ from their usual representation.

*Results*

The moment model for nanopowder synthesis has been applied first to a case considered as "reference" [50] to validate the model, and then to the realistic case of a laboratory scale ICPT system developed by EMPA (Switzerland)[16] to investigate in detail the physical processes occurring during the synthesis of nanopowders.

*Moment model validation*

First computations were carried out to validate the library written in C language that allows FLUENT to solve the equations for the transport of the three moments of the nanopowder PSD function. Comparisons have been made with previously published results by Girshick for the synthesis of Fe nanopowders in a cylindrical reaction chamber[50]. In figure 3 the mean diameter of synthetized nanopowders at the reactor outlet for different feed rates of the Fe micro-sized precursor has been reported. Good agreement has been obtained with results obtained by Girshick both from experiments and from modelling. Moreover, the obtained distribution of nanopowders inside the reaction chamber is similar to the one reported by Girshick (not shown). As reported by Girshick, some discrepancies arise from the comparison of experimental and modelling results: first of all, the effect of turbulence in the reaction chamber is to make more uniform the distribution of nanopowders along the radial dimension; if not taken into account in the model, as done by Girschick, the laminar flow results in a

strong radial dependence of the nano-powder PSD; second, it is still difficult to make comparison between mean diameter obtained from experiments and from modelling because different definitions of a mean diameter lead to strongly different results. Thus, the validation of our code is mostly on the basis of the comparison between our results and those of Girschick obtained through the same modelling approach.

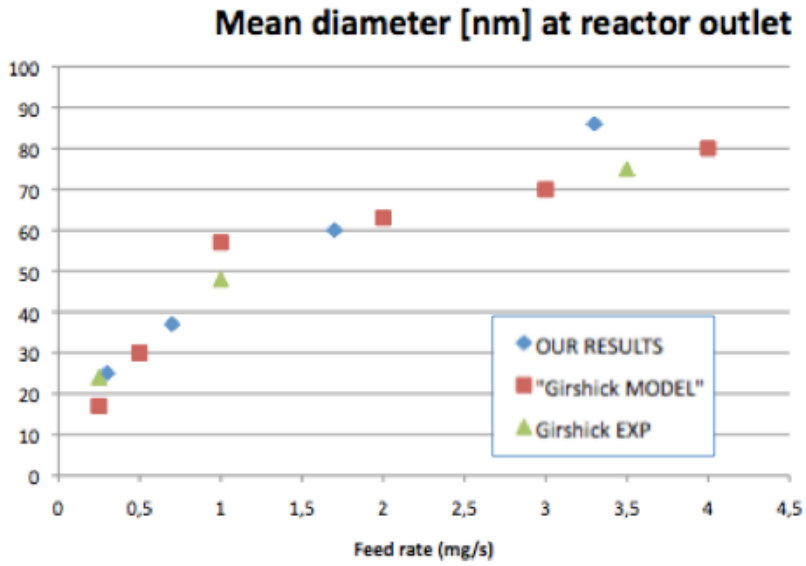


Fig. 3 – Validation of the model for nanopowder synthesis in thermal plasmas: comparison with results reported by Girshick et al.

*Silicon nanopowder synthesis in EMPA ICPT systems*

The validated code has been used to investigate the physical process undergoing in Si nanopowder synthesis in a realistic lab-scale ICPT systems developed at EMPA (Switzerland). The apparatus has been reported in figure 4. The computational domain has been assumed two-dimensional and axisymmetric. Two different reaction chamber configurations have been investigated: 1) without quenching ring; 2) with quenching ring. A schematic of the reaction chamber and of the quenching device has been reported in figure 4.

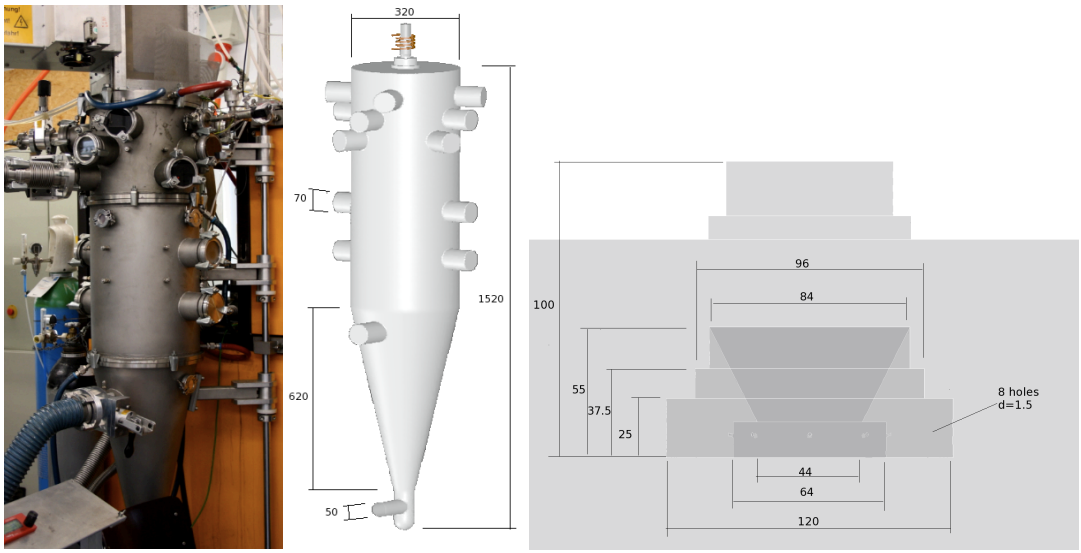


Fig. 4. Picture of the Empa ICPT system (left); computational model for the Empa reaction chamber (center) and quenching ring geometry (right). Dimensions in mm.

A preliminary computation has been carried out to calculate the thermo-fluid-dynamic field in the reaction chamber and the precursor evaporation for both the case with and without the quenching device. The operating conditions for the considered cases are reported here:

- Coupled power: 5 and 10 kW
- Coil current frequency: 13.56 MHz
- Sheath gas [slpm]: 60 Ar + 4.5 H2
- Plasma gas [slpm]:12 Ar
- Carrier gas [slpm]: 4 Ar
- Quenching gas [slpm]: 56 Ar
- Chamber pressure: 40 kPa

Results for the temperature field in the 10 kW case have been shown in figure 5. With the aid of the quenching device the plasma plume is strongly cooled resulting in high quench rate (see figure 5-c) whereas in the case without quench (figure 5-a) the cooling of the plasma tail is mainly due to turbulent heat diffusion to the chamber walls. In both cases a strong recirculating flow pattern is highlighted in the middle of the reaction chamber by streamlines (figure 5-b and 5-d). With the use of the quench ring, the recirculating pattern at the top of the chamber is enhanced.
Results for mean diameter of the synthetized Si nanopowders and for vapour consumption have been reported in figure 6. In the case without quench ring (figure 6-a), the nucleation of nanopowders occurs in the middle of the reaction chamber whereas with the quench ring the nucleation is concentrated inside the quench ring. This phenomenon can be seen in the vapour consumption field reported in figure 6. The mean diameter at the reactor outlet is greater in the case with quenching ring; even if these results contrast with the common opinion that the use of a quench ring leads to smaller nanopowders, the explanation of this fact relies on the position of the nucleation zone: in the case without quench ring, the powders nucleate in a region which is closer to the chamber outlet with respect to the case with quench ring and

they have less time to coagulate before leaving the chamber. This is demonstrated by results of simulations carried out without considering the coagulation process (figure 7), which result in a inverse trend: in the case without quench ring bigger primary nanopowders are produced with respect to the case with quench ring. Considering only nucleation and condensation as processes for the formation of nanopowders, the final mean diameter depends only on the quench rate, which is high in the case with quenching device, resulting in lower nanopowder mean diameter. Finally, when strong coagulation occurs, the position of the nucleation zone becomes important to determine the final particle mean diameter.
Similar conclusion can be drawn for the computations carried out with a lower power coupled to the torch, 5 kW (figures 8-11). However, with lower power the mean diameter at the reactor outlet is higher for the case of no quenching device also considering the coagulation process. The effect of turbulence on the synthesis of nanopowders has been shown in figure 11: a stronger diffusion of nanopowders results in a lower residence time and thus a lower diameter at the reactor outlet.

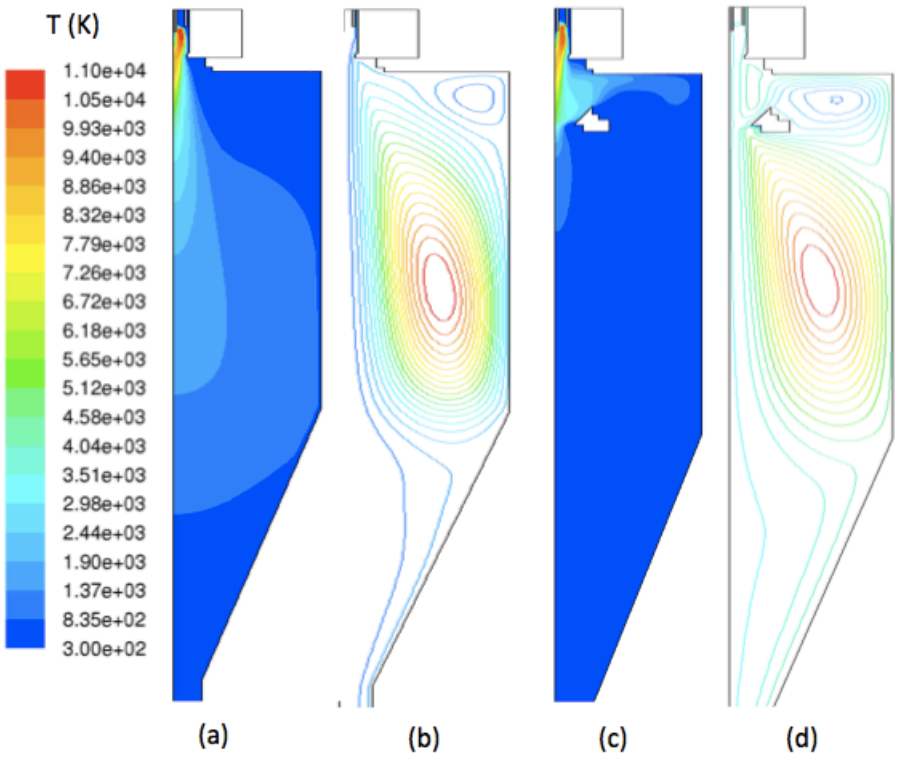


Fig. 5 – Temperature field in the reaction chamber for case without quench ring (a) and with quench ring (c); stream-function isolines for the case without quench ring (b) and with quench ring (d). Coupled plasma power = 10kW.

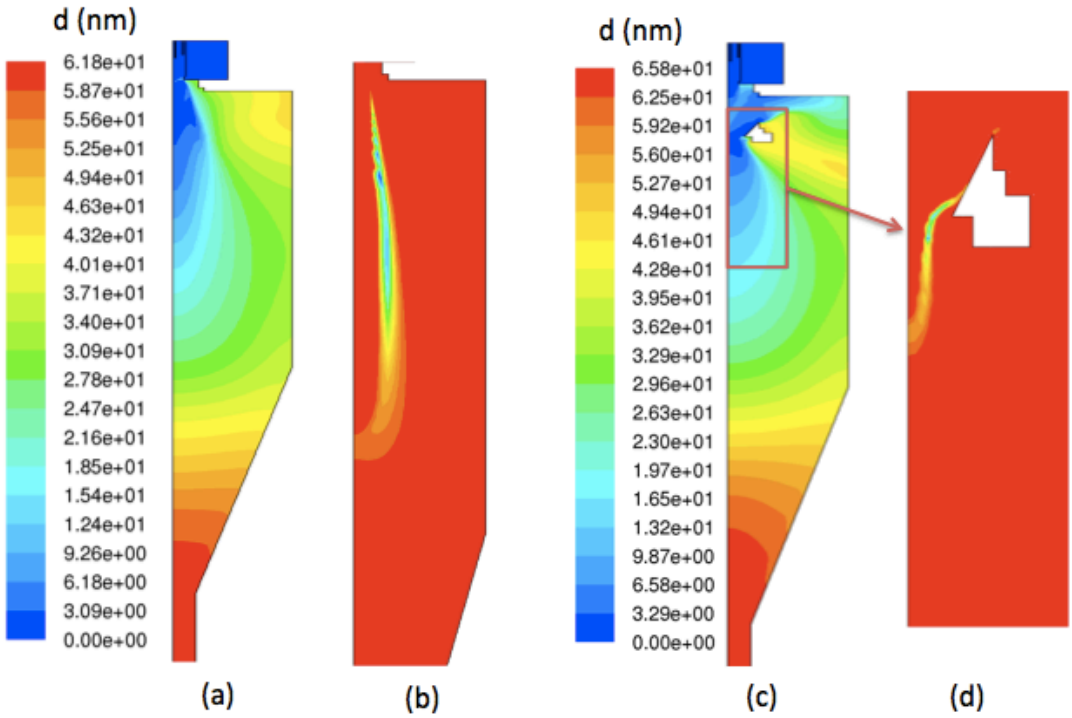


Fig. 6 – Mean diameter field in the reaction chamber for case without quench ring (a) and with quench ring (c); vapour consumption for the case without quench ring (b) and with quench ring (d). Coupled plasma power = 10kW.

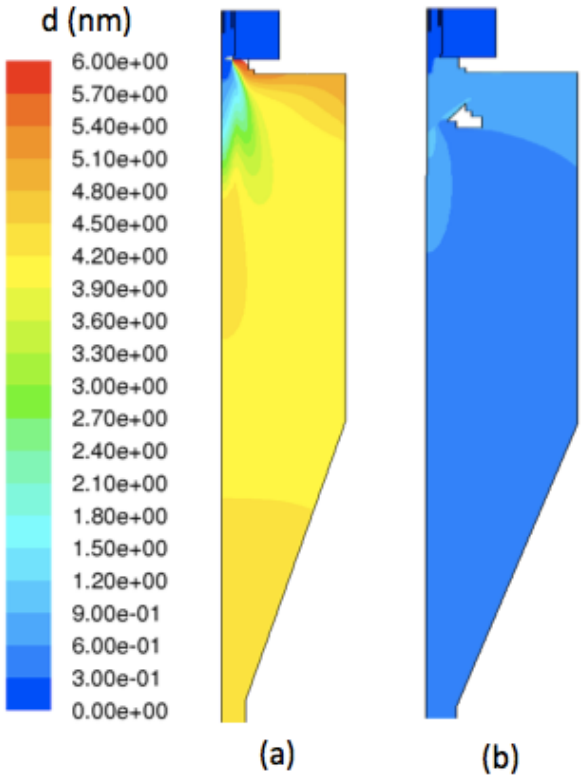


Fig. 7 – Mean diameter field in the reaction chamber for case without quench ring (a) and with quench ring (b) considering no particle coagulation. Coupled plasma power = 10kW.

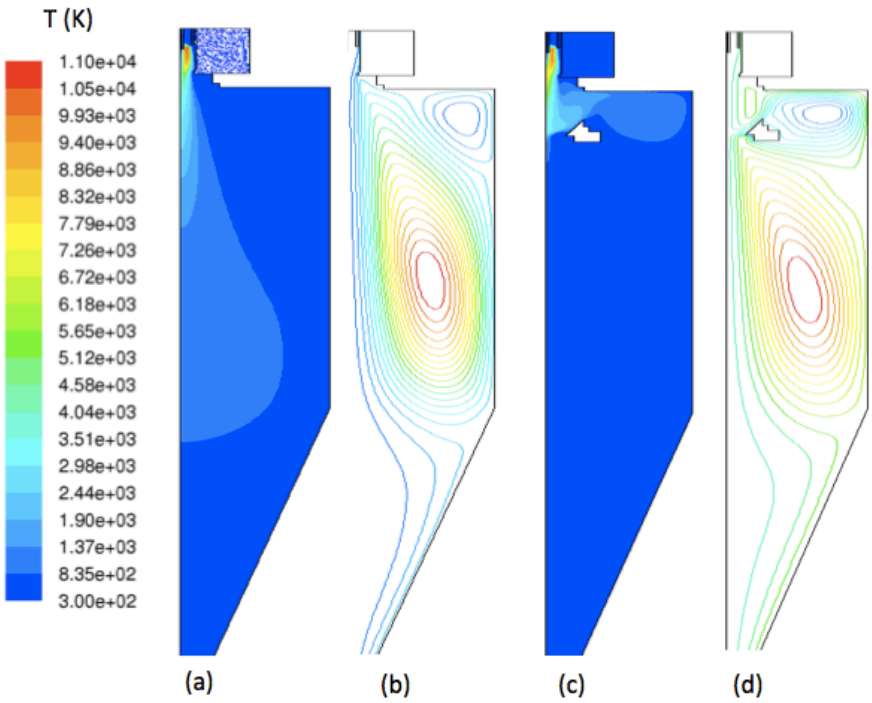


Fig. 8 – Temperature field in the reaction chamber for case without quench ring (a) and with quench ring (c); stream-function isolines for the case without quench ring (b) and with quench ring (d). Coupled plasma power = 5 kW.

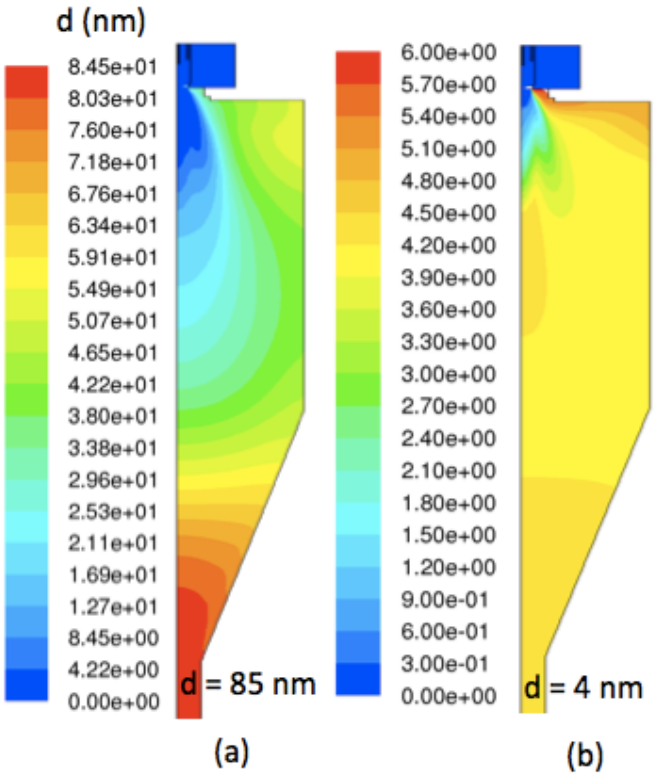


Fig. 9 – Mean diameter field in the reaction chamber for case without quench ring considering particle coagulation (a) and considering no particle coagulation (b). Coupled plasma power = 5 kW.

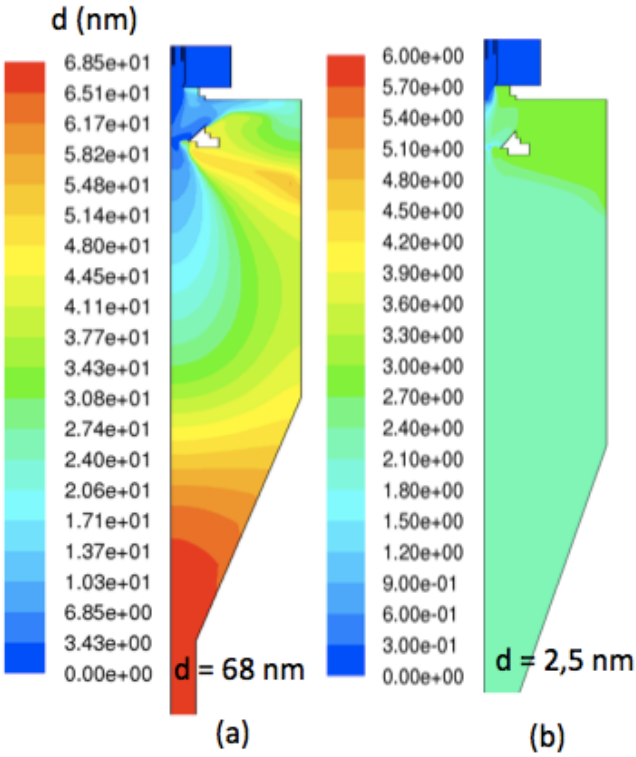


Fig. 10 – Mean diameter field in the reaction chamber for case with quench ring considering particle coagulation (a) and considering no particle coagulation (b). Coupled plasma power = 5 kW.

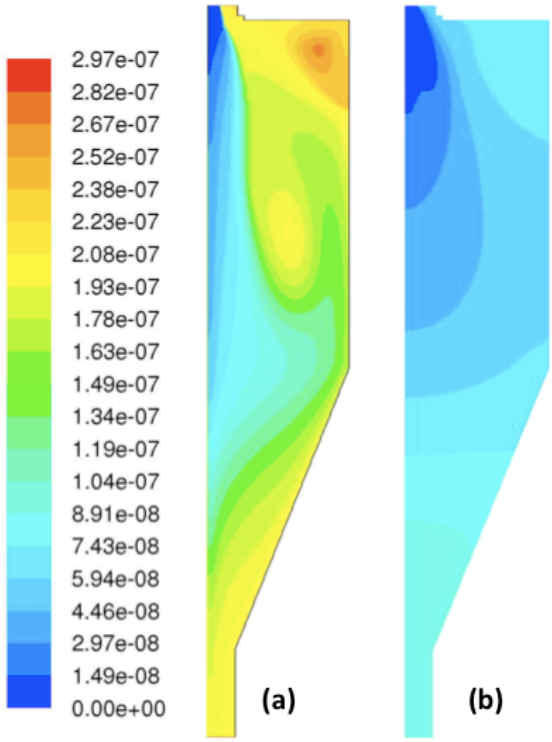


Fig. 11. Particle mean diameter (m) inside the reaction chamber without the quench ring without considering the effects of turbulence (a) and considering the effects of turbulence (b). Coupled plasma power = 5 kW.

**Charging effects on nanopowder synthesis in inductively coupled plasma torches**

In this study, which has been done in a collaboration between the *Research Group for Industrial Applications of Thermal Plasmas* and Prof. Valerian Nemchinsky, I considered particle-charging effects during nanopowder synthesis in RF thermal plasma torches.
During this process, the homogeneous nucleation of the precursor vapour occurs in the tail of the plasma jet, usually in regions with temperatures below 2000 K; in this region the LTE electron concentration is negligible, but a finite electron recombination rate could lead to a non-equilibrium (NLCE) composition and thus to a high degree of ionization. The effects of NLCE electron composition on particle charging have not been considered in previous works. However, this effect could be critical in the evaluation of the characteristic particle charging time, since the latter depends strongly on electron concentration.
The following main results have been obtained: 1) electron concentration in the reaction chamber is substantially higher than LTE concentration; 2) considering non-equilibrium electron concentration, it was found that nano-particles reach floating potential at the beginning of their trajectories and continue to be in equilibrium at local floating potential along their trajectories; 3) coagulation is affected by particle charging resulting in a lower collision rate with respect to the "no-charging" case and thus a lower mean particle diameter and lower diameter dispersion at the outlet of the reactor.

*Non-equilibrium electron concentration*

We assume that electrons are in chemical equilibrium upon exiting discharge zone. In that zone, ionization is balanced by recombination [29]:

$$\alpha n_e n_a = \beta n_e^3 \qquad (1)$$

Once the plasma exits the discharge zone, temperature drops and ionization equilibrium fails. Downstream the discharge zone, in reaction zone, the electron concentration is described by equation

$$v\frac{dn}{dx} = \alpha n - \beta n^3 \qquad (2)$$

Since ionisation coefficient a depends on temperature in a very strong way, ionization drops almost instantly as temperature decreases. Therefore, one can neglect ionisation in reaction zone . Electron concentration for different given temperature axial profiles can be obtained by solving the following equation:

$$\frac{dn}{dx} = -\frac{\beta(T)n^3}{v} \qquad (3)$$

Above, n is the electron concentration, v is the plasma velocity and β is the three-body or pure argon.
We kept axial velocity fixed at 80 m/s.

We obtained a high degree of chemical non-equilibrium for typical reaction chamber temperature profiles (figure 2). Similar results have been obtained also by Murphy 2007a.

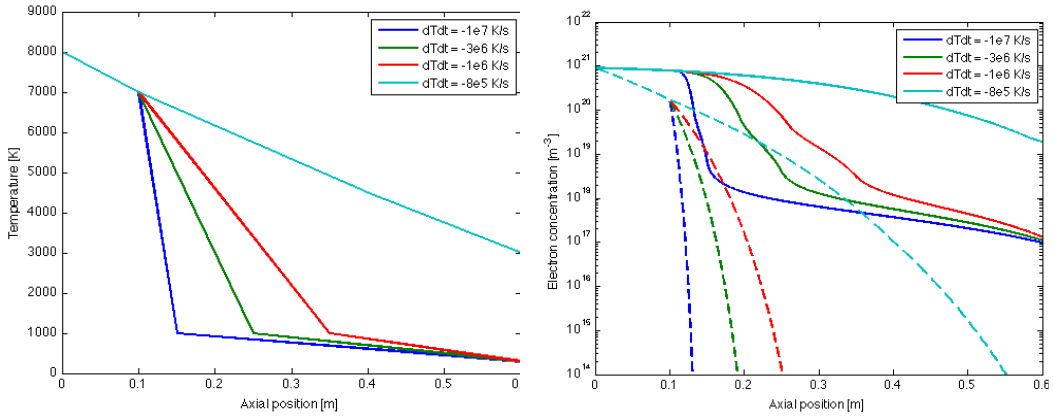


Fig. 1 - Temperature (left) and electron density (right) axial profile for different quenching rates considered. Dashed lines represent LTE electron concentrations.

Besides of three-body (electron-ion-electron) "homogeneous" recombination, we also considered "heterogeneous" recombination on the surface of nanoparticle: electrically insulated nanoparticle, being at floating potential (we will see that this condition holds almost throughout the whole particles trajectory), collects equal fluxes of ions and electrons. They recombine on particle's surface. Effectiveness of this type of recombination is different in different parts of the reaction zone. Effectiveness follows the value of the combined surface of the all the particles in unit volume. It is low close to the exit from the discharge zone, because of low particles density there. The effectiveness increases as the density of particles increases downstream. Even further downstream, the effectiveness of "heterogeneous" recombination could drop again as particles become larger and their combined surface decreases.

*Ion and electron fluxes to particle. Floating potential*

Nanoparticles that are created in reaction zone are exposed to electron and ion fluxes. Particle charging process can be modelled in the free-molecular assumption, since particle size is very low in comparison with electron and ion's mean-free-paths. The classical probe theory can be used to calculate electron and ion current densities to the particle:

$$j_e = n\bar{v}_e \exp(\frac{-eV}{kT})$$
$$j_i = n\bar{v}_i \times (1 + eV/kT) \qquad (4)$$

where V is the particle potential. (Hereafter potential of a negatively charged particle considered as "positive" potential)
Electrons, due to their higher mobility, are more effective in charging. Therefore, initially particles attain negative charge. The potential of the particles increases and electron flux to it decreases until electron and ion flux become equal. At this moment

on, the potential of the particles (floating potential) quits changing. The floating potential, as could be seen from (4), depends on plasma temperature only:

$$V_{float} = T \times ln\left[\frac{\sqrt{M/m}}{1+V_{float}/T}\right]^{1}$$

After this initial charging, the particle could additionally be charged with electrons or discharged by ions during its flight as the size of the particles and gas temperature change in the reaction zone.

*Effects of particle charging in coagulation*

In this section, we estimated the effect of particle charge on its formation assuming that particle is at local floating potential. Validity of this assumption is checked in the next section. It is shown there that this assumption is well justified when electron density is relatively high, $n \sim 10^{18}\ m^{-3}$. It is not justified at low electron density $n \sim 10^{15}\ m^{-3}$. This case needs special, self-consistent consideration.

To take into account the effect of charged particles on coagulation rate, we used the following exponential term in the collision rate for the free-molecular regime:

$$\alpha = exp(-\frac{Q^2}{8\pi\varepsilon RkT})$$

where Q is the particle charge at floating potential. (Where is the equation?) As mentioned above, the particle charge was calculated according its local floating potential and size:

$$Q = 4\pi\varepsilon R V_{float}$$

A sectional method [51] has been used to accurately calculate particle size distributions including the effects on coagulation of particle charging. Results of these calculations are shown in Fig. 4 (mean diameter of particles) and Fig. 5 (standard deviation of diameter to average diameter ratio). One can see:

a) Effect of particle charging leads to a substantial decrease of their size at the exit of reaction chamber. In the considering case, the effect is twofold.
b) Charged particles size distribution is narrower than corresponding distribution of non-charged particle.

[1] This equation can be easily solved by iteration. For Ar, solution gives: $V_{float}/T=4.0$

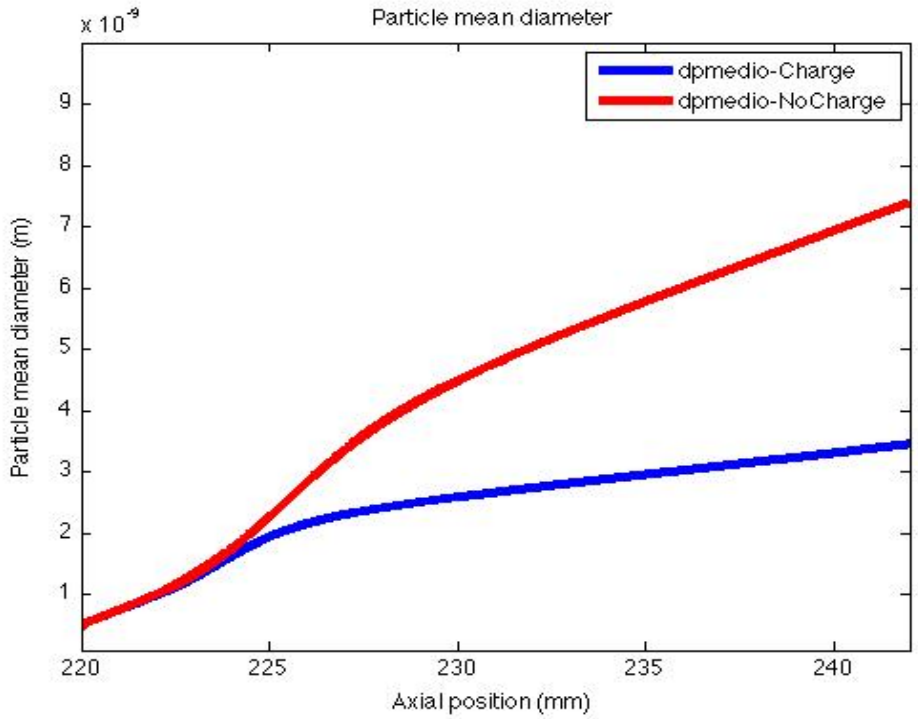


Fig. 2 - Particle size with and without considering charging effects for the case with dT/dt = -4e5 K/s. Molybdenum with initial vapour pressure of 50 Pa.

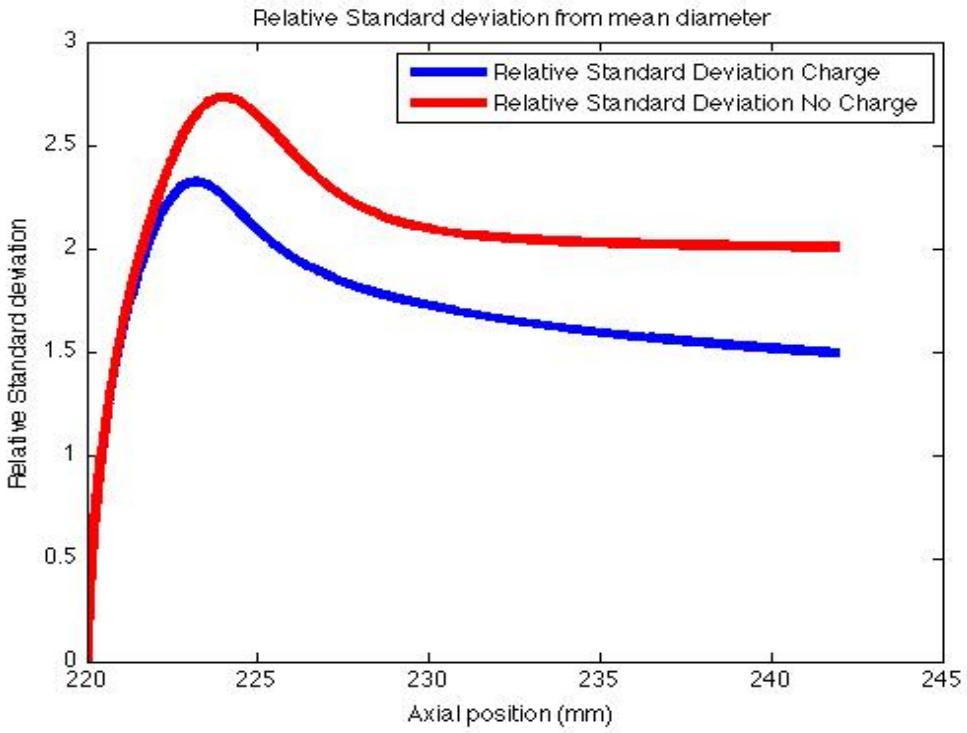


Fig. 3 - Particle size standard deviation DR/R with and withut considering charging effects for the case with dT/dt = -4e5 K/s. Molybdenum with initial vapour pressure of 50 Pa.

*Kinetics of nano-particle charging*

In this section, we consider particle charging in average approach: It is assumed that all the particles can be characterized by average radius $R_p(x)$ and density $N_p(x)$. Theses parameters are changed along the gas flow due to nucleation, condensation and coagulation.
Charge of a particle and its potential are connected in a standard way:

$$V = \frac{Q}{C} = \frac{Q}{4\pi\varepsilon R} \qquad (5)$$

Let us proceed to the kinetic of particle charging.

The total electric charge in a unit of volume is $Q_{total}=QN_p=4peR_pN_pV$. It changes along the trajectory

$$v\frac{dQ_{total}}{dx} = v\frac{d}{dx}\left[4\pi\varepsilon R_p N_p V\right] = 4\pi N_p R_p^2\left[j_e - j_i\right] \qquad (6)$$

From here, we find how the average potential of the particle changes along the trajectory

$$v\frac{dV}{dx} = -v\frac{V}{R_p}\frac{dR_p}{dx} - v\frac{V}{N_p}\frac{dN_p}{dx} + \frac{R_p}{\varepsilon}\left[j_e(V) - j_i\right] \qquad (7)$$

Functions $R_p(x)$, $N_p(x)$ depend on particle potential V(x). Therefore, generally speaking, the equations for $R_p$, $N_p$ and V should be solved simultaneously, in a self-consistent way. This is a difficult task. To estimate the importance of the considered effect of particle charging, we made the following simplification.
Functions $R_p(x)$ and $N_p(x)$ obtained in the previous section were used in solving equation (7 ) for potential of an average particle . With thus obtained function V(x), the validity of our a priory assumption on particles potential can be checked. Comparisons of particle potential (green lines) and local plasma potential are presented in Fig. 6 ($n=10^{18}m^{-3}$) and Fig.7 ($n=10^{15}m^{-3}$). One can see that in case of relatively high electron concentration, the particles achieve the local floating potential very soon and keep it updated during the rest of the trajectory. The situation with lower electron density is more complicated. This case needs self-consistent consideration of V,$R_p$, and $N_p$ distributions.

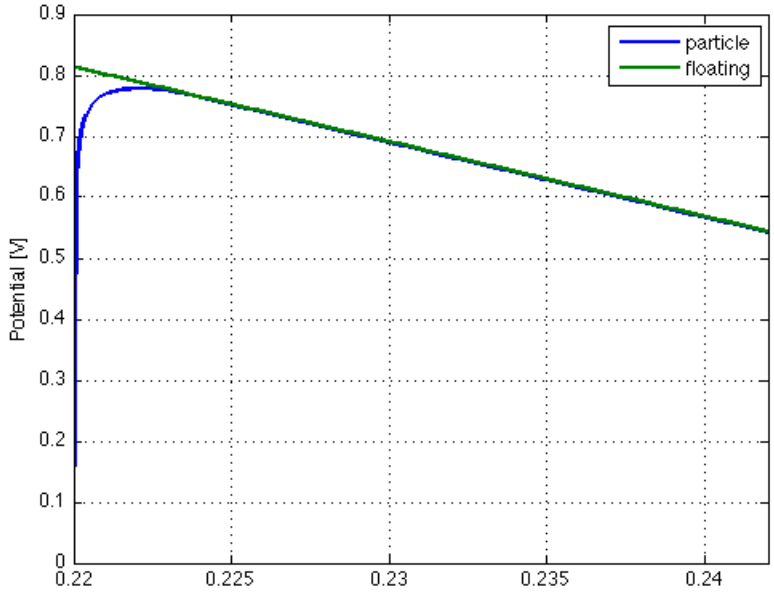


Fig. 4 - Local plasma potential (blue line) and particle potential (green line). $n=10^{18}$ $m^{-3}$.

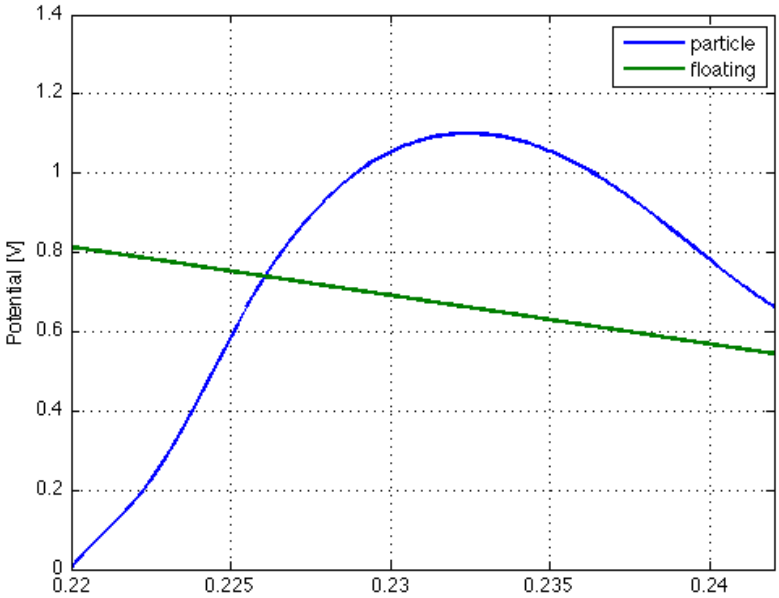


Fig. 5 - Local plasma potential (blue line) and particle potential (green line). $n=10^{15}$ $m^{-3}$.

## Conclusions

A fully three-dimensional model of a commercial ICP torch with laboratory scale reaction chamber has been developed using a commercial CFD software (FLUENT). Numerical results, which completely characterize the electromagnetic and thermo-fluid-dynamic behaviour of the system, are presented for an atmospheric pressure argon-hydrogen mixture using the RNG k-ε turbulence model and the combined diffusion approach of Murphy. Two different cases have been considered with different coil current frequency (3 MHz and 13.56 MHz), the other operating conditions being fixed (mass flow rates, total Joule power dissipated, inlet gas composition).
This approach has allowed a deeper insight in the three-dimensional effects of the coil current frequency: non-axisymmetric velocity, temperature, Joule dissipation and Lorentz force fields have been found for current frequency equal to 3 MHz, whereas for the case at higher frequency the discharge in the torch is almost axisymmetric.
At higher frequency, the lower absolute value of Lorentz forces and the smaller volume of the discharge where they are applied, induces a lower unbalance between the force exerted on the discharge by the first and the last coil turn; thus, it is argued that fluid-dynamic inertia prevails over the torque applied to the discharge by the coil and the resulting temperature field is more axisymmetric.
Moreover, the distribution of hydrogen mass fraction inside the torch and inside the reaction chamber has been accurately predicted, in agreement with previous works which accounted for demixing effects in thermal plasmas.
Different diffusion mechanisms have been investigated, considering the effects on mass fraction field of thermal diffusion due to mole fraction gradients and temperature gradients.
Finally, the temperature field in the reaction chamber has been simulated: its three-dimensional shape has been correlated to different types of recirculation flow arising when a non-axisymmetric reaction chamber, which include a lateral outlet tube, is used.

Predictions of the trajectory and thermal history of spherical particles injected into the inductively coupled plasma torch and the reaction chamber have been performed taking into account the effects of coupling between particles and plasma and the turbulent dispersion of the particles, in the frame of a stochastic approach.
Two cases have been considered in which the frequency has been set at 3 MHz and 13.56 MHz, respectively. Moreover, computations have been carried out for different values of the powder feed rate and of the axial position of the probe.
Numerical results reported in this study have shown that particle trajectories are strongly influenced by the thermo-fluid-dynamic field: for the cases with frequency set at 3 MHz, a non-axisymmetric velocity field induces non-axisymmetric particle trajectories, whereas an axisymmetric stream of particle has been predicted for higher frequency because, in this case, fluid-dynamic inertia prevails over unbalanced Lorentz forces due to three-dimensional shape of the coil resulting in an almost axisymmetric velocity field.
For the cases with lower frequency a higher heat flux to the particles has been obtained inside the torch, resulting in higher particle temperatures; on the contrary, in the reaction chamber for the case at 3 MHz the plasma temperature is generally lower than for the case at 13.56 MHz, inducing lower heat flux to particles. The net effect is that for the case at lower frequency the energy transferred to the particles is higher.

Plasma cooling due to loading effect is less pronounced for the case at 3 MHz than for the one at 13.56 MHz, since in the first case powders are injected in the hot core of the plasma where Joule dissipation balances the plasma-particle heat losses; for the case at 13.56 MHz the lower skin depth induces a Joule distribution concentrated near the torch walls, resulting in a central region where the plasma-particle cooling is balanced only by conduction: this leads to a higher loading effect. The same behaviour has been obtained for the cases with probe tip shifted towards the torch outlet (thus towards the plasma tail where there is no Joule dissipation).

A numerical model for the prediction of aerosol growth in plasmas has been developed in the framework of FLUENT and it has been applied to the case of nanoparticle synthesis in Inductively coupled plasma torches with reaction chamber.

From our estimation it seems that non-equilibrium electron concentration play a decisive role in determining the nanoparticles charging process, leading to negatively charged particles. This has not been highlighted in previous works. We estimated that the effect of particle charging on the coagulation process could be substantial, leading to an overestimation of the particle mean radius when neglecting particle charging. However, electron emission by thermo-ionic effect, which has been neglected in this study, has to be considered in future calculations because if particles nucleate in a high temperature region it could result even in positively charged particles.

Accurate modelling of devices characterized by inherently non-axisymmetric geometries such as inductively coupled plasma torches, requires the implementation of three-dimensional codes to analyse the magnitude of non-axisymmetric effects on plasma properties arising under different operating conditions.
This is true in particular for the modelling of powder treatment processes such as powder spheroidization and nano-particles production, since the behaviour of injected raw materials and of nucleated aerosols in the reaction chamber depends strongly on temperature and velocity fields.

References


1. ANSYS, *ANSYS FLUENT 12.0 Theory guide*. (Canonsburg, Pennsylvania, USA, 2009).
2. V. Colombo and et al., Journal of Physics D Applied Physics **43** (10), 105202 (2010).
3. V. Colombo, E. Ghedini and P. Sanibondi, Plasma Sources Science and Technology **19** (6), 065024 (2010).
4. M. I. Boulos, Pure Appl. Chem. **68** (5), 1007 (1996).
5. Z. Karoly and J. Szepvolgyi, Powder Technology **132** (2-3), 211-215 (2003).
6. R. Ye, T. Ishigaki, J. Jurewicz, P. Proulx and M. I. Boulos, Plasma Chemistry and Plasma Processing **24** (4), 555-571-571 (2004).
7. V. Colombo, E. Ghedini, G. Masini, D. Russo, F. Andreola, L. Barbieri, D. Belviso, I. Lancellotti and P. Pozzi, High Temp. Mater. Process. **10** (2), 207 (2006).
8. J. Amouroux, D. Morvan, S. Cavadias, P. Adam, M. Gonnord, K. Coulibaly, A. Vincent, S. Morel, F. Daou, S. Ognier, P. Rousseau and L. Martin, Technical Physics **50** (5), 603-612 (2005).
9. A. B. Murphy, M. I. Boulos, V. Colombo, P. Fauchais, E. Ghedini, A. Gleizes, J. Mostaghimi, P. Proulx and D. C. Schram, High Temperature Material Processing **12**, 255-336 (2008).
10. G. Schiller, M. Muller and F. Gitzhofer, J. Therm. Spray **8** (3), 389 (1999).
11. K. Shinoda, Y. Kojima and T. Yoshida, J. Therm. Spray Technol. **14** (4), 511 (2005).
12. C. M. Hollabaugh, D. E. Hull, L. R. Newkirk and J. J. Petrovic, J. Mater. Sci. **18** (11), 3190 (1983).
13. T. Uesugi, O. Nakamura, T. Yoshida and K. Akashi, J. Appl. Phys. **64** (8), 3874 (1988).
14. T. Kameyama, K. Sakanaka, A. Motoe, T. Tsunoda, T. Nakanaga, N. I. Wakayama, H. Takeo and K. Fukuda, J. Mater. Sci. **28** (17), 4630 (1993).
15. J. Y. Guo, F. Gitzhofer and M. I. Boulos, J. Mater. Sci. **30** (22), 5589 (1995).
16. J. W. Shin, H. Miyazoe, M. Leparoux, S. Siegmann, J. L. Dorier and C. Hollenstein, Plasma Sources Science and Technology **15** (3), 441 (2006).
17. R. Ye, J. G. Li and T. Ishigaki, Thin Solid Films **515** (9), 4251 (2007).
18. S. Siegmann and et al., High Temp. Mater. Process. **12**, 205 (2008).
19. T. B. Reed, J. Appl. Phys. **32** (5), 821 (1961).
20. M. P. Freeman and J. D. Chase, J. Appl. Phys. **39** (1), 180 (1968).
21. H. U. Eckert, J. Appl. Phys. **41** (4), 1520 (1970).
22. M. I. Boulos, Pure Appl. Chem. **57** (9), 1321 (1985).
23. P. Proulx, J. Mostaghimi and M. I. Boulos, Plasma Chem. Plasma Process. **7** (1), 29 (1987).
24. Y. Bartosiewicz, P. Proulx and Y. Mercadier, J. Phys. D: Appl. Phys. **35** (17), 2139 (2002).
25. K. Chen and M. I. Boulos, J. Phys. D: Appl. Phys. **27** (5), 946 (1994).
26. J. Mostaghimi, P. Proulx and M. I. Boulos, J. Appl. Phys. **61** (5), 1753 (1987).
27. N. Atsuchi, M. Shigeta and T. Watanabe, Int. J. Heat Mass Transfer **49** (5-6), 1073 (2006).
28. Y. Tanaka, J. Phys. D: Appl. Phys. **37** (8), 1190 (2004).
29. Y. Tanaka and T. Sakuta, J. Phys. D: Appl. Phys. **35** (5), 468 (2002).

30. R. Ye, T. Ishigaki, H. Taguchi, S. Ito, A. B. Murphy and H. Lange, Journal of Applied Physics **100** (10), 103303-103310 (2006).
31. A. B. Murphy, Physical Review E **48** (5), 3594 (1993).
32. A. B. Murphy, Journal of Physics D: Applied Physics **34** (20), R151 (2001).
33. P. Rini, D. Van den Abeele and G. Degrez, J. Thermophys. Heat Transfer **20** (1), 31 (2006).
34. D. Bernardi, V. Colombo, E. Ghedini and A. Mentrelli, The European Physical Journal D - Atomic, Molecular, Optical and Plasma Physics **22** (1), 119-125 (2003).
35. D. Bernardi, V. Colombo, E. Ghedini and A. Mentrelli, The European Physical Journal D - Atomic, Molecular, Optical and Plasma Physics **25** (3), 279-285 (2003).
36. S. Xue, P. Proulx and M. I. Boulos, Plasma Chem. Plasma Process. **23** (2), 245 (2003).
37. D. Bernardi, V. Colombo, E. Ghedini, A. Mentrelli and T. Trombetti, Plasma Science, IEEE Transactions on **33** (2), 424-425 (2005).
38. V. Colombo, E. Ghedini and J. Mostaghimi, IEEE Transaction on Plasma Science **36** (4), 1040-1041 (2008).
39. X. Fan, E. Gitzhofer and M. I. Boulos, J. Therm. Spray Technol. **7** (2), 247 (1998).
40. J. D. Ramshaw and C. H. Chang, Physical Review E **53** (6), 6382 (1996).
41. T. Watanabe and N. Sugimoto, Thin Solid Films **457** (1), 201 (2004).
42. T. Watanabe, M. Shigeta and N. Atsuchi, Int. J. Heat Mass Transfer **49** (25-26), 4867 (2006).
43. S. Xue, P. Proulx, A. B. Murphy and M. I. Boulos, Proc. 17th Int. Symp. on Plasma Chemistry (2005).
44. X. Chen, M. Sugasawa and N. Kikukawa, J. Phys. D: Appl. Phys. **31** (10), 1187 (1998).
45. R. Ye, A. B. Murphy and T. Ishigaki, Plasma Chem. Plasma Process. **27** (2), 189 (2007).
46. V. Colombo, E. Ghedini and P. Sanibondi, Journal of Physics D: Applied Physics **42** (5), 055213 (2009).
47. J. J. Beulens, D. Milojevic, D. C. Schram and P. M. Vallinga, Phys. Fluids **3** (9), 2548 (1991).
48. D. Bernardi, V. Colombo, E. Ghedini and A. Mentrelli, The European Physical Journal D - Atomic, Molecular, Optical and Plasma Physics **25** (3), 271-277 (2003).
49. S. K. Friedlander, Smoke, Dust and Haze, Fundamentals of Aerosol Dynamics (2000).
50. S. L. Girshick, C. P. Chiu, R. Muno, C. Y. Wu , L. Yang, S. K. Singh and P. H. McMurray, J. Aerosol Sci. **24** (3), 367-382 (1993).
51. M. Shigeta and T. Watanabe, Thin Solid Films **515** (9), 4217 (2007).

# SIMBA - SCALING-UP OF ICP TECHNOLOGY FOR CONTINUOUS PRODUCTION OF METALLIC NANOPOWDERS FOR BATTERY APPLICATIONS

During my Ph.D. course, I participated to the European research project SIMBA - "Scaling-up of ICP technology for continuous production of Metallic nanopowders for Battery Applications" – Call identifier: FP7-NMP-2008-2.1-2 where the University of Bologna has been involved as leader in the work-package on the modelling of induction plasma sources.
My contribution to these activities has been both on the development of models for the fluid-dynamic simulations of lab-scale ICPT systems and on the design of a new reaction chamber for the optimization of nanopowder synthesis process. In particular, I calculated thermodynamic and transport properties for typical plasma mixtures used in nanopowder synthesis and I implemented a 3D non-equilibrium model for fluid-dynamic simulation of ICPTs. Moreover, I tested different turbulence models implemented in ANSYS FLUENT with the final aim of choosing which one better reproduce experimental enthalpy probe measurements. These studies have been done in collaboration with A. Concetti[1]. In the following paragraphs, some of the results obtained in this research field have been reported.

## Description of the SIMBA project

Although nanotechnology, and particularly the development of nanoparticles-based materials, has advanced rapidly in recent years, industrial production techniques have not kept pace. At this point there is a substantial need for safe production facilities, enabling the synthesis of large amounts of metallic nanoparticles with controlled and uniform quality (particle size, particle size distribution, chemical composition, etc.). The SIMBA project will respond to this need by developing an industrial production line including on-line monitoring systems, assuring at the same time a high quality of the synthesized product as well as safety for the operating personnel and surrounding environment. The nano-structured materials of interest for this project are silicon and silicon-based alloyed nanoparticles, which have a huge potential as anode material in battery applications.
The production technology proposed is the Inductively Coupled Plasma (ICP) technique, which generates a high temperature thermal plasma discharge at atmospheric pressure. Since most of the ICP processes currently available are batch processes, the core of this project is the transfer of the ICP towards an industrial scale permitting the continuous production of a wide range of semiconductor or metallic (alloyed) nanoparticles. In order to achieve this, major scientific breakthroughs are required such as the incorporation of a novel on-line functionalization technique, the design of an industrial powder injection system to ensure a continuous production, on-line monitoring techniques to ensure quality and safety and advanced modelling of the particle trajectories in the ICP plasma.

The resulting industrial production line will provide maximum production efficiency by virtue of fully automated and controlled feeding of raw materials and optimal reactor processing including evacuation of the processed powders. An additional advantage of this industrial line will be the recovery and recycling of excess precursor components and gases. The overall objective of this project is to transfer the ICP processing knowledge and technology investigated at a lab-scale (10-100 g/h) to an industrial scale apparatus for the continuous production of tailored oxygen-free Si-based nanopowders at a production rate between *1 and 10 kg/hour*.
The *modelling* of the plasma flow dynamics and particle trajectories will permit to define the process at different scales, to predict the influences of the main process parameters and to design an optimum reactor chamber to increase the flow of particles for collection.

## Characterization of the lab-scale ICPT system at EMPA

The first task addressed within the SIMBA project was the development of codes for the fluid-dynamics simulation of induction plasma sources with reaction chamber operated under soft vacuum (40kPa – 60kPa) and with argon-hydrogen mixture of gases.

### *Calculation of plasma properties for mixtures used for nanopowder synthesis*

Thermodynamic and transport properties of argon-hydrogen mixtures have been calculated for different operating pressure and different relative concentrations of the two gases[2-9]; calculation have been carried out also for thermal non-equilibrium conditions, i.e. when the electron temperature is higher than the one of atomic and molecular species. Non-equilibrium conditions were expected in the tail of the plasma discharge in case a cold stream of gas is injected to quench the supersaturated vapour coming from the plasma torch during nanopowder synthesis. Moreover, since the evaporated precursor is expected to modify the thermodynamic and transport coefficients of the mixture, the vapour (Si) has been included in the computation of plasma properties. Some results are reported below.

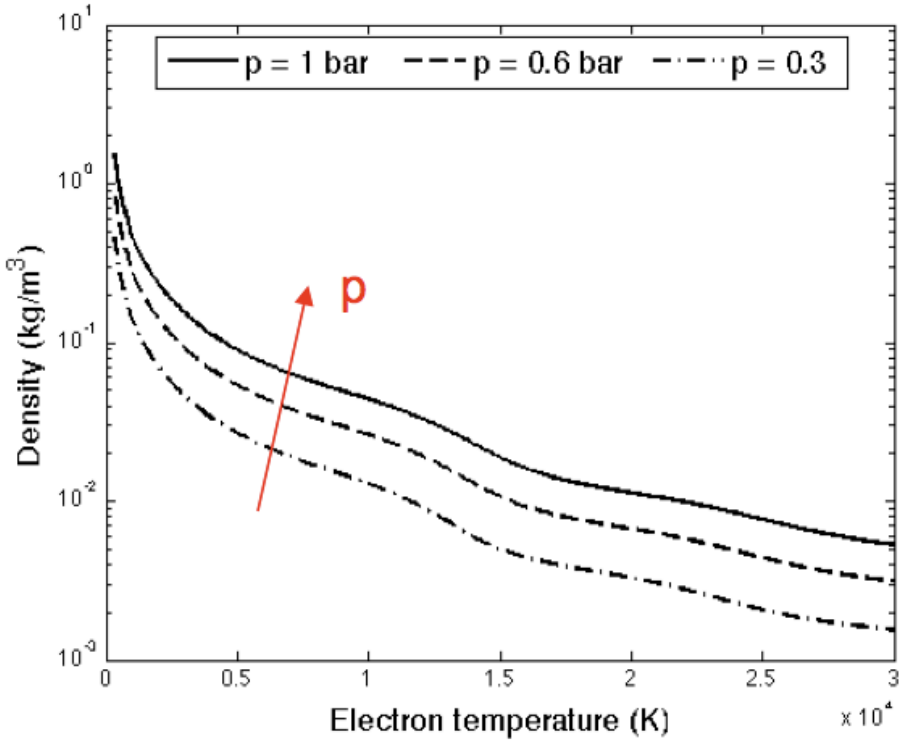


Fig. 1 – Temperature dependence of the density for a 50% Ar - 50% H2 mixture for different value of the pressure.

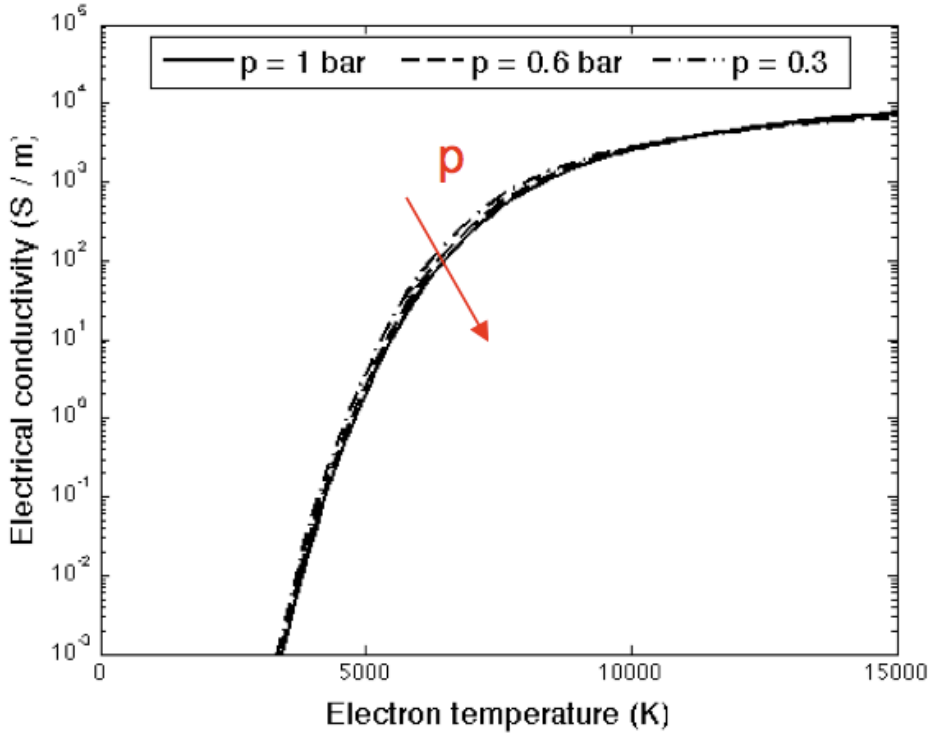


Fig. 2 – Temperature dependence of the electrical conductivity for a 50% Ar - 50% H2 mixture for different value of the pressure.

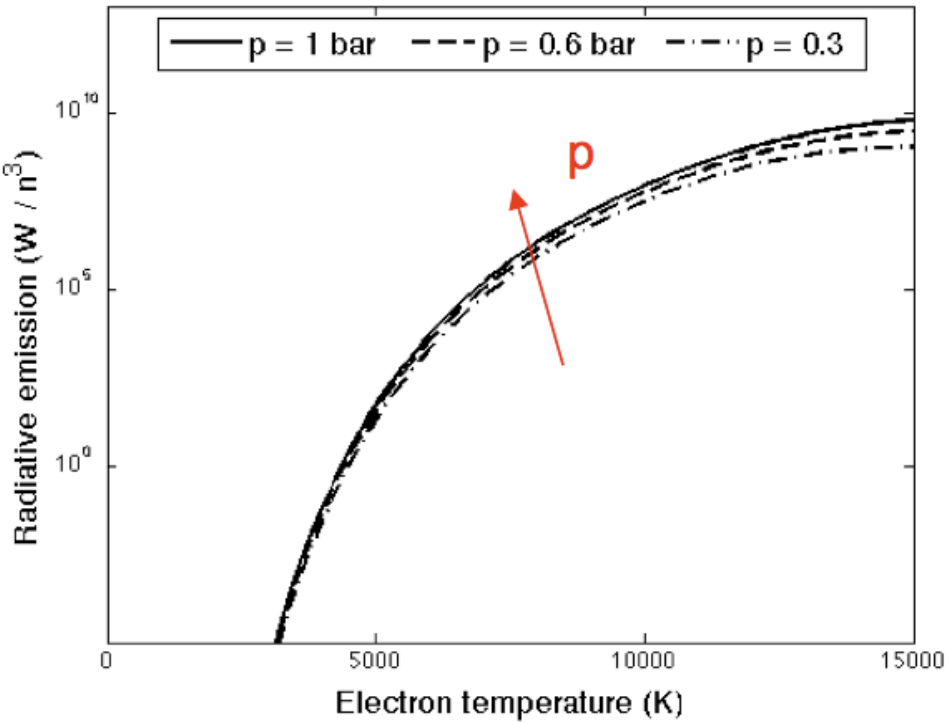


Fig. 3 – Temperature dependence of the radiative emission for a 100% Ar mixture for different value of the pressure.

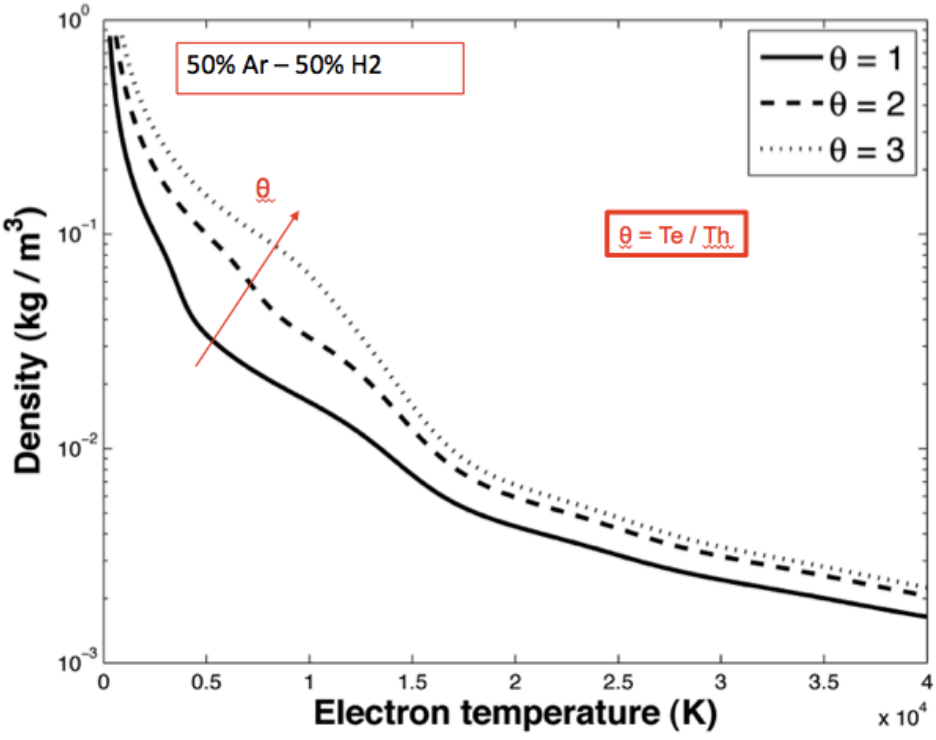


Fig. 4 – Temperature dependence of the density for a 50% Ar - 50% H2 mixture for different value of the non-equilibrium parameter.

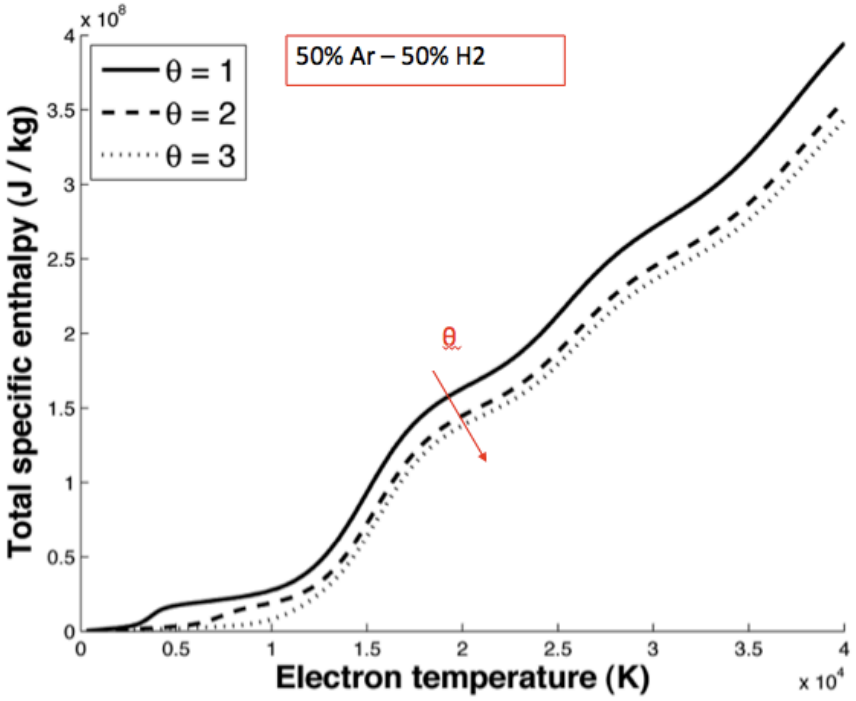


Fig. 5 – Temperature dependence of the total specific heat for a 50% Ar - 50% H2 mixture for different value of the non-equilibrium parameter.

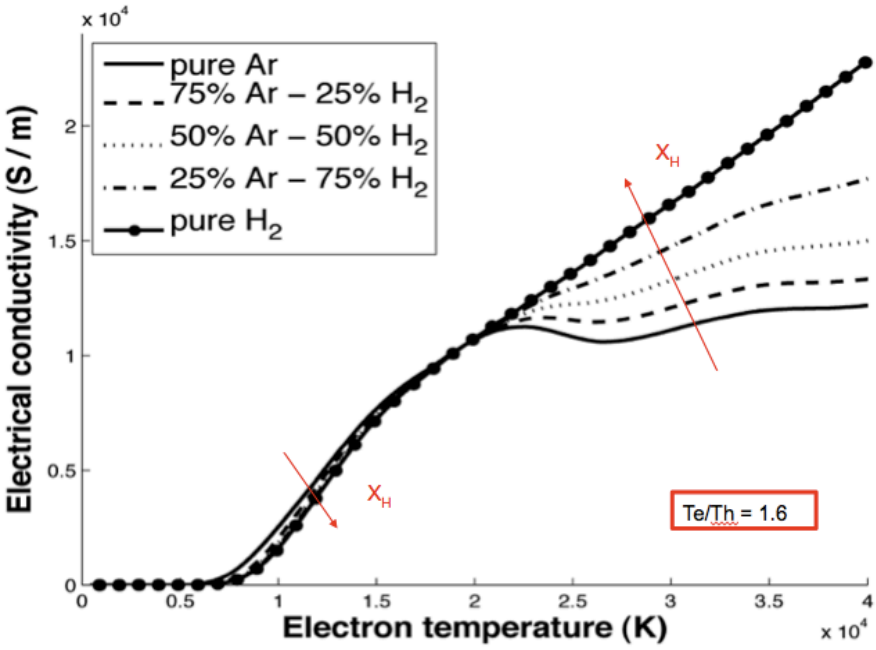


Fig. 6 – Temperature dependence of the electrical conductivity for different Ar-H2 mixtures in thermal non-equilibrium.

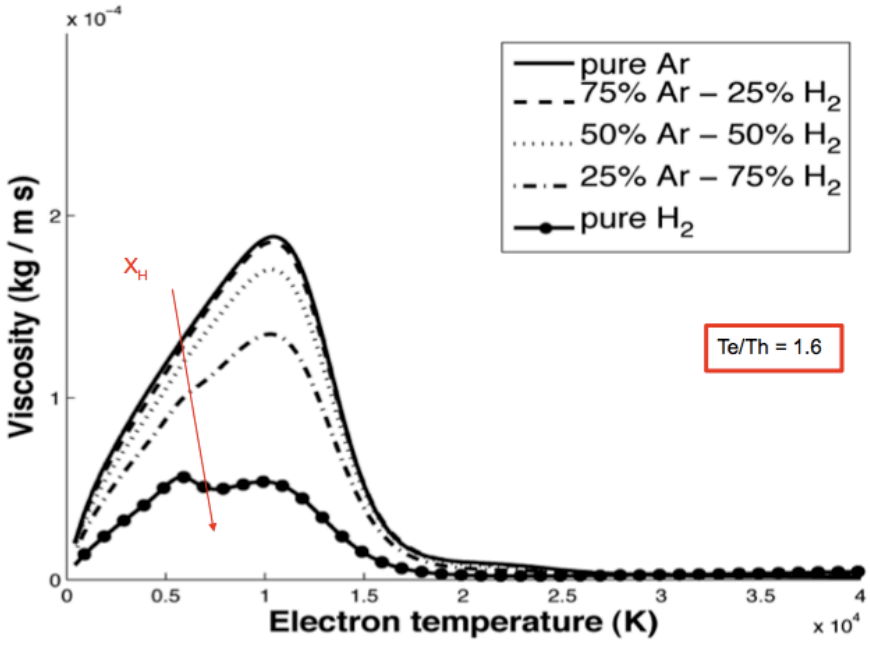


Fig. 7 – Temperature dependence of the viscosity for different Ar-H2 mixtures in thermal non-equilibrium.

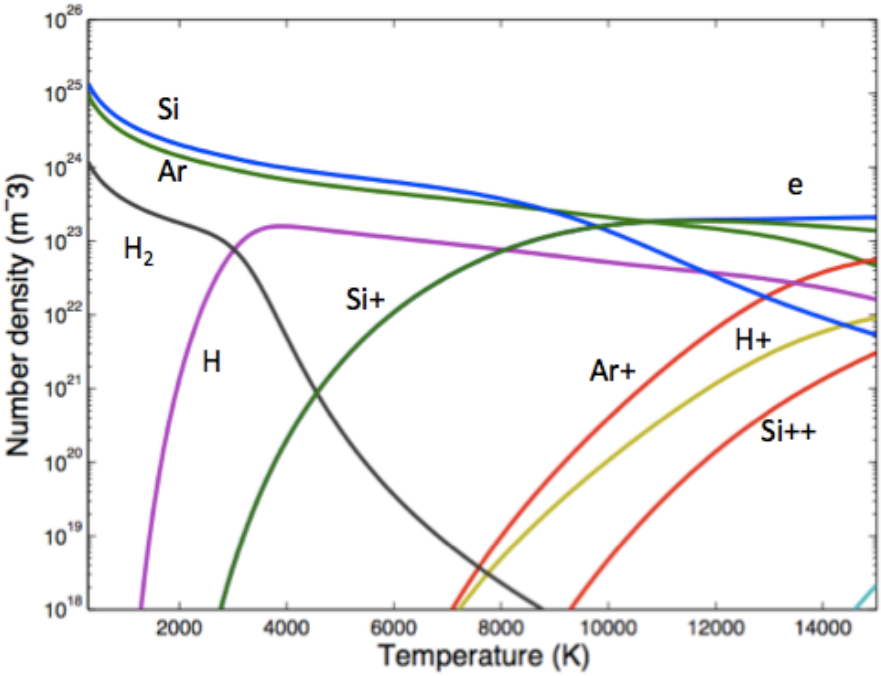


Fig. 8 – Temperature dependence of the composition for a 40%Ar - 6%H2 – 54% Si mixture at atmospheric pressure.

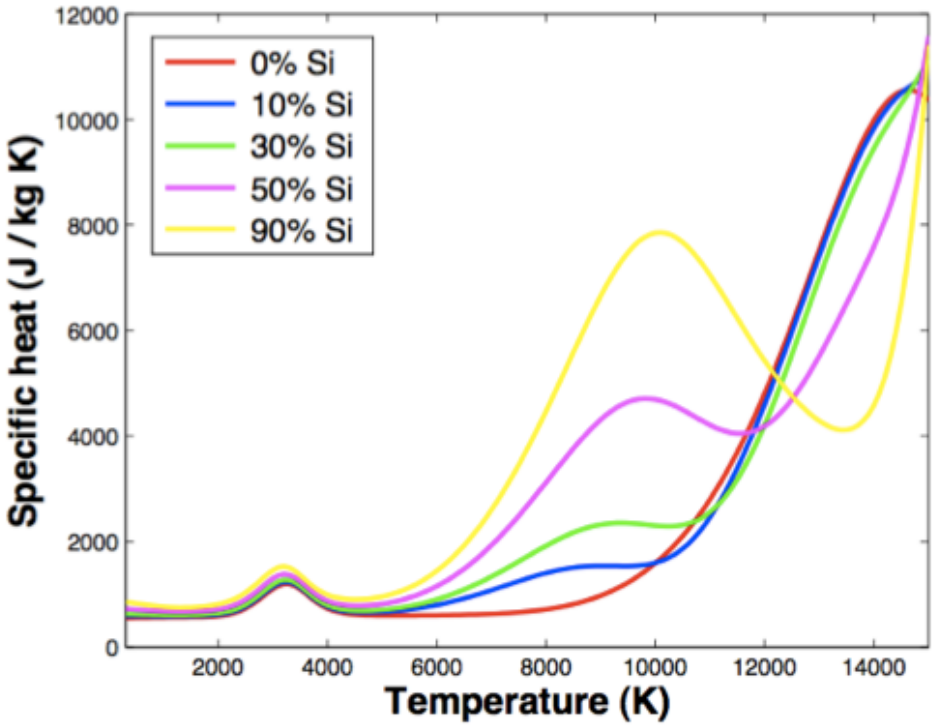


Fig. 9 – Temperature dependence of the specific heat for a Ar-6%H2 mixture with different concentration of Si at atmospheric pressure.

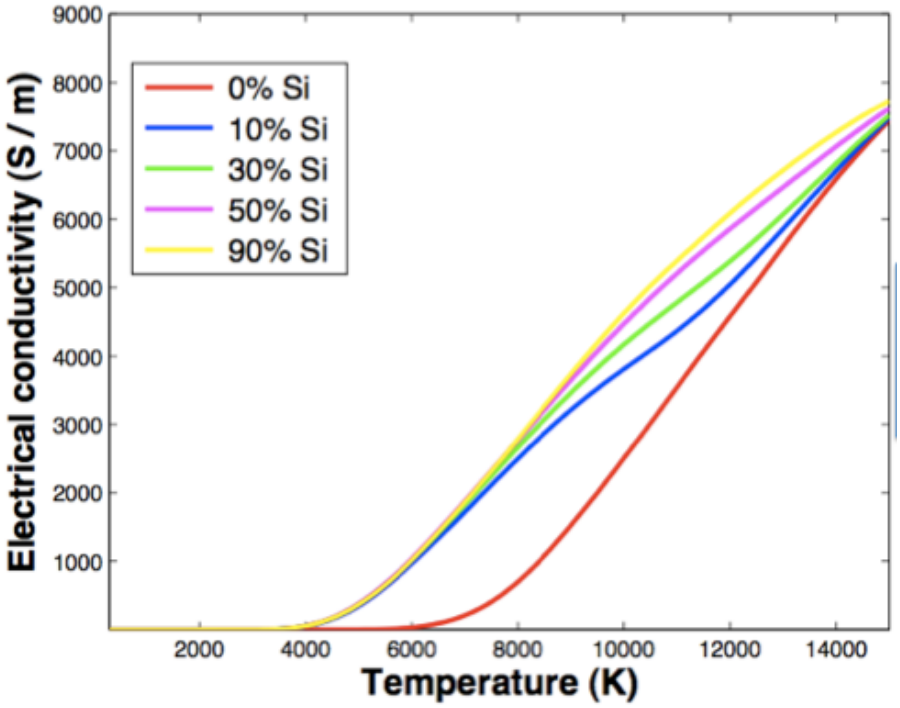


Fig. 10 – Temperature dependence of the electrical conductivity for a Ar-6%H2 mixture with different concentration of Si at atmospheric pressure.

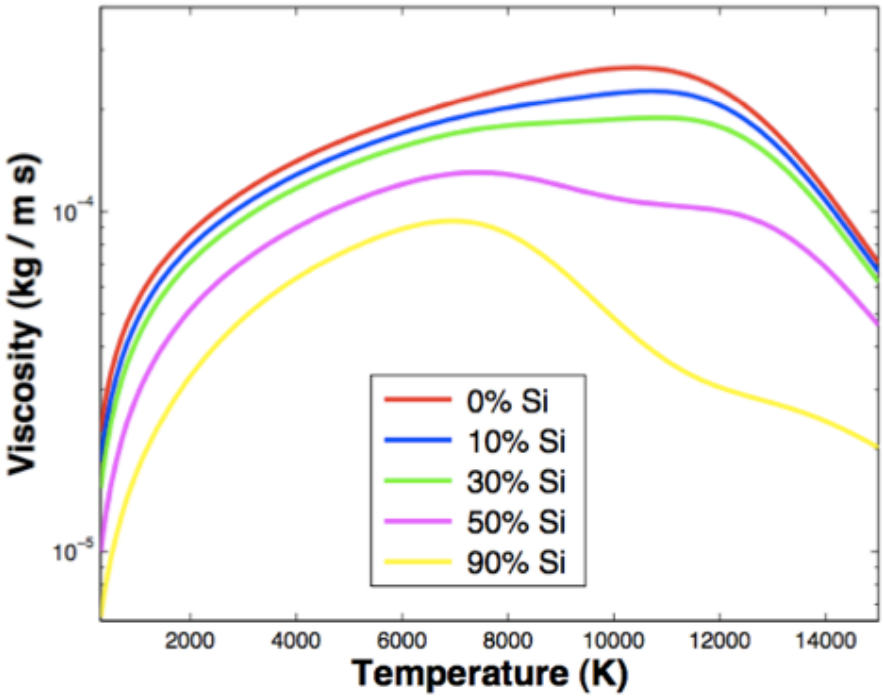


Fig. 11 – Temperature dependence of the viscosity for a Ar-6%H2 mixture with different concentration of Si at atmospheric pressure.

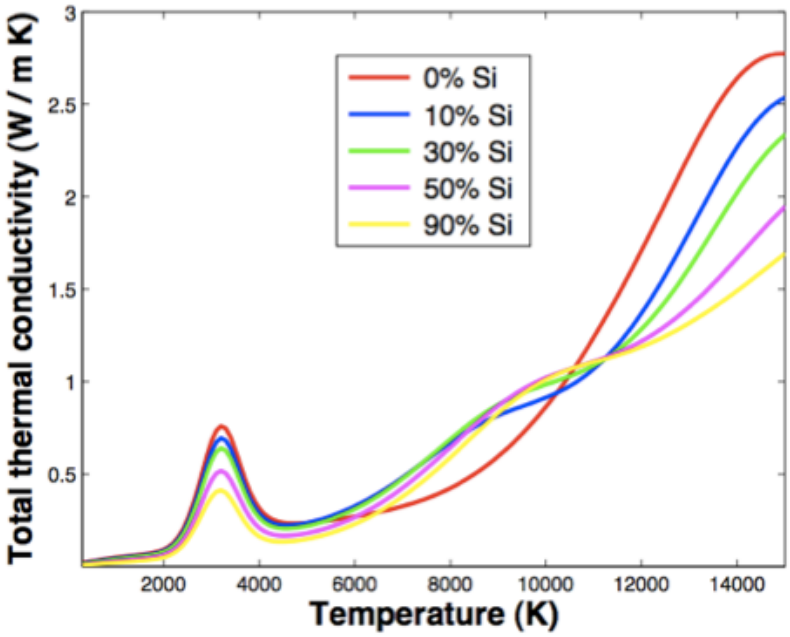


Fig. 12 – Temperature dependence of the thermal conductivity for a Ar-6%H2 mixture with different concentration of Si at atmospheric pressure.

*Evaluation of thermal non-equilibrium conditions*

The ICPT system developed by EMPA has been considered. The geometry is shown in figure 13. In order to simulate the ICP torch under operating conditions typical for nanopowder synthesis, the quench ring with funnel has been included in the

computational domain. Computations have been carried out using a modified version of the commercial software ANYSYS FLUENT 12.0[10]. The geometry for this component has been reported in figure 14. A polyhedral mesh has been constructed using the commercial software GAMBIT[10]; a finer grid has been used along the torch and reactor axis.

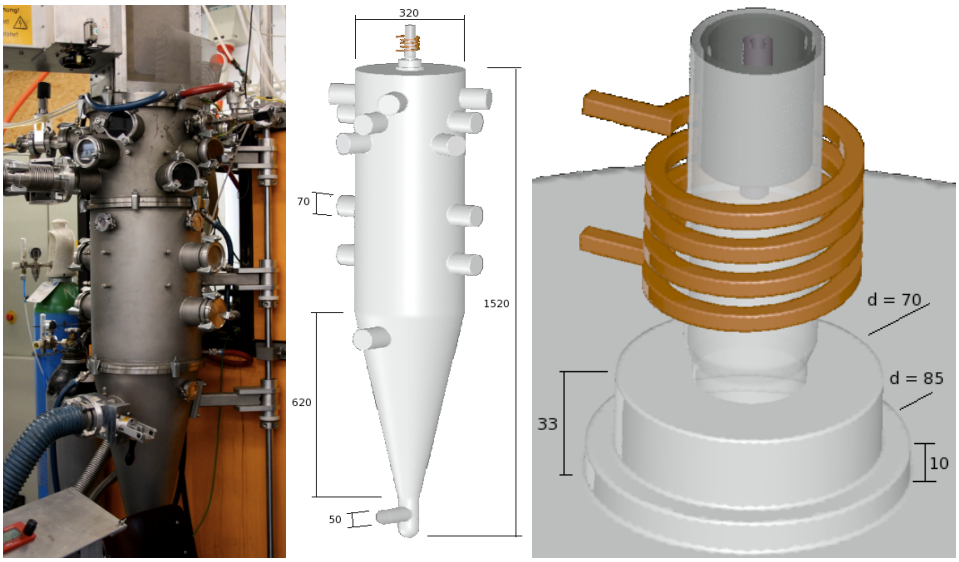


Figure 13. Empa reaction chamber (left) and simulation geometry (right). Dimensions in mm.

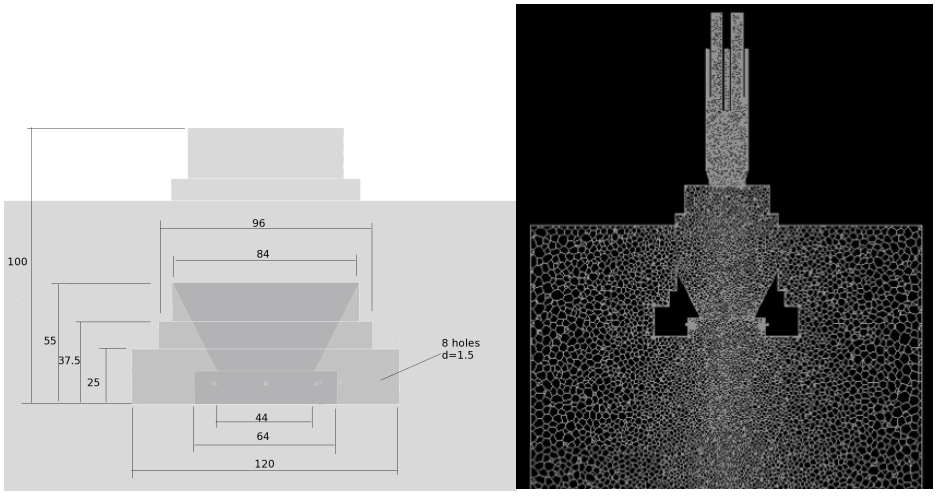


Figure 14. Quench ring and funnel geometry (left); detail of the mesh for the reaction chamber and the torch domain (right).

Simulations have been carried out for typical operating conditions for nanopowder synthesis, that is:

- Coupled power: 10 kW
- Coil current frequency: 13.56 MHz
- Sheath gas [slpm]: 60 Ar + 4.5 H2
- Plasma gas [slpm]: 12 Ar
- Carrier gas [slpm]: 4 Ar

- Quenching gas [slpm]: 56 Ar
- Chamber pressure: 60 kPa

Non-equilibrium simulations were initially carried out under axisymmetric assumption, in order to develop and check FLUENT User-Defined Functions that include the two-temperature model. The previously calculated database for non-equilibrium argon-hydrogen properties has been implemented in the FLUENT library and two additional User Defined Scalars have been used to model the energy equations for electrons and for heavy particles.
Preliminary calculations have been done to validate the model through comparison with results reported by Xue et al.[11], see figure 8. The small differences that can be seen between these results have been attributed to different data used for the calculation of plasma properties.
Results from the 2D non-equilibrium analysis showed that 2T model and LTE model give similar results for the temperature and velocity fields (see figures 15-16).
Once the code has been validated in the 2D framework, the more time-consuming 3D simulation has been carried out using parallel processing techniques. A fully 3D non-equilibrium model has been developed and implemented in the FLUENT environment and simulations have been performed for typical operating conditions for nano-powder synthesis (figures 12-17).
Electron temperature field and velocity field have been reported in figure 12 and 13 respectively: no significant deviations from axial symmetry can be seen, with the exception of regions close to the quench gas injection holes where a strong velocity magnitude results in substantial local cooling of the plasma (figure 14).
Non-equilibrium appears in the fringes of the discharge and in the near-wall regions. As can be seen in figure 17, the zone with thermal non-equilibrium are concentrated in regions where the electron temperature drops below 6000 K: since chemical equilibrium electron concentration in these regions is negligible, we concluded that 2T model in the case of argon-hydrogen mixtures gives negligible contribution to the main characteristics of the flow.

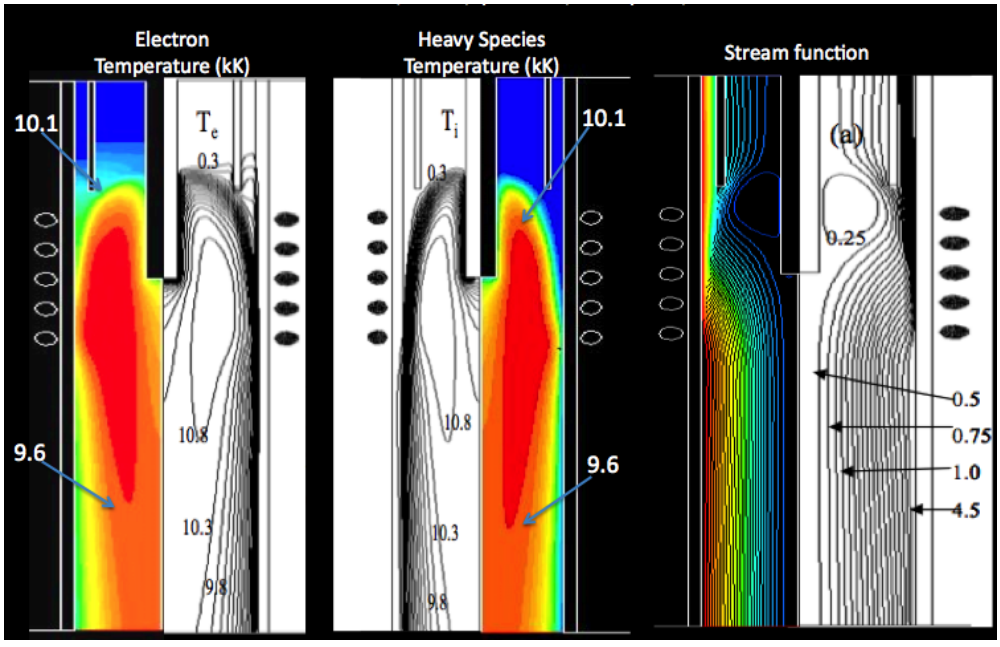

Figure 15: Thermo-fluid-dynamic field for a PL-50 torch under non-equilibrium conditions (in colours). Comparison with results reported by Xue et al. 2003 (B&W iso-countours).

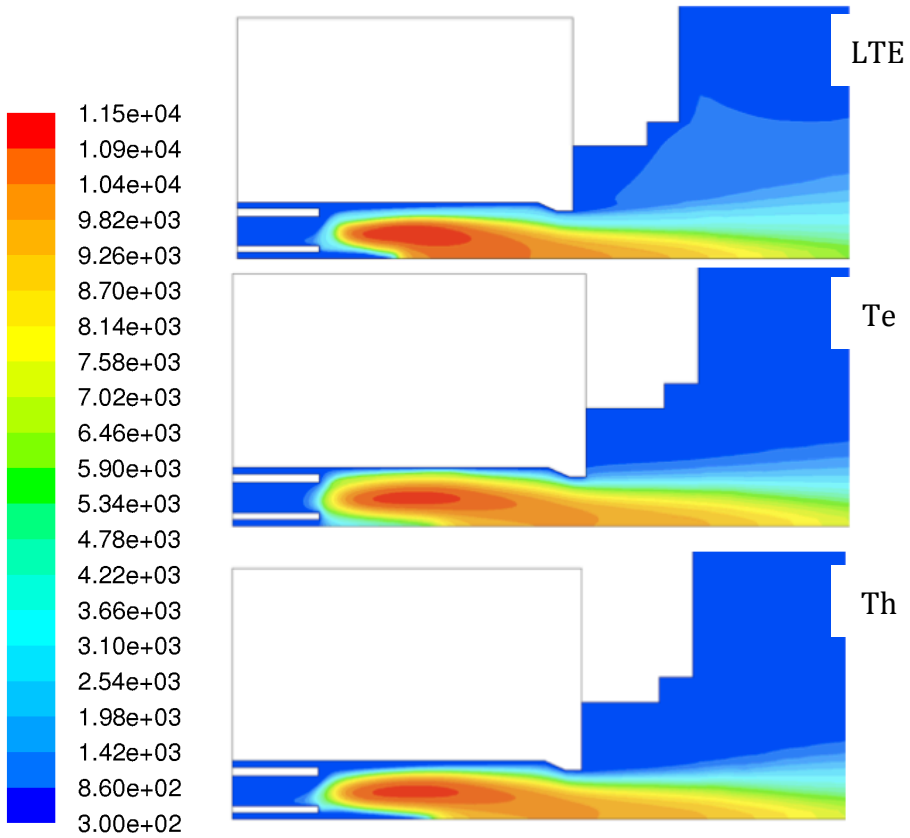


Figure 16. LTE temperature (top), electron temperature (center) and heavy particle temperature (bottom). 2D axisymmetric simulation with no turbulence model for a completely mixed argon-hydrogen mixture.

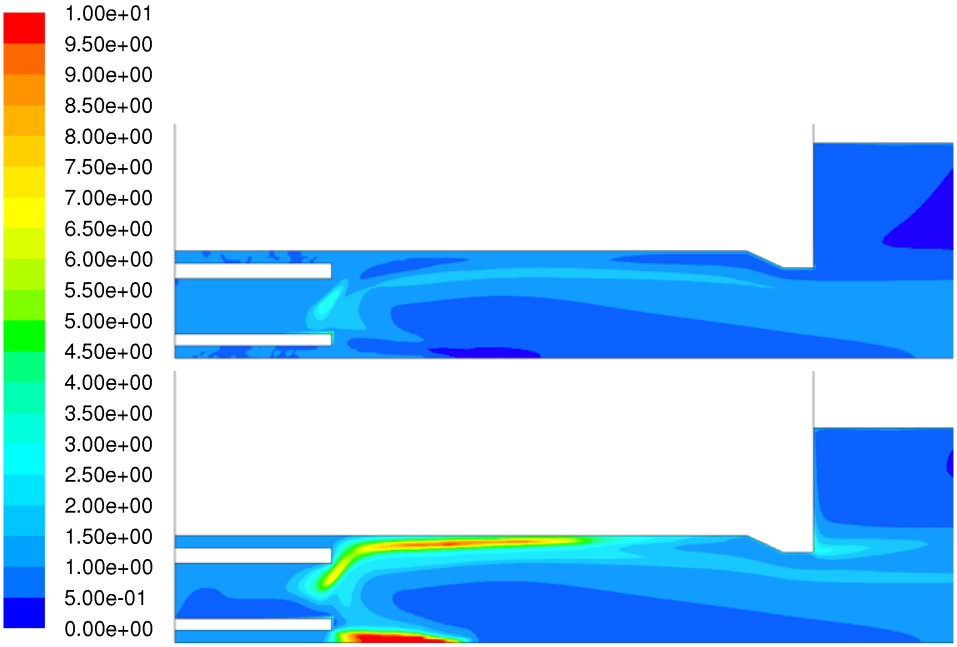

Figure 17. Ratio between heavy particle temperature and LTE temperature (top) and Ratio between electron temperature and LTE temperature (bottom). 2D axisymmetric simulation with no turbulence model for a completely mixed argon-hydrogen mixture.

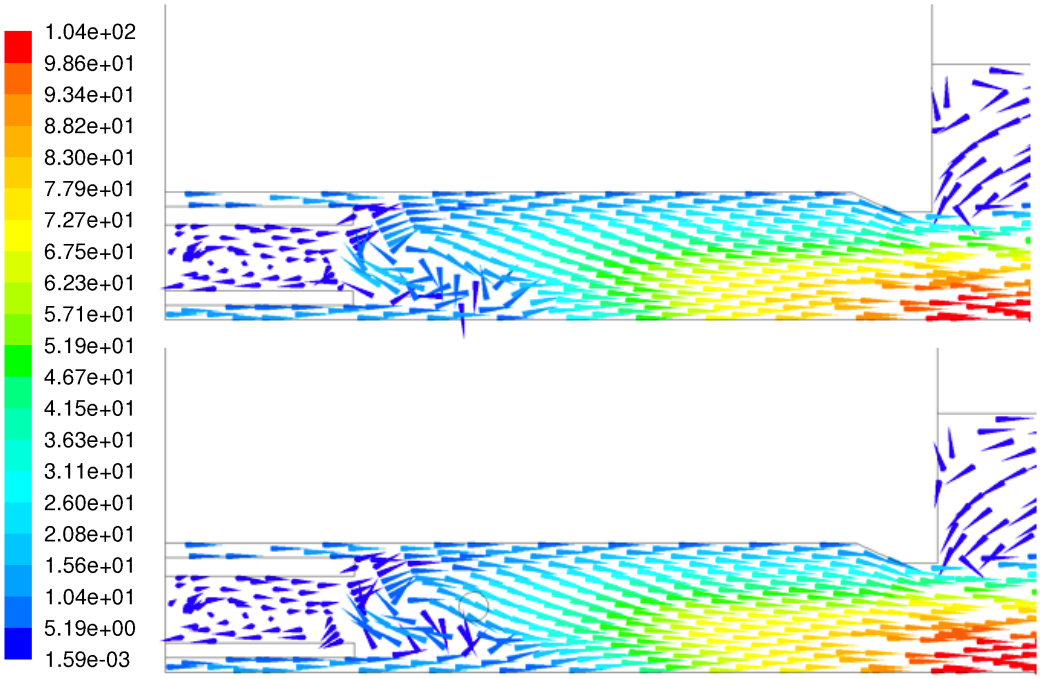


Figure 18. Velocity field vectors for LTE simulation (top) and non-equilibrium simulation (bottom). 2D axisymmetric simulation with no turbulence model for a completely mixed argon-hydrogen mixture.

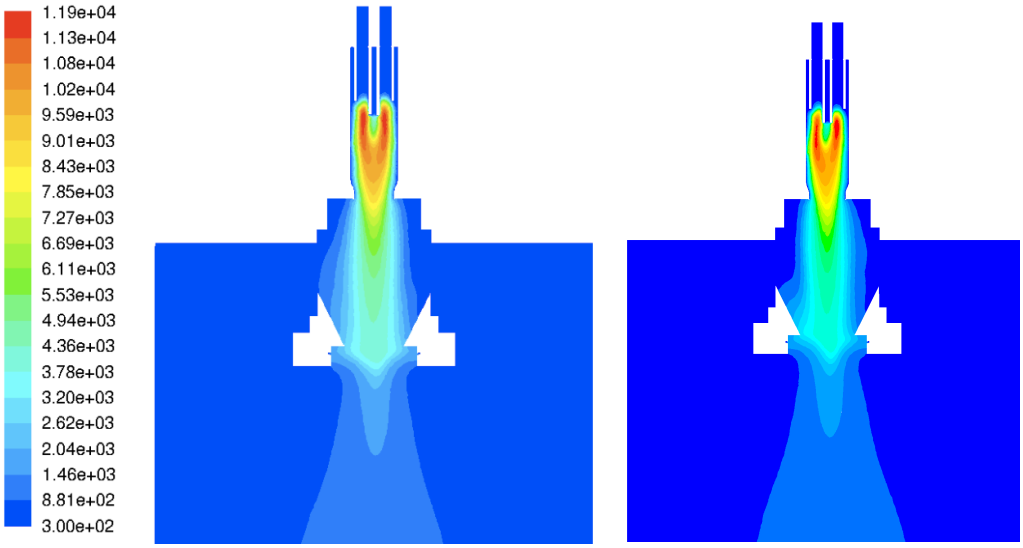


Figure 19. 3D simulation: electron temperature field [K] on the xz plane (left) and on the yz plane (right).

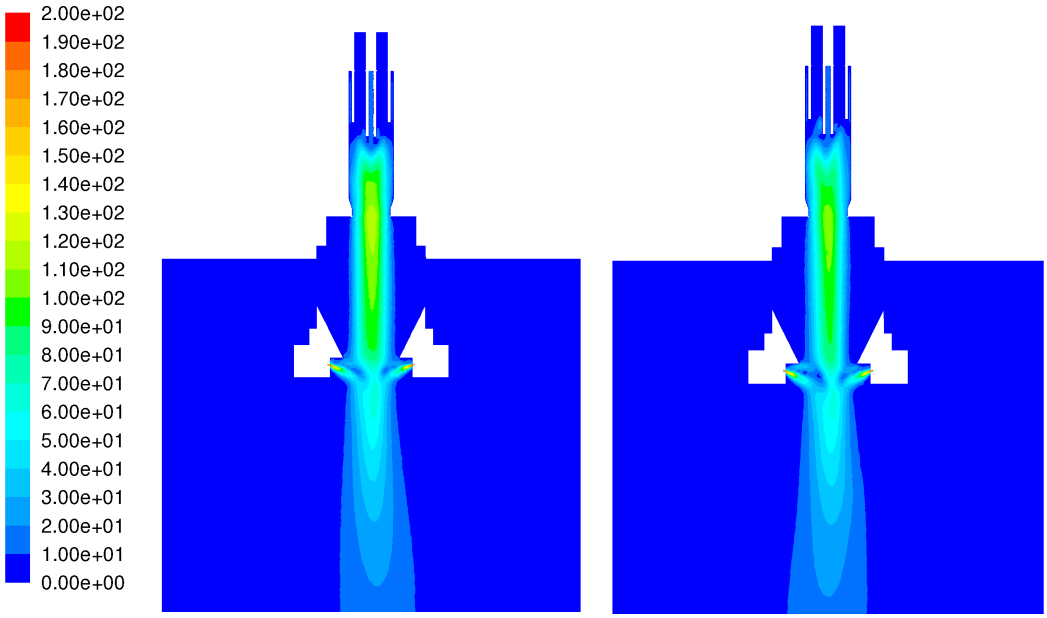


Figure 20. 3D simulation: velocity magnitude field [m/s] on the xz plane (left) and on the yz plane (right).

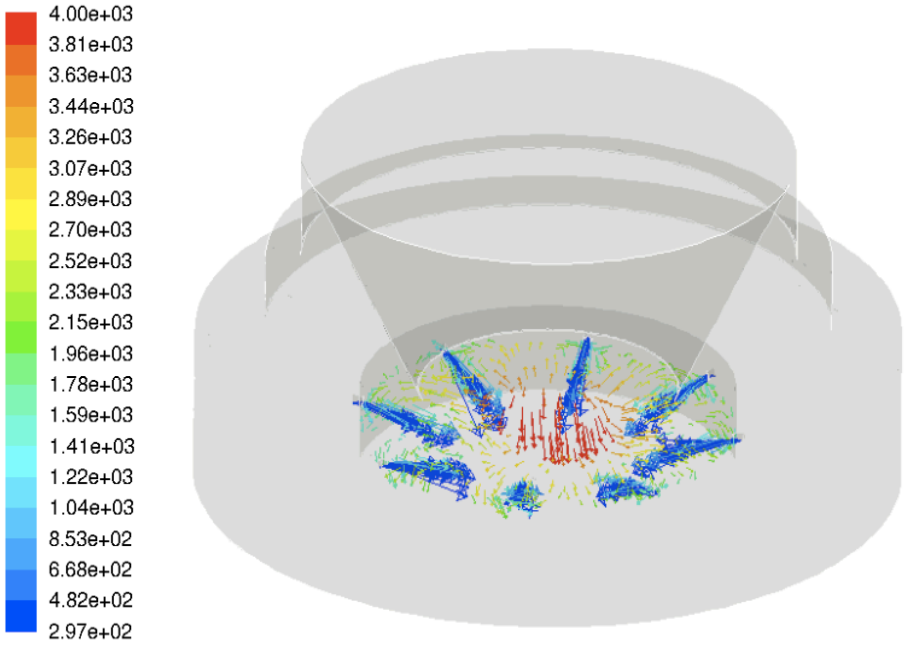


Figure 21. 3D simulation: temperature field (Th) and velocity vectors on plane xy at the axial position of the quench gas injection holes.

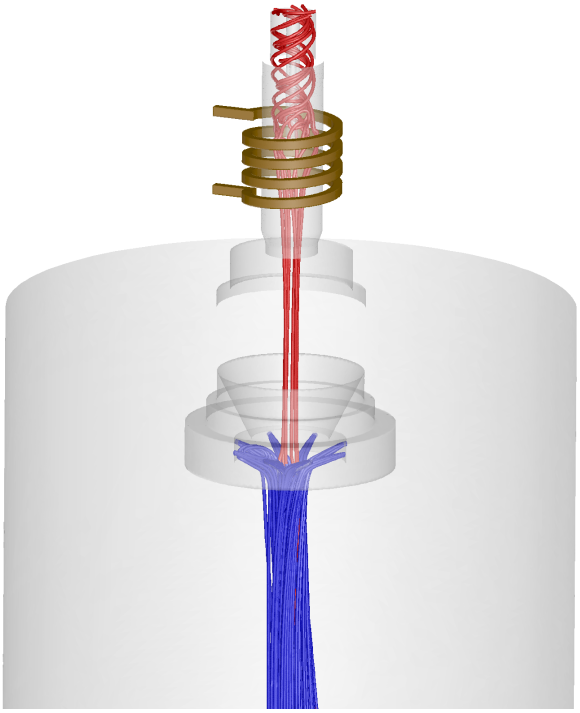

Figure 22. 3D simulation: pathlines released from plasma gas (red line) and quench gas (blue line).

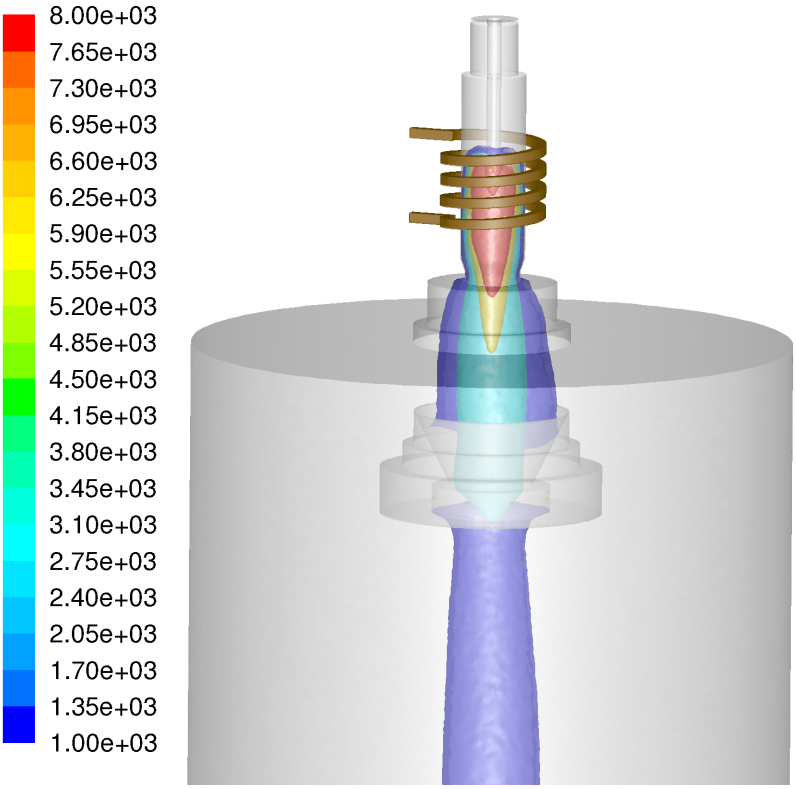


Figure 23. 3D simulation: heavy particle temperature iso-contour at 1000 K, 3000 K, 6000 K and 8000 K.

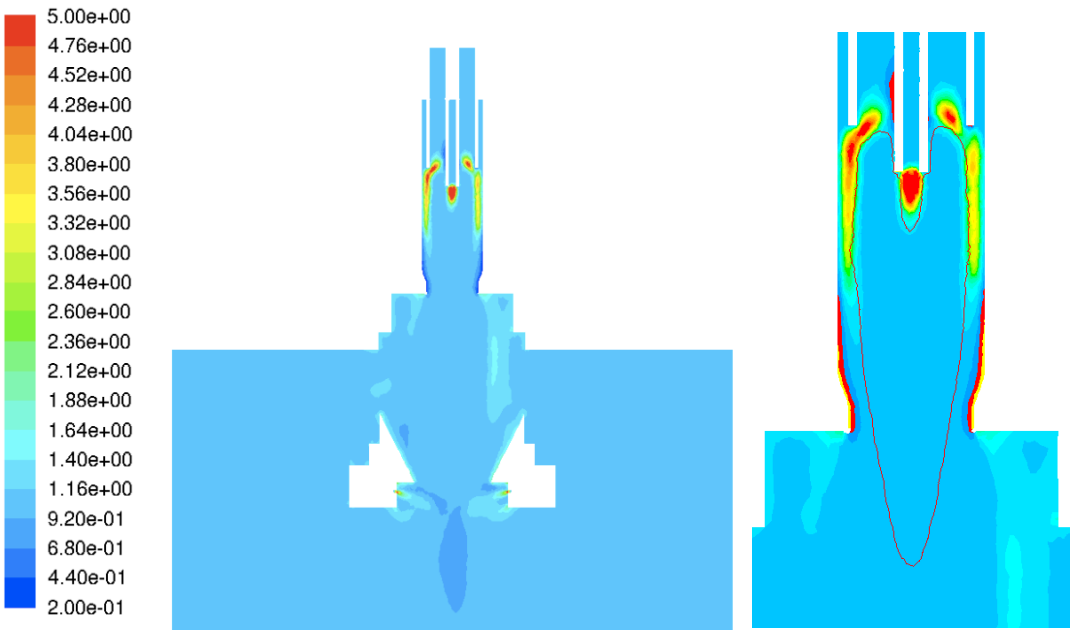


Fig. 24 - 3D simulation: non-equilibrium parameter field (Te/Th) on the xz plane and electron temperature iso-contour at 6000 K (red line).

A 3-D thermal non-equilibrium model (two-temperature model) able to investigate plasma thermo-fluid-dynamic fields under different operating conditions has been implemented in a commercial CFD code (FLUENT) by means of a library written in C code. A self-consistent computer code for the calculation of thermodynamic and transport properties for plasmas under non-equilibrium conditions has been developed; plasma properties for Ar-$H_2$ mixtures at different pressures have been obtained and collected in look-up tables suitable for fluid-dynamic simulations. The thermal non-equilibrium model has been validated through comparison with results reported in studies recently published in literature. Some selected results have been reported for Pl-35 torch with EMPA reaction chamber operating in standard conditions for nano-powder synthesis. Non-equilibrium regions are concentrated in the near-wall regions and in the fringes of the discharge where electron chemical equilibrium concentration drops under appreciable levels: as a consequence, thermal non-equilibrium results in negligible effects on the main characteristics of the thermo-fluid-dynamic fields.

*Evaluation of different turbulence models*

The expansion of the plasma jet from the torch to the reaction chamber induces strong flow recirculation and turbulence. The latter heavily influence the thermo-fluid-dynamic field in the reaction chamber and consequently the synthesis of nanopowders is affected the same way.
Turbulent flows are characterized by fluctuating velocity fields. These fluctuations mix transported quantities such as momentum, energy, and species concentration, and cause the transported quantities to fluctuate as well. Since these fluctuations can be of small scale and high frequency, they are too computationally expensive to simulate directly in practical engineering calculations. Instead, the instantaneous (exact)

governing equations can be time-averaged, ensemble-averaged, or otherwise manipulated to remove the resolution of small scales, resulting in a modified set of equations that are computationally less expensive to solve. However, the modified equations contain additional unknown variables, and turbulence models are needed to determine these variables in terms of known quantities. It is an unfortunate fact that no single turbulence model is universally accepted as being superior for all classes of problems. The choice of turbulence model will depend on considerations such as the physics encompassed in the flow, the established practice for a specific class of problem, the level of accuracy required, the available computational resources, and the amount of time available for the simulation.
The choice of an appropriate model for the prediction of turbulence in the reaction chamber is thus crucial for the proper study of physical phenomena that occur during the synthesis of nanopowders in laboratory scale reactors and for the subsequent optimization of the system. Predicting the largest eddies and the overall flow behaviour is a key point for the design of reaction chambers for powder treatment and particularly for nanoparticles production, in order to avoid recirculation and deposition of powder on the walls.
Two alternative methods can be employed to render the Navier-Stokes equations tractable so that the small-scale turbulent fluctuations do not have to be directly simulated: Reynolds-averaging (or ensemble-averaging) and filtering. Both methods introduce additional terms in the governing equations that need to be modelled in order to achieve a "closure" for the unknowns.
The Reynolds-averaged Navier-Stokes (RANS) equations govern the transport of the averaged flow quantities, with the whole range of the scales of turbulence being modelled. The RANS-based modelling approach therefore greatly reduces the required computational effort and resources, and is widely adopted for practical engineering applications. An entire hierarchy of closure models are available in FLUENT including k-ε models, k-ω models and RSM.
LES provides an alternative approach in which large eddies are explicitly computed (re- solved) in a time-dependent simulation using the "filtered" Navier-Stokes equations. The rationale behind LES is that by modeling less of turbulence (and resolving more), the error introduced by turbulence modeling can be reduced. It is also believed to be easier to find a "universal" model for the small scales, since they tend to be more isotropic and less affected by the macroscopic features like boundary conditions, than the large eddies. Filtering is essentially a mathematical manipulation of the exact Navier-Stokes equations to remove the eddies that are smaller than the size of the filter, which is usually taken as the mesh size when spatial filtering is employed as in FLUENT. Like Reynolds-averaging, the filtering process creates additional unknown terms that must be modeled to achieve closure[10].

Different turbulent models have been used to predict the thermo-fluid-dynamic field and comparisons have been carried out between results from different models and from enthalpy probe temperature measurements performed at EMPA. The turbulence models used are those implemented in the FLUENT environment: the k-ε models (standard, RNG, realizable), the k-ω model, the SST model and the RSM model. Different wall functions have also been used: standard and two-layer wall function.
As shown in figure 25, the same model for turbulence may results in different temperature field if different model constants are used. The turbulence model must be tuned according to experimental results.

In figures 26 and 27 the enthalpy profile at different distances from the torch outlet computed using different turbulence models is reported together with the results of the enthalpy probe measurements. The RSM model is the one that predicts better the enthalpy profile, even if the coupled plasma power in the simulations has to be set at 5 kW for complete agreement.

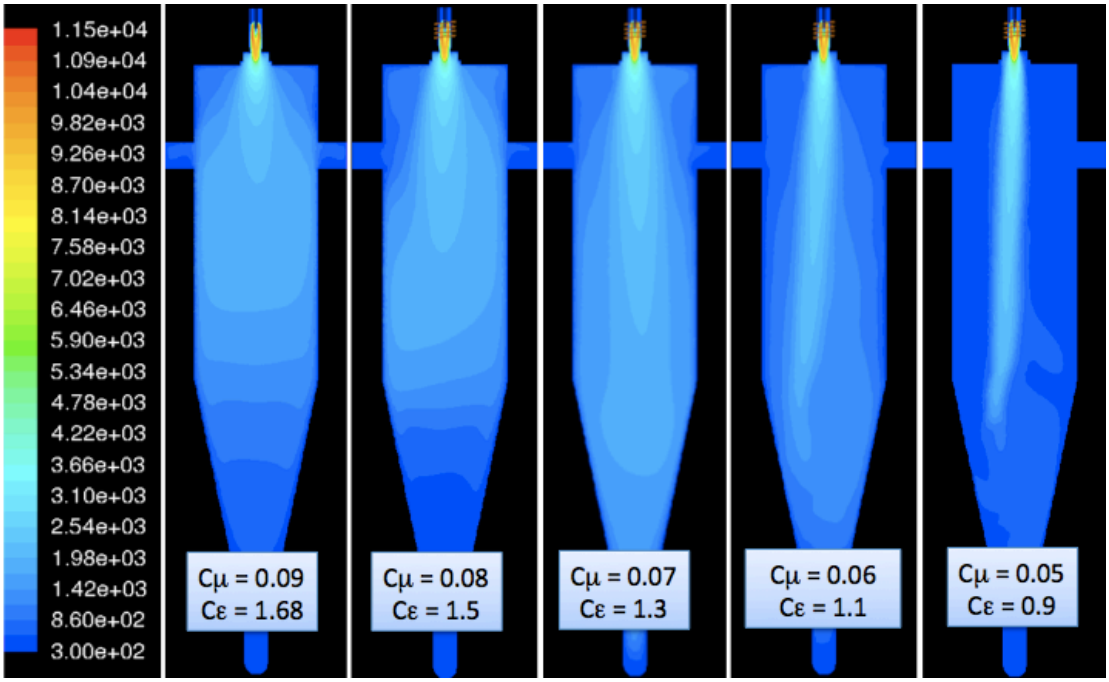


Fig. 25 – Temperature field in the reaction chamber for different parameters of the turbulence k-ε model.

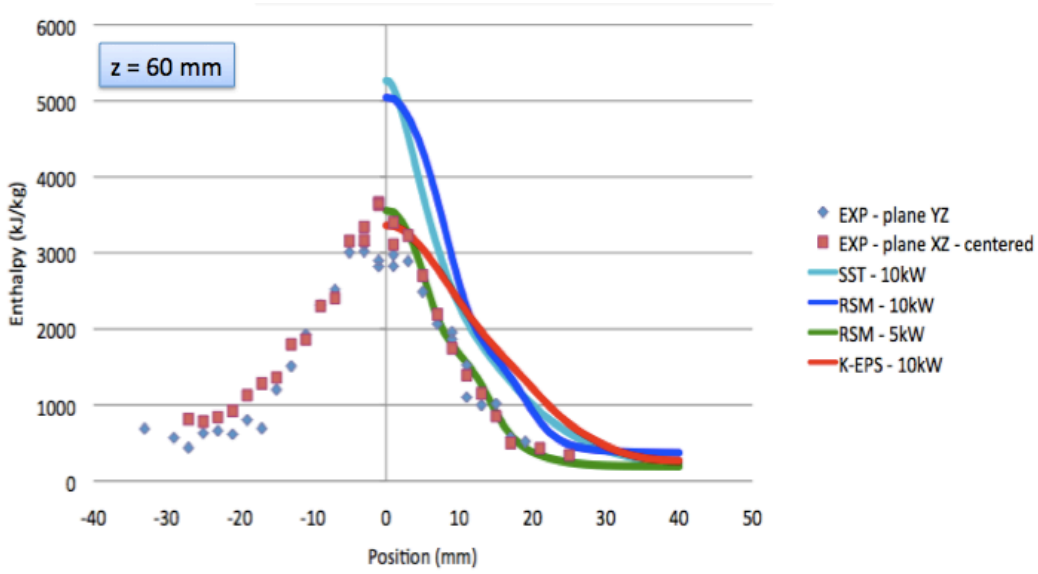


Fig. 26 – Enthalpy radial profile in the reaction chamber at a distance of 60 mm from the torch outlet for an 72 slpm Ar – 6 slpm $H_2$ plasma at 18 kW and 60kPa: comparison between results of different turbulence models and experimental enthalpy probe measurements.

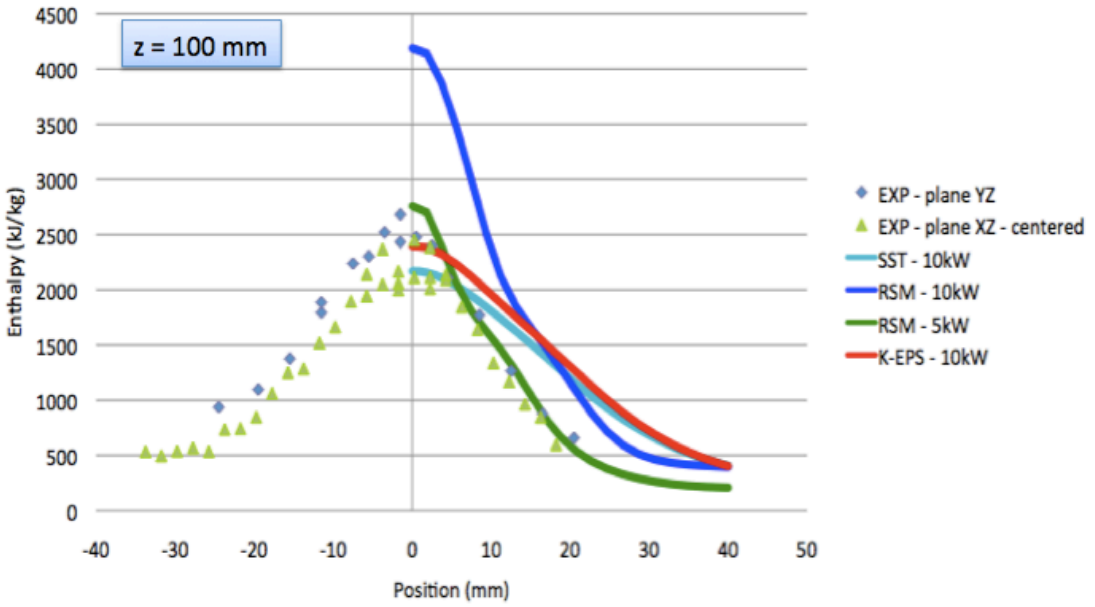


Fig. 27 – Enthalpy radial profile in the reaction chamber at a distance of 100 mm from the torch outlet for an 72 slpm Ar – 6 slpm $H_2$ plasma at 18 kW nd 60kPa: comparison between results of different turbulence models and experimental enthalpy probe measurements.

A Large Eddy Simulation (LES) model has been used to predict instantaneous flow fields in a 3-D time dependent framework without any time filtering as done in the RANS models (for example k-e or RSM). Turbulent flows are characterized by eddies with a wide range of length and time scales: the largest eddies are comparable in size to the characteristic length of the mean flow; they are mostly responsible for the transport of mass, momentum and energy and are directly predicted by LES; the smallest eddies, not linked to the geometrical boundary conditions, are isotropic and are responsible for the dissipation of turbulence kinetic energy; they can be predicted by LES using semi empirical models. In figure 28 temperature isosurfaces in the reaction chamber region are shown for a fixed time step. The maximum temperature (around 11,200 K) is located inside the torch, within the coil region; in the chamber region the temperature drops rapidly below 5,000 K. In the upper half of the chamber the plasma jet lays on the axis with a coherent structure while the surrounding region is dominated by several cold low velocity eddies; in the lower part of the chamber the jet brakes up due to the effects of recirculation. This behaviour is clearly depicted in figure 28 (right), showing velocity versors coloured by log scale velocity magnitude (m/s). The maximum value of velocity is about 100 m/s and it is found in the hot jet region; it drops to 20 m/s where the jet breaks up. The cold surrounding region shows lower velocities, in the order of 5 m/s. The plasma jet remains in laminar regime since plasma gas viscosity at 5,000 K is an order of magnitude higher than the room temperature value. In the lower chamber region the temperature drops and the fluid viscosity decreases inducing turbulence rise and jet structure brake up. A no-plasma cold gas jet would be broken up well before reaching the middle of the chamber.

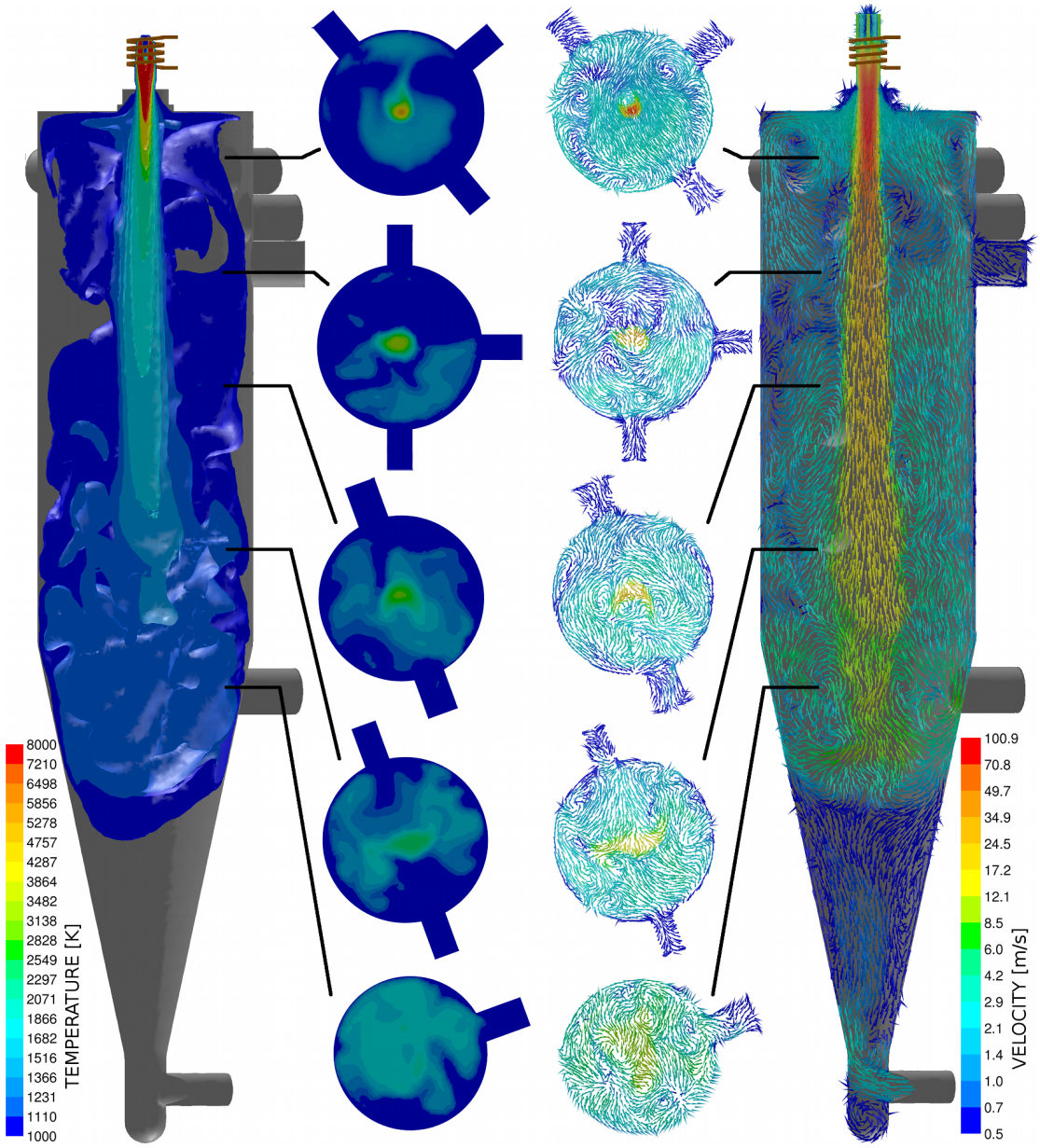


Fig. 28 – Temperature field and velocity field in the reaction chamber for a 72 slpm Ar – 6 slpm $H_2$ plasma at 10 kW coupled to the torch: results of the time-dependent LES turbulence model.

In figure 29 a comparison between results of the time-dependent LES model and those of the steady state RSM model has been reported, showing good agreement
In figure 30.results from the 3D simulations were compared with those of the 2D models: good agreement has been found even if the 2D model slightly over predict the enthalpy along the reactor axis.
Finally, we have chosen to use the 2D axi-symmetric model with RSM turbulence model. The temperature field in the reaction chamber obtained with this model has been reported in figure 31.

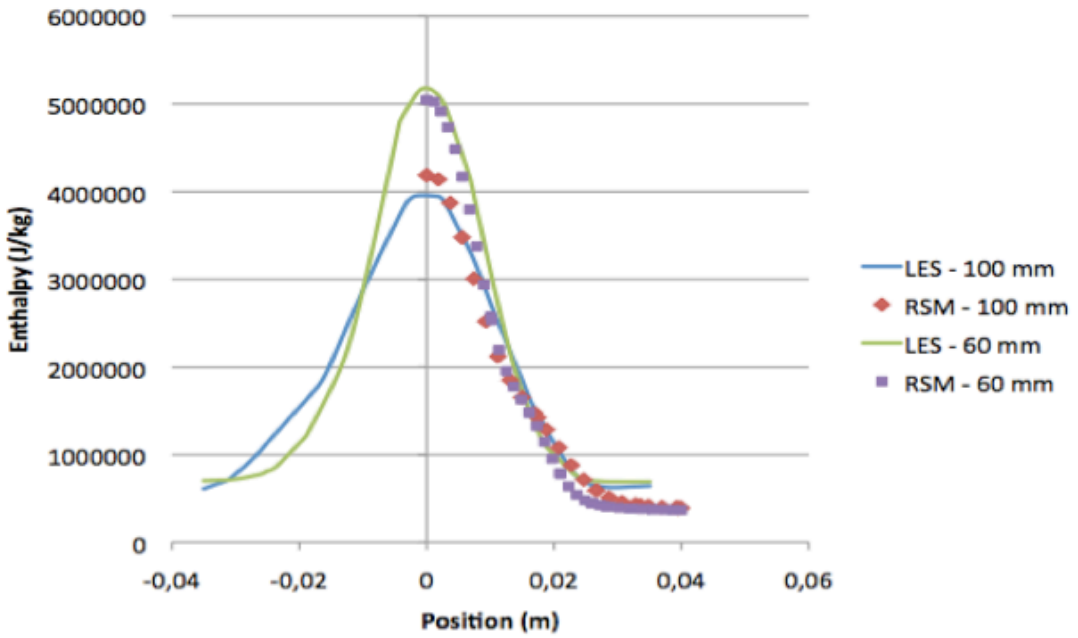


Fig. 29 – Enthalpy radial profile in the reaction chamber at different distances from the torch outlet for a 72 slpm Ar – 6 slpm $H_2$ plasma at 10 kW coupled to the torch: comparison between results of the time-dependet LES turbulence model and steady-state RSM turbulence model.

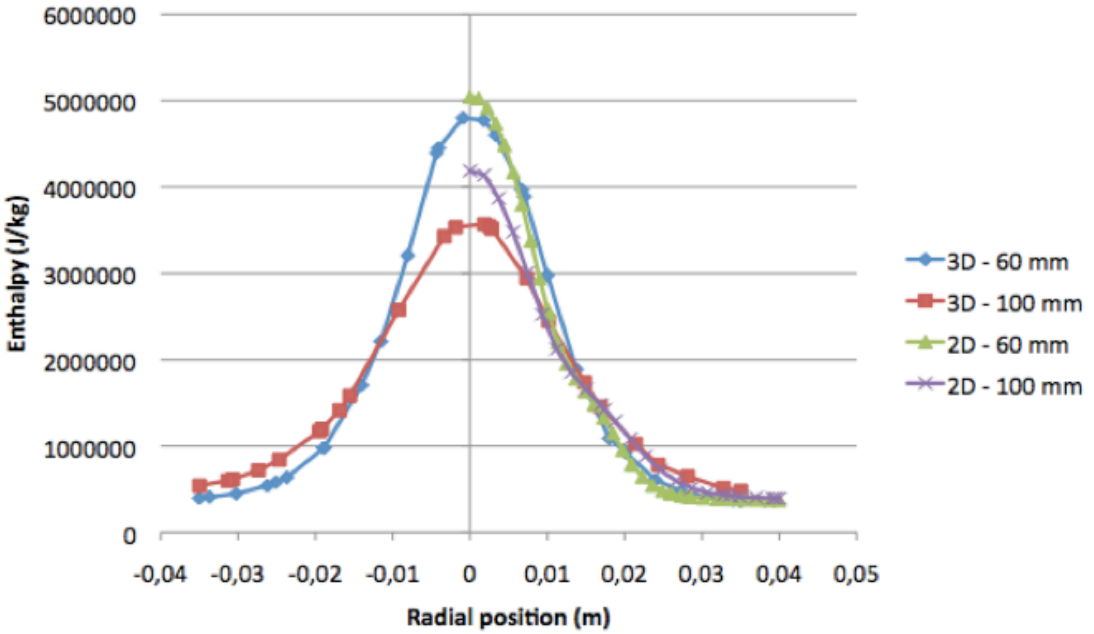


Fig. 30 – Enthalpy radial profile in the reaction chamber at different distances from the torch outlet for a 72 slpm Ar – 6 slpm $H_2$ plasma at 10 kW coupled to the torch: comparison between results of the 3D model and the 2D axi-symmetric model. RSM turbulence model.

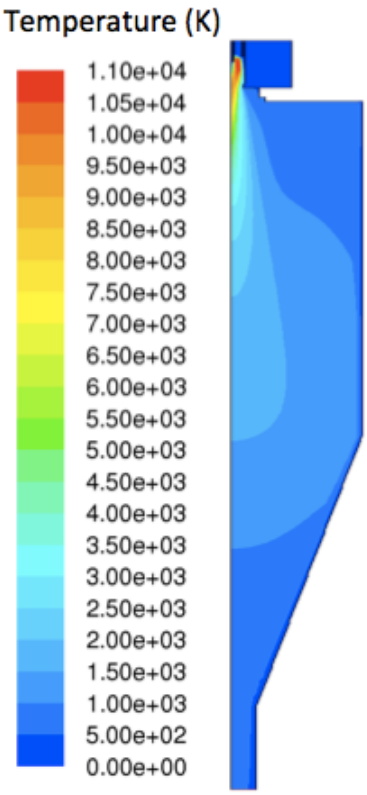


Fig. 31 – Temperature field in the reaction chamber for a 72 slpm Ar – 6 slpm $H_2$ plasma at 10 kW coupled to the torch at 60 kPa: results of the 2D axi-symmetric model with RSM turbulence model.

*Characterization of the EMPA ICPT system: evaporation rate of the Si precursor*

One of the most important technologic issues for the scaling up of the nanopowder production is the evaporation of the precursor. Especially when the precursor is solid, the energy subtracted to the plasma by the heated powders can be enough to cool down the plasma discharge (loading effect) and to be a technological limit in the evaporation process. This is a know issue from experimental point of view but a modelling approach to this problem gives new insight in how it could be avoided[12, 13]. Several simulations have been carried out with different types of Silicon powder precursors and different powder feed rates. Two distributions of commercial powders have been used: Keyvest powders (mean diameter = 14um) and Brodmann powders (mean diameter = 33um). PSD for these powders are shown in figure 32. Compuatation have been carried out for these operating conditions reported in table 1.

Table 1

| Power coupled (kW) | Sheath gas | Central gas | Feed gas | pressure | f(MHz) |
|---|---|---|---|---|---|
| 10 kW – 20 kW | 60 Ar + 6 H2 | 12 Ar | 6.5 Ar | 400 mbar | 3-13.56 |

A bigger precursor will have a higher thermal inertia but it will result in a lower loading effect with respect to a smaller precursor: thus, it is difficult to find which one will results in a higher evaporation rate. Simulations have been carried out for these two types of precursor, for different powers coupled to the torch (from the usual value

of 10 kW up to the unrealistic value of 20 kW) and different precursor feed rates (from 1 to 5 g/min). Results are shown in figure 33. For powder feed rate higher than 2 g/min no complete evaporation can be achieved even with the unrealistic power of 20 kW. For the case at 10kW, Brodmann powders generally have higher evaporation rate than Keyvest powders, except for precursor feed rate lower than 1 g/min where the loading effect still doesn't create a cold central channel with plasma temperature below the evaporation temperature of Silicon (see figure 34). For the unrealistic power of 20 kW, the Keyvest powders have higher evaporation rate for the whole range of powder feed rate considered. In figure 35 the evaporation efficiency is reported.

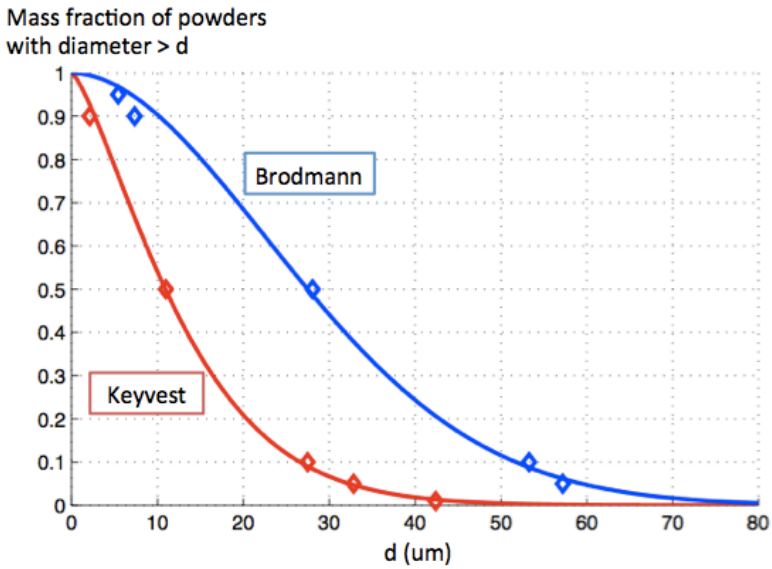


Fig. 32 – Particle size distribution of Keyvest and Brodmann powders.

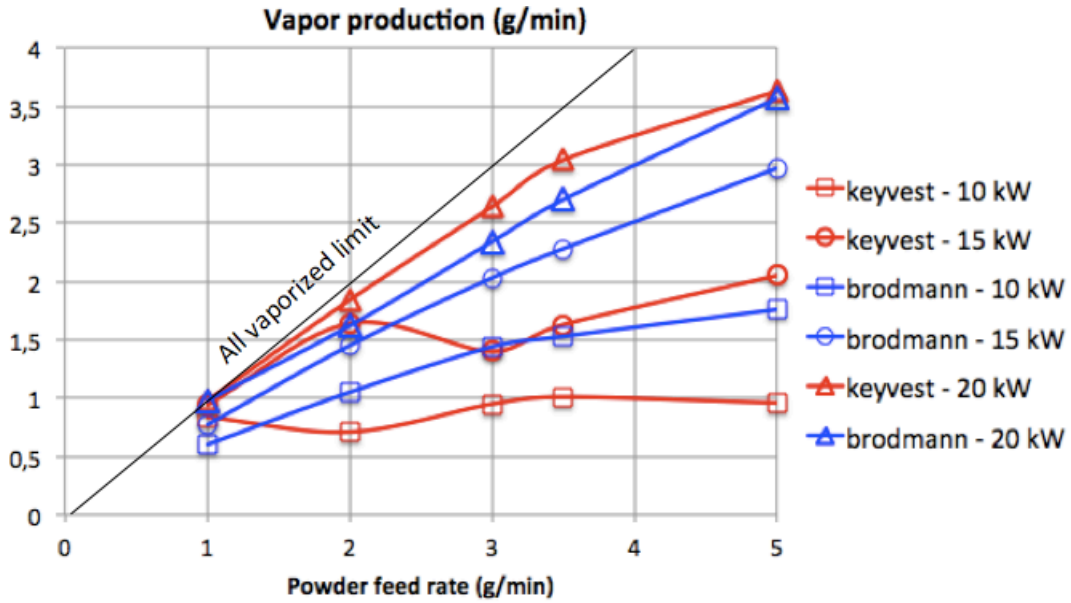


Fig. 33 – Evaporation rate as a function of powder feed rate for different types of precursor and different values of power coupled to the plasma torch.

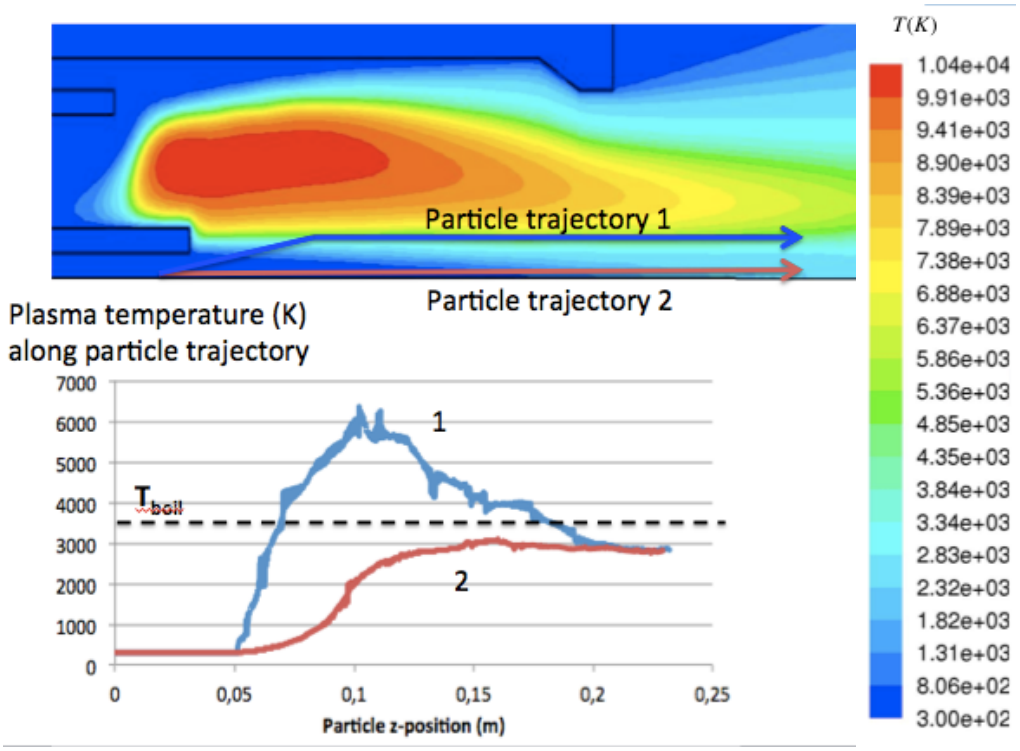


Fig. 34 – Temperature field inside the torch in presence of a strong loading effect with two sketched particle trajectories (top); Particle temperature along particle trajectory for a particle passing in the hot plasma region, part. 1, and a particle passing through the cold central channel, part. 2, (bottom).

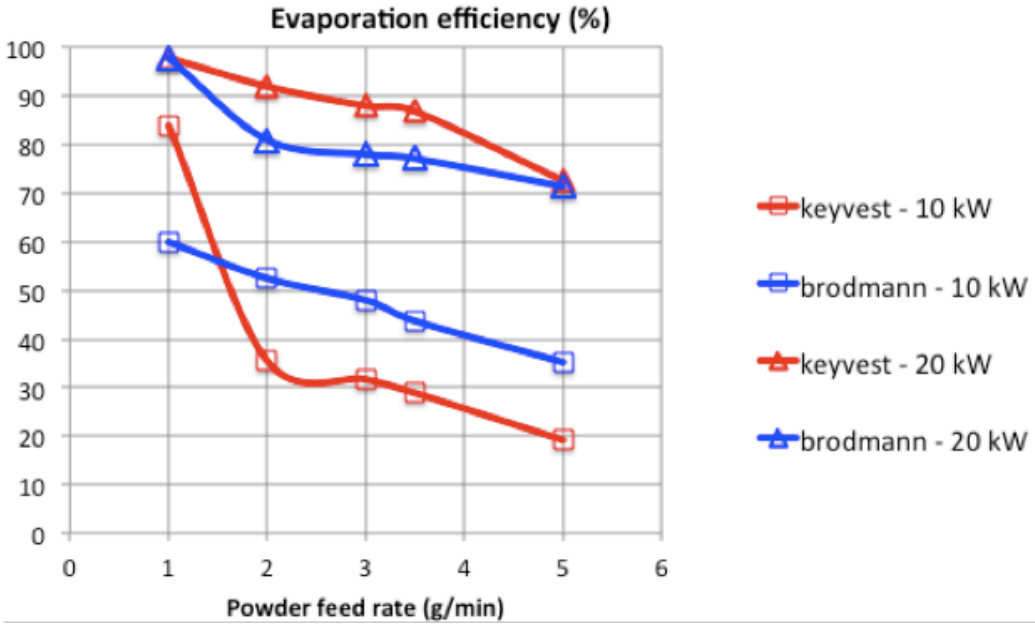


Fig. 35 – Evaporation efficiency defined as evaporation rate/precursor feed rate for different precursor types and different values of power coupled to the torch.

## Conclusions

As part of this project, properties for typical plasma mixtures used in Silicon nanopowder synthesis have been calculated, a non-equilibrium model for predicting thermo-fluid-dynamic fields has been developed, different turbulence models have been tested and validated through comparison with experimental enthalpy probe measurements, and finally, the precursor evaporation efficiency has been estimated for different operating conditions.
An important design parameter for the up-scaling of the lab-scale process is the coil current frequency because it has a strong effect on power distribution inside the plasma torch. Lower frequency induces a more uniform power distribution, which may result in less cooling of the plasma discharge by particle loading. The EMPA system operates at 13.56 MHz but the same torch could be used also with lower frequency, down to about 3 MHz. In order to estimate the effect of frequency on particle evaporation, a new set of simulations at 13.56 MHz and 3 MHz for different powder types and different powder feed rates has been scheduled. In order to increase the value of the critical feed rate for a given process, the use of a dispersion probe to inject the precursor could be a solution: this particular type of probe injects powders with a cone of dispersion realized by means of a secondary gas injected at high velocity near the probe tip through micro-sized holes. Even if precursor evaporation could be enhanced, however, this technological solution seems to fit only industrial-scale torches because for small torch diameters it could induce strong deposition of vapours to the torch internal walls.

References


1. A. Concetti, Ph. D. thesis, Alma Mater Studiorum - University of Bologna, 2011.
2. M. I. Boulos, P. Fauchais and E. Pfender, Thermal Plasmas: Fundamentals and Applications **1** (1994).
3. J. O. Hirschfelder, C. F. Curtiss and R. B. Bird, *Molecular Theory of Gases and Liquids*. (1954).
4. V. Colombo, E. Ghedini and P. Sanibondi, Progress in Nuclear Energy **50** (8), 921-933 (2008).
5. V. Colombo, E. Ghedini and P. Sanibondi, Journal of Physics D: Applied Physics **42** (5), 055213 (2009).
6. R. S. Devoto, Physics of Fluids **9** (6), 1230-1240 (1966).
7. R. S. Devoto, Physics of Fluids **10** (10), 2105-2112 (1967).
8. R. S. Devoto, Physics of Fluids **10** (2), 354-364 (1967).
9. V. Rat, P. André, J. Aubreton, M. F. Elchinger, P. Fauchais and A. Lefort, Physical Review E - Statistical, Nonlinear, and Soft Matter Physics **64** (2 II), 264091-2640920 (2001).
10. ANSYS, *ANSYS FLUENT 12.0 Theory guide*. (Canonsburg, Pennsylvania, USA, 2009).
11. S. Xue, P. Proulx and M. I. Boulos, Proc. 16th Int. Symp. on Plasma Chemistry (2003).
12. V. Colombo and et al., Journal of Physics D Applied Physics **43** (10), 105202 (2010).
13. V. Colombo, E. Ghedini and P. Sanibondi, Plasma Sources Science and Technology **19** (6), 065024 (2010).

# DIAGNOSTIC TOOLS FOR THERMAL PLASMA

During my Ph.D. course, I developed a set of diagnostic tools to investigate thermal plasmas: a Schlieren optical apparatus, a multi-view optical setup for high-speed imaging, an optical emission spectroscopy system (OES) and an apparatus for calorimetric measurements in ICP torches. Selected results of these studies have been submitted for publication[11,12]. In the following section, details about these activities have been reported.

**Schlieren setup for diagnostics of cutting torches**

A recent diagnostic technique is based on the use of high-speed cameras (HSC), coupled with Schlieren photography, a special photographic technique that allows the visualization of density gradients in fluids.
These technologies are an important visual instrument to investigate the phenomena that characterize the plasma arc cutting, as they allow us to study phenomena that could not be investigated by a theoretical point of view or through computer simulations. Indeed, through the high-speed camera you can study phenomena that occur in very short time intervals, which would not be visible using standard cameras. The commonly used standard film provides a frame rate of 24 frames per second (fps), and is not capable of displaying phenomena whose characteristic time is less than $1 / 24 \approx 0.04$ seconds.
The high-speed digital cameras, however, use CCD sensors that can capture images at high speeds. The latest models of high-speed camera allows time resolutions of less than 50 picoseconds, representing more than 20 billion frames per second.
The camera used in this study allows to take 10,000 frames per second and allows the visualization of phenomena such as the attack on the tip of the pilot nozzle, the transition of the pilot arc cathode attachment from the copper part of the electrode to the emitting area of the hafnium insert, the behaviour of the emitting area during different phases of the pilot arc, the double arcing non-destructive phenomena during the cutting phase, the mechanisms of erosion of the cathode, the movement of particles ejected from the surface of hafnium emitter, the dross formation, the effects of a non-perfect alignment of components, the location of the shock wave at the exit of the nozzle.
Only very recently, the use of Schlieren photography, coupled with high-speed recordings has made it possible to display the fluid turbulence that is created by the interaction between the plasma jet, the secondary gas and the surrounding atmosphere. The high-speed Schlieren movies provide qualitative information on the fluid dynamics of the plasma, but the statistical analysis of these films can also provide valuable quantitative information. The purpose of this study is to explore different methods of statistical analysis of data from a movie Schlieren high-speed, find out what information can be extracted from video.
These studies have been done in collaboration with A. Concetti[13]

*Schlieren photography*

Schlieren photography was invented in 1864 by German physicist August Toepler to study the supersonic motion. Since then, the Schlieren photography has found widespread use in the aviation industry to see the air flow around the aircraft. This technique makes it possible to photograph the density gradients in a fluid, resulting in gradients of its index of refraction.
In fact, when in a fluid there is a refractive index gradient, the rays of light passing through it are deflected. The refractive index depends on many parameters such as composition, temperature and density of the medium. Also, its value changes significantly if a gas is ionized.

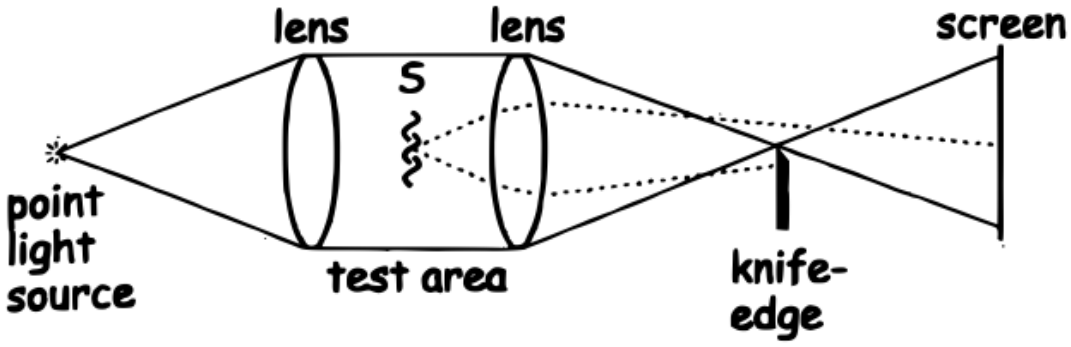


Fig. 1 - Diagram of an apparatus for Schlieren photography with point light source (taken from Ref. 1)

Figure 1 is a schematic of an ideal Schlieren apparatus, which uses a point light source. Even if a real Schlieren apparatus is significantly different from that shown in the diagram, to consider the ideal system is still very useful for understanding the principles of Schlieren photography. In this scheme, the light rays are emitted isotropically from the light source and subsequently collimated by a lens that produces a beam of parallel rays. This beam passes through the object to be tested (S) and then meets a second lens that focuses the rays to a single point, where a knife-edge is placed. After that point, the rays are reversed and produce an inverted image of the object S on the screen. In absence of the knife-edge, the screen cannot display transparent objects present in the test area.
However, if in the focal point of the second lens is introduced the knife-edge, the latter blocks part of the rays refracted by the object S. Since these rays are deflected from their original direction, they do not converge at the focal point, but instead are focused towards neighbouring points. The figure illustrates very clearly the action of the knife-edge on the refracted rays. In fact, the beams deflected upwards illuminate a point on the screen, whereas the beams deflected downward meet the knife and cannot proceed to the screen. The point of the screen where the beam was supposed to come will therefore be dark.
So it's clear that, depending on the orientation of the blade, the image on the screen will be different. The knife blocks only those rays that are refracted perpendicular to the plane of its blade. A vertical knife shows only the horizontal density gradients because the horizontal component of the gradient deflects the rays only laterally but not through it without causing changes in brightness. Conversely, a vertical knife may

show only the horizontal density gradients. Depending on the physical phenomenon in question is therefore very important to choose the proper orientation of the knife.

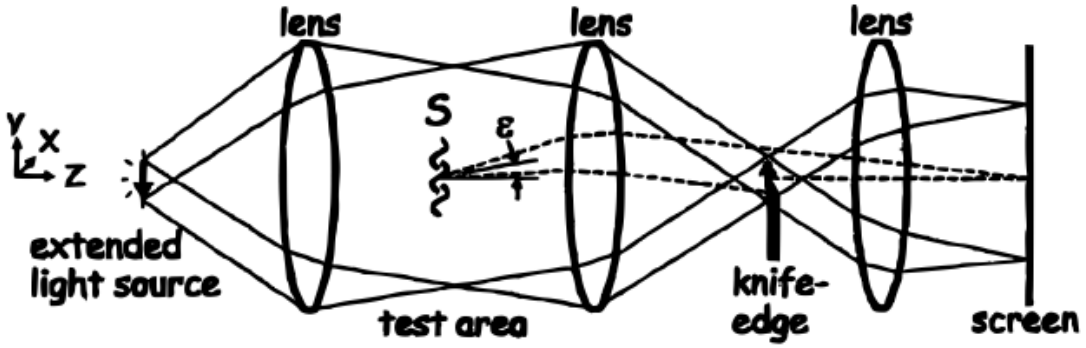


Fig. 2 - Diagram of an apparatus for Schlieren photography with extended light source. (taken from Ref. 1)

Using a point light source is an ideal case. A more realistic case is the one with a light source extended in space (see fig. 2). In this system a third lens downstream of the knife is used to focus an inverted image of the test area on the screen. The plane of the light source and the plane of the knife-edge are a pair of optically conjugated planes, as they are the plane of the screen and the plane of the test. This implies that an image of the light source is focused on the plane of the knife, as well as an image of the object S is projected on the screen. The image obtained on the screen with this apparatus is a grey-scale image.

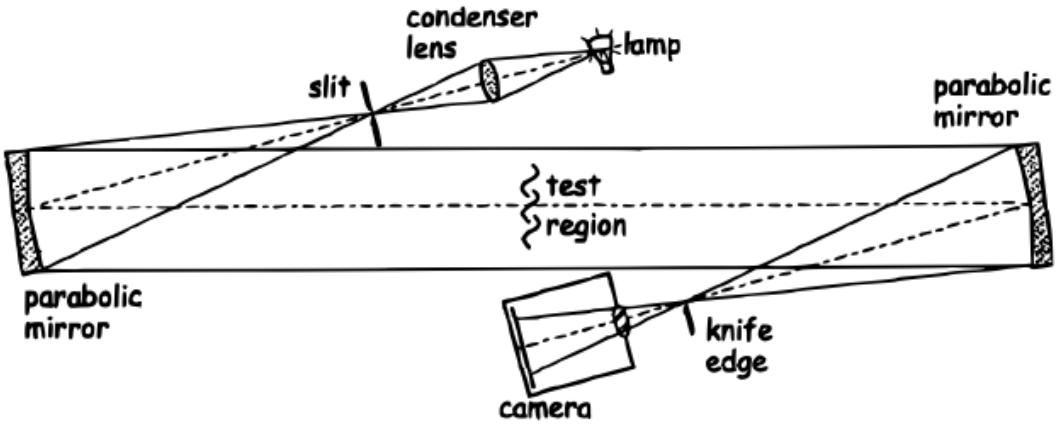


Fig. 3 - Diagram of an apparatus for Schlieren photography: Z-type configuration. (taken from Ref. 1)

The experimental apparatus that was used for this work was built using parabolic mirrors arranged in a Z-setup, as shown in figure 3. In this system, a non-coherent light beam produced by a 450W Xenon lamp is collimated by a lens on a small slit. Next, a parallel beam is produced by two parabolic mirrors tilted in opposite directions. The test area is located between two mirrors, which are positioned at a distance of 2f from each other, where f is the focal length of the mirror.

*Experimental setup*

In designing the Schlieren apparatus for the tests it was necessary to take into account a fundamental characteristic of the physical phenomenon being analyzed: the arc plasma is characterized by a strong light and a very high density gradient. Schlieren photography must have a beam of intensity comparable to that of the phenomenon to observe to get a satisfactory quality image. It was subsequently chosen as light source a Xenon arc lamp, 450W of power. In addition, the slit was adjusted to its maximum opening allowed in order to ensure the highest level of brightness and trying to create an illumination as uniform as possible.
The knife was positioned to cover 50% of the source image. In this way, you create a situation symmetrical to the positive and negative density gradients. To observe the plasma is not necessary to push to the limits the sensitivity of the instrument, because there is a strong plasma density gradient and thus the Schlieren effect is very pronounced.

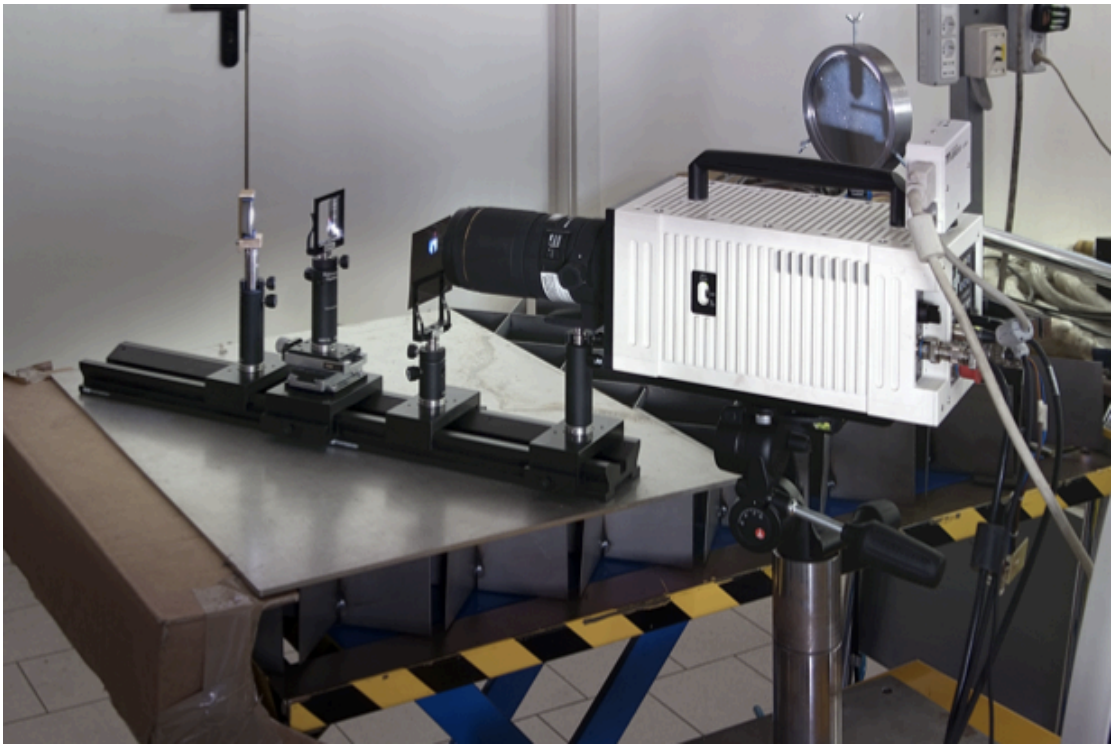

Fig. 4: Picture of the experimental Schlieren setup. At increasing distances from the lens of the camera: a neutral density filter, the knife and one of two small secondary mirrors. It can be seen also in the second floor of the second parabolic mirror, on which it is visible the shadow of the torch and of the workpiece.

For the acquisition of images, the high speed camera NAC Memrecam K3R HS was used, combined with a lens with focal length 180 mm. The high-speed camera used is capable of recording color images with resolutions up to 1280x1024 pixels at 1,000 frames per second, but lower resolution can go up to 10,000 frames per second.

A preliminary study has been carried out with cutting torches with no plasma ignited. The cold flow exiting the torch at supersonic velocity creates density variation that

can be detected with Schlieren imaging. In figure 5, the flow obtained with different operating conditions of the torch has been reported. Shock diamonds can be clearly seen when plasma gas is used. In figure 6, the turbulence pattern created by the flow of a cutting torch in pilot arc phase can be seen. Using different knife-edge orientations it is possible to highlight vertical and horizontal components of the density gradient in the flow. In figure 7, a Schlieren image of a cutting torch during the cutting phase of a mild steel plate has been reported. Strong turbulence can be seen in the upper part of the workpiece that disturb the arc.

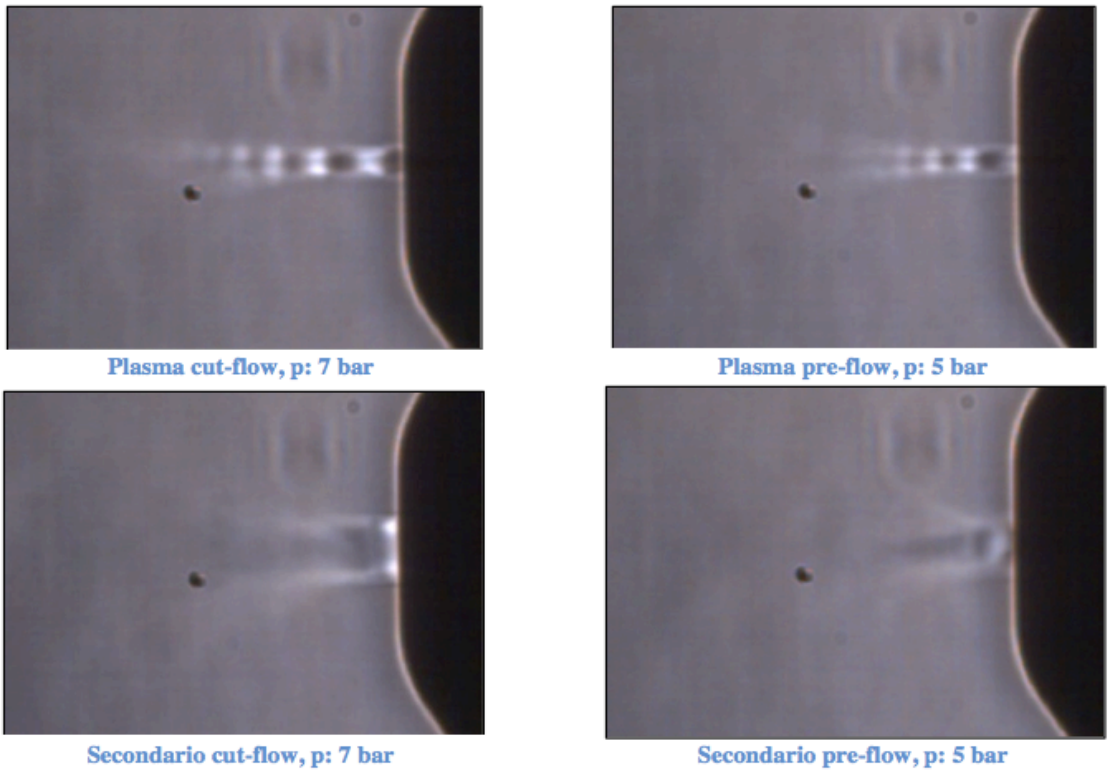


Fig. 5 – Schlieren images of the supersonic flow at the cutting torch nozzle outlet with no plasma power – Acquisition at 5000 fps. Horizontal knife-edge.

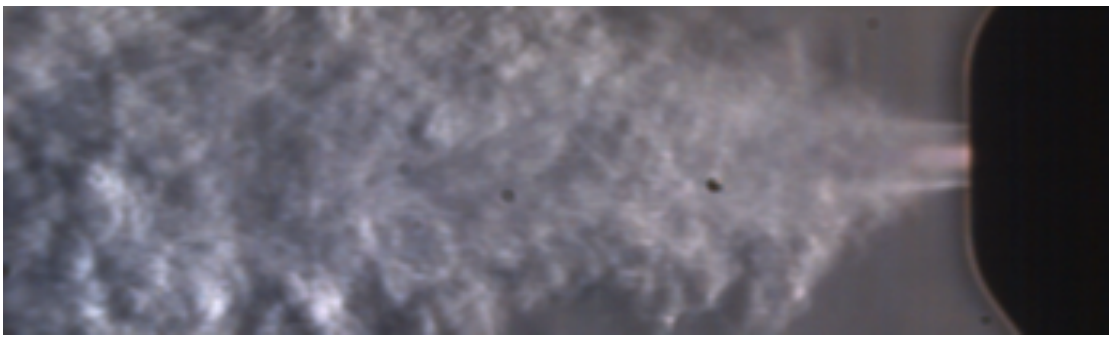

Fig. 6 – Schlieren images of the flow at the cutting torch nozzle outlet during pilot arc phase – Acquisition at 5000 fps. Horizontal knife-edge.

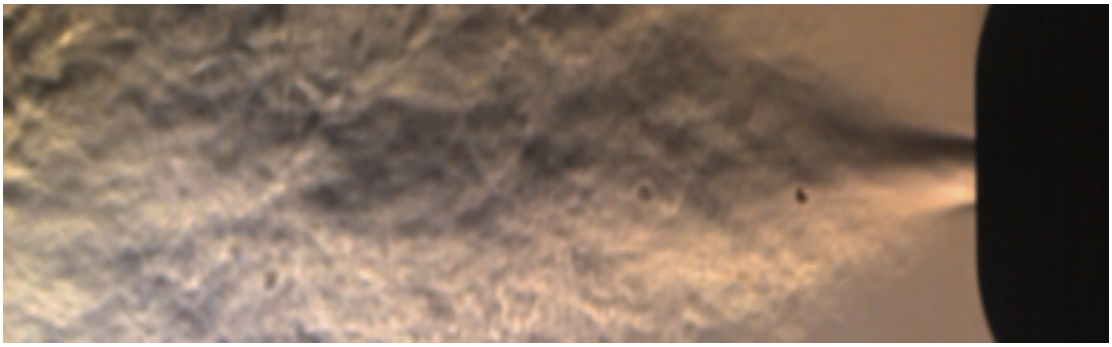

Fig. 7 – Schlieren images of the flow at the cutting torch nozzle outlet during pilot arc phase – Acquisition at 5000 fps. Vertical knife-edge.

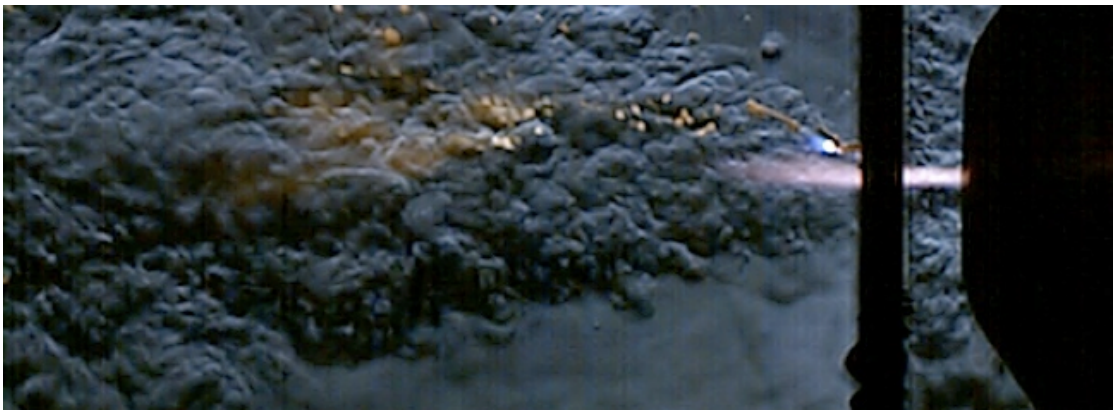

Fig. 8 – Schlieren images of the flow at the cutting torch nozzle outlet during cutting phase – Acquisition at 4000 fps. Vertical knife-edge.

*Statistical Analysis of High-Speed Schlieren Imaging in PAC*

The interaction of plasma gas with the surrounding atmosphere in plasma arc cutting (PAC) has been investigated using high-speed Schlieren imaging. The time-series corresponding to the recorded intensity of each pixel have been post-processed using statistical analysis. Two different methods that highlight the time variation of the amplitude of the fluctuations in the density field have been compared: the windowed standard deviation and the GARCH approach. Whereas a mean-variance analysis can provide at most time-averaged results, GARCH can model the instantaneous variation of the luminous signal, thus providing new insights on the time evolution of the turbulence around the arc.

The high-definition cut requires high power density and high velocity in the plasma jet. Increasing attention has been given to fluid-dynamic instabilities in the fringes of the arc, where the plasma gas (usually $O_2$ for mild steel cutting) mixes with the air coming from both the surrounding atmosphere and the secondary gas, creating strongly fluctuating turbulence patterns. Optical methods like Schlieren and shadowgraphs have proven to be effective in order to visualize these patterns, mainly because they can be associated with high-speed image recording. The Schlieren method is based on the angular deflection undergone by light rays when passing through a region characterized by refractive index gradients.

In this work a Schlieren Z-type setup connected with a high-speed camera (NAC K3) is used to visualize a 25 A arc discharge of a CEBORA manual torch, cutting a 2 mm mild steel workpiece, using $O_2$ both for primary and secondary gas.

The video at 10,000 fps has been post-processed using two statistical methods. In the first one, the "windowed standard deviation", the raw video was divided into 25 frames sub-videos. Each of these was collapsed in a unique frame, where the value of each pixel represents the standard deviation of its corresponding 25 values in the sub-video. A 400 fps video was then constructed using the post-processed frames. The 25-frame window was chosen as a compromise between time-resolution and accuracy of the estimated standard deviation. Since most of the values were truncated due to overexposure of the film, the calculated standard deviation was adjusted hypothesizing an underlying Gaussian distribution. In the second method, the GARCH analysis, the intensity of each pixel was extracted frame-by-frame from the raw movie, yielding a time series of values. Each time series was normalized to zero mean and unit variance and fitted with an AR(1) + GARCH(1,1) model, interpreting each value as the sum of a deterministic trend plus a random noise drawn from a Gaussian distribution with time-dependent variance. For each frame, the value of each pixel in the raw video can be substituted with the value of its corresponding GARCH volatility, the standard deviation of the Gaussian noise, yielding a video representing the instantaneous turbulence in the plasma flow. In Fig. 9 results from windowed standard deviation method and the GARCH analysis have been reported for different time steps together with the corresponding non-processed Schlieren images.

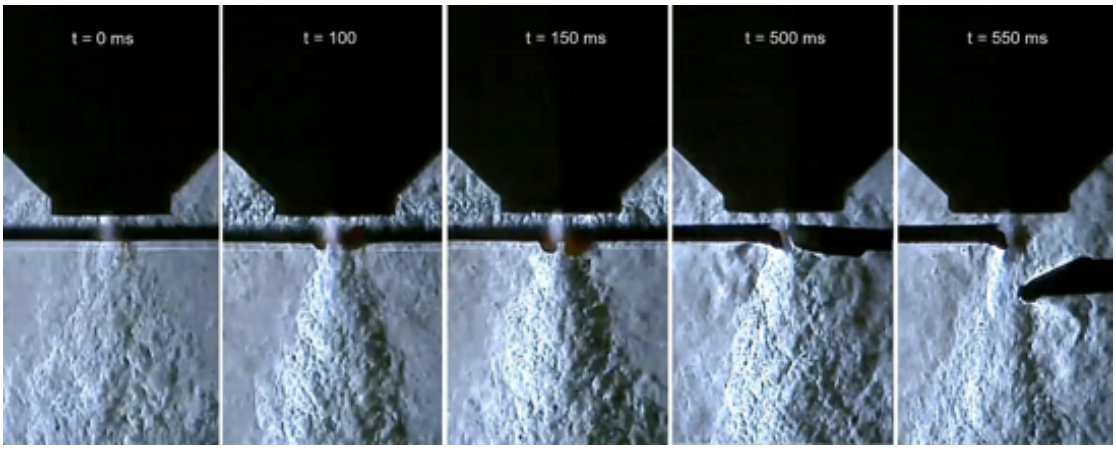

Fig. 9. Schlieren field at different time steps during realistic cutting conditions. (taken from Ref. 12)

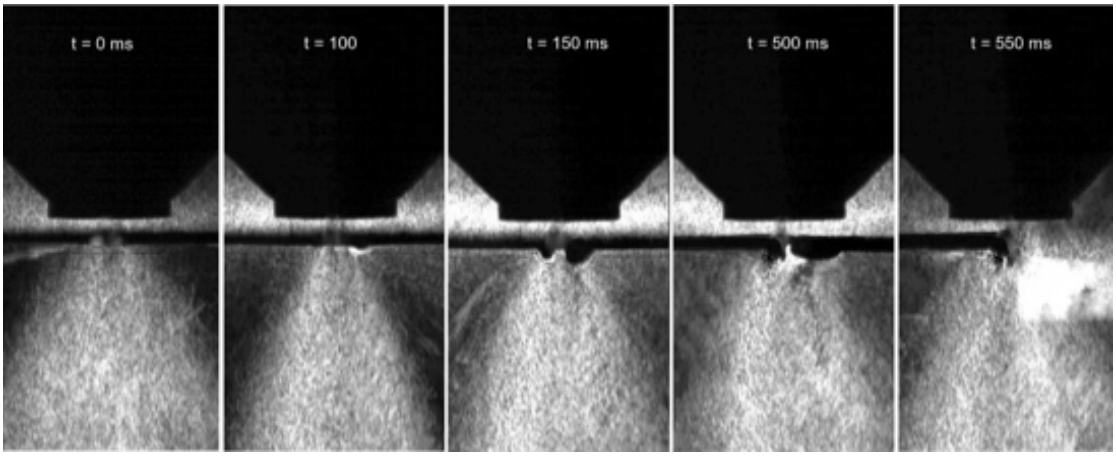


Fig. 10. Windowed standard deviation of the Schlieren field at different time steps during realistic cutting conditions. The scale for the windowed standard deviation is set from black (low) to white (high). (taken from Ref. 12)

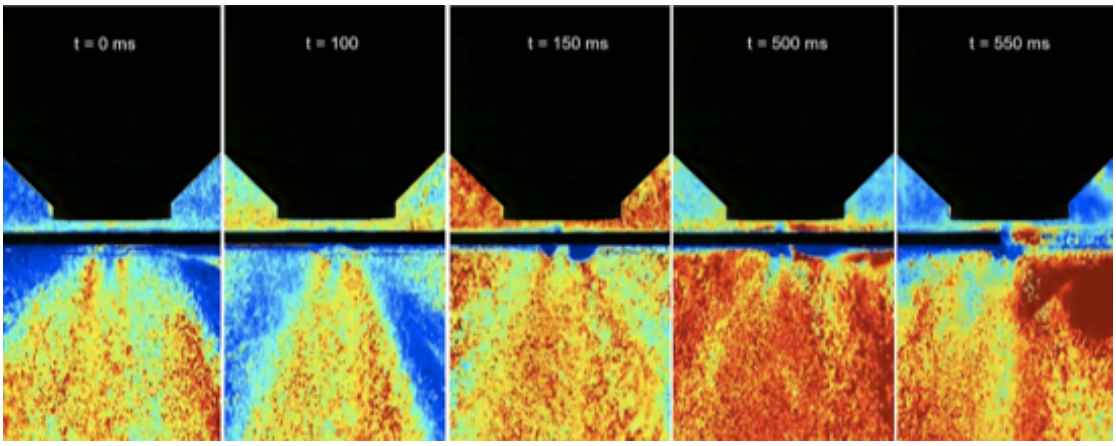


Fig. 11. GARCH volatility of the Schlieren field at different time steps during realistic cutting conditions. The scale for GARCH volatility is set from blue, which means low volatility, to red, which means high variance of the Gaussian noise. (taken from Ref. 12)

**Multiple View and Tomographic Reconstruction of Pilot Arcing Transients**

High-speed imaging of the pilot arc transient phase in plasma arc cutting (PAC) has been carried out synchronizing the use of two high-speed cameras in conjunction with an optical system suitably designed for producing multiple synchronized views of the same phenomenon. Such imaging techniques have allowed a deeper understanding of the pilot arcing process, thanks to the simultaneous visualization of anode and cathode attachments and through the development of tomographic reconstruction of the pilot arc.

During the start-up phase, a low-current (25 A) pilot arc is ignited between the cathode and the nozzle by means of a short high-frequency pulse; the pilot arc is subsequently blown out of the nozzle by the gas flow. Deeper understanding of the non-transferred start-up transient can provide useful information on consumables wear.

In this study, which have been done in collaboration with A. Concetti[13], we report some results obtained with an imaging apparatus composed by two high-speed cameras, a Nac Memrecam K3R and GX3 (180-mm and 200-mm focal-length lens), by an optical system with four plane mirrors and by a digital oscilloscope (LeCroy LT374M) synchronizing the start acquisition time of both cameras. Experiments were carried out with the Cebora multi-gas plasma torch CP251G. In a first set-up (Fig. 12a), one camera, focusing on the cathode surface along the axis of the torch; while the other one can capture the arc loop attachment on the nozzle tip from two side-view points. In a second set-up (Fig. 12b), both cameras are used to capture the pilot arc behaviour outside of the nozzle from three points; a three dimensional tomographic reconstruction of the arc has then been accomplished.

On this basis, the behaviour in time of the anodic attachment during the pilot arcing phase could eventually be fully investigated, also highlighting the spot location and the rotation frequency. Some selected results will be here presented. Figures 13-16 show the axial view focused on the cathode surface together with the synchronized side views showing the behaviour of the arc loop attachment on the nozzle tip; the high frequency impulse being at t=0, the first frame in which the anodic attachment becomes visible in side views is at t=1 ms; the behaviour of the cathodic attachment seen by the axial view has been previously described. For t=1.2 ms, Hf vapours emissions from inside the plasma chamber are visible. For t=5.3 ms, the left side view shows a double anodic attachment, which is hidden in the right side visualization; it is can also be put in correlation with the two bright spots evidenced by the axial view. For t=7.7 ms, massive Hf vapours emissions are shown on both views and can be related to the transition event described by Colombo et al.

In Fig. 17, three synchronized images of the pilot arc are shown; Fig. 18 shows the slices of the reconstructed total emissivity field on four planes located at different heights along the torch axis; Fig 18 shows the three-dimensional total emissivity field reconstructed using images of Fig. 18 and visualized by a single iso-contour surface and volume rendering method, to qualitatively show the arc shape.

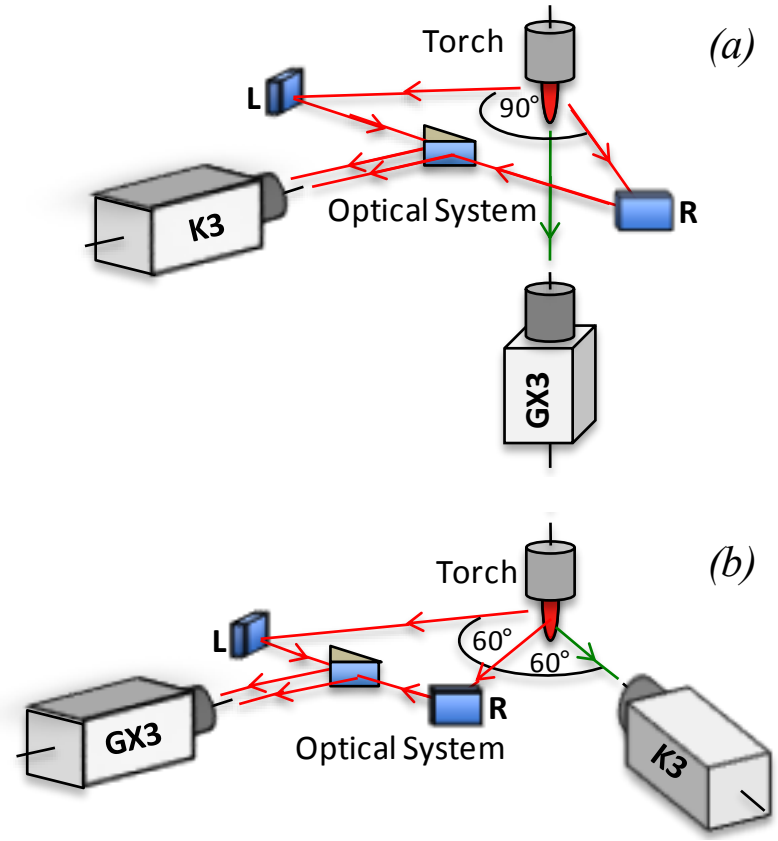


Fig. 12: Scheme of the (a) first experimental set-up and of the (b) second experimental set-up. (taken from Ref. 11)

Fig. 13: Picture of the optical setup for multi-view high-speed imaging. (taken from Ref. 11)

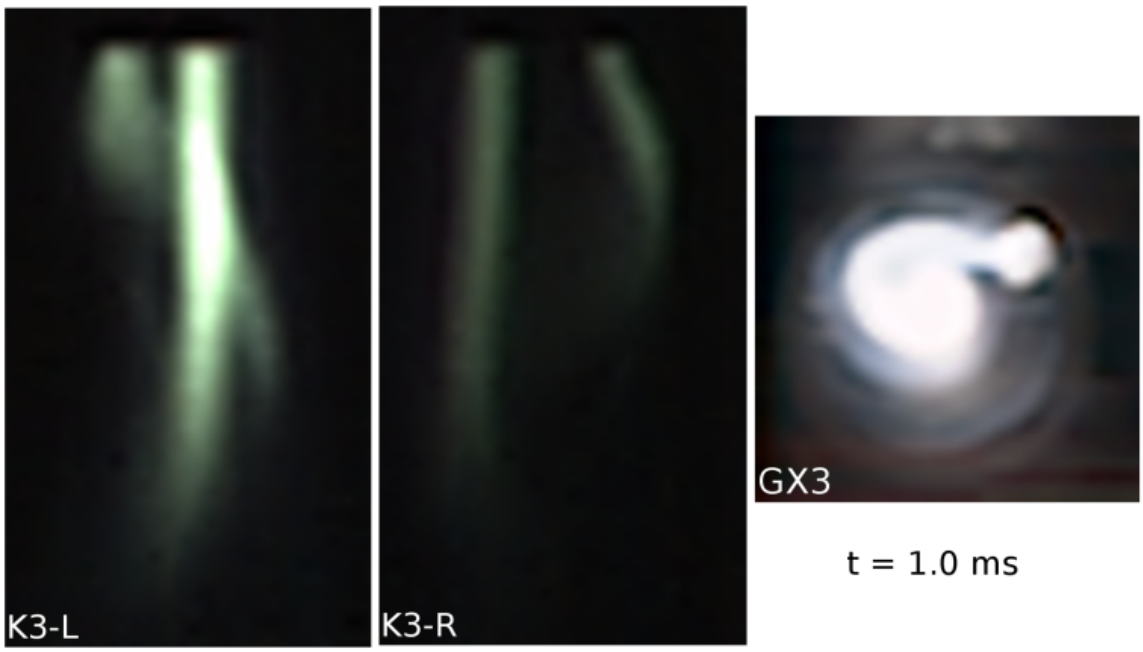


Fig. 14. Side and axial views of the pilot arc at t =1.0ms. Images acquired at 10,000 fps (K3) and 100,000 fps (GX3) and 1/200,000 s shutter time, without any filtering. (taken from Ref. 11)

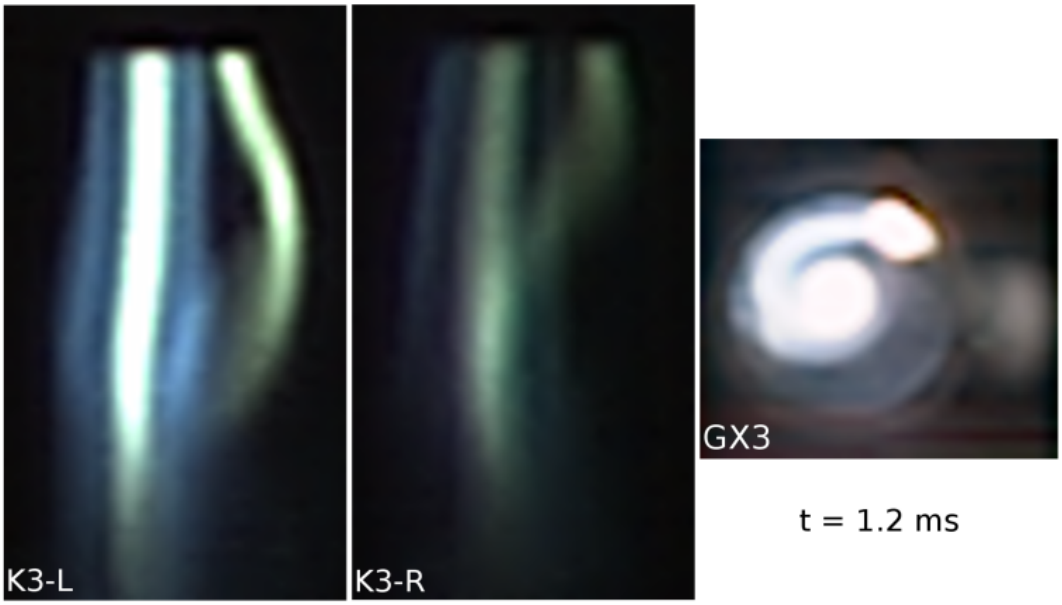


Fig. 15. Side and axial views of the pilot arc at t =1.2ms. Images acquired at 10,000 fps (K3) and 100,000 fps (GX3) and 1/200,000 s shutter time, without any filtering. (taken from Ref. 11)

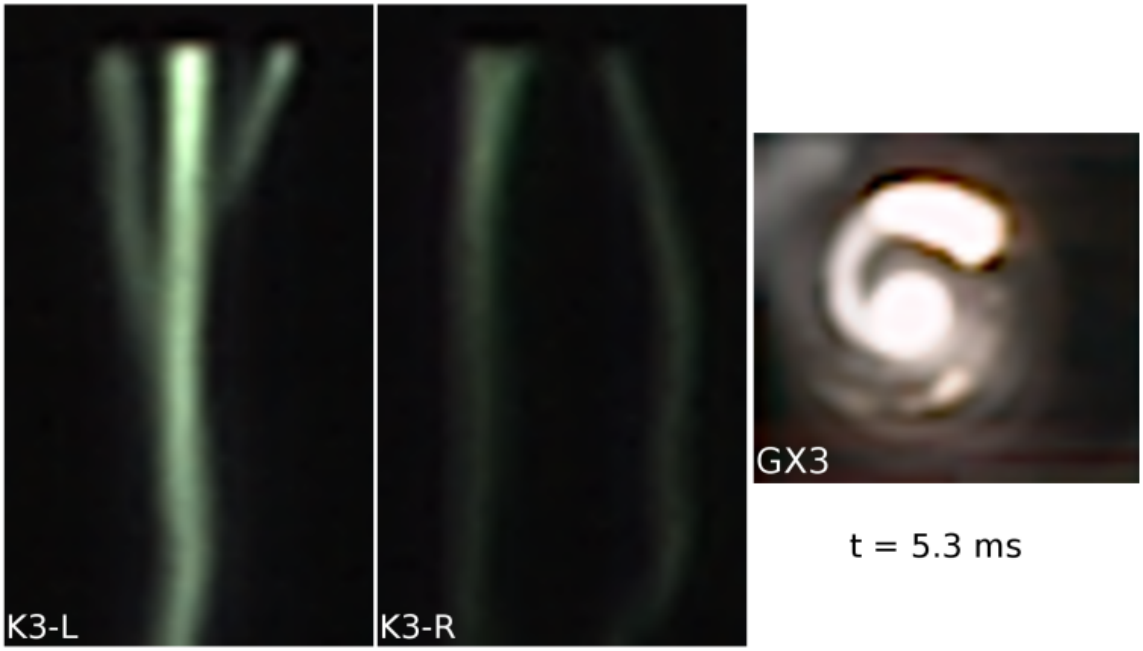


Fig. 16. Side and axial views of the pilot arc at t =5.3ms. Images acquired at 10,000 fps (K3) and 100,000 fps (GX3) and 1/200,000 s shutter time, without any filtering. (taken from Ref. 11)

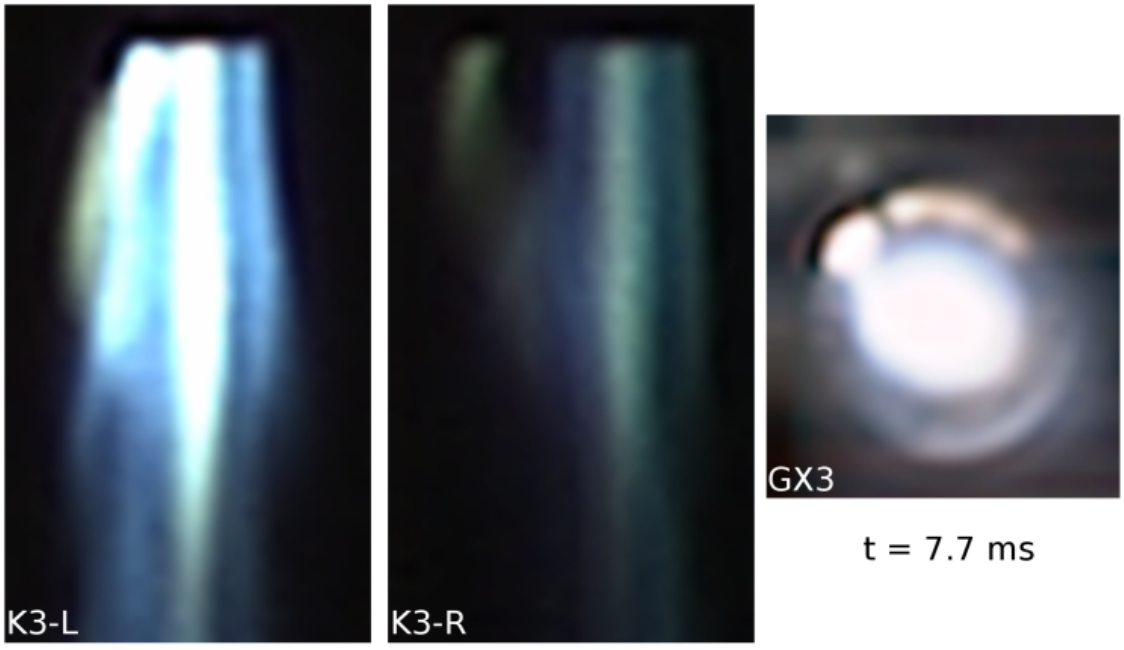


Fig. 17. Side and axial views of the pilot arc at t =7.7ms. Images acquired at 10,000 fps (K3) and 100,000 fps (GX3) and 1/200,000 s shutter time, without any filtering. (taken from Ref. 11)

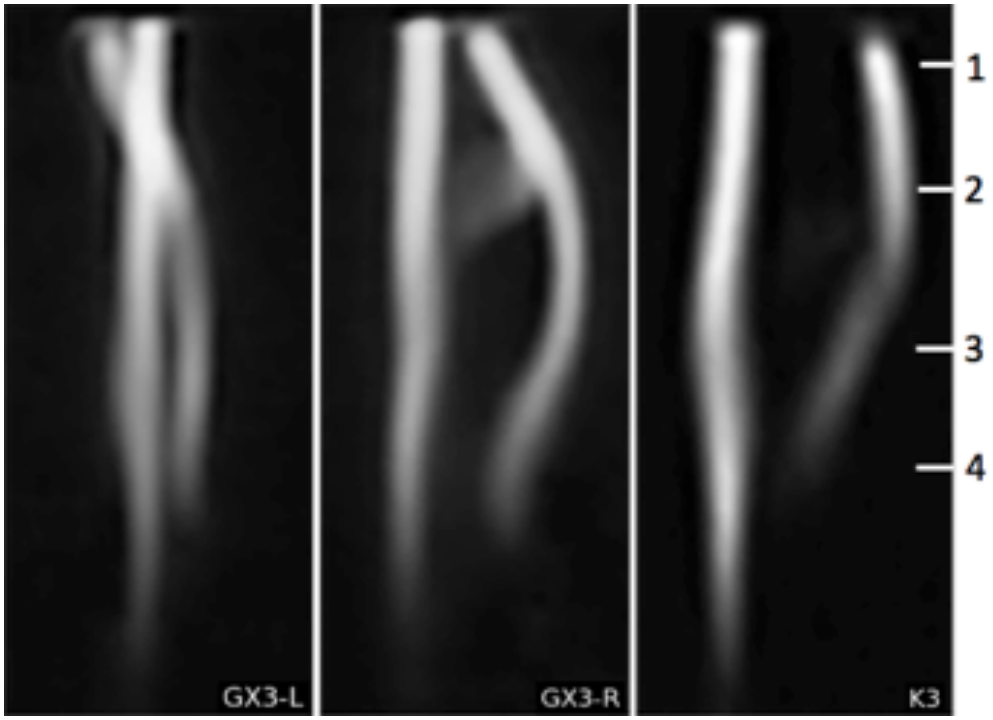

Fig. 18 - Synchronized images of the pilot arc acquired at 10,000 fps and 1/200,000 s shutter time. (taken from Ref. 11)

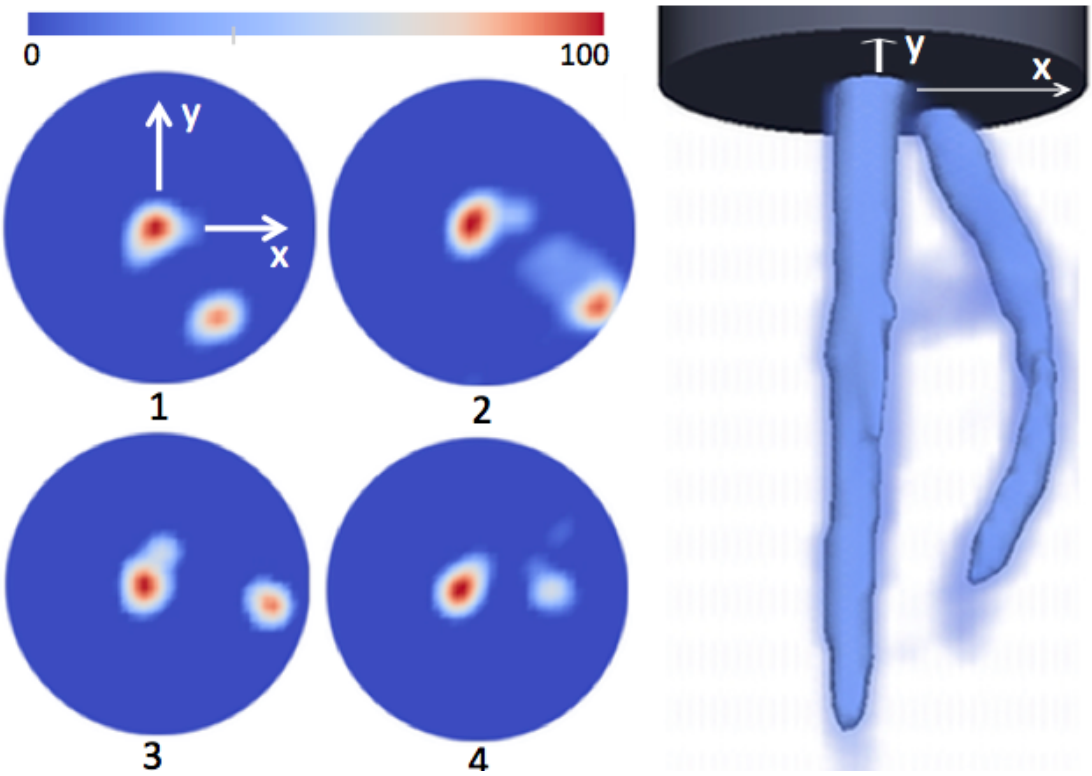

Fig. 19. Total emissivity field slices at different heights (left) and three-dimensional reconstructed emissivity field (right). The GX3-R line of sight lies on the y-axis. (emissivity has been normalized for each slice). (taken from Ref. 11)

**Preliminary results from Optical Emission Spectroscopy (OES) analysis**

Measurement of plasma properties in industrial plasma sources can greatly improve the understanding and performance of these plasma applications. Emission spectroscopy is one of the most widely applied diagnostic methods for the study of plasma sources. During my Ph.D. course I designed and installed at DIEM laboratories an OES system fit for diagnostics of both DC and RF plasma torches. A schematic of the apparatus has been reported in fig. 20.

As a preliminary study, spectroscopic data from a RF plasma torch were obtained using a 500mm focal length spectrometer with a CCD detector. An optical fiber is used to focus the light from the arc onto the entrance of the spectrometer. At the output of the spectrometer a CCD camera is used to record the data. The spectrometer can be operated with three different gratings. This spectrometer with the CCD detector used has the spectral characteristics reported in table 1. The exposure time for data collection can be controlled from a range of milliseconds to seconds depending on whether filters are used and on the intensity of the emission being measured. The repetition rate is about one measurement every 3 s. Spectroscopic constant have been collected from NIST database for different species that are excited in thermal plasma mixture for industrial applications (see figure 21).
In figure 22, an example of experimental spectra recorded from a RF plasma torch (Tekna PL-35) operating in pure argon at a power of 18 kW and discharging in open air atmosphere has been reported. As can be seen in fig. 22, the spectral lines present in the recorded spectra coincide mainly with those of argon but some infiltration of oxygen and nitrogen from surrounding air induces emission at characteristic wavelength of monoatomic oxygen ($\lambda$ = 777nm). No emission from nitrogen can be seen in the recorded spectra.

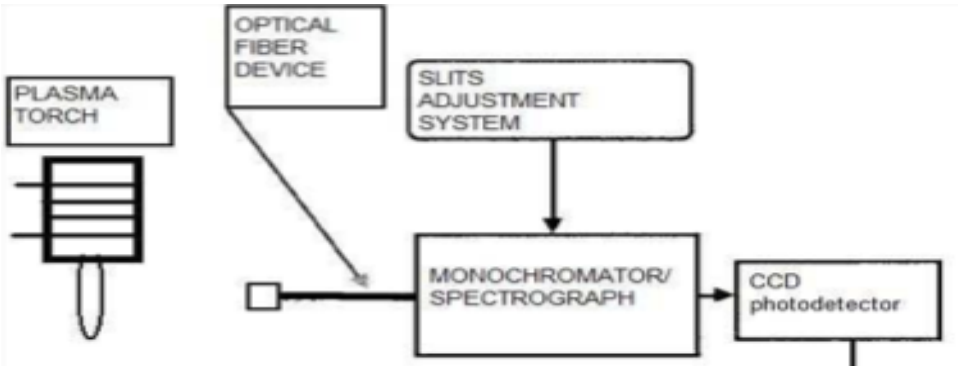


Fig. 20 – Schematic of the experimental setup for optical emission spectroscopy analysis.

Table 1. Range and resolution for different types of grating (central wavelength = 500nm)

| Grating type (grooves/mm) | Range [nm] | Resolution [nm/pixel] |
|---|---|---|
| 150 | 250-700 | 0.34 |
| 1200 | 478-522 | 0.033 |
| 1800 | 485-515 | 0.022 |

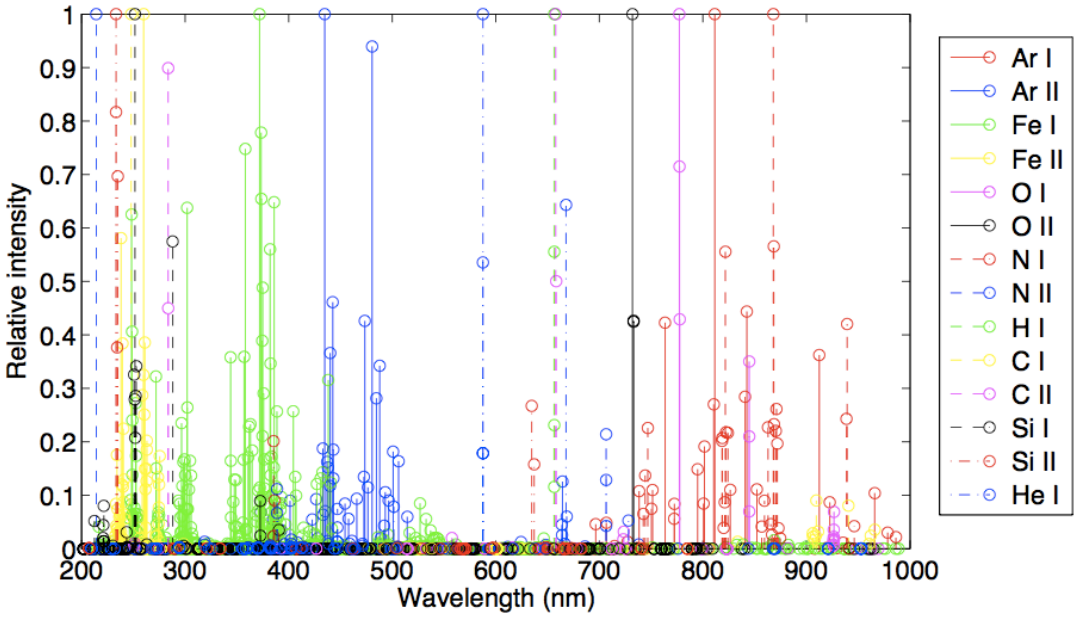


Fig. 21 – Theoretical relative intensity of spectral emission lines for different species at 10,000K normalized to the highest value of each series.

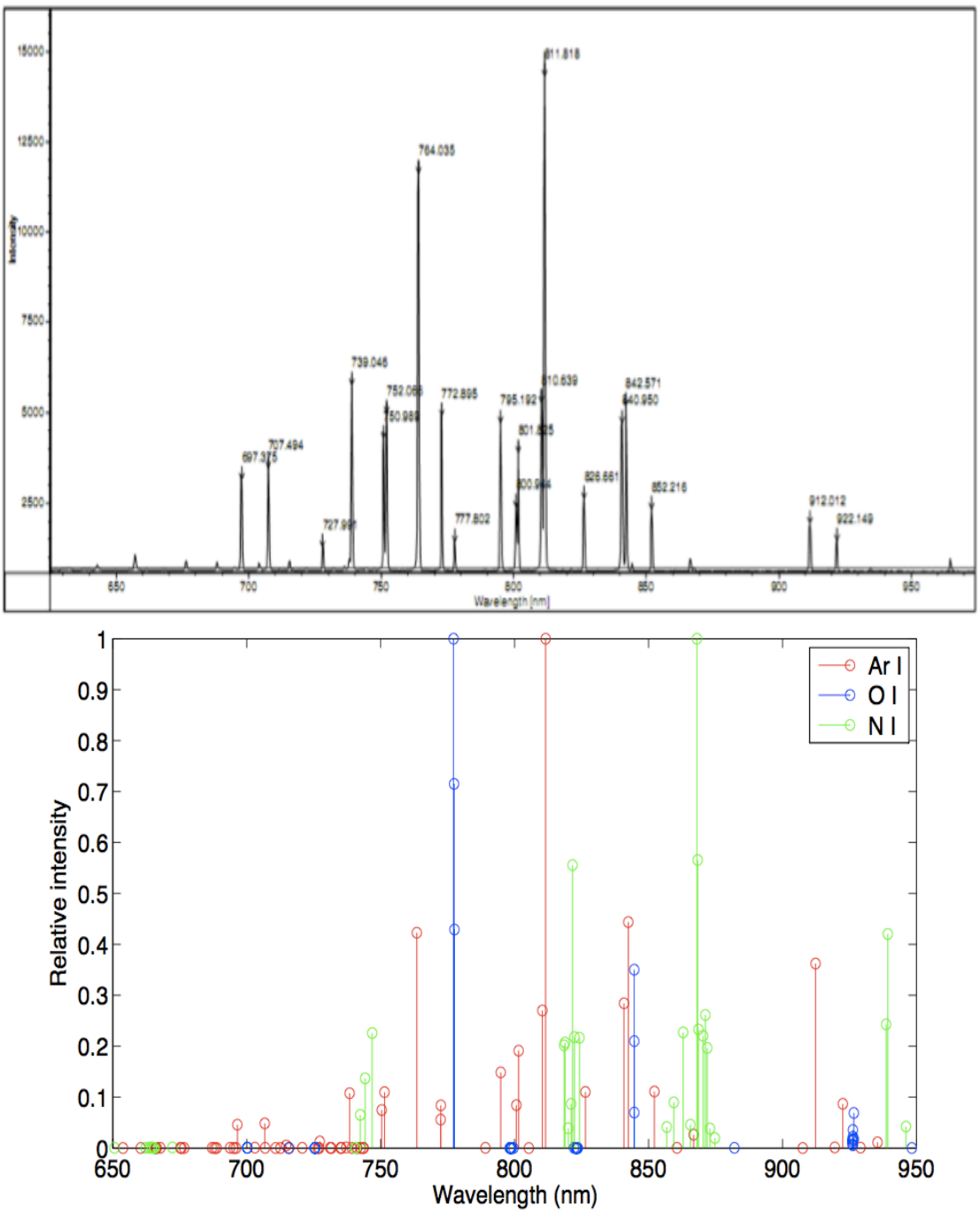


Fig. 22 – Experimental spectral emission from a RF argon plasma discharge (top) and theoretical relative intensity of spectral lines for atomic argon, oxygen and nitrogen at 10,000 K normalized to the highest value of each series (bottom).

**Calorimetric measurements of an induction plasma torch systems**

Considerable research work over the past two decades has been devoted to the mathematical modelling of the inductively coupled radio frequency plasma. These provide a valuable insight in to the basic transport phenomena involved under a wide range of operating conditions. Most of the proposed models assume, however, as the induction power a numerical value given by the user, estimated from total power input to the radio-frequency generator using the generator efficiency reported in literature for similar systems.
The goal of the present study is to experimentally determine the power coupled to the torch using a calorimetric approach. Other research groups have successfully tested the latter. During my Ph.D. thesis I developed and installed the apparatus for calorimetric measurements of the ICP torch system at DIEM laboratories. The calorimetric apparatus that I developed will serve to investigate the torch efficiency under different operating conditions, resulting in a complete characterization of the efficiency of the lab-scale torch at DIEM. Data obtained in this study will be used as input for the modelling activities of the research group.
As done by Merkouf et al.[10], the cooling water temperature has been separately measured for different components of the ICP system: coil, triode, torch, probe, and camera. The energy balance, neglecting the contribution of the inlet and outlet gases, can be written as:

$$P_{dc} = P_{coil} + P_{tride} + P_{torch} + P_{probe} + P_{camera}$$

where $P_{dc}$ in the total power input given by the product of measured DC voltage and current in the generator; $P_{coil}$ and $P_{triode}$ are the losses in the induction coil and in the oscillator tube, respectively; $P_{torch}$ and $P_{probe}$ are the cooling losses in the torch walls and injection probe, respectively; $P_{camera}$ is the cooling losses in the reaction chamber.
The cooling losses can be calculated from cooling water temperature measurements:

$$P_i = \dot{m}_i C_p (T_{out} - T_{in})$$

where $m_i$ is the mass flow rate of the cooling water and $C_p$ is the specific heat of water.
The *generator efficiency* can be defined as the ratio between power coupled to the plasma discharge $P_{plasma}$ and the total inlet power to the generator $P_{dc}$, where

$$P_{plasma} = P_{torch} + P_{probe} + P_{camera}$$

whereas the *torch efficiency* can be defined as the ratio between the power coupled to the plasma discharge and the power entering the reaction chamber.
The *total efficiency*, defined as the ratio between power entering the chamber and input DC power to the generator, can be calculated as the product of generator efficiency and torch efficiency.
Selected results are reported in figure 23 and table 2. The generator efficiency is around 62%, as reported in literature, and it is almost constant for different pressures; whereas the torch efficiency is decreasing with increasing pressure as the radiation losses to the torch wall increase.

Table 2 - Results from calorimetric measurements on a 28kW PL-35 torch with reaction chamber operated with 16 slpm Ar and 60 splm $N_2$ for different values of the reactor pressure.

| **Reactor pressure (kPa)** | **30** | **60** | **90** |
|---|---|---|---|
| **P dc (kW)** | 28 | 28 | 28 |
| **P coil + P triode (kW)** | 10,7 | 10,6 | 10,6 |
| **P probe (kW)** | 1,6 | 1,8 | 1,8 |
| **P torch (kW)** | 3,2 | 4,5 | 5,5 |
| **P camera (kW)** | 12,3 | 11,0 | 10,3 |
| ***Generator efficiency (%)*** | 61,2 | 61,8 | 63,0 |
| ***Torch efficiency (%)*** | 71,9 | 63,3 | 58,5 |
| ***Total efficiency (%)*** | 44,0 | 39,1 | 36,9 |

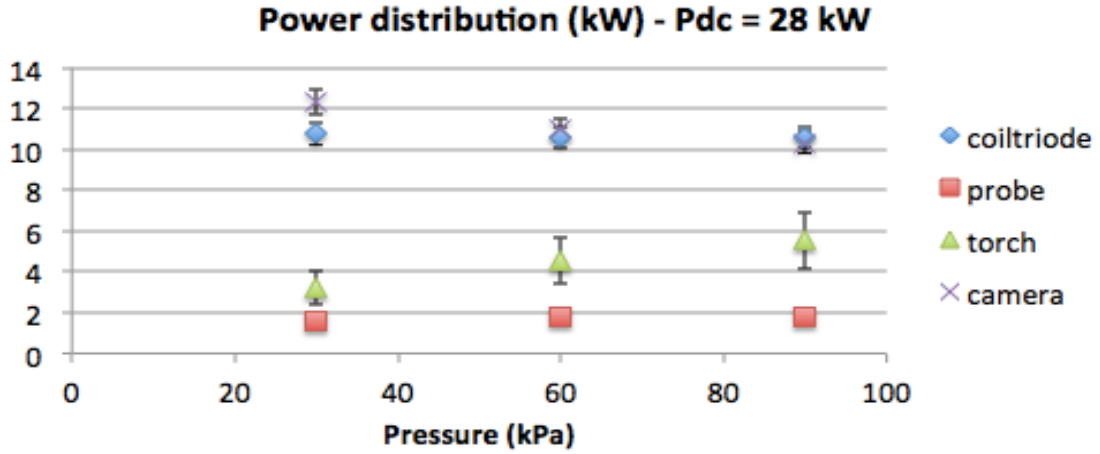


Fig. 23 – Cooling water losses for a plasma discharge in a Tekna PL-35 torch operated at 3 MHz with 16 slpm Ar/60 splm N2 for different values of the reactor pressure.

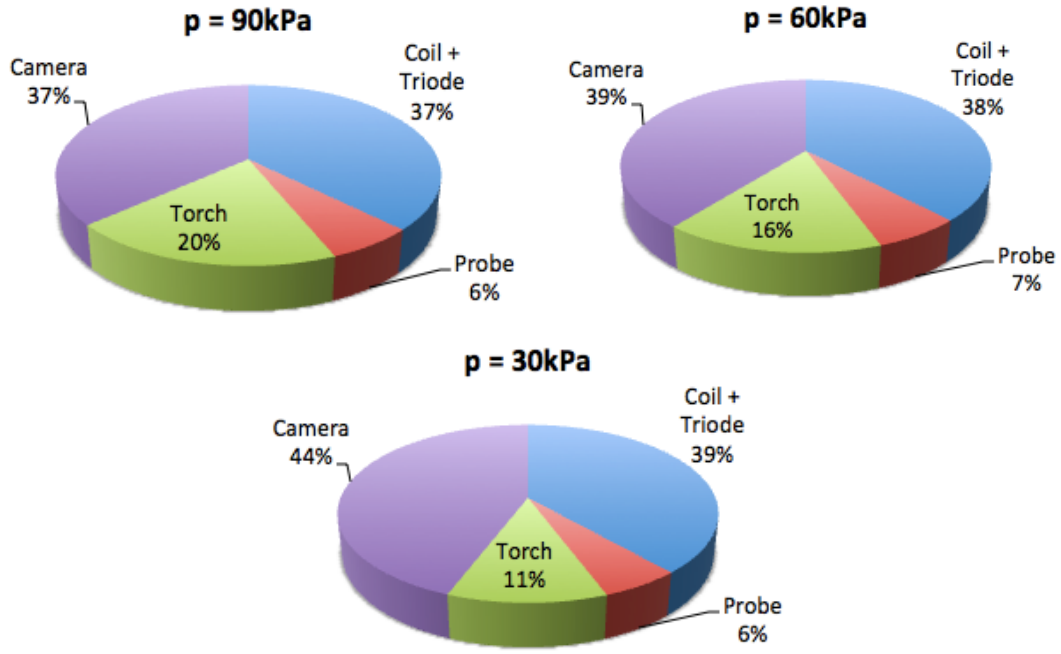


Fig. 24 – Energy distribution in a Tekna PL-35 torch operated at 3 MHz with 16 slpm Ar/60 splm N2 for different values of the reactor pressure.

References


1. G. S. Settles, “Schlieren and shadowgraph techniques”, 2001, Springer-Verlag, Berlin Heidelberg, New York
2. V. A. Nemchinsky and W. S. Severance, “What we know and what we do not know about plasma arc cutting” Journal of Physics D: Applied Physics, vol. 39, 2006, pagg. R423-R438.
3. S. Kim, J. Heberlein, J. Lindsay and J. Peters, “Control of fluid dynamic instability in oxygen plasma arc cutting” Proceedings of ISPC 19, Bochum, 2009.
4. V. Colombo, A. Concetti, E. Ghedini, S. Dallavalle, and M. Vancini, “High-speed imaging in plasma arc cutting: a review and new developments” Plasma Sources Science and Technology, vol. 18, 2009, pag. 023001.
5. L. Prevosto, G. Artana, B. Mancinelli, e H. Kelly, “Schlieren technique applied to the arc temperature measurement in a high energy density cutting torch” Journal of Applied Physics, vol. 107, 2010, pag. 023304.
6. T. Bollerslev, "Generalized Autoregressive conditional Heteroskedasticity", Journal of Econometrics, vol. 31, 1986, pag. 307-327.
7. Kavka T et al. 2009 “Anode processes during pilot arcing in cutting torch” 19th International Symposium on Plasma Chemistry - ISPC19 (Bochum, Germany).
8. Colombo V, Concetti A, Ghedini E and Nemchinsky V 2010 “High-speed imaging investigation of transition phenomena in the pilot arc phase in Hf cathodes for plasma arc cutting” Plasma Sources Sci. Technol. 19 065025
9. Mishra D, Muralidhar K and Munshi P 1999 “A robust mart algorithm for tomographic applications” Numerical Heat Transfer, Part B: Fundamentals 35:4 pp. 485-506.
10. Merkhouf A and Boulos M I 2000 “Distributed energy analysis for an integrated radio frequency induction plasma system” J. Phys. D: Appl. Phys. 33 1581
11. Boselli M, Cantoro G, Colombo V, Concetti A, Ghedini E, Gherardi M, Sanibondi P, “High-Speed Imaging in PAC: Multiple View and Tomographic Reconstruction of Pilot Arcing Transients”, submitted to IEEE-TPS Image in Plasma Science
12. Cantoro G, Colombo V, Concetti A, Ghedini E, Sanibondi P and Zinzani F, “Statistical Analysis of High-Speed Schlieren Imaging in PAC”, submitted to IEEE-TPS Image in Plasma Science
13. A. Concetti 2011 “Integrated approaches for designing and optimizing thermal plasma processing for metal cutting and material treatment”, Ph. D. thesis, Alma Mater Studiorum – University of Bologna, Italy.

# INVESTIGATION ON THE EFFECTS OF METALLIC VAPOURS ON THE CHARACTERISTICS OF THE ANODE LAYER IN HIGH-INTENSITY CURRENT ARC

In this chapter, I will show some preliminary results obtained in collaboration with Prof. Valerian Nemchinsky - now at Keiser University, Florida, USA – on the investigation of the anode region of high intensity arcs at atmospheric pressure in presence of metallic vapours.

## Introduction

Anode in a high-current arc is subjected to a high heat flux. Total thermal flux to an anode may be up to a few times higher than that of cathode although the anode flux is not so concentrated. The anode may evaporate under influence of this flux. Anode evaporation changes the properties of the near-anode plasma and of an adjacent arc column. Influence of anode evaporation on the characteristics of arc column was explored in a number of papers [1-9]. Its influence on the near-anode plasma (anode layer) is considered in this paper.

Anode layer is a relatively narrow (on order of $10^{-3}$ m) close to the anode region of plasma, which properties are distorted by the anode proximity. Although cooling the near anode plasma reduces its conductivity, the average electric field in the layer is lower than in arc column (negative anode layer voltage). Reduction of the electric field in the anode layer has a very simple explanation: decreasing towards anode temperature results in a sharp reduction in electron concentration. This gives rise to a diffusion flux of electrons in the anode direction. Diffusion can contribute a substantial part of the total arc current thus causing reduction of the electric field. In some places the diffusion current can even overcome the whole current so that electric field changes its sign in these places to keep the current constant.

Importance of the anode layer in the whole arc behavior can be seen from the following. The voltage across the anode layer is about a few volts whereas the total voltage at a free-burning arc is about 15 to 20 volts. Taking into account that about 10 volts of this total voltage is due to cathode voltage drop, the importance of anode layer characteristics becomes even more evident.

The effect of electron diffusion in anode layer was examined in many works, both theoretically [10-25] and experimentally [26-28]. Presence of vapors of material with low ionization potential in the anode proximity can substantially change properties of the anode layer. In particular, in [2] the following scenario of “snow ball” instability was suggested: local increase in the anode temperature causes local increase in evaporation rate, which leads to a local increase in electrical conductivity of plasma. This causes the current redistribution over the anode surface: current concentrates on this particular spot, thus increasing evaporation and so on. On the other hand, another scenario was described in [23]. According to [23], evaporation, by virtue of delivering extra electrons into anode layer, decreases the electron concentration

gradient, and thus reduces electron diffusion toward the anode and, therefore, prevents local current and heat flux concentration.

It should be noted that entrance of a low ionization vapor to the anode layer not necessarily decreases electron diffusion. Presence of a low ionization vapor close to the anode leads to reduction in plasma temperature, factor that at the given plasma column temperature, increases the concentration gradient. As a result, electron concentration close to the anode could change in both directions: it could increase and it could decrease. Only quantitative consideration can answer the question, which way it changes. The aim of this paper is to show the results of such calculations and to perform experiments to check them.

It is worthwhile to consider briefly the structure of an anode layer before proceeding to describe our modeling of anode layer (the more detailed consideration of the anode layer structure one can elsewhere, see, for example, works [10-12] and a recent review [29, 30]).

The most remote sub-layer corresponds to ionization equilibrium, quasi-neutral plasma, which single temperature decreases toward the anode due to its cooling effect. Closer to anode there is a sub-layer where two temperatures (one of electrons and another of heavy particles) split: heavy particle temperature approaches the anode temperature whereas the electron temperature remains relatively high to maintain plasma electrical conductivity. The next closer to anode sub-layer is a region where ionization equilibrium fails: decrease the electron concentration towards the anode leads to a situation when ionization (proportional to the first power of electron concentration) is not balanced by recombination (proportional to a higher power of electron concentration). Outside of this sub-layer the ionization equilibrium holds. Finally, the closest to the anode sub-layer is the sheath where the quasi-neutrality fails. Here the unbalanced net charge is located (positive if ion concentration prevails and negative in the opposite case). The net space charge exists only inside this very thin layer.

In the case of evaporating anode, there is additional characteristic length: the size of the evaporating region at the anode surface. One should distinguish between two extreme cases. One is when the evaporating part of the anode layer is comparable to or smaller than the thickness of the layer (small protrusions). In this case, plasma composition changes throughout the layer. This is two-dimensional or even three-dimensional case. In the opposite case the size of the evaporation region is substantially larger that thickness of the layer. As a result, concentration of the evaporated particles remains constant throughout the layer. One may neglect parameters variation along the anode, and the problem becomes one-dimensional. This is the case we are going to consider in the first part of this paper.

**Peculiarity of electron conductivity close to evaporating anode**

The most important fact is that anode material atoms have substantially lower ionization potential than that of the main plasma atoms. Therefore, even a small amount metal atoms change the ionization state of plasma especially close to anode where temperature is low and ionization degree of the main plasma gas is low.

It is worthwhile to note that presence of metal ions do not increase plasma conductivity but rather decrease it. The electrical conductivity can be expressed as $\sigma = \frac{ne^2}{m\nu}$, where electron collision frequency n is $\nu = \bar{v}_e(n_i S_{ei} + n_a S_{ea})$. Here $n_i=n_e$ is the charged particles concentration, $S_{ei}$ and $S_{ea}$ are the Coulomb and electron-atom scattering cross-sections, respectfully and $v_e$ is electron thermal velocity. Typical value of Coulomb scattering cross-section is $10^{-13}$ $cm^2$, whereas $S_{ea}$ has $10^{-16}$ $cm^2$ order of magnitude. Because this big difference in orders of magnitude of the cross-sections, the influence of electron-neutral atoms scattering is negligible unless the degree of ionization falls below $\sim 10^{-3}$, which could happen either very close to the anode or in the arc fringes. In the case when Coulomb scattering dominates, electrical conductivity depends on plasma temperature, not on the electron concentration. That is why, entrance of evaporated atoms into the near-anode region, which cools the plasma, mostly reduces its electrical conductivity.

Electron diffusion plays the most important role in current flow inside the anode layer. Taking the diffusion into account, the generalized Ohm's law can be written as

$$J = \sigma(E - \frac{T}{n}\frac{dn}{dx}). \qquad (1)$$

The electron concentration in an ionization equilibrium plasma is a function of the plasma temperature: n=N(T). After substitution this in the Ohm's law, we have

$$J = \sigma(E - \frac{dLn(N)}{dLn(T)}\frac{dT}{dx}). \qquad (2)$$

In view of high temperature gradients, and high logarithmic derivative of concentration with respect to temperature logarithm $\gamma = \frac{dLn(N)}{dLn(T)}$, diffusion plays a special role in current flowing inside the anode layer.

The typical behavior of logarithmic derivative g is as flows. At low temperatures, when plasma has low degree of ionization, N is proportional to $\exp(-E_{ion}/2T)$ and, therefore, $g=E_{ion}/2T >>1$. The value of g decreases as temperature increases. When plasma reaches the fully ionized state, γ turns to zero. Further temperature increase reduces g even further, at higher temperatures it asymptotically approaches –1. The graph of g(T) dependence for Ar plasma at atmospheric pressure is shown in figure 1. Note that this graph doesn't depend on electron concentration.

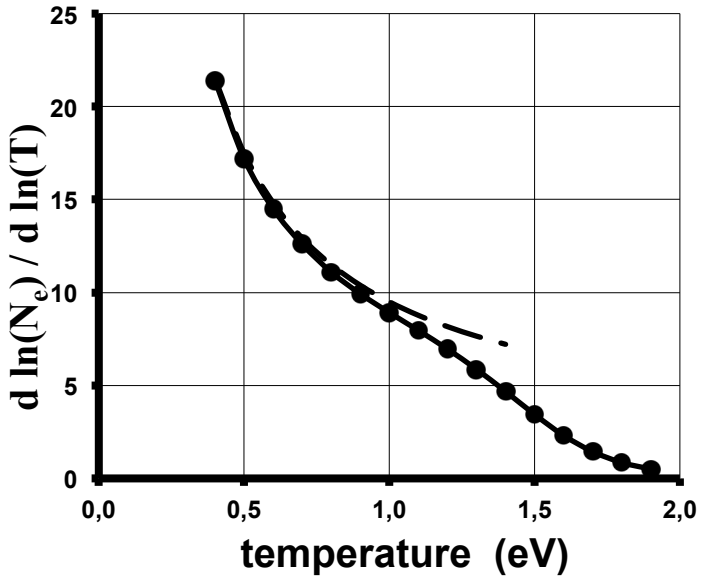

Fig. 1. Logarithmic derivative of electron concentration with respect to the plasma temperature (parameter γ.) Argon. 1 atmosphere.

Now let us consider γ behaviour in plasma made of mixer of two type of atoms; small addition of atoms first kind (with relatively low ionization potential $E_{ion,1}$) to bulk of gas of another kind with higher ionization potential $E_{ion,2}$. Presence of even a small amount of easily ionized atoms changes γ dependence on temperature dramatically. One can see this from the following simple consideration.

For γ one can write an approximate expression

$$\gamma = \frac{N_{i,1}}{N_{i,1} + N_{i,2}}\gamma_1 + \frac{N_{i,2}}{N_{i,} + N_{i,2}}\gamma_2 . \qquad (3)$$

Here $N_{i,1}$ and $N_{i,2}$ are concentration of ions of first and second kind ($N_{i,1}+N_{i2}=N_e$), and $g_1$ and $g_2$ are the corresponding parameters for type one and type two gases. Now, let us see how γ changes as plasma temperature increases.

At very low temperature only atoms of type 1 are ionized. The coefficient $N_{i,1}/N_e$ is close to unity and the second coefficient $N_{i,2}/N_e$ is much less than unity. The total g follows the temperature dependence of $g_1$: it decreases or even changes its sign if atoms of the first type become fully ionized before any significant number of ions of the second type arrives. At higher temperatures, concentrations of both types of ions become comparable. Total g then leaves the $g_1$ curve and approaches the $g_2$ graph. At even higher temperatures, when most of ions are of the second type (gas of the first type is a small addition to the bulk gas 2), the total g follows the $g_2$ curve.

We calculated behavior of the g parameter for the mixture of argon (gas 2) and small addition of copper vapor (gas 1). Total pressure of the mix is one atmosphere. Copper concentration is characterized by parameter

$$c = \frac{N_{Cu} + N_{Cu^+}}{N_{Ar} + N_{Ar^+}} . \qquad (4)$$

Figure 2 shows the result of these calculations for some specific values of parameter c.

One can see that presence of even a small amount of copper atoms changes the parameter γ dramatically. Since this parameter determines diffusion contribution to the current flow, this could affect the characteristics of the whole anode layer. Namely, anode evaporating could deteriorate flow conditions of the electric current: it could result in increase of the voltage across the layer instead of its decrease as it might appear at the first glance. The aim of this work is to analyze this phenomenon quantitatively.

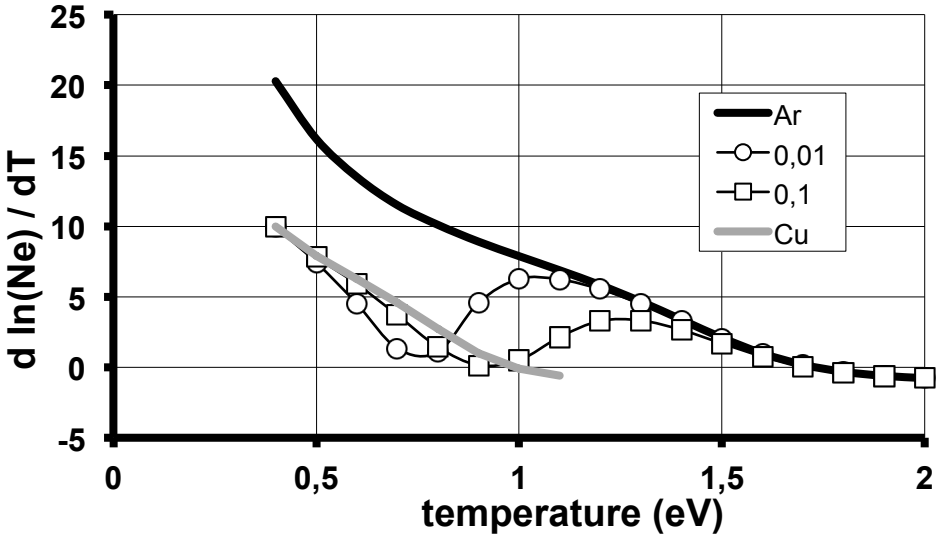


Fig. 2. Parameter γ for different Argon-copper vapor compositions. Bold line: pure Ar, Grey line: Pure copper vapor. Circles: 99 mol. % Ar + 1 mol %Cu; squares: 90 mol.% Ar + 10 mol.% Cu.

**Description of the mathematical modelling**

Let us start with the energy balance of electrons. The electron heat flux density $q_e$ consists of two terms: heat conduction ($- k_e \frac{dT_e}{dx}$) term and heat convection ($3.2\frac{j}{e}T_e$) term:

$$q_e = -\kappa_e \frac{dT_e}{dx} + 3.2\frac{J}{e}T_e \qquad (5)$$

Electrons either gain their energy from electric field (if the field moves them toward the anode: E>0) or they lose their energy if electric field acts in the opposite direction (E<0). Also, they lose energy by radiation and in electrons collisions with heavy particles. The energy balance for electrons has the following form

$$\frac{dq_e}{dx} = JE - W - 3\frac{m}{M}n_e\nu(T_e - T_h). \qquad (6)$$

Here J is current density, E is electric field (we remind that $J = \sigma(E - \frac{T}{n_e}\frac{dn_e}{dx})$). W is power of radiation per unit volume, m and M are masses of electrons and heavy particles, and $T_e$ and $T_h$ [1] are temperatures of electrons and heavy particles, respectfully.
The heat flux density of heavy particle, $q_h$ is due to conduction

$$q_h = -\frac{dT_h}{dx} \qquad (7)$$

It changes due to electron-heavy particles collisions

$$\frac{dq_h}{dx} = 3\frac{m}{M} n_e \nu (T_e - T_h) \qquad (8)$$

To describe ionization non-equilibrium part of anode layer, one should consider ions diffusion and ionization-recombination of both sorts of particles (copper and argon) in the layer. Strictly speaking, diffusion of two sorts of ions should be described by a diffusion matrix:

$$J_{Ar+} = -D_{Ar,Ar}\nabla n_{Ar} - D_{Ar,Cu}\nabla n_{cu} \qquad (9)$$

$$J_{Cu+} = -D_{Cu,Ar}\nabla n_{Ar} - D_{Cu,Cu}\nabla n_{cu} \qquad (10)$$

Divergences of these flux densities are equal to rates to ionization-recombination of the corresponding ions:

$$\frac{d}{dx}(J_{Ar^+}) = \alpha_{Ar} n_{Ar} n_e - \beta_{Ar} {n_e}^2 n_{Ar^+} \qquad (11)$$

$$\frac{d}{dx}(J_{Cu^+}) = \alpha_{Cu} n_{Cu} n_e - \beta_{Cu} {n_e}^2 n_{Cu^+}, \qquad (12)$$

where $\alpha_{Ar}$, $a_{Cu}$ and $b_{Ar}$, $b_{Cu}$ are ionization and recombination coefficients of the argon and copper, respectively. To calculate concentrations of all plasma species equations (11) and (12) should be added by the Dalton's law:

$$T_h(n_{Ar} + n_{Ar+} + n_{Cu} + n_{Cu+}) + T_e n_e = p, \qquad (13)$$

by neutrality condition:

$$n = n_{Ar+} + n_{Cu+}, \qquad (14)$$

and by equation (4 ) that determines Cu to Ar ratio.

The above equations (1,4-14) constitute a compete set for twelve unknown functions: $T_e$, $T_h$, $n_e$, $n_{Ar}$, $n_{Ar+}$, $n_{Cu}$, $n_{Cu+}$, $q_e$, $q_h$, E, $J_{Ar+}$, and $J_{Cu+}$ .

[1] We use energy units for temperatures.

Ion diffusion in the case of two different ions is a rather complicated phenomenon (see [31,32]), especially combined with ionization-recombination equations (11,12).

The substantial simplification that we have used in this work, is substitution equations describing diffusion of two sorts of ions with a equation describing diffusion of a single "average ion". According to the "average ion" approach, the equation that describes non-ionization equilibrium plasma, has the following form[2]

$$D\frac{d^2 n_e}{dx^2} + \beta n_e N_e^2 - \beta n_e^3 = 0 \qquad (15)$$

Here D is the common average diffusion coefficient, *b* is the average recombination coefficient, $N_e$ is the ionization-equilibrium electron concentration.
Hereafter capital letters denote ionization equilibrium densities.

Let us consider boundary conditions starting with far from the anode side of the layer. We assumed that far from the anode, the Joule heating is balanced by heat losses due to radiation:

$$\frac{J^2}{\sigma(T_\infty)} = W(T_\infty). \qquad (16)$$

Condition (16), at a given current density, determines $T_\infty$, the plasma temperature far from the anode:

$$T_e(x \to \infty) = T_\infty$$
$$T_h(x \to \infty) = T_\infty \qquad (17, 18)$$

Boundary condition for (15) takes into account that each species are in ionization equilibrium far from the anode:

$$n_e(x \to \infty) = N_e(T_\infty) \qquad (19)$$

Now, let us proceed to boundary conditions at the anode side of the layer, or, speaking more accurately, at the sheath-neutral plasma boundary. Here we have to specify boundary conditions for electron current density, ion current density and for both temperatures, $T_e$ and $T_h$.

According to the Bohm criterion, ion velocity equals to $\sqrt{\frac{T_e}{M}}$ at this boundary

$$-D\left.\frac{dn_e}{dx}\right|_{x=0} = n_e(0)\sqrt{\frac{T_e}{M}} \qquad (20)$$

[2] Although it is not essential in the "average ion" approach, we used the common average diffusion coefficient to describe ambipolar diffusion of both kinds of ions. Also, we used the same recombination coefficient for both ions. Note that in the Thompson's simple theory of three body recombination there are no specific parameters of the recombining ion.

For temperature of heavy particles we have obvious condition: heavy particles temperature at the anode proximity equal to the anode temperature

$T_h(0) = T_{anode}$ (21)

At the neutral plasma – sheath boundary one can write

$$J = \frac{e}{4} n_e(0)\bar{v}_e \times \exp(-\frac{\Delta V_{sh}}{T_e(0)}), \quad (22)$$

where $DV_{sh}$ is the voltage drop inside the sheath (repelling electrons moving toward anode), and $n_e(0)$ is the electron concentration at the sheath-plasma boundary, see (20). For DV one obviously have

$$\Delta V_{sh} = T_e(0) \times \ln\left(\frac{en_e(0)\bar{v}_e}{4j}\right). \quad (23)$$

Electrons that arrive from plasma at the sheath-plasma boundary should have enough energy to path over the potential barrier inside the sheath. This means the following condition should be satisfied

$$-\kappa_e \frac{dT_e}{dx}\bigg|_{x=0} = J \times T_e(0) \times \ln\left(\frac{en_e(0)\bar{v}_e}{4j}\right) \quad (24)$$

Our preliminary calculations have showed that potential barrier in the Langmuir sheath is low, no more than 0.2V. This led us to the following set of boundary conditions at the anode surface:

$$n_e(0) = \frac{4J}{e\bar{v}_e} \quad (25)$$

$$\kappa_e \frac{dT_e}{dx} = 0 \quad (26)$$

These boundary conditions replace conditions (22-24). It is shown there that both approaches give very close results.

One can see that we have correct number of boundary conditions. For three second-order ordinary differential equations we have the following: Three boundary conditions: (12,13) and condition of ionization equilibrium for the far from the anode region. Close to the anode we also have three boundary conditions: (18, 22, 23).

The relaxation method was used to solve the problem. For this purpose equation were written in "time-dependant" form:

$$C_e \frac{\partial T_e}{\partial t} = \frac{\partial}{\partial x}\left(\kappa_e \frac{\partial T_e}{\partial x} - 3.2\frac{j}{e}T_e)\right) + jE - W - 3\frac{m}{M} n_e \nu (T_e - T_h) \quad (27)$$

$$C_h \frac{\partial T_h}{\partial t} = \frac{\partial}{\partial x}\left(\kappa_h \frac{\partial T_e}{\partial x}\right) + 3\frac{m}{M} n_e \nu (T_e - T_h). \quad (28)$$

$$C_n \frac{\partial n_e}{\partial x} = \frac{\partial}{\partial x}(D_{amb} \frac{\partial n_e}{\partial x}) + \beta_{rec}\left[n_e N_e(T_e, T_h, c)^2 - n_e{}^3\right] \qquad (29)$$

While solving the system (27-29) we faced some difficulties with convergence. They can be avoided by corresponding choice of "specific heats" $C_e$ , $C_h$ and "density" $C_n$ in such a way that both temperatures and electron concentration relax to steady state at approximately the same rate.

These equations were solved at some fixed interval $[0,x_{max}]$, where $x_{max}$ was several times longer than the longest characteristic length. Special calculations with larger $x_{max}$ confirmed solution independence on the $x_{max}$ value.

Electric conductivity and translational electron thermal conductivity were calculated according Spitzer and Harm formulae with correction factor to account for electron-neutral atoms collisions [33]. Of electron-neutrals collisions only electron-argon collisions were taken into account, corresponding cross-section was taken from the paper by Devoto [34]. Reactive part of electron thermal conductivity was calculated as $n_{Ar}n_e f(T)$, with function $f(T_e)$ that approximates data by [34] on the reactive thermal conductivity of argon. Thermal conductivity of heavy particles (sum of neutral atoms and ions) has been calculated according simple kinetic formulae [35]; $S_{aa} = 5 \cdot 10^{-16} cm^2$ and $S_{ia} = 2 \cdot 10^{-15} cm^2$ were used as cross sections for neutral-neutral and ion-neutral collisions, respectively.

Radiation losses in argon-copper plasma were taken from the book [35]. For recombination coefficient we used coefficient of argon measured in [36], which is approximated by the formula.

$$\beta_{rec}(cm^6/s) = 3 \cdot 10^{-32}\left(\frac{11.6}{T_e(eV)} + 2\right)\exp\left(\frac{4.2}{T_e(eV)}\right) \qquad (30)$$

We used the following formulae to calculate the "average ion" diffusion coefficient. Ions diffusion is important at non-equilibrium ionization sub-layer. Here temperature is low and so is degree of ionization. Also, we are interested in the situations when copper vapor is a small admixture main plasma gas – argon. Therefore, the major scattering mechanism of both sorts of ions is collision with neutral argon atoms. For average diffusion coefficient we used

$$D = \frac{D_{amb}^{(Ar)} + D_{amb}^{(Cu)}}{2} \qquad (31)$$

where

$$D_{amb}^{(Ar)} = \frac{1 + T_e/T_h}{3} \frac{\bar{v}_{Ar}}{n_{Ar} S_{Ar^+,Ar}} \qquad D_{amb}^{(Cu)} = \frac{1 + T_e/T_h}{3} \frac{\bar{v}_{Cu}}{n_{Ar} S_{Cu^+,Ar}} \qquad (32)$$

For charge exchange $Ar^+$-Ar and $Cu^+$-Ar collisions cross-sections we used average of $S_{Ar+,Ar} = 3\ 10^{-15}$ cm$^2$ and $S_{Cu+,Ar} = 1\ 10^{-15}$cm$^2$ values. Special calculations showed that

anode layer characteristics are rather insensitive to the value of the ion diffusion coefficient.

**Results of calculations**

First, we calculated parameters of anode layer in one atmosphere of pure Argon arc. This was done to have the reference point. Figure 3 shows typical voltage distribution in this case. One can see that electric field changing its sign when approaching the anode. The extrapolated plasma voltage drop $V_{pl}$ is shown. It is negative.

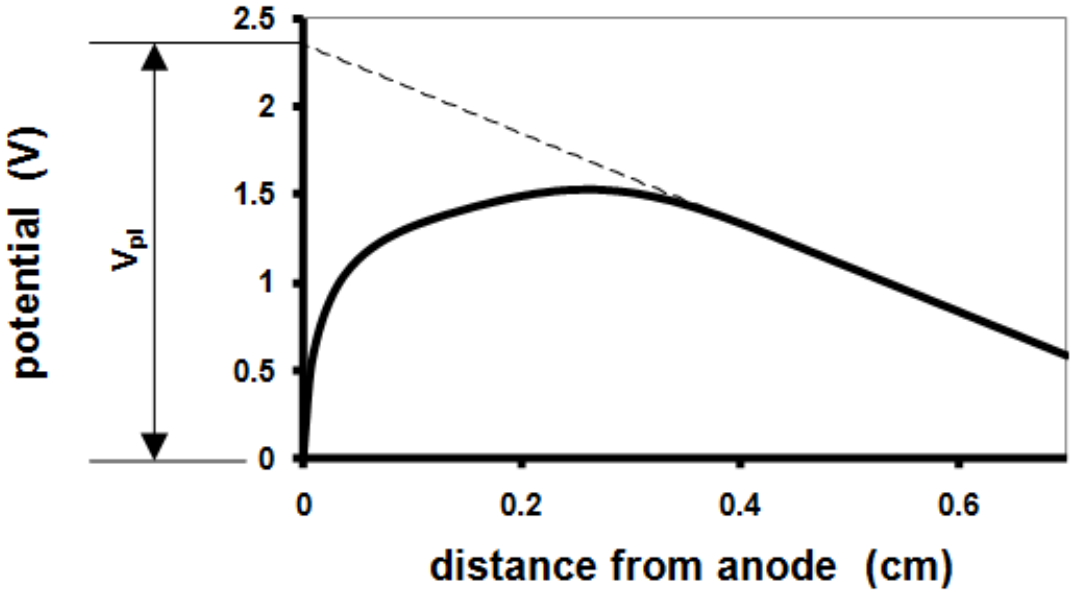


Fig. 3. Potential distribution close to anode. Argon. J=120A/cm$^2$. Anode layer voltage drop (2.3 V) is shown.

Presence of anode vapor leads to a substantial redistribution of potential inside the layer, which can be clearly seen on figure 4. This figure shows potential distributions at approximately the same current density of 414 A/cm$^2$ with and without copper vapor.

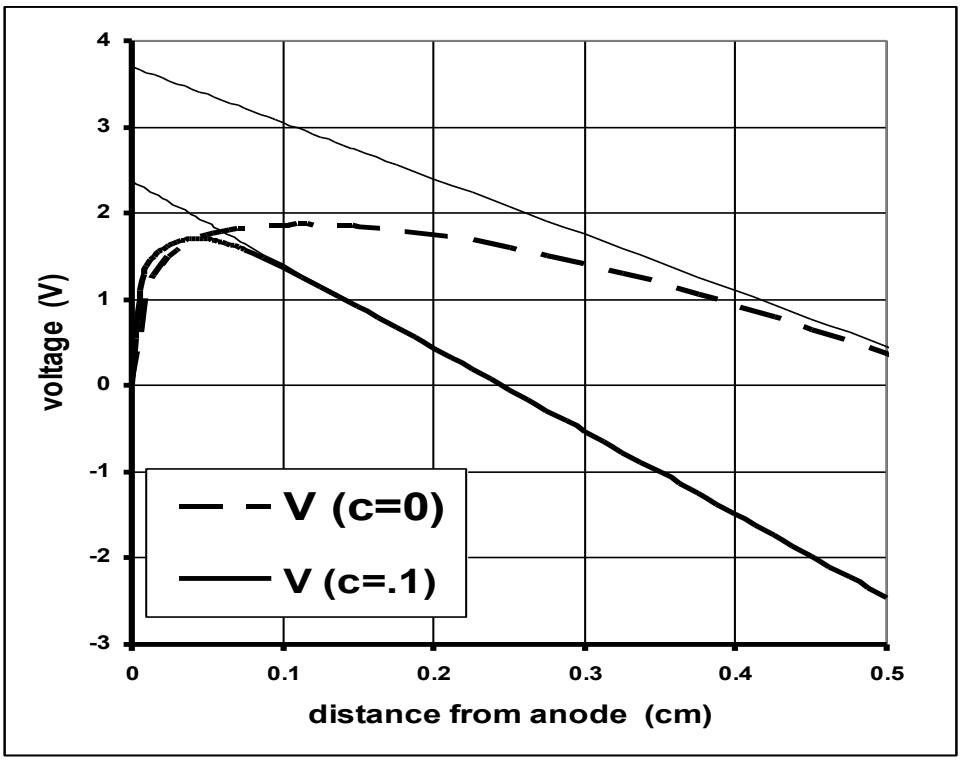


Fig. 4. Potential distribution close to anode. J = 120 A/cm$^2$. Dashed line: Pure Ar, solid line: Ar + 10 mol. % copper vapor.

As one can see from this picture, in pure argon, the electric field starts to decrease and then changes its sign relatively far from the anode. On the contrary, with evaporating anode, electric field remains positive up to a close distance from the anode. It changes its sign at the very proximity of the anode, where the main gain in voltage occurs.

Electron temperature distributions for the same conditions as in figure 4 are shown in figure 5.
As it was indicated in the introduction, one of the main goals of this paper is to calculate the voltage-current density characteristic of the anode layer. These characteristics at c=0% (pure argon), c=1% and c=10% are show in figure 6.

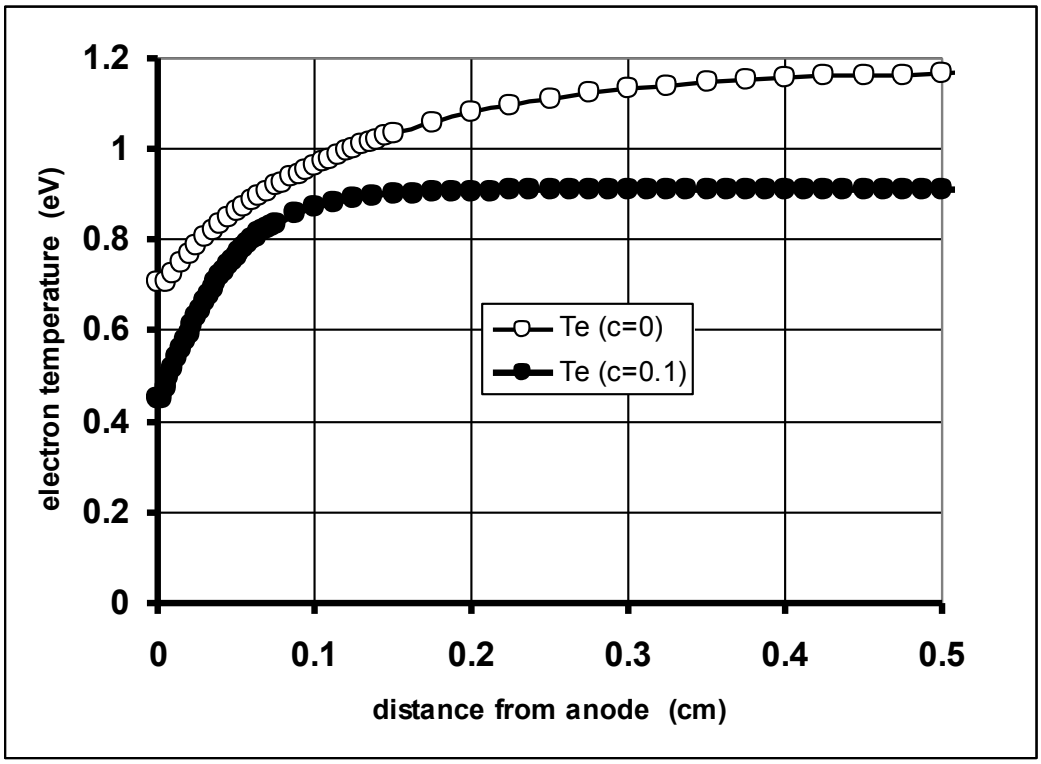


Fig. 5. Electron temperature distribution. Circles: pure Ar, triangles: c=10%.

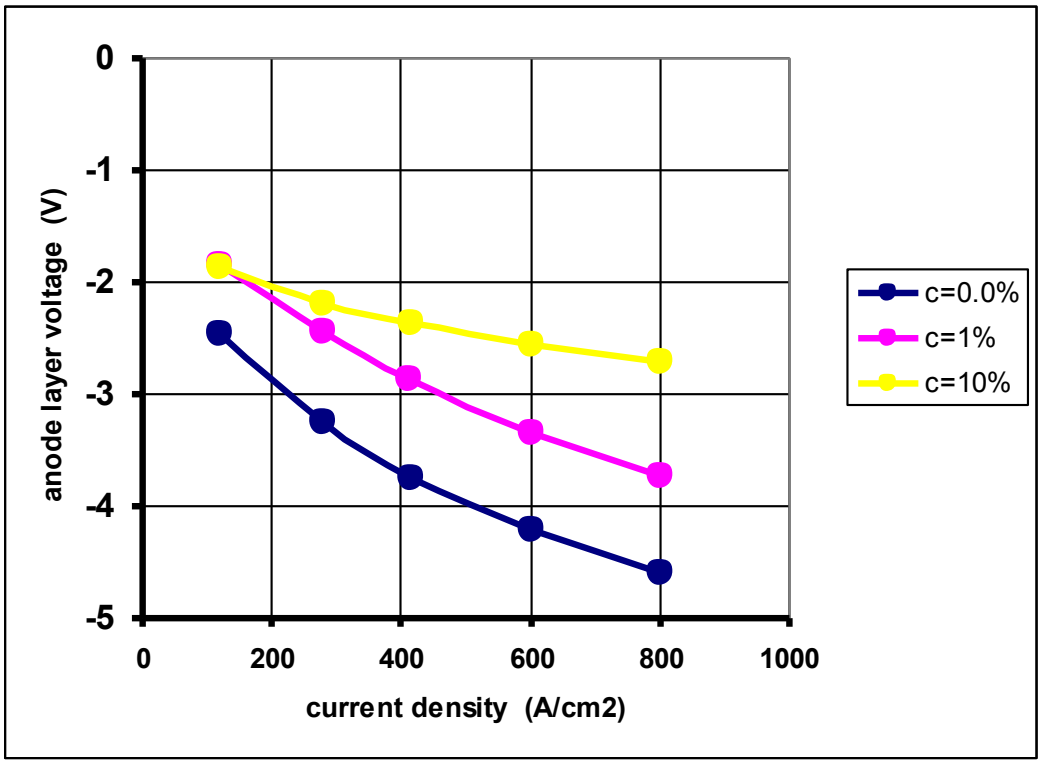


Fig. 6. Anode layer voltage – current density characteristics at different copper vapor concentrations.

For better understanding the data depicted in figure 6, it is useful to calculate the anode layer thickness. It can be defined in different ways. We defined it in the following way

$$\Delta x = \frac{\int_o^\infty x\left[T_e(x) - T_\infty\right]dx}{\int_o^\infty \left[T_e(x) - T_\infty\right]dx}. \qquad (33)$$

Figure 7 shows Dx as function of current density. Note, as it was shown in [10], the anode layer contracts as current density increases.

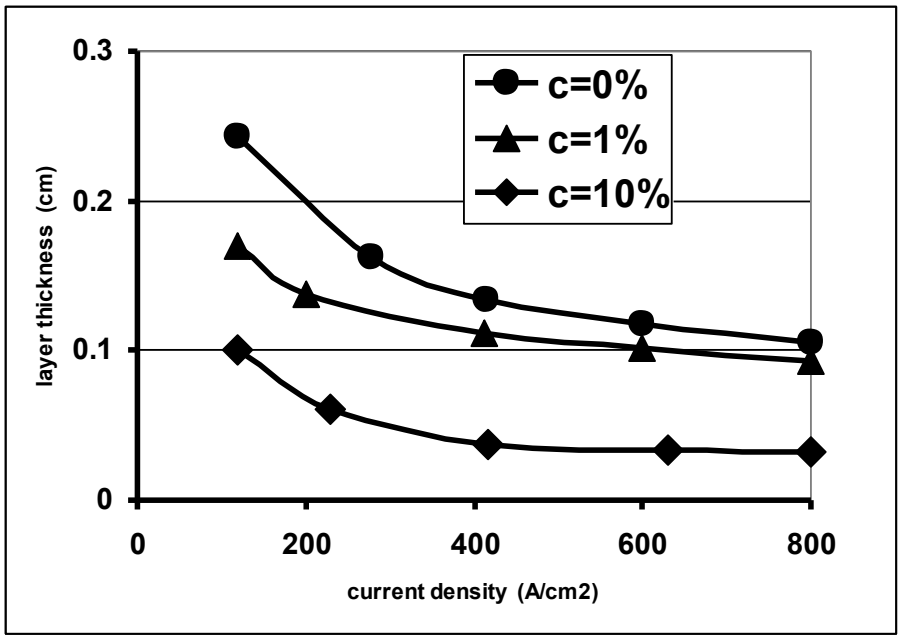


Fig. 7. Thickness of the anode layer as function of the current density.

According to the qualitative consideration given in Introduction, increase in vapor density should give rise to the voltage across the anode layer. As one can see from the figure 6, in general, it is true. However, curves at c=1% and c=10% at low densities do not follow this rule. The obtained dependence of the anode layer voltage on current density and on vapor concentration has the following qualitative explanation. The voltage across the anode layer is determined by two competing factors: voltage gain due to electron diffusion and voltage loss due to fall of the electrical conductivity on the anode approaching. These two factors depend on current density in different ways. The voltage gain due to the first factor can be estimated as $\overline{T}_e \ln\left(\frac{n_e(\infty)}{n_e(0)}\right)$, where $\overline{T}_e$ is an average electron temperature in the anode layer, $n_e(\infty)$ and $n_e(0)$ are the electron densities far and close to the anode, respectively. This voltage gain is almost independent on the current density: it slightly increases mostly due to rise in $\overline{T}_e$ when current density increases. On the other hand, the voltage loss due to electrical conductivity decline depends on the thickness of the anode layer in much

stronger way: the narrower the layer, the less is the extra voltage. Since the anode layer thickness decreases as current density increases, the second factor (voltage losses) becomes less and less important, and voltage gain due to the first factor becomes more visible.

The above consideration is valid for both evaporating and non-evaporating anode. Now let us return to the curves in figure 6. At relatively low current densities (~200A/cm$^2$ and lower), the anode layer at c=10% is substantially narrower than that of c=1% layer, see figure 7. Therefore, anode layer at 10% has advantage due to a relatively low voltage loss in the region of low electrical conductivity. At higher current densities, as thicknesses of anode layer shrink and influence of the second factor decreases, the curves at different vapor densities become arranged according to influence of the first factor: the higher the vapor density, the less is the voltage gain.

**Arc voltage measurements and anode layer voltage evaluation**

The most direct comparison of our calculation could be provided by probe measurements. Unfortunately, there is no such data. The available information is limited to influence of anode evaporation on total arc voltage. However, even this information is contradictory. Etemadi and Pfenfer [2] measured voltage of an argon arc with copper anode at 10 mm inter-electrode gap and current in 150A to 250A range. They found that anode evaporation decreases the arc voltage: by 0.8 V at 150A, by 0.1V at 200A and by 0.7 V at 250A. Experimenting with short (5mm) arc with stainless steel anode, Farmer et. al. [37] didn't found any significant change in arc after onset of anode evaporation. Gonzalez et. al., in their experiments with 90A arc [5], didn't find any arc voltage difference between arc with and without anode evaporation. On the other hand, calculations performed by the same Toulouse group (Lago et al. [38]) for 200A, 10 mm long arc in Argon arc with iron anode showed that evaporation increases the arc voltage by 1.5V. Menart and Lin [8] performed modelling of the 200A, 10 mm argon arc with copper anode. Their conclusion for the arc voltage was: 17.4 V for pure Argon and 17.2 for arc with evaporating anode. Note that in these calculations Non-LTE ionization non-equilibrium plasma was not considered. Anode layer, considered in these papers, therefore, was not included.

In view of scarce and ambiguity of these data, we performed our own measurements. The experimental set up is shown in figure 8. It consisted of GTAW torch, two different anodes (see below), the high-speed camera that allowed us to monitor the arc, and the oscilloscope to measure the arc voltage. Presence of the anode evaporation was indicated by the characteristic green glow.

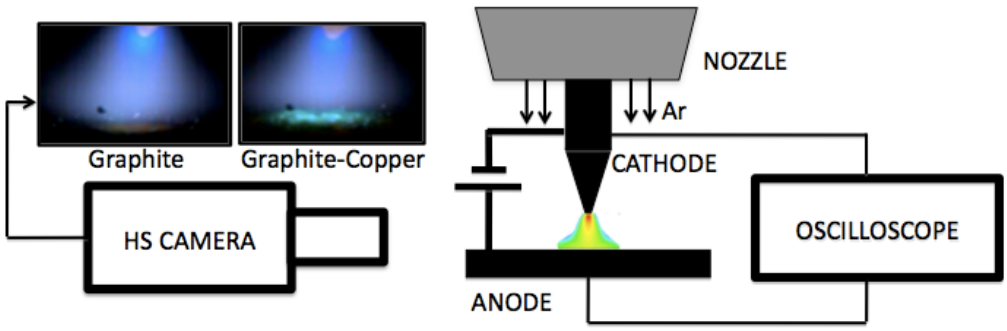


Fig. 8. Experimental set up.

Experiments were performed with the same torch and two different anodes. One, the control one, was made of solid graphite. Another, also made of graphite had a cavity where the piece of copper was placed. After the arc was struck, this piece of copper was melted and created a bubble filling the cavity. In this way, the second anode was formed. Plasma gas was Argon; cathode was made of thoriated tungsten of 1.2 mm diameter.

The measurements were performed at the arc current in the range from 50A to 250A. At lower currents it was difficult to obtain anode evaporation. Also, arc was not very stable. At currents 250A at higher, the surface of the copper insert became violent, anode attachment along it moved randomly. It was difficult to monitor the inter-electrode gap at these circumstances.

Every data point at each current and at each inter-electrode gap is an average of three measurements. To increase accuracy of measurements, the inter-electrode gap was re-established every time for each of these three measurements (it was intentionally increased and then set up back to the predetermined value). In the case of the curved anode surface (copper insert in form of a bubble), there is uncertainty on what should be considered as the inter-electrode gap. Special experiments were performed to verify that the arc voltage depends on the shortest cathode-to-anode distance not on the shape of the anode.

Figure 9 and figure 10 show the measured arc voltages, figure 11 shows DV= $V_{arc}$(with anode evaporation) – $V_{arc}$ (without anode evaporation).

To interpret these data, note that voltage, measured by a voltmeter consists of a number of components: voltage drop inside the cathode stick, near-cathode voltage drop in plasma, voltage drop inside the plasma column (if any), voltage drop across the anode layer in plasma, and the voltage drop inside the anode body (see the figure 12). It is known that the voltage across the cathode parts of the arc is rather autonomous. In our opinion, the voltage drop inside the plasma column is either low or the onset of anode evaporation does not effect it much. That conclusion follows from the experimental observation that, within accuracy of our measurements, DV doesn't depend on inter-electrode gap. It also follows from the experimental observations that vapour doesn't penetrate into column deeper than by one to two millimetres, see for example [8, 38] and recently published review [9]. We conclude that DV is associated with difference between anode layers and voltage drops inside the anode bodies (the latter will be discussed below).

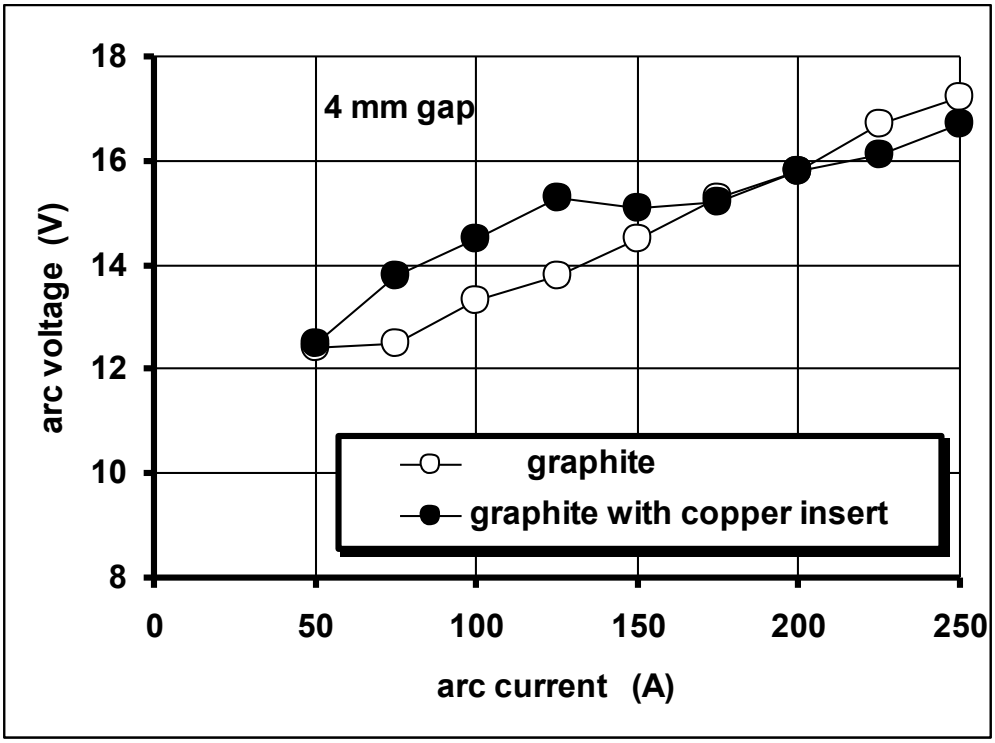


Fig. 9. Arc voltage at 4 mm inter-electrode gap

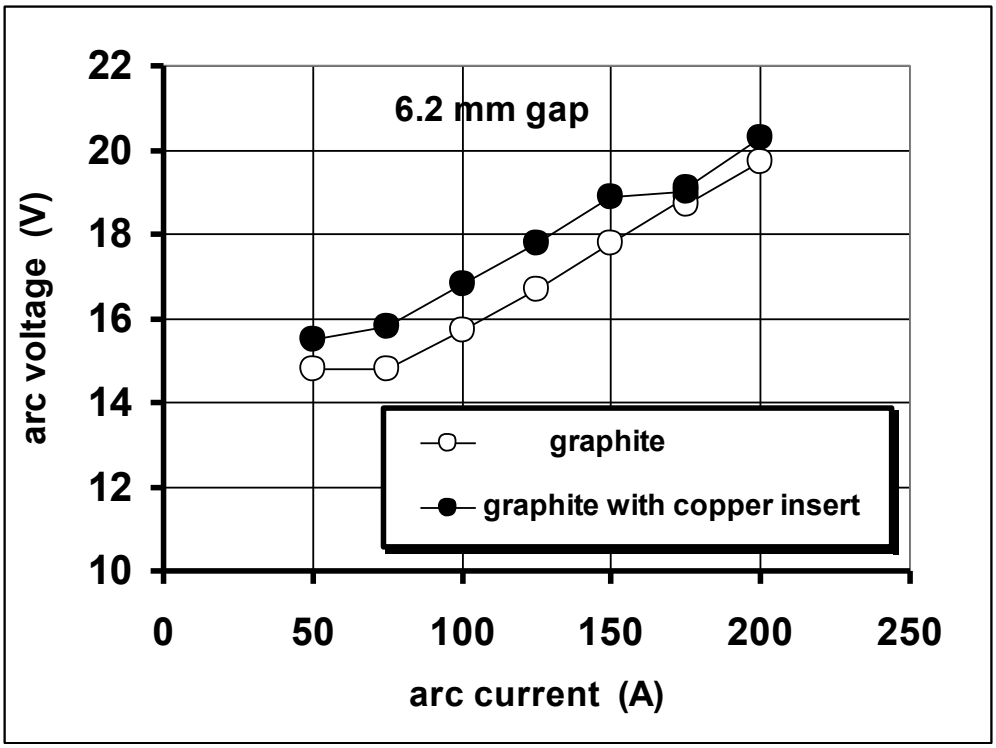


Fig. 10. Arc voltage at 6.4 mm inter-electrode gap.

From figure 11, one can see that the whole current range can be divided in to regions: relatively low current region (50A to 150A) and relatively high current region: 150A and higher. Let us consider the DV behaviour at low current region first. The most important experimental fact is that DV is positive. This means that arc voltage in the case of evaporation anode is higher than in the case of arc with non-evaporating

anode. The difference is relatively low at low currents, increases with current, and then approximately saturates.
However, at higher currents, DV starts to decline and in some measurements it changes its sign at the end of the high current region. We attribute this change in voltage behaviour to the voltage drop inside the body of anode. Since current is concentrated at the anode attachment, there is a voltage drop on the order of $Ar(pJI)^{1/2}$. Here r is resistivity of the anode material, I is the arc current, J is the current density at the arc attachment, and A is a number on the order on unity, which depends on the current distribution inside the anode attachment (it is ¼ if current is distributed uniformly and 1/p for the Gaussian distribution). In the case of anode with the copper insert, current exits the anode from the material with very low resistivity (copper), see figure 13. Therefore, the corresponding voltage drop is negligible. However, in the case of the solid graphite, which resistivity is not low, the corresponding voltage drop is substantial, especially at high arc currents.
To obtain the difference between anode layers with and without evaporating anodes one has to subtract from the arc voltage with graphite anode the voltage drop inside the body of the anode. Without pretending to any significant accuracy, the following consideration semi-quantitatively shows that the corresponding correction eliminates the DV decline at the high currents.

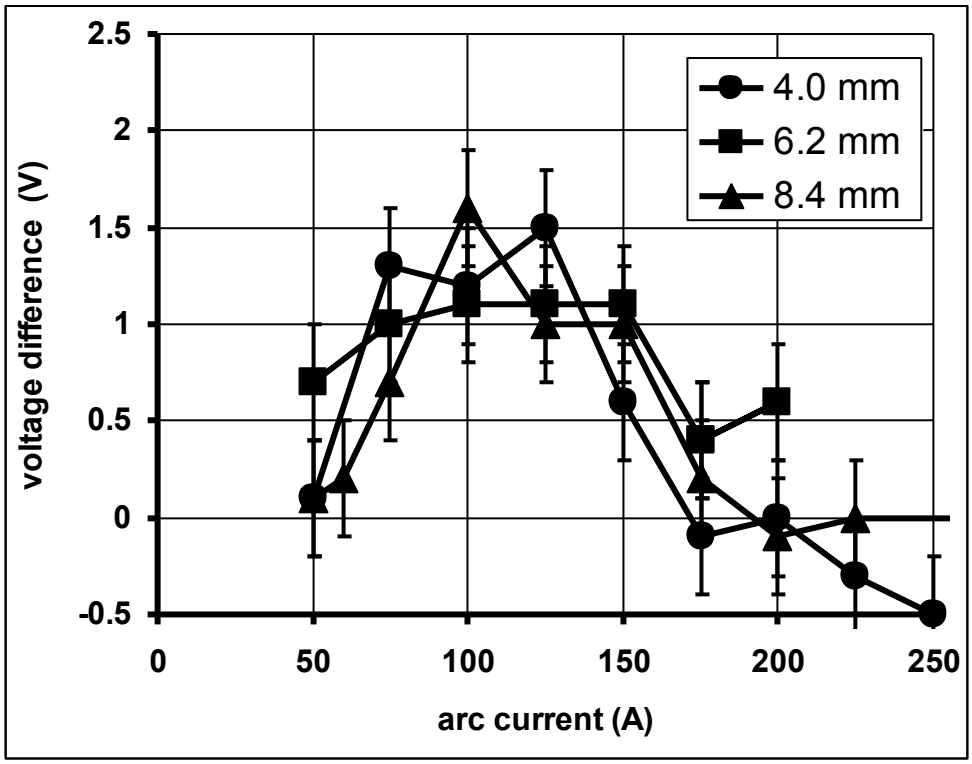


Fig. 11. $DV=V_{arc}$(copper insert) – $V_{arc}$(graphite), difference between the voltage of the arc with copper insert in graphite and the voltage of the arc with pure graphite anode.

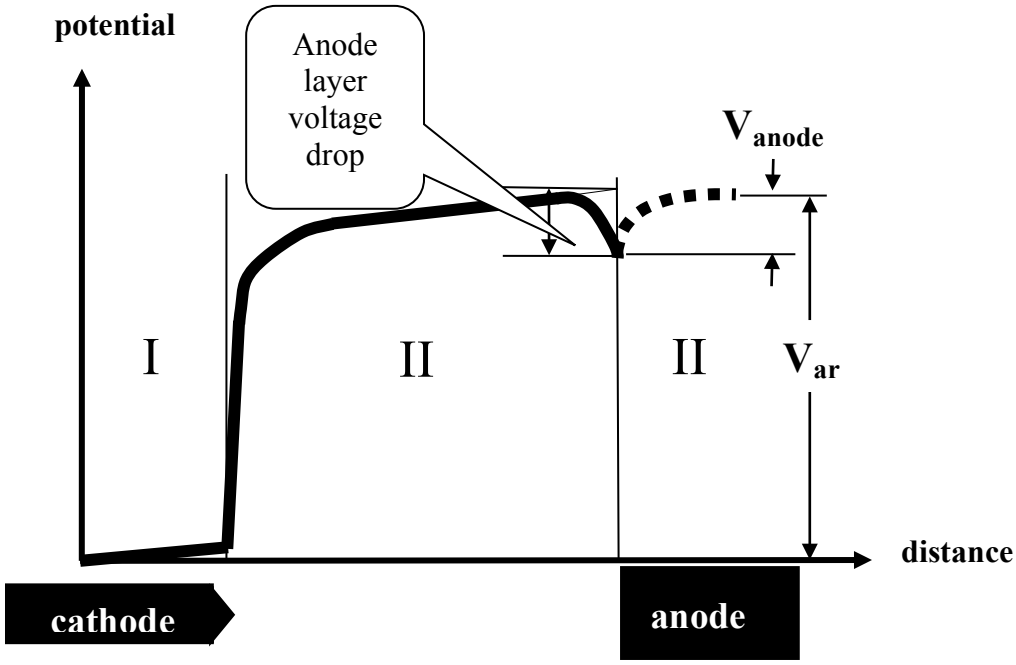


Fig. 12. Schematic distribution of potential in the arc (electrodes included ). Dashed line shows $V_{anode}$, voltage drop inside graphite anode.

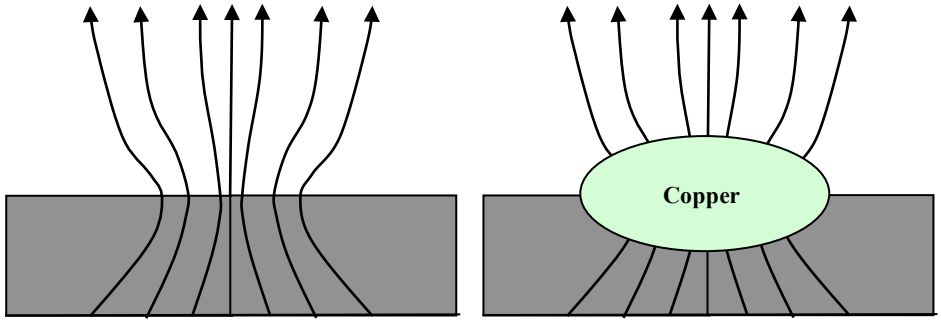


Fig. 13. Schematic of the current lines in case of solid graphite anode (left) and anode with copper insert (right).

Figure 14 shows the average DV dependence on the arc current averaged over all three inter-electrode gaps. It is shown in figure 14 by filled circles. To calculate the voltage drop inside the anode body, graphite resistivity should be known. Different types of graphite have very different resistivity. To eliminate this uncertainty, we cut a rectangular specimen of the graphite used and measured its resistance, and from that, its resistivity. It turned to be 0.01 Wcm. We didn't measure graphite high temperature resistivity assuming it is approximately the same [39]. We estimated current density at the anode to have order of magnitude 300 A/cm$^2$ - 400 A/cm$^2$. With this current density, the corrected DV dependence on the arc current is shown in figure 14, open circles. One can see that corrected in the above described way, DV(I) do not decline as much any more at high currents .

It is necessary to relate arc current and current density at anode in order to compare the above experimental data to our calculations. Unfortunately, the corresponding experimental data on current density dependence on the arc current is very scattered even for pure argon plasma gas not saying about argon contaminated with the products of anode evaporation. Experiments with pure argon and arc current from 50A to 300A, give axial current density at anode values from 100A/cm$^2$ [40] up to about 2000A/cm$^2$ [30]. As a consequence of these results, it is not easy to transform our experimental $\Delta V$ dependence on current into a $\Delta V$ dependence on current density. However, the average of most experimental data on current density at the anode [41-45] is about 300 A/cm$^2$ - 400 A/cm$^2$. According to our experiments, anode voltage increases (becomes less negative) by approximately 1-2 V on evaporation onset, see figure 14; calculations give $\Delta V \sim 1$ - 1.5 V in this range of current densities.

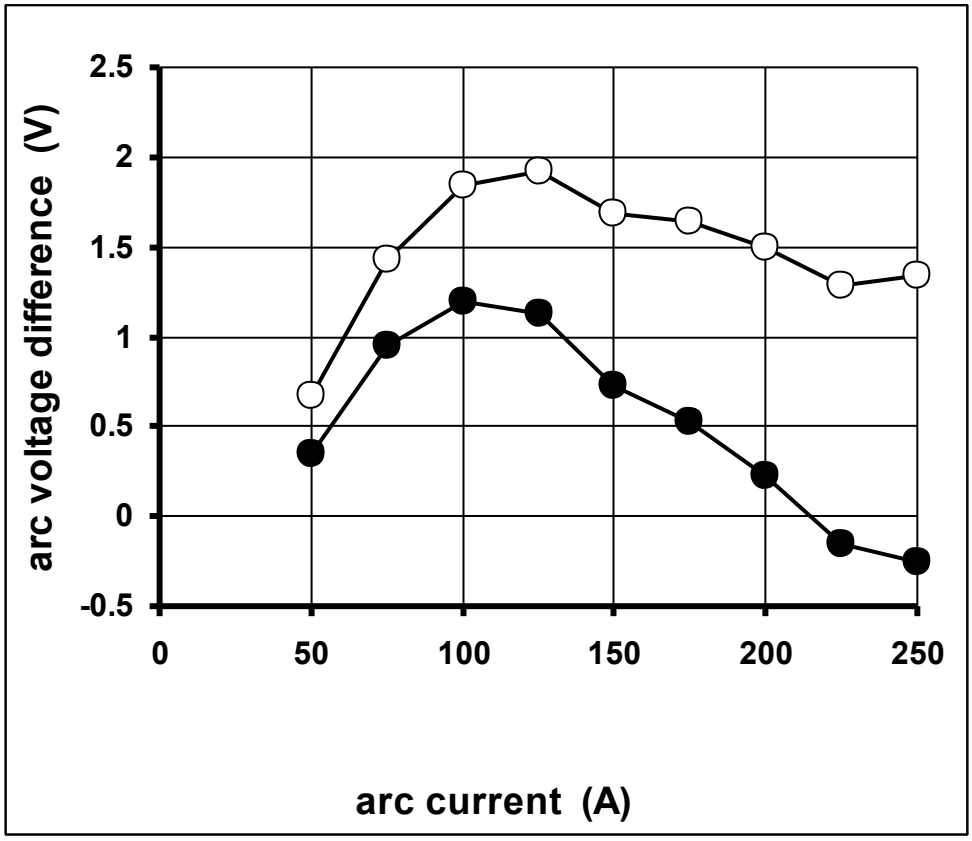


Fig. 14. Dependence of the DV = $V_{arc}$(copper insert) – $V_{arc}$(graphite) averaged over three different inter-electrode gaps. Filled circles – without correction on voltage drop inside the graphite, open circles – with this correction.

We conclude that a) experiments confirm voltage increase upon anode evaporation and b) the voltage increase is close to that predicted by calculations. As for dependence of $\Delta V$ on current density, available experimental data do not allow us to compare them to our calculations. Two-dimensional calculations are necessary. They would allow one to include plasma flow, this being the effect that cannot be included in one-dimensional calculations.

Finally, the answer to the question posed in the Introduction regarding the arc behaviour on the anode evaporation onset, depends on whether arc voltage increases or decreases on anode evaporation. In case it decreases, one might expect snow-ball

effect. In the opposite case of voltage increase, the arc would try to avoid hot places at the anode surface thus trying to minimize the arc voltage. Our calculations and experiments point to that second case. Another observation also confirms this conclusion: at high currents, when anode evaporation level is high, the anode attachment starts to move randomly, obviously trying to avoid hot places at the anode surface.

## Conclusions

The anode layer of a high-current, high-pressure arc with evaporation anode was considered in one-dimensional approximation.
Calculations were performed for arc in Argon of one atmosphere pressure with 1% and 10% amounts of copper vapor. As one would expect, even small amounts of anode material are enough to substantially change properties of anode layer.
It was shown that evaporation reduces the effect of electron diffusion toward the anode. As a result, the voltage across the anode layer increases (becomes less negative), although at all the calculated current densities this voltage remained negative.
Experiments to check this conclusion were performed with a typical welding GTAW arc with non-evaporating graphite anode and evaporating copper anode. Comparison of the arc voltages with these two types of anode showed that anode evaporation increases the arc voltage. It was shown that the arc voltage change is due to increase of the voltage inside the anode layer close to the evaporating anode. The experimental results are, therefore, in agreement with our calculations.

References


1. L.E.Eroshenko, V.S.Mechev and A.S.Dem'yanchuk "Study of an Argon Arc Near an Evaporating Anode" J.Appl. Spectr. **30** 1-3 (1979)
2. K.Etemadi and E.Pfender "Impact of Anode Evaporation on the Anode Region of a High-Intensity Argon Arc" Plasma Chem. Plasma Proc. 5, 175-182 (1985)
3. H.Ouojji, B.Cheminat and P.Andanson "Model of an Electric Arc Column" J.Phys. D. **20**, 635-638 (1987)
4. G.Y. Zhao, M. Dassanayake and K. Etamadi "Numerical Simulation of Free-Burning Argon Arc with Copper Evaporation from the Anode." Plasma Chem. Plasma Proc. **10**, 87-98, (1990)
5. J. J. Gonzalez, M.Bouaziz, M.Razafinimanana, and A. Gleizes. "The Influence of Iron Vapor on an Argon Transferred Arc" Plasma Sources Sci. Techn. **6**, 20-28 (1997)
6. Gonzalez et.at. " Mathematical Modeling of a Free-Burning Arc in the Presence of Metal Vapor" J. Appl. Phys. **74**, 3065-3070 (1993)
7. A.Gleizes, M.Bouaziz, J.J.Gonzalez, and M.Razafinimanana "Influence of the Anode Material on an Argon Arc" IEEE Trans. Plasma Sci. **25**, 891-896 (1997)
8. J. Menart and L.Lin "Numerical Study of a Fee Burning Argon Arc with Copper Contamination from the Anode" Plasma Chem. Plasma Proc. **19**, 153-157
9. A. B. Murphy, M.Tanaka, K.Yamamoto, S.Tashiro, T.Sato, and J.J.Lowke "Modeling of thermal plasmas for arc welding: The role of the shielding gas properties and of metal vapour" J.Phys.D. **42**, 194006 (2009)
10. V.A.Nemchinsky, L.N.Peretts "Anode Sheath in a High-Pressure, High-Current Arc" Sov. Phys. Tech. Phys 22, 1083-1087 (1977)
11. H.A.Dinulescu and E.Pfender " Analysis of the Anode Boundary Layer of High Intensity Arcs" J.Appl.Phys. 51, 3149-3157 (1980)
12. V.A.Nemchinsky "Plasma Parameters Near a Small Anode in a High-Pressure Arc (Gas Metal Arc Welding)" J.Phys.D. 27, 2515-2521 (1994)
13. J.J.Lowke and J.C.Quartel "Use of Transport Coefficients to Calculate Properties of Electrode Sheaths of Electric Arcs" Australian J.Phys. 50, 539-552 (1997)***)***
14. J.Jenista, J.V.Heberlein, and E.Pfender "Numerical Model of the Anode Region in High-Current Electric Arcs" IEEE Trans. Plasma Sci. 25, 883 (1997)***)***
15. T.Amakawa, J.Jenista, J.Heberlein, and E. Pfender "Anode-Boundary-Layer Behavior in a Transferred, High-Intensity Arc." J.Phys. D. **31**, 2826-2834 (1998)
16. C.S.Wu, M.Ushio, and M.Tanaka "Determining the Sheath Potential of Gas Tungsten Arcs" Comput. Material Sci. **15**, 341-345 (1999)
17. C.S.Wu, M.Ushio,and M.Tanaka "Modeling the Anode Boundary Layer of High-Intensity Argon Arcs" Comput. Material Sci. **15**, 302-310, (1999)
18. M.Tanaka, M.Ushio, and C.Wu "One –Dimensional Analysis of the Anode Boundary Layer in Free-Burning Argon Arcs" J.Phys.D. **32**, 605-611 (1999)
19. L. Sansonnes, J.Haidar, and J.J.Lowke "Prediction of Properties of Free Burning Arcs Including Effects of Ambipolar Diffusion" J.Phys.D. **33** 148-157 (2000)
20. J.J.Lowke and M.Tanaka "LTE-Diffusion Approximation for Arc Calculations" J.Phys.D. **39**, 3634-3643 (2006)
21. V.A. Nemchinsky "Anode Layer in a High-Current Arc in Atmospheric Nitrogen" J.Phys.D. **38**, 4082-4089 (2005)

22. G.Yang and J.Heberlein “Anode Attachment Modes and Their Formation in a High Intensity Argon Arc” Plasma Sources Sci. Techn. **16**, 529-542 (2007)
23. G.Yang and J.Heberlein “Instabilities in Anode Region of Atmospheric Pressure Arc Plasmas” Plasma Sources Sci. Techn. **16**, 765-773 (2007)
24. S. Ghorui, J.Heberlein, and E.Pfender “Non-equilibrium Modeling of an Oxygen-Plasma Cutting Torch” J.Phys.D. **40**, 1966-1976 (2007)
25. H.-P. Li and M.S.Benilov “Effect of Near-Cathode Sheath on Heat Transfer in High Pressure Arc Plasmas” J.Phys.D. **40** 2010-2017 (2007)***)***
26. N.Sander, K.Etemadi, K.C.Hsu and E.Pfender “Studies of the Anode Region of a High-Intensity Argon Arcs” J.Appl.Phys. **53**, 4136-4145 (1982)
27. N.A.Sanders and E.Pfender “Measurement of Anode Falls and Anode Heat Transfer in Atmospheric Pressure High Intensity Arcs” J.Appl.Phys. **55**, 714-722 (1984)
28. M.Tanaka, M.Ushio “Observations of the Anode Boundary Layer in Free-Burning Argon Arcs” J.Phys.D. **32**, 906-912 (1999)
29. M.S.Benilov “Understanding and modeling plasma-electrode interaction in high-pressure arc discharges: a review” J.Phys.D. **41**, N14, 14400 (2008)
30. J. Heberlein, J. Mentel and E. Pfender " The anode region of electric arcs: a survey" J. Phys. D: Appl. Phys. **43**, 023001 (2010)
31. A.B.Murphy “Diffusion in equilibrium mixtures of ionized gases” Phys.Rev.E **48**, 3594-3603 (1993).
32. A.B.Murphy “A comparison of treatments of diffusion in thermal plasmas” J.Phys.D. **29**,1922-1932 (1996)
33. J.P.Hirshfelder, C.Curtiss, and R.B.Bird. Molecular Theory of Gases and Liquids John Wiley & Sons, Inc., New York, 1954
34. R.S.Devoto. “Transport coefficients of partially ionized argon” Phys. Fluids **10**, 354 (1967)
35. M.I.Boulos, P.Fauchais, and E.Pfender. Thermal Plasmas. Fundamentals and Applications. vol.1 Plenum.N.Y. 1994
36. T. G. Owano, C. H. Krueger, and R. A. Beddini, “Electron–ion three-body recombination coefficient of argon,” AIAA J., vol. **31**, no. 1, pp. 75–82 (1993).
37. A J D Farmer, G.N.Haddad and L E Cram “Temperature determination in a free-burning arcs: III Measurement with molten anodes” J.Phys.D. **19**, 1723-1730 (1986)
38. F.Lago, J.J.Gonzalez, P.Frenton and A.Gleizes “ A numerical modeling of an electric arc and its interaction with the anode: PartI. The two-dimensional model” J.Phys.D. **37**, 883-897 (2004)
39. A.Cezairliyan and A.P.Miller “Heat capacity and electrical resistivity of POCO AXM-5Q1 graphite in the range 1500-3000K by a pulse-heating technique” Int. J. Thermophysics. **6**, 285-300 (1985)
40. J. Heberlein and E. Pfender "Investigation of the anode boundary layer of an atmospheric pressure argon arc" IEEE Trans. Plasma Sci. **5** (3), 171-180 (1977)
41. O. H. Nestor "Heat intensity and current density distribution at the anode of high current, inert gas arcs" J. Appl. Phys. **33** (5), 1638-1648 (1962)
42. P. F. Bulanyi and S. P. Polyakov "Effect of arc-burning regimes on specific thermal flux and current density distributions at the anode" Sov. Phys. Techn. Phys. **26** (3), 324-327 (1981)
43. N. H. Olson "Physical properties of the open argon arc" Linde Research report No 20. Speedway research laboratory. Indianapolis (1958)
44. J. A. Menart "Theoretical and experimental investigations of radiative and total heat transfer in thermal plasmas" *PhD Thesis* Department of Mechanical Engineering, University of Minnesota (1996)

45. G. A. Dyuzhev, N. K. Mitrofanov and S. M. Shkol’nik "Experimental investigation of the anode region of a free-burning atmospheric-pressure inert-gas arc" Tech. Phys. **42** (1), 30-34 (1997)

# ACKNOLEGDEMENTS

My thanks go firstly to my supervisor Emanuele Ghedini, for his continuous support throughout my doctoral studies and for his advices in directing my research activities. I am also very thankful to Prof. Vittorio Colombo, for his valuable inputs, his experience and constant encouragement to do my best.
I would like to acknowledge the help and support from former and current members of the Research Group for Industrial Applications of Thermal Plasmas of the University of Bologna. Particularly, I would like to express my gratitude to Alessia Concetti, Matteo Gherardi, Marco Boselli, Gianmatteo Cantoro, and Brais Vazquez for their friendship and for our numerous discussions that helped me settle many issues faced during my studies.
I would like to express my gratitude also to Silvano Dallavalle, Mauro Vancini, Riccardo Fazzioli, Marco Aiello, Angelo Romanini, and Paolo Rossin for their availability to share instrumentations, laboratories, and experience.
I would like to also thank Prof. Valerian Nemchinsky, now at Keiser University - Hollywood, Florida, USA - for his assistance and guidance during our collaboration in Bologna and for many helpful Internet conversations once he was back home.
I would also thank Prof. Masaya Shigeta, now at Tohoku University – Sendai, Japan – for the fruitful collaboration we had during his stay in Bologna and Dr. Tony Murphy, now at CSIRO – Lindfield, Australia - for our discussions during his brief visit in Bologna.
My gratitude goes also to people I supervised for their BA and MA thesis: Filippo Zinzani, Diego Zanini, Federica Mossa, Luca Gasperini, Federico D'Alessandris, Fabio Federici, Patrizia D'Annunzio, and Igor Zanardo.
I would like to thank my parents and relatives for their constant support throughout my life.
To my wife Giulia, I dedicate this thesis.